



Swansea University
Prifysgol Abertawe



Swansea University E-Theses

Multiscale modelling and experimentation of hydrogen embrittlement in aerospace materials.

Jothi, Sathiskumar

How to cite:

Jothi, Sathiskumar (2015) *Multiscale modelling and experimentation of hydrogen embrittlement in aerospace materials..* thesis, Swansea University.

<http://cronfa.swan.ac.uk/Record/cronfa42212>

Use policy:

This item is brought to you by Swansea University. Any person downloading material is agreeing to abide by the terms of the repository licence: copies of full text items may be used or reproduced in any format or medium, without prior permission for personal research or study, educational or non-commercial purposes only. The copyright for any work remains with the original author unless otherwise specified. The full-text must not be sold in any format or medium without the formal permission of the copyright holder. Permission for multiple reproductions should be obtained from the original author.

Authors are personally responsible for adhering to copyright and publisher restrictions when uploading content to the repository.

Please link to the metadata record in the Swansea University repository, Cronfa (link given in the citation reference above.)

<http://www.swansea.ac.uk/library/researchsupport/ris-support/>



Swansea University
Prifysgol Abertawe

DOCTOR OF PHILOSOPHY

**MULTISCALE MODELLING AND
EXPERIMENTATION OF HYDROGEN
EMBRITTLEMENT IN AEROSPACE MATERIALS**

by

SATHISKUMAR JOTHI

College of Engineering
Swansea University

Thesis submitted to Swansea University in fulfilment of the
requirements for the Degree of Doctor of Philosophy

April 2015

ProQuest Number: 10797914

All rights reserved

INFORMATION TO ALL USERS

The quality of this reproduction is dependent upon the quality of the copy submitted.

In the unlikely event that the author did not send a complete manuscript and there are missing pages, these will be noted. Also, if material had to be removed, a note will indicate the deletion.



ProQuest 10797914

Published by ProQuest LLC (2018). Copyright of the Dissertation is held by the Author.

All rights reserved.

This work is protected against unauthorized copying under Title 17, United States Code
Microform Edition © ProQuest LLC.

ProQuest LLC.
789 East Eisenhower Parkway
P.O. Box 1346
Ann Arbor, MI 48106 – 1346

Declaration and Statements

DECLARATION

This work has not previously been accepted in substance for any degree and is not being concurrently submitted in candidature for any degree.

Signed..... (Candidate)

Date..... 08/sep/2015.....

STATEMENT 1

This thesis is the result of my own investigation, except where otherwise stated.

Where correction services have been used, the extent and nature of the correction is clearly marked in a footnote(s).

Other sources are acknowledged by footnotes giving explicit references. A bibliography is appended.

Signed..... (Candidate)

Date..... 08/sep/2015.....

STATEMENT 2

I hereby give consent for my thesis, if accepted, to be available for photocopying and for inter-library loan and for the title and summary to be made available to outside the organisation.

Signed.. (Candidate)

Date..... 08/sep/2015.....



MULTISCALE MODELLING AND EXPERIMENTATION OF HYDROGEN EMBRITTELEMENT IN AEROSPACE MATERIALS

ABSTRACT

Pulse plated nickel and nickel based superalloys have been used extensively in the Ariane 5 space launcher engines. Large structural Ariane 5 space launcher engine components such as combustion chambers with complex microstructures have usually been manufactured using electrodeposited nickel with advanced pulse plating techniques with smaller parts made of nickel based superalloys joined or welded to the structure to fabricate Ariane 5 space launcher engines. One of the major challenges in manufacturing these space launcher components using newly developed materials is a fundamental understanding of how different materials and microstructures react with hydrogen during welding which can lead to hydrogen induced cracking.

The main objective of this research has been to examine and interpret the effects of microstructure on hydrogen diffusion and hydrogen embrittlement in (i) nickel based superalloy 718, (ii) established and (iii) newly developed grades of pulse plated nickel used in the Ariane 5 space launcher engine combustion chamber. Also, the effect of microstructures on hydrogen induced hot and cold cracking and weldability of three different grades of pulse plated nickel were investigated. Multiscale modelling and experimental methods have been used throughout. The effect of microstructure on hydrogen embrittlement was explored using an original multiscale numerical model (exploiting synthetic and real microstructures) and a wide range of material characterization techniques including scanning electron microscopy, 2D and 3D electron back scattering diffraction, in-situ and ex-situ hydrogen charged slow strain rate tests, thermal spectroscopy analysis and the Varestraint weldability test. This research shows that combined multiscale modelling and experimentation is required for a fundamental understanding of microstructural effects in hydrogen embrittlement in these materials. Methods to control the susceptibility to hydrogen induced hot and cold cracking and to improve the resistance to hydrogen embrittlement in aerospace materials are also suggested. This knowledge can play an important role in the development of new hydrogen embrittlement resistant materials.

A novel micro/macro-scale coupled finite element method incorporating multi-scale experimental data is presented with which it is possible to perform full scale component analyses in order to investigate hydrogen embrittlement at the design stage. Finally, some preliminary and very encouraging results of grain boundary engineering based techniques to develop alloys that are resistant to hydrogen induced failure are presented.

Keywords: Hydrogen embrittlement; Aerospace materials; Ariane 5 combustion chamber; Pulse plated nickel; Nickel based super alloy 718; SSRT test; Weldability test; TDA; SEM/EBSD; Hydrogen induced hot and cold cracking; Multiscale modelling and experimental methods.

ACKNOWLEDGEMENTS

First and foremost, I would like to thank Shanthini! My wife, you have always been there for me during these years showing you love and support even at times of struggle and when I have been far away around the world for conferences, visiting research, experimental works and technical meetings. I also want to thank my daughter Sasha that I would never been able to manage this work without your tremendous support. Thank you, I love you. We three are looking forward to a new phase of our lives.

I wish to thank my grandmother who is no more and my mother Selvi and father Jothi for their constant guidance, support and encouragement. Thanks to my brother Hari Prasath for his support and encouragement throughout the journey; without whom I would never have had the opportunity to complete this thesis.

I would like to thank Prof. Stephen GR Brown and Dr. Nick Croft who supervised my work with continuous encouragement, support and for providing me freedom I seemed to need and also for scientific and non-scientific discussions.

The author wants to express their thanks to European Union (EU) 7th framework (FP7) for funding through Multiscale modelling of hydrogen embrittlement “MultiHy” project. The author also wants to express thanks to Prof. Guido Schmitz from Stuttgart-Germany, Prof. Kenichi TAKAI from Tokyo-Japan, Dr. Mattias Thuvander from Chalmers-Gothenburg-Sweden, Dr. Joel Andersson from University of West-Trollhattan-Sweden, for giving access to laboratory test equipment and especially Dr. Sergiy Merzlikin from Max-Planck institute- Düsseldorf-Germany, Dr. Nick Winzer from Fraunhofer Institute for Mechanics of Materials (IWM)-Friburg-Germany for carefully carrying out the SSRT testing on alloy 718 and permeation test on nickel. I have been privileged to interact with Dr. Alan Turnbull from NPL-UK a Fellow of the Royal Academy of Engineering and fellow of Royal Society regarding hydrogen embrittlement and hydrogen trapping, etc... and I want to express my thanks to him for valuable discussions.

I want to express my thanks to Miss. Louise Wright from NPL-UK, Dr. Mark Coleman from Swansea University-UK, Dr. Soran Biroasca from Swansea University-UK, Mr. Peter Davies, Dr. Zoltan Balogh, Dr. Mattias Thuvander and Dr. Geoff West for valuable discussions on EBSD, SEM, Atom probe tomography (APT), FIB and metallurgical topics. Special thanks to Dr. Matous Mrovec –IWM-Friburg-Germany for valuable discussions related to grain boundary energy, atomic modelling and presentation my paper on Hydrogen

Embrittlement symposium at DPG meeting in Berlin-Germany (March/2015). The author also gratefully acknowledges the assistance of the MACH1 Laboratories at Swansea University-UK.

Special thanks to Dr.Eggert D.Reese and Dr.Torsten Sebald from AIRBUS-Munich-Germany for supplying the Ariane 5 combustion chamber materials and for valuable discussions related to Ariane 5 space launcher engines and combustion chambers and its manufacturing techniques and etc... and Special thanks to Dr. Joel Andersson from GKN Aerospace-Trollhattan-Sweden for supplying Nickel based superalloy materials.

I want to thank my friend Bharath Alex, Sivakumar, Thangadurai, Vasanthavel, Dr. Joel Andresson, Dr. Manickavasagam, Dr.Jianjun Chen (i.e Jeff), Dr.Kiran Vijayan, Dr. Ricardo Rodrigues Martins, Dr. Amarpal Singh regarding common thread to our thoughts that has provided many hours of stimulating conversation and I also wish to thank all my friends for their never ending light-heartedness and good humour.

PUBLICATIONS ARISING FROM THE THESIS

In the frame of this PhD thesis several journal publications, conferences papers and FP7 EU MultiHy project reports were published and presented as well as some invited lectures. Details are summarised below.

Peer-reviewed publications

- 1 S. Jothi, T.N. Croft, S.G.R. Brown, Modelling the influence of microstructural morphology and triple junctions on hydrogen transport in Nano-polycrystalline Nickel, *Composites Part B: Engineering*, 75 (2015) 104-118, [DOI:10.1016/j.compositesb.2014.09.042].
- 2 S. Jothi, T.N. Croft, S.G.R. Brown, Coupled Macroscale-Microscale model for hydrogen embrittlement in polycrystalline materials, *International Journal of Hydrogen Energy*, 40 (2015) 2882-2889, [DOI: 10.1016/j.ijhydene.2014.12.068].
- 3 S. Jothi, T.N. Croft, S.G.R. Brown, Meso-microstructural computational simulation of the hydrogen permeation test to calculate intergranular, grain boundary and effective diffusivities, *Journal of alloys and Compounds* (2014) (In Press), [DOI:10.1016/j.jallcom.2014.12.247].
- 4 S. Jothi, T.N. Croft, S.G.R. Brown, Multiscale multiphysics model for hydrogen embrittlement in polycrystalline nickel, *Journal of Alloys and Compounds* (2014);(In Press), [DOI:10.1016/j.jallcom.2014.12.073].
- 5 S. Jothi, T.N. Croft, S.G.R. Brown, Influence of grain boundary misorientation on hydrogen embrittlement in bi-crystal nickel, *International Journal of Hydrogen Energy* 2014;39:20671-20688,[DOI: 10.1016/j.ijhydene.2014.07.020].
- 6 S. Jothi, T.N. Croft, S.G.R. Brown, E.A. de Souza Neto, Finite element microstructural homogenization techniques and intergranular, intergranular microstructural effects on effective diffusion coefficient of heterogeneous polycrystalline composite media, *Composite Structures* 2014;108:555-564,[DOI: 10.1016/j.compstruct.2013.09.026].
- 7 S. Jothi, T.N. Croft, L. Wright, A. Turnbull and S.G.R.Brown, Multi-phase Modelling of Intergranular Precipitates and hydrogen segregation/Trapping for hydrogen embrittlement, (2015) (*International Journal of Hydrogen energy: In Review*).
- 8 S. Jothi, Sergiy V. Merzlikin, Joel Andersson, T.N.Croft, and S.G.R.Brown, An investigation of micro-mechanisms in hydrogen induced cracking in nickel based superalloy 718, (2015) (*In Review*).
- 9 S. Jothi, T.Seald, T.N.Croft, E.Reese, and S.G.R.Brown, Effect of microstructure and hydrogen on weldability of advance material for aerospace application, (2015) (*In preparation*).

Note: There are few more journal papers related to experimental and modelling work in preparation.

Conference Papers

- 1 S. Jothi, T.N. Croft, S.G.R. Brown, Multiscale multiphysics atomistic-meso-continuum critical dislocation method for hydrogen embrittlement, 14th International Symposium on Metal-Hydrogen Systems (MH2014), 20-25 July 2014, Salford, Manchester, UK.
- 2 S. Jothi, T.N. Croft, S.G.R. Brown, E.A. de Souza Neto, Influence of Triple Junctions on Hydrogen Transport in Electrodeposited Nanopolycrystalline Material, XIV International conference on intergranular and interphase boundaries in materials (iib2013), June 23, 2013, GREECE.
- 3 S. Jothi, T.N. Croft, S.G.R. Brown, Micromechanical analysis of hydrogen induced cracking in nickel based superalloy 718, HySEA2014, 26-30 Oct 2014, Rio de Janeiro, Brazil.
- 4 S. Jothi, T.N. Croft, S.G.R. Brown, E.A. de Souza Neto, Analysis of the effect of grain boundaries and trapping on the effective diffusivity of hydrogen in polycrystalline nickel, International conference on hydrogen Production(ICH2P-14), Feb 2014, Fukuoka, JAPAN.
- 5 S. Jothi, T.N. Croft, S.G.R. Brown, E.A. de Souza Neto, Computational analysis of Hydrogen Diffusion in Polycrystalline Nickel and Anisotropic Polygonal Micro, Nano Grain Size Effects, International Conference on Hydrogen Safety (ICHS2013), 9-11 Sep 2013, Brussels, BELGIUM.
- 6 S. Jothi, T.N. Croft, N. Winzer, S.G.R. Brown, Multiscale experimental-atomic-continuum coupled model to study the effects of microstructure on hydrogen diffusion in pulse plated nickel, International conference on hydrogen storage, Embrittlement and applications (HySEA2014), 26-30 Oct 2014, Rio de Janeiro, Brazil.
- 7 S. Jothi, T.N. Croft, S.G.R. Brown, Mass transport in nanopolycrystalline composite media using mesoscale model, 23rd International Conference on composites/nano engineering (ICCE-22), 13-19 July 2014, MALTA.
- 8 S. Jothi, T.N. Croft, S.G.R. Brown, Mesoscale microstructural computational simulation of hydrogen permeation test to calculate grain boundary diffusivity, 14th International Symposium on Metal-Hydrogen Systems (MH2014), 20-25 July 2014, Salford, Manchester, UK.
- 9 S. Jothi, T.N. Croft, S.G.R. Brown, E.A. de Souza Neto, Microstructural homogenization to calculate the effective diffusivity of polycrystalline composite media, 17th International conference on composite structures (ICCS17), 17-21 June 2013, Porto, PORTUGAL.
- 10 S. Jothi, T.N. Croft, S.G.R. Brown, E.A. de Souza Neto, Multiscale modelling of hydrogen embrittlement in polycrystalline materials, ESIA12 - Engineering Structural Integrity Assessment: Where are we now?, May 28, 2013, Manchester, UK.
- 11 T.N. Croft, S. Jothi, S.G.R. Brown, E.A. de Souza Neto, Coupled macroscale - microscale simulation of hydrogen diffusion in pulse plated nickel, Hydrogen Embrittlement – Multi-scale modelling and measurement What is the

impact?, 6-8 October 2014, National Physical Laboratory, Teddington, UK,

- 12 T.N. Croft, S. Jothi, S.G.R. Brown, E.A. de Souza Neto, A multiscale chemo-mechanical model of hydrogen embrittlement in polycrystalline nickel, 2nd International Conference on Metals and Hydrogen (Steel&Hydrogen2014), 5-7 May 2014, Ghent, BELGIUM, (http://www.steelyhydrogen2014.be/page/2/Final_Programme/).
- 13 T.N. Croft, S. Jothi, S.G.R. Brown, E.A. de Souza Neto, Numerical Modelling of Hydrogen Aggregation Mechanism of Annealed Electrodeposited Polynanocrystalline Nickel, 9th International conference on Diffusion in solids and Liquids DLS2013, June 2013, Madrid, SPAIN.
- 14 S. Jothi, T.N. Croft, S.G.R. Brown, Hydrogen embrittlement in aerospace materials, Hydrogen in metals Symposium, DGP Spring meeting in 15-20 March 2015, Berlin, Germany.

ABBREVIATIONS

APT	Atom Probe Tomography
BM	Base Metal
CHAM	Critical High Angle Misorientation
CMCD	Continuum Critical Defect Modelling
CSL	Coincidence Site Lattices
DFT	Density Function Theory
EBSD	Electron Back Scattering Diffraction
EU	European Union
FCC	Face Centred Cube
FE	Finite Element
FEA	Finite Element Analysis
FEG	Field Emission Gun
FEMRVE	Finite Element Microstructural Representative Volume Element
FIB	Focused Ion Beam
FNG	Fine Nano Grains
FZ	Fusion Zone
GB	Grain Boundary
GBAZ	Grain Boundary Affected Zone
GBCD	Grain Boundary Character Distribution
GBE	Grain Boundary Engineering
GBSE	Grain Boundary Segregation Engineering
GD	Growth Direction
GI	Grain Interior
GND	Geometric Necessary Dislocation density
GRVE	Global RVE
HAGB	High Angle Grain Boundary
HAZ	Heat Affected Zone
HE	Hydrogen Embrittlement
HELP	Hydrogen Enhanced Localised Plasticity
HHAM	High End High Angle Misorientation
HIC	Hydrogen Induced Cracking

HRVE	Homogeneous RVE
Ig	Intergranular
IHE	Intergranular Hydrogen Embrittlement
IHIC	Intergranular Hydrogen Induced Cracking
LAGB	Low Angle Grain Boundary
LAM	Low Angle Misorientation
LHAM	Low End High Angle Misorientation
MPFM	Microstructural Phase Field Model
MRVE	Microstructural Representative Volume Element
ND	Normal to Growth Direction
NPC	Nano Poly Crystalline
OIN	Orientation Image Microscopy
PP-Ni	Pulse Plated Nickel
RD	Rolling Direction
RGB	Random Grain Boundary
SCSL	Special Coincidence Site Lattice
SE	Secondary Electron
SEM	Scanning Electron Microscopy
SIMS	Secondary Ion Mass Spectroscopy
SRGB	Special Random Grain Boundary
SSRT	Slow Strain Rate Test
TCL	Total Crack Length
TD	Perpendicular to Growth Direction
TDA	Thermal Desorption Analysis
TDS	Thermal Desorption Spectroscopy
TGB	Tilt Grain Boundary
TJ	Triple Junction
TJCD	Triple Junction Character Distribution
UEL	User Element Subroutine

NOMENCLATURE

ϕ	Normalized hydrogen concentration
ϕ_0	Unstressed state of the normalized concentration under the condition of hydrogen-metal equilibrium
δ	the average thickness of the random polygon
∇	The gradient operator
Δ	The Laplace operator
σ_h	hydrostatic stress gradient
Ω	heterogeneous polycrystalline composite domain
Γ	boundary
ε	the length scale ratio called small parameter $0 < \varepsilon \ll 1$
Ω_{mss}	substructure micro domain
Ω_{msm}	submodel micro domain
$\partial\Omega_t$	tie boundary
Ω_c	the continuum domain
$\partial\Omega_c$	cut boundary
ΔE	the activation energy barrier,
ν	real normal mode frequency
[A] and [B]	interpolation matrices
A	area of the sample specimen
C_g	Intragranular hydrogen concentration
C_{gb}	Intergranular hydrogen concentration
C_{eff}	Effective concentration of hydrogen
C	Concentration of hydrogen
D_{ig}	intragranular diffusion coefficient
D_{gb}	intergranular diffusion coefficient
D_{eff}	effective diffusion coefficient
D_h	Homogeneous diffusion coefficient
\mathbf{D}_{ij}	Second order diffusivity tensor
E_c	elementary charge ($1.6 \times 10^{-19} C$)
[\mathbf{F}_i]	Represents the diffusion flux vector columns
i	represent the component vector column

I_{\max}	maximum current
j	the number of nodes
J	Hydrogen flux vector
J_c	Hydrogen concentration gradient
$\overline{I}_i(\mathbf{x})$	Macroscopic mass flux
$I_i(\mathbf{y})$	Microscopic mass flux
k_{ig}	Intragranular coefficient
k_{gb}	Intergranular coefficient
$[K_{ij}^l]$	Represents the diffusion matrix
ℓ	Microscopic length scale
L	macroscopic length scale
$[M_{ij}]$	Represents the concentration capacity matrix
n_i	The outward vector component normal to the boundary
n	numerical coefficient which depends on the initial and final position of hydrogen
$N_j(\mathbf{r})$	element shape functions
R	the ideal gas constant equal to 8.314 J/mol K
s	Solubility
t	time dependent variable
t_L	Time lag
V_h	the partial molar volume of hydrogen (2000 mm ³ /mol)
x	macroscopic field variable
X	Represents three dimensions (3D) x,y,z
y	local variable or microscopic field variable
ΔZPE	the difference in zero-point vibrational energies between ground state and transition state

TABLE OF CONTENTS

Abstract

Acknowledgements

Publications

Abbreviations

Nomenclature

1	Introduction.....	1
1.1	MultiHY.....	5
2	Literature review	7
3	Aims and objectives.....	23
4	Multiscale Experimental methods.....	25
4.1	Materials.....	25
4.2	Sample preparations.....	27
4.3	SEM/2D-3D EBSD.....	28
4.4	Slow strain rate test.....	30
4.5	Heat treatment	32
4.6	Weld-ability test	32
4.7	Thermal desorption spectroscopy.....	35
5	Mathematical model.....	37
5.1	Hydrogen diffusion Fick's model	37
5.2	Stress assisted diffusion model	39

6	Multiscale computational methods.....	42
6.1	Synthetic microstructural model	42
6.2	Microstructural homogenization method.....	45
6.3	Real microstructural RVE model and virtual permeation test.....	49
6.4	Micro-macro coupling techniques.....	52
6.5	Multi-scale specimen model.....	56
7	Results and Discussion	59
7.1	Effect of microstructure on hydrogen diffusivity.....	63
7.1.1	Experimental results	63
7.1.2	Discussion.....	67
7.2	Effect of microstructure on hydrogen diffusion in micro and nano polycrystalline nickel	71
7.2.1	Experimental results	72
7.2.2	Discussion.....	90
7.3	Real microstructure based 2D mesoscale FE simulation to predict intergranular hydrogen diffusivity and isotropic effective bulk diffusion of hydrogen in conventional electrodeposited nickel.....	94
7.3.1	Experimental results	94
7.3.2	Discussion.....	98
7.4	Real microstructure based 3D mesoscale FE simulation to calculate effective anisotropic hydrogen diffusivity of Ariane 5 combustion chamber pulse plated nickel.....	100
7.4.1	Experimental results and discussion	100
7.5	Effect of GB misorientation on hydrogen embrittlement in bi-crystal and polycrystal Nickel.....	111
7.5.1	Experimental results	111
7.5.2	Discussion.....	135
7.6	Coupled micro-macro model for hydrogen diffusion	136
7.6.1	Experimental results	136

7.6.2	Discussion.....	142
7.7	Coupled micro-macro model for hydrogen embrittlement	144
7.7.1	Experimental results and discussion.....	144
7.8	Multiscale modelling for localized hydrogen induced cracking.....	150
7.8.1	Experimental results and discussion.....	150
7.9	Hydrogen embrittlement in nickel based superalloy 718.....	157
7.9.1	Experimental results	157
7.9.2	Discussion.....	177
7.10	Hydrogen embrittlement in Pulse Plated Nickel.....	179
7.10.1	Experimental results	179
7.10.2	Discussion.....	189
7.11	Weldability test of Ariane 5 combustion chamber Pulse Plated Nickel	190
7.11.1	Experimental results	190
7.11.2	Discussion.....	197
8	Conclusions	207
9	Future focus.....	214
	Preliminary results: GBE, APT and fully coupled component model	216
10	Appendices.....	221
10.1	Trap model.....	221
10.2	Experimental EBSD Results of Ariane 5 combustion chamber: Supplementary images.....	233
11	References.....	241

CHAPTER 1

1. INTRODUCTION

Hydrogen embrittlement (HE) is defined as structural degradation of material due to loss of ductility because of hydrogen attack leading to potentially catastrophic failure. It is one type of corrosion problem. HE is an extremely dangerous phenomenon that needs to be addressed in engineering industries such aerospace automotive, civil and construction, semiconductor, offshore, ship, oil and gas, nuclear power and renewable energy sector including wind energy, fuel cells and hydrogen energy. Contact with hydrogen in structural materials may occur at any time during a component's life time, during fabrication in a manufacturing process or during operational use under service environmental conditions. HE play a prominent role in manufacturing engineering and aerospace components which are typically made of high strength, high toughness, corrosion resistant and high temperature metallic materials such as nickel, titanium and nickel based super alloys. Nickel and nickel-based super alloys are often made up of complex microstructures and have been used in aerospace applications for many years. Manufacturing process such as electrodeposition and welding may introduce hydrogen into aerospace components made of nickel and nickel based super alloys. Several catastrophic failures have

occurred in nickel and nickel-based super alloys due to environmental cracking, hydrogen stress cracking and HE. Even though there is a considerable amount of information about hydrogen embrittlement mechanisms in polycrystalline structural materials, there are still number of different types of pending embrittlement problems caused by atomic transport of hydrogen elements which are not clearly understood [1-12].

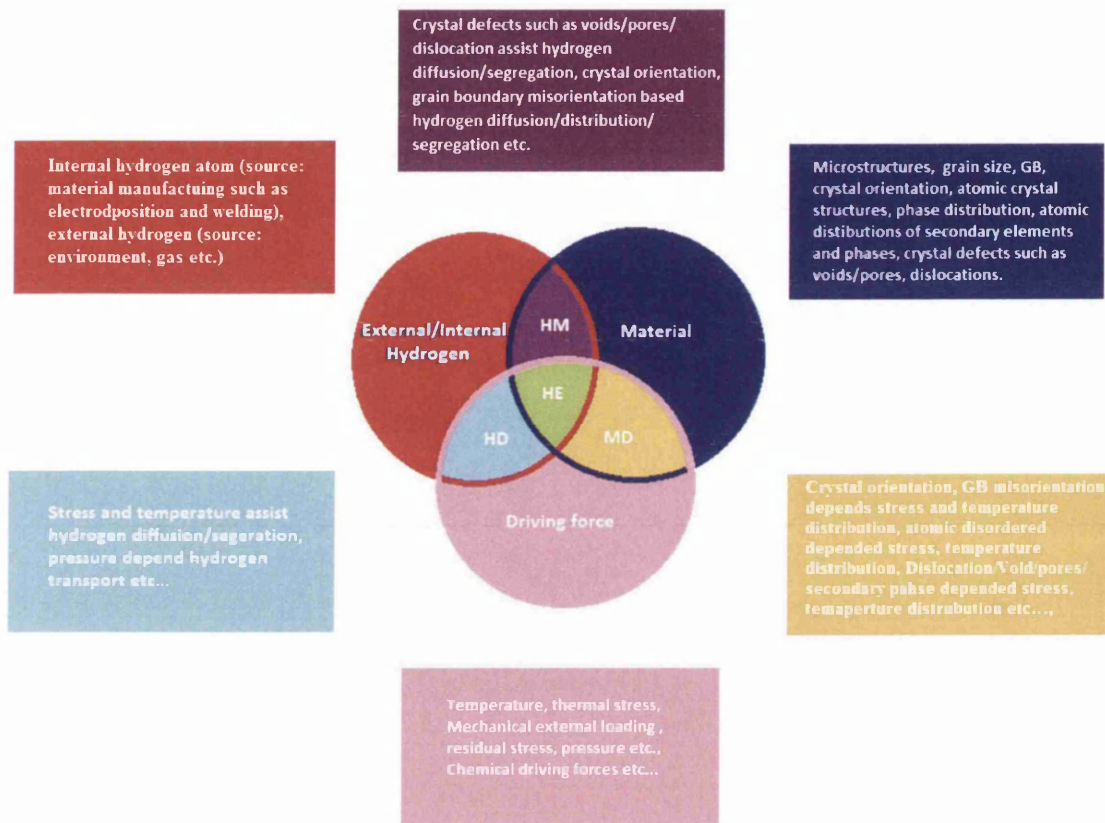
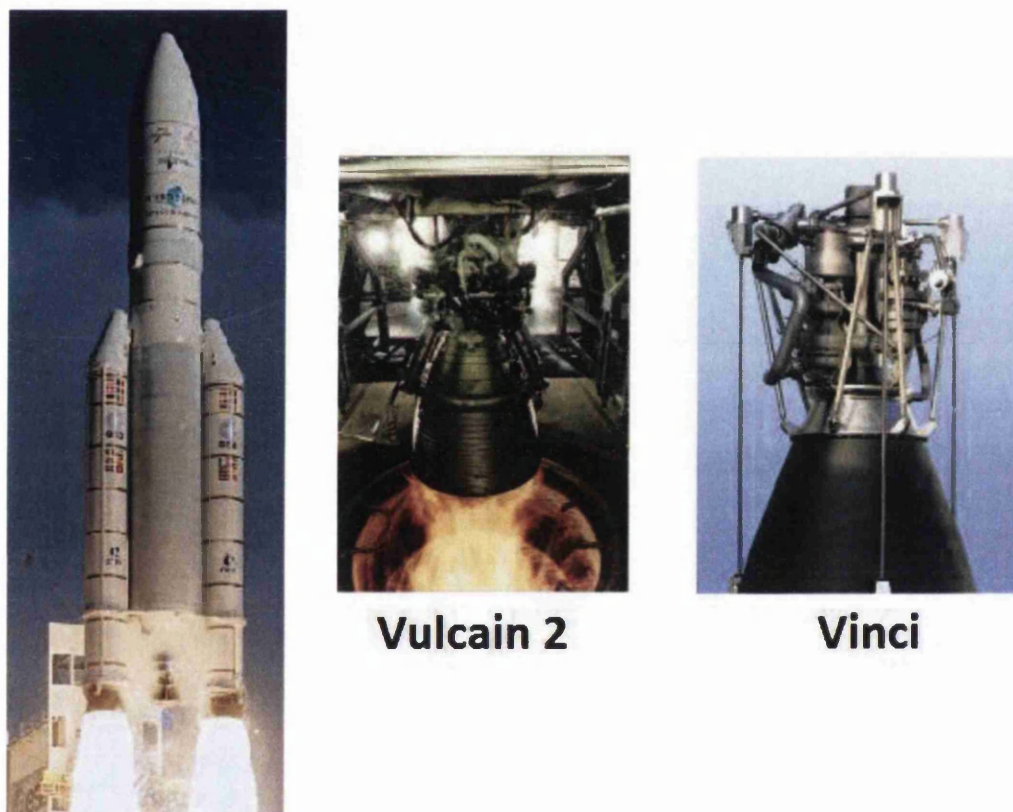


Figure 1.1 Multiscale and multiphysics integration aspects of hydrogen embrittlement.

Material scientists in all of these engineering industries are developing high toughness and high strength metals and alloys. HE exhibits a wide spread of multiphysics and multiscale effects that degrade the fracture resistance of these high strength metal and alloys. Figure 1.1 shows the multiphysics and multiscale interaction aspect of hydrogen embrittlement. Both computational and experimental multiphysics investigations at different length scales, from atomic to component level, are needed for a better understanding of hydrogen embrittlement and its mechanism.

An example of aerospace component failure due to hydrogen embrittlement has been reported as shown in figure 1.3 (b). The hydrogen induced cracks observed in nickel material on space launcher combustion chamber a decade ago were handled by AIRBUS by developing a new advanced pulse-plated (PP) Ni material by changing manufacturing parameters and moving to more advanced manufacturing techniques. But understanding the HE mechanism in this PP-Ni aerospace material is still of major interest to material scientists and AIRBUS in order to develop newer advanced materials with higher strength in addition to a resistance to HE and to remain as a front runner in the global aerospace materials market.



Vulcain 2

Vinci

Figure 1.2 The Ariane 5, Vulcain 2 and Vinci combustion chambers [Jokob Norgaard, New concept for Rocket engines, Force Technology presentation].

HE also has a very important economic impact in the aerospace industry, especially in the European space industry, for example, in the main and upper stage of the combustion chamber components of Ariane 5 system known as Vulcain 2 and Vinci as shown in figure 1.2. (Vulcain 2 is approximately 2.3m tall and 2.1m in diameter, 400kg weight, 150 ton thrust, 250kg/s fuel consumption, approximate flame temperature 3000°C, exhaust gas velocity 4000m/s, coolant liquid hydrogen

temperature of -240°C and engine life time is approximately 10 minutes. [Jakob Norgaard, New concept for Rocket engines, Force Technology presentation]). HM7 combustion chambers are made of thick pulse-plated nickel shell as shown in figure 1.3 (a). There is an approximately 2cm thick PP-Ni layer in the case of the Vulcain 2 combustion chamber, which is deposited over a copper and copper alloy substrate using a complex electrochemical plating process. The plating material is exposed to hydrogen which is a by-product of the plating process and after the plating process the plated material undergoes further manufacturing processes such as joining and machining resulting in residual stresses.

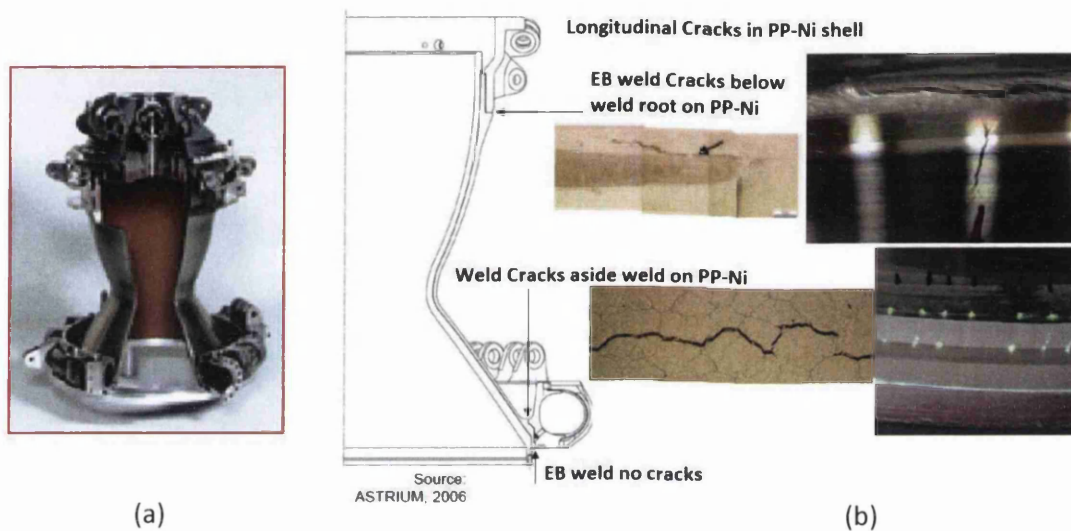


Figure 1.3 (a) shows the pulse plated nickel shell on space launcher combustion chamber, (b) shows the some of the hydrogen induced cracks observed in nickel material on space launcher combustion chamber. [102,218,219].

The manufactured components are left in storage for several years and depending on the combination of plating and manufacturing parameters residual stresses may be sufficient to cause cracking. Due to strict aerospace rules concerning component qualification requirements, failure in one component would result in the entire batch of components being rejected and the economic losses associated with such failures are enormous. The later the failure occurs, the higher the economic loss. The worst case scenario is failure occurring during operation of the space launcher (i.e. if the technical failure is realised at the moment of launch) and this would result in an economic loss of several million euro. A more advance multiscale and multiphysics approach using both computational modelling and experiment approaches will be

used in this study in order to investigate and understand the hydrogen embrittlement mechanism in pure nickel and nickel based super alloy. Part of this study sits within the 7th European Union (EU) Framework Project “MultiHy”, (Multiscale modelling of hydrogen embrittlement in crystalline material).

1.1. MULTIHY PROJECT

MultiHy project is funded by the European Union 7th framework program under the theme “Nanosciences, Nanotechnologies, Materials and new Production Technologies”. The project starts at 1st May 2011 and ends at 30th April 2015. The project had a funding budget of €5.3 million including both partner contributions and European Union contribution. Hydrogen embrittlement is serious and costly industrial problem that need to be addressed. There is an urgent need for better understanding of real industrial problems related to hydrogen embrittlement in three different industrial sectors such as aerospace, automotive and renewable energy. The aim of the MultiHy project is to develop industrially-relevant and industrially applicable computational models to assist in the evaluation of the susceptibility to hydrogen embrittlement of advance complex materials. The project aims to achieve this by developing an advanced multiscale framework to evaluate the impact of hydrogen on the structural integrity of industrial components made of advance complex materials. The primary focus of the project is the description of hydrogen transport in the complex microstructures of industrially developed existing and newly developed advance materials. The project brings together 11 partners across industries, academic universities and research institutes from 6 different European countries as shown in figure 1.1.1. There are three different case studies involved in this project as follows,

Case study 1: Optimisation of the pulse-plating process used in the fabrication of the nickel combustion chambers of the Ariane 5 satellite launcher.

Case study 2: Minimising the impact of hydrogen embrittlement on the application of advanced high strength steels to future automobile chassis components.

Case study 3: Maximising the efficiency of the next-generation wind turbine bearings by predicting the impact of hydrogen embrittlement on bearing lifetime.

Further detail information about the MultiHy project can be found in World Wide Web source multihy.eu. The author worked on close collaboration with aerospace industries related to Ariane 5 satellite launcher combustion chamber investigation involved in case study 1 on the MultiHy project.

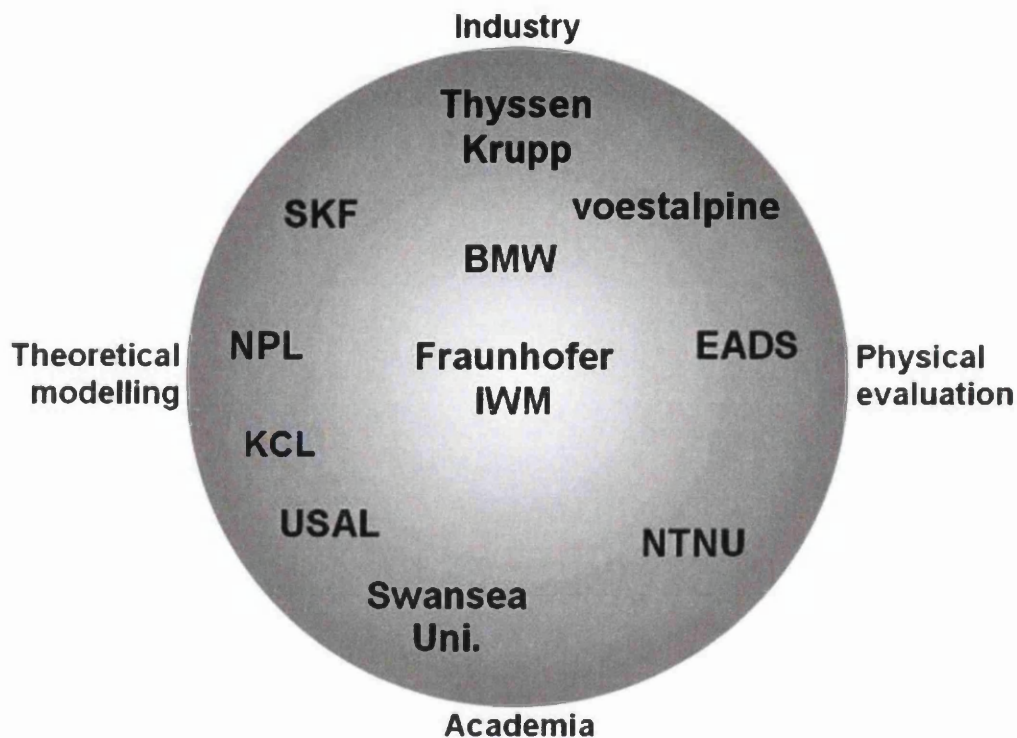


Figure 1.1.1 shows the MultiHy project partners.

2. LITERATURE REVIEW

Synthetic microstructural phase field model to calculate effective hydrogen diffusivity:

Even though there is a considerable amount of information about the embrittlement mechanism of polycrystalline structural materials [1-6], there are still a number of different types of pending embrittlement problems caused by atomic mass transport of impurity elements (hydrogen, sulphur, oxygen, carbon, phosphorous, nitrogen, boron etc.) and inclusion elements that are not clearly understood [7,8,11,20-23,25-26,28]. By better understanding the microstructural intergranular behaviour of high performance polycrystalline materials, the embrittlement problem may be solved by expanding the concept of microstructural intergranular engineering into design and analysis [8, 24]. One such example of understanding microstructural intergranular behaviour of polycrystalline material produced an innovative solution for repairing the nuclear steam generator using electrodeposition of continuously bonded nanocrystalline nickel [27]. Mass transport properties of impurity elements such as hydrogen and sulphur in the polycrystalline material are one of several pending embrittlement problems [4, 6, and 9-12].

Prediction of the effective mass diffusion properties of advanced heterogeneous polycrystalline composite materials has been an active research area for many years [14, 17-19, and 29]. Fisher [14] developed an analytical model for a two phase heterogeneous crystalline composite material by considering the fast diffusion along a single isolated grain boundary with slow diffusion in the bulk which is a simple model for polycrystalline material. Hart [17] developed an analytical model to predict the effective diffusivity of two phase intragranular heterogeneous composite material based on composite rule of mixtures method. Hart's model was modified by Mortlock [29] and Kalnin [30] by taking into account segregation for parallel and series intergranular phases. Later the analytical model was demonstrated to be valid for a realistic two phase heterogeneous polycrystalline material [38, 31]. Wang *et al.* [18] developed a model based on the same composite rule of mixtures for a three phase heterogeneous polycrystalline composite material by including triple junctions as the third phase. In the past few decades, a number of analytical micromechanical studies have been reported in the literature [14, 17-19] to predict effective mass transport properties by treating heterogeneous materials containing intergranular and intragranular microstructures as a composite media. A robust polycrystal mass diffusion numerical model is essential for forecasting the effective mass transport properties for realistic heterogeneous polycrystalline materials [13]. The diffusion behaviours of the polycrystalline materials are strongly affected by microstructural phases [1-4, 6, 9-12]. Intergranular and intragranular distributions play a key role in determining diffusion behaviour. Typically, the intergranular phase consists of grain boundaries and triple junctions and the intragranular phase contains the grains and the defects throughout these models.

In this work it is anticipated that the diffusivity in the intergranular phase has a higher value than the intragranular case as reported by many researchers. A few examples of this trend are:-

- Tsuru *et al.* [4] investigated the diffusion permeability of hydrogen along intergranular and intragranular phase in heterogeneous polycrystalline pure nickel (99.97 % Ni) Ni 270 material with average grain size of about 100 μm and an implicit grain boundary thickness of 1 μm and observed the hydrogen diffusion coefficient

along the intergranular phase was approximately 60 to 100 times accelerated compared to the intragranular phase.

- Harris and Latanision [2] studied the hydrogen diffusivity along grain boundaries in fine grained nickel produced by electrodeposition and estimated the hydrogen diffusion coefficient along the grain boundary is 40 times larger than lattice diffusion at 30 °C.
- Palumbo *et al.* [1] determined that the hydrogen diffusion in the grain boundary is approximately 70 times faster the intragranular region in electrodeposited nano polycrystalline Ni with average grain size of 17 nm.
- Some other researchers demonstrated faster diffusivity in intergranular phases compared to intragranular phases in Face Centred Cubic (FCC) structural materials, examples of this can be found in Bokstein *et al.* [5], Oudriss *et al.* [3].
- Portavoce *et al.* [6] determined higher mass diffusion of atoms in intergranular phases compared to intragranular phases in heterogeneous polycrystalline silicon material.
- Hoffman and Turnbull [15, 16] observed that self-diffusion of silver in a grain boundary was several orders of magnitude greater than in the lattice.

In terms of numerical models the Voronoi tessellation technique is a well-established approximation technique used to model the actual microstructure of polycrystalline materials (e.g. Ghosh *et al.* [13]) which can avoid the problems inherent in experimental techniques [33-37] as stated in Table 1. Modified Voronoi tessellation techniques can be developed for microstructural phase field models (MPFM) based on intragranular and intergranular phase constituents. A numerical finite element microstructural homogenization technique and microstructural representative finite element model (MRVE) with intragranular and intergranular phase constituents can be used to calculate the effective mass transport coefficient and investigate microstructural effects in a heterogeneous polycrystalline material. Initially the Voronoi tessellation technique is adopted to geometrically represent the

heterogeneous polycrystalline material allowing exploration of the effect of average grain size and intergranular phase thickness.

	Experimental techniques	Measurements	Difficulties
1	X-ray Computer micro tomography	Microstructures such as grains and micro cracks	In determining the orientation of intragranular microstructural phases such as grains [33]
2	3D Electron back scatter diffraction methods	Microstructure including orientation of intragranular phase constituent such as grains	Expensive, complicated, Impossible to gain data from large number of samples and, in order to get significantly high spatial resolution, the sample size should be very small i.e. there will be a compromise between maximum sample size and resolution [34, 35].
3	Ion beam serial sectioning electron back scatter diffraction method	Microstructural morphology	Post processing is complicated and requires enormous aggregate data which leads to non-unique topologies owing to the overlapping of intragranular phase constituents [35, 36, and 37].

Table 1 Experimental technique to measure the real microstructural topography of polycrystalline materials and its difficulties.

Analytical effective medium theorems have been used previous to calculate the effective electric and mass diffusion properties. Respectively, the Maxwell-Garnett effective medium approximation [38, 39] and the Hashin-Shtrikman upper bound

effective medium approximation [40, 41] formula for heterogeneous polycrystalline material, with intergranular and intragranular phases, are shown below.

$$D_{eff} = D_{ig} \left[\frac{2D_{ig}V_{fig} + D_{gb}(1+2V_{fgb})}{D_{ig}(3-V_{fig}) + D_{gb}(1-V_{fgb})} \right]$$

$$D_{eff} = D_{gb} + \left[\frac{V_{fig}}{\left(\frac{1}{D_{ig}-D_{gb}} \right) + \left(\frac{V_{fgb}}{3D_{gb}} \right)} \right]$$

Where, diffusivity of intragranular, intergranular phases and effective diffusivity are D_{ig} , D_{gb} and D_{eff} respectively. V_{fig} and V_{fgb} are volume fractions of intragranular and intergranular phase respectively [38-41].

Hydrogen diffusion in nanopolycrystalline material

Many researchers, scientists and industrialists are working towards a greater understanding of microstructural triple junction (TJs) in nano-polycrystalline (NPC) material because of the change in properties of this material with changing micro/nano grain sizes [1, 18, 32, 41-52, 54-73, and 76-78]. The observed changes in the properties of NPC materials, when decreasing the grain size of NPC material, are partially explained by the increase in the density of TJs [1, 42-44]. The microstructural morphology such as grain size, interfacial grain boundary (GB), pores in TJs, fine grains in TJs and TJ shapes (width and size) may also affect the physical properties, atomic transport and properties in NPC materials [6,47-55, 67-70, 78]. The microscale TJ diffusivity in NPC materials is higher than the diffusivity at microstructural interfacial GBs due to the structurally weaker bonding nature of TJs [18, 42, 56-58, 71 and 72]. Rapid TJ diffusion has important consequences for a range of properties of NPC materials such as hydrogen transport, super elasticity and diffusional creep [1, 43, 44, 59, 60-62 and 68].

Electrodeposited NPC nickel has several engineering and aerospace industrial applications; one such application in aerospace industries is in the thrust chambers of rocket engines. Typical applications have been in the Ariane satellite launcher and the main engine of the NASA Space Shuttle [1, 74]. Production of NPC material using electrodeposition pulse-plating techniques have been subjected to extensive research in recent years due to the economic viability of the process [73,75]. During the manufacturing process of NPC nickel, hydrogen impurities are introduced into

the material. The presence of hydrogen atoms in steel and nickel increases the potential for embrittlement related failures [3, 79, and 80]. Consequently electrodeposited NPC nickels have gained the attention of the scientific community. The diffusivity properties of hydrogen atom transport in electrodeposited NPC nickel are different in the grain interior (GI), the grain boundary (GB), the grain boundary affected zone (GBAZ) and the triple junction (TJ) [43]. The intergranular (Ig) region is composed of GBAZ and TJ. A high density of TJs is found in such materials due to their small grain size. To control the hydrogen embrittlement of electrodeposited NPC nickel it is important to consider the properties and microstructural characteristics of the TJ. The hydrogen diffusivity in the TJ is approximately three times the diffusivity in GBs which in turn is approximately seventy times the diffusivity in the GI [43]. Locations where the concentration of hydrogen atoms is higher in this material will have an increased tendency for the initiation of embrittlement related failure. The TJ, where three grain boundaries meet, plays an important and dominant role in NPC electrodeposited nickel with respect to hydrogen transport due to the higher relative volume fraction, weaker bonding structures and higher diffusivity compared to the GB and the GI [44]. The presence of residual pores, cluster vacancies and very fine grains in NPC nickel have been reported previously [5, 44 and 45] showing that the NPC nickels are different from conventional coarse grain nickel materials. Thus it is important to treat the TJ as an independent defect and consider its microstructural morphology to investigate the hydrogen transport in electrodeposited NPC nickel both in computational and experimental studies.

Grain size and trapping effect on hydrogen diffusion

Hydrogen is a common fuel in rocket engines and these rocket engines are made of polycrystalline materials. It is well known that hydrogen causes embrittlement in many polycrystalline materials, including high nickel content polycrystalline materials and catastrophic failure can occur in hydrogen fuel rocket engine components [20, 22-23, 83-92, 102, 132-136]. Hydrogen induced intergranular and transgranular embrittlement in polycrystalline materials are well established as causes of catastrophic brittle failure and have been studied extensively

for more than five decades [22-23, 83-92, 102]. Apart from rocket systems, hydrogen diffusion, segregation and trapping in metallic polycrystalline materials is also significant as a cause of hydrogen embrittlement in clean energy fuel storage systems used as power sources in the aerospace and automotive sectors. Physical microstructural factors such as grain size, grain boundaries, and dislocations, grain boundary segregation of impurities, carbides and non-metallic particles have been identified as playing important roles in this phenomenon [3-4, 16, 23, 32, 42-47, 92 - 103, 112-114, 119-124, 137-152]. For example, segregation of phosphorous and sulphur assists hydrogen embrittlement in nickel based superalloys [143, 144]. Some of these microstructural features, such as grain boundaries, may also promote faster diffusion of hydrogen due to the locally disordered atomic structure [2-4, 95, 99-103, 112-114, and 142]. GBs may also act as hydrogen trap (or segregation) sites when the probability of atomic hydrogen jumping into GB sites (capture) is greater than that of atomic hydrogen jumping out of GB sites (escape) [115-118]. Grain boundary segregation engineering (GBSE) is fundamental to understanding intergranular hydrogen embrittlement [2, 115, 118, 119, and 142]. Dislocation sites may also act as traps for hydrogen atoms (by providing a deeper potential energy well) and hydrogen atoms jumping into these sites may reside for longer times than in lattice sites [115-118]. These trapping effects can lead to an overall decrease in the rate of hydrogen transport over time [23, 92, 104-108]. The processes of hydrogen transport through/near such microstructural features are important for understanding the different modes of hydrogen induced cracking (HIC) in polycrystalline nickel [e.g. 2, 94].

Intergranular and transgranular failures are two different modes of HIC. HIC commonly occurs along grain boundaries where high concentrations of hydrogen can exist [94]. These concentrations highlight the importance of including the random grain boundaries in any numerical model designed to predict embrittlement. Detailed descriptions of the importance of grain boundary diffusion of hydrogen in nickel can be found in Harris [2, 115]. In nickel components combinations of micro polycrystalline and nano polycrystalline nickel microstructures are often encountered. These are complex composites comprising irregular polygonal grains, random grain boundaries and triple junctions. The detailed nature of random irregular micro and nano polygonal grains and random irregular grain boundaries is

significant when considering the processes of hydrogen diffusion and segregation mechanisms that lead to embrittlement failure in nickel [2, 95, and 96]. Plastic deformations in polycrystalline metallic materials are accommodated by clusters of dislocation. Dislocations are classified as statistically sored dislocation and geometrically necessary dislocations (GNDs) by Nye [130]. Statistically sored dislocations are dislocations consist of loops; dipoles and multiples larger than the Burger's circuit and GNDs represent the dislocations stored within a Burger's circuit and contribute to lattice curvature [48]. Manufacturing processes such as casting, electrodeposition and welding of polycrystalline materials and post-manufacturing processes such as hot rolling, cold rolling, heat treatment and hardening using thermo-mechanical processing produces residual plastic strain and GB misorientation which is directly associated with geometric necessary dislocation density (GND). In order to understand GBSE for hydrogen transport based on elastic and plastic strains developed by manufacturing processes, a trap model and multi-scale multi-phase microstructural model has been developed to study the effect of GB misorientation, GND density and trap density in hydrogen segregation mechanisms in polycrystalline material. GB misorientations accommodate GNDs [3, 115, 125, and 142]. Hydrogen diffusion and segregation may increase or decrease depending on GB misorientation, GND density and GB energy, and GNDs can act as trapping sites for hydrogen in polycrystalline materials. It is also reported that hydrogen diffusion and segregation is influenced by GNDs, dislocation density, triple junctions (TJs), GB misorientation and GB connectivity [3, 125, and 126]. The GND density may also vary depending on the GB misorientation types, angle and the GB energy. Previously hydrogen diffusion in FCC polycrystalline material has been studied using a SIMS technique and it was reported that high energy GBs accelerate the diffusivity of hydrogen [3, 118, 125, 127-131 and 142]. Raabe *et al.* observed double nano layers in grain boundary interfaces with thicknesses of 10 to 15 nm in polycrystalline steel material. Impurity segregation and nano precipitation in this intergranular double layer was also reported [119, 120]. Micro precipitation in intergranular double layers in nickel-based polycrystalline alloys have been reported [151]. This indicates that it is important to take into account this intergranular double layer interface when studying the GBSE of impurity segregation and trapping in polycrystalline materials.

Real microstructure and GB diffusivity

Grain boundary (GB) diffusion plays an important role in many processes occurring in engineering materials [3, 112, 113, 153-155], including intergranular cracking due to hydrogen embrittlement (HE) [4, 26, 28]. Reliable information on GB diffusion properties can be used in the development and processing of new and existing metals and alloys in order to reduce their susceptibility to cracking and failure [3-4, 90-91, 112, 113, 156, 157, 160, 161]. Traditionally, grain boundary diffusion may be characterised experimentally using radioactive tracers, secondary ion mass spectroscopy (SIMS) or by using bi-crystal electrochemical permeation tests. These techniques are expensive, time consuming, challenging to perform and only provide data for one specific grain boundary orientation [156-159]. Van Loo also noted that small experimental errors can result in significant errors in the measurement of GB diffusivity [158, 159]. It would therefore be useful to develop the ability to estimate GB diffusivity using computational techniques that could also allow the accuracy of experimental diffusion measurements to be assessed. This thesis presents a microstructure-based multi-scale finite element (FE) computational approach that uses experimentally-collected electron backscatter diffraction (EBSD) data to calculate the GB diffusivity of hydrogen in polycrystalline nickel.

Coupled Macro-Micro model for hydrogen diffusion

Hydrogen embrittlement often plays an important role in the catastrophic failure or premature brittle rupture of a structural component. Prediction of hydrogen embrittlement phenomena within a component requires multiple length scales to be accounted for and has attracted research attention over a significant period [162, 147]. Some mechanisms that affect hydrogen embrittlement include hydrogen diffusion in short circuit paths such as grain boundaries [1, 163-165]. Intergranular mechanisms such as segregation of hydrogen and hydrogen traps along grain boundaries and triple junctions affect hydrogen embrittlement in the form of intergranular embrittlement [11 and 166]. The hydrogen embrittlement mechanisms of cracking occur intrinsically at a microstructural level and have frequently been regarded as microstructural intergranular phenomena [167,-168]. So it is important to

include these microstructural intergranular phenomena at the design stage to investigate the hydrogen embrittlement mechanisms and life prediction analyses of structural materials at the component level. Computational investigation of the component macro-scale hydrogen embrittlement problem, including detailed heterogeneous microstructure, usually requires the use of multi-core processor or supercomputers. In practice, to avoid this complexity the component macro-scale hydrogen embrittlement problem is investigated by neglecting the detail of the microstructure of the polycrystalline material. But such component level macro-scale models provide limited understanding of the hydrogen embrittlement problem. In this thesis a multiscale modeling technique is proposed which accounts for the effects of the heterogeneous microstructure in an investigation of hydrogen embrittlement phenomena at the component level.

Effect of GB misorientation on hydrogen embrittlement

Crystallographic interfaces and micro-textures such as GB misorientation are characterized by specific arrangements of their atoms. They play a prominent role in aerospace components which are typically made of high strength, high toughness, and corrosion resistant as well as high temperature metallic materials such as nickel, titanium and nickel-based super alloys [4, 26, 28, 103, 166, 176-181]. Nickel and nickel-based super alloys are made up of complex microstructures and have been used in aerospace applications for many years. Several catastrophic failures have occurred in polycrystalline material including nickel and nickel-based super alloys in aerospace components due to environmental cracking, hydrogen stress cracking and hydrogen embrittlement [1-2, 22, 26, 28, 206-213]. Hydrogen embrittlement is a costly problem in which structural degradation of the susceptible material leads to catastrophic failure. Atomic impurities in structural materials may arise at different times, during fabrication in a manufacturing process or during operational use under service environmental conditions. The susceptibility of structural materials to hydrogen embrittlement depends on many factors including hydrogen atom-microstructural interactions [26, 28, 166, 181], microstructural intergranular engineering [103, 177, 178] and texture morphological behaviour [178-180]. By understanding and controlling some of these factors the susceptibility of materials

can be reduced [166, 182-185]. Even though there is a considerable amount of information available regarding the relationship between crystallographic micro-textures of materials such as TGB misorientation angles and hydrogen induced stress cracking [177, 186, 187], there has not been enough research done implementing this information into computational tools in order to understand material design and material design optimization based on GB engineering using finite element analysis (FEA). It is important to understand both the GB engineering and the relationship between misorientation angle and chemical and mechanical material degradation and properties at the design stage to develop new materials and to optimize existing materials to improve efficiency and increase the resistance of materials to hydrogen induced intergranular cracking, ideally implementing this approach into industrially applicable simulations.

The presence of GBs, interphase boundaries and the segregation of impurities (which is affected by GB misorientation) significantly affects chemical, and mechanical properties as well as fracture processes such as crack nucleation and crack propagation in textured polycrystalline metallic materials [103, 176-180]. It is already known that high densities of GBs, the types of GBs and GB misorientations with specific angles are important. These could potentially be optimized to increase properties such as the strength, ductility and fracture toughness of textured polycrystalline metallic materials. On the other hand, GBs and GB misorientation can also be potential sites for segregation of impurities, cracks and fracture and their behaviour is responsible for GB embrittlement depending on the characteristics of the GBs misorientations within them [166, 179, 181-189]. It has been recently found that low angle grain boundaries and low Σ coincidence boundaries or coincidence site lattices (CSL) are immune to intergranular fractures that lead to intergranular cracking and intergranular embrittlement [179, 180]. On the other hand high angle boundaries are preferential sites for fractures leading to crack nucleation and propagation [166, 179, 180, and 182]. Watanabe introduced the concept of 'grain boundary design and control' suggesting that GB misorientation and grain boundary character distribution (GBCD) are key microstructural parameters controlling the fracture toughness of polycrystalline metallic materials [103, 166, 177-181]. Palumbo developed this concept as grain boundary engineering (GBE) and improved intergranular susceptibility by implementing GBE in nickel-based super alloys [27,

166, 181-185]. The GB misorientation and the distributions of GB misorientation angles are important parameters controlling the propensity of segregation of impurities and stress induced hydrogen fractures that can lead to catastrophic GB embrittlement failure of textured polycrystalline metallic materials. It is well known from the literature that texture and GB misorientation play important role in impurity-induced cracking [103, 177-179, 181-189]. Therefore, it would be of interest to implement GB misorientation in finite element modelling and develop a procedure to quantify the effect of GB misorientation and crystallographic texture on the stress induced mass diffusion of impurities in polycrystalline textured nickel developed for aerospace applications.

Most existing studies of the effect of environmental impurities (i.e. sulphur, hydrogen, oxygen, boron etc.) on embrittlement and cracking mechanisms in polycrystalline structural materials are based on global, macro mechanical properties. However microstructural inhomogeneity and micro-texture can result in micro-cracks and dislocation formation which may lead to macroscopic environmental failures of polycrystalline materials [4, 26, 28]. Since a polycrystalline material is an aggregate of crystal grains of various sizes and shapes, its macroscopic properties are affected by the properties of individual grains. Each individual crystal in polycrystalline nickel may exhibit elastic anisotropy due to its crystal symmetric characteristics. The elastic deformation of single crystals may exhibit anisotropy depending on the orientation of the crystal. The presence of microstructural inhomogeneity, morphological and crystallographic textures will certainly affect the correlation between experimental observation and prediction based on an assumed homogeneous deformation [190-194]. So with a better understanding of microstructural local behaviour of high performance polycrystalline materials, the embrittlement problem may be reduced or perhaps solved by expanding the concept of microstructural local behaviour of polycrystalline engineering structural materials into design and analysis.

The local microstructural multi-physics stress induced hydrogen behaviour of materials is strongly affected by GB misorientation angles. The macroscopic environmental embrittlement cracking behaviour of materials is associated with local dislocation stresses generated at the interface between crystals due to the GB

misorientation angles and the segregation and accumulation of hydrogen to these dislocations. Segregation of hydrogen has been experimentally observed at GBs in bi-crystalline and polycrystalline nickel and an increase in the amount of segregated hydrogen increases the possibility of intergranular hydrogen embrittlement where fracture is observed along the intergranular region [26, 116, and 195]. It has also been observed that the GB misorientation angle affects the GB diffusion of hydrogen in a material [16, 196]. Thus, it is important to understand the relationship between GB misorientation angle and hydrogen segregation in nickel. The GB misorientation angle that allows the highest segregation of hydrogen along the GBs plays a key role in determining the structural integrity of nickel when considering intergranular hydrogen embrittlement.

The geometric distribution of grains shapes, sizes, grain boundary lengths and statistical distributions of GB misorientation angles of metallic materials can be acquired experimentally using the electron back scattering diffraction (EBSD) technique and X-ray diffraction [197-199]. In numerical models the Voronoi tessellation technique is a well-established approximation technique used to model the actual microstructure of bi-crystal polycrystalline materials and GB misorientation. The angle of rotation between different crystals can be assigned directly onto a meso-scale microstructural framework consisting of a Voronoi tessellation [13, 199]. The advantage of FEA simulation of bi-crystalline and polycrystalline materials is that GB misorientation angles, crystallographic morphology and textures such as grain size and shape of the grains can be defined as needed. The meso-scale microstructural polycrystalline model can be embedded into a macro scale continuum model [61, 200-202]. Thus it may be possible to computationally study the relationship between GB misorientation angles, stress/strain distributions and hydrogen embrittlement using FEA. If the FEA is performed before processing real bi-crystal and polycrystalline specimens, characteristics of localized stress, strain, hydrogen distribution in mesostructure can be predicted.

In the mechanical stress analysis of bi-crystal and polycrystalline aggregates, the local microstructural elastic deformation behaviour of individual FCC single crystal structures will generally be anisotropic exhibiting orthotropic behaviour in nature [7, 203-205]. Previous research by den Toonder et al. [204] concluded that

using the average isotropic elastic properties is incorrect for cubic bi-crystal and polycrystalline aggregate microstructures. FCC crystals are mechanically anisotropic due to the orientation dependence of the activation of crystallographic deformation mechanisms, and dependence on other mechanical phenomena such as strength, shape change and crystallographic texture (orientation distribution) etc. [7, 205, 206].

Multi-physics Coupled Macro-Micro model for hydrogen embrittlement

The aerospace industry has experienced unexpected hydrogen embrittlement problems for many years and the structural failures due to hydrogen embrittlement of aerospace components made of polycrystalline face-centred cubic (FCC) nickel and nickel based super alloy are often sudden and unpredictable. They may occur after a few hours, a few days or sometimes it may take years after manufacturing the component using manufacturing process such as welding, electroplating, etc. [e.g. 86, 101, 102, 215-222]. Hydrogen embrittlement generally concerns interactions between the microstructure, dislocations, hydrogen absorption/diffusion and stress [1-4, 164]. Hydrogen and stress may be introduced into the metal during the manufacturing process. The chemical diffusion of hydrogen is inhomogeneous at the microstructural level in nickel due to the difference in the diffusivity within grains and at grain boundaries as reported by Harris *et al.* [2], Palumbo *et al.* [1] and Gertsman *et al.* [164]. The initial stress distribution in FCC polycrystalline nickel is often inhomogeneous at the microstructural level due to the random crystallographic texture and the anisotropic properties of individual crystals, even under uniform applied stress. Inhomogeneous local stress distributions will impact on the stress assisted diffusion of hydrogen in polycrystalline nickel. They may play a critical role in the initiation of small micro cracks, such as intergranular cracks. The behaviour of these intergranular cracks is dependent on the inclination of the local grain boundary with respect to the tensile axis as reported in Kamaya *et al.* [223]. The growth of such cracks contributes to the potential failure of the material. It is therefore important to try to account for important microstructural phenomena within a component scale model to aid prediction of hydrogen embrittlement.

Micro-mechanism analysis of hydrogen induced cracking in nickel based superalloy 718

Superalloys are commonly used in aerospace engines, land based gas turbines, nuclear power plants as well as chemical plant application just to mention a few areas of interest. As the name “superalloy” indicates, this group of material possess “super good” properties at elevated temperatures and is rarely challenged today by any other group of material [226]. One reason for this advantage is their strength at high temperature ($>500^{\circ}\text{C}$) coupled with adequate ductility behaviour. A multi-component system, such as Alloy 718, contains many alloying elements and is one of the most commonly used superalloys being used today in the aerospace industry [88-89, 227 and 228]. Alloy 718 is useful in a very large range of different type of applications. It can be used in big static casings, Figure 1, as well as in rotating disks used in i.e., aero engines. Alloy 718 possesses a complex microstructure which is susceptible to ductility and delayed failure due to the presence of hydrogen through embrittlement phenomena.

Microstructure plays a significant role in hydrogen induced cracking / hydrogen embrittlement in polycrystalline metallic materials including superalloy Alloy718 [90, 103, 143, 166, 177-179, 180-189, 198, 231-242]. It is well known that the intergranular regions play critical role as preferential sites for crack nucleation and propagations in intergranular hydrogen induced cracking (IHIC)/ intergranular hydrogen embrittlement (IHE) of polycrystalline metallic materials [103, 118, 122, 127, 137, 142-143, 147, 173, 198, 231-235, 248-252]. It has been previously reported that GBCDs based on coincidence site lattice (CSL) such as high angle grain boundaries (HAGBs) act as preferential sites for crack nucleation. Cracks never nucleate at low angle grain boundaries (LAGBs). Surprisingly coherent ($\Sigma 3$) twin boundaries act as potential sites for crack nucleation. Twin boundaries are also reported to have higher resistance to intergranular cracking in FCC and BCC polycrystalline materials [90, 103, 166, 177-179, 181-189]. Grain boundary Engineering has been applied in nickel based super alloys to enhance the resistance to fracture [90, 178, 179, 186, and 241]. TJs also play significant role in the IHIC in FCC and BCC polycrystalline materials due to generation of compatibility stresses in

TJs which act as preferential sites for cavitation causing crack nucleation and propagation [103, 118, 122, 127, 142, 177, 183, 184, 248, and 249].

AIMS AND OBJECTIVES

The aim of this research is to investigate and understand the factors and microstructural features that affect the hydrogen embrittlement of materials such as nickel and nickel based super alloy 718 using multiscale modelling and experimental approaches. The weldability and effect of hydrogen on three different grades of pulse plated nickel will also be investigated.

The research objectives are as follows.

- Initially investigate various effects of microstructure such as grain size, grain boundaries, triple junctions and defects on hydrogen diffusion in polycrystalline nickel using microstructural modelling.
- Characterize conventional electrodeposited and pulse plated nickel using 2 dimensional and 3 dimensional electron backscattering diffraction (EBSD) analysis.
- Develop a microstructural based finite element (FE) model of the hydrogen permeation test to predict the hydrogen diffusion properties in conventional and pulse plated nickel.
- Investigate the effect of GB misorientation on hydrogen embrittlement in bi-crystal and polycrystalline nickel using a multiscale FE model.
- Develop microscale – macroscale coupling techniques to investigate hydrogen diffusion and the multi-physics of hydrogen embrittlement problems.

- Investigate the micro-mechanism of hydrogen embrittlement in nickel based super alloy 718 and pulse plated nickel using in-situ and ex-situ hydrogen charging slow strain rate tests (SSRT), scanning electron microscopy and EBSD.
- Investigate the susceptibility to cracking using a weldability test on three different grades of pulse plated nickel (including an established grade and newly developed grades).
- Increase the strain to failure in pulse plated nickel using grain boundary engineering (GBE) control and design.

MULTISCALE EXPERIMENTAL METHODS

4.1 Materials

The materials used in these experiments were a pure electrodeposited nickel, three different grades of pulse plated nickel (PP-Ni), a nickel based super alloy Inconel 718.

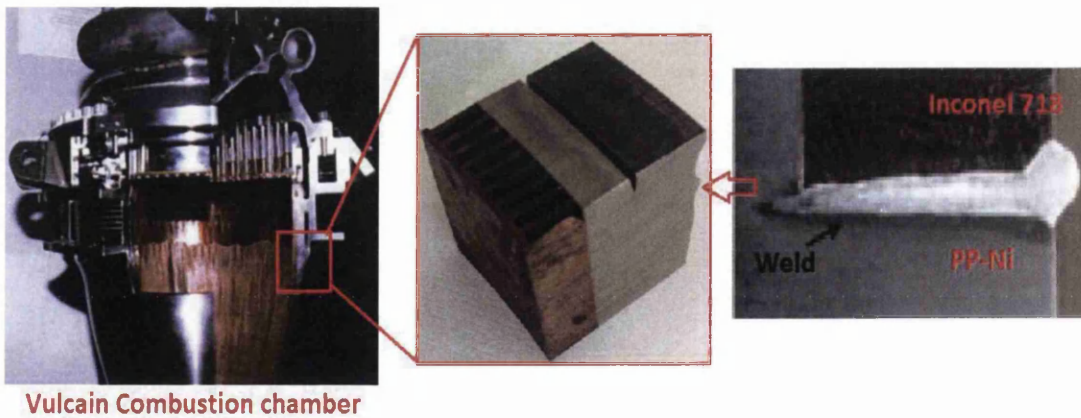


Figure 4.1.1 shows the Ariane5 Vulcain combustion chamber and a magnified view near the weldment. [260]

The PP-Ni is deposited over copper and copper alloy (e.g. CuAgZr alloy) substrates during the production process. Two fuel manifolds made from Inconel 718 are

welded onto the PP-Ni chamber as shown in figure 4.1.1. Nickel based super alloy 718 is manufactured by GKN aerospace (previously known as Volvo Aero). Volvo Aero is the world's largest supplier of combustion chambers and nozzles to commercial launch vehicles and is also the European centre of excellence for rocket turbines [Jokob Norgaard, New concept for Rocket engines, Force Technology presentation]. The as-manufactured chemical composition of the alloy 718 sample specimens is shown in table 4.1.2 in weight percentage (wt. %).

Al	B	C	Nb	Co	Cr	Cu	Fe	Mn	Mo	Ni	P	S	Si	Ti	Ta
0.58	0.004	0.067	4.93	0.55	18.10	0.07	18.50	0.23	3.06	53.10	<0.005	<0.002	0.06	1.03	<0.05

Table 4.1.2 shows the impurities compositions measured in PP-Ni.

Units: PPM (mean value / std. deviation)	Hydrogen	Oxygen	Sulphur	Carbon	Nitrogen
Grade 1	7/2	34/9	31/16	44/12	3/1
Grade 2	5/2	25/7	50/25	42/23	2/1
Grade 3	1/1	12	12	14	0.5

Table 4.1.1 shows the impurity compositions measured in PP-Ni.

Examples of the PP-Ni weldability test sample specimens and IN718 SSRT test samples specimens are shown in figure 4.1.2.

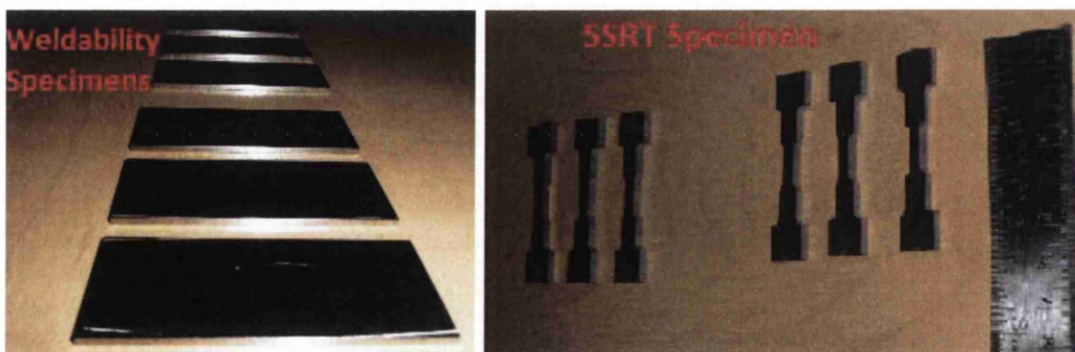


Figure 4.1.2 shows the some of the weldability test samples and SSRT test sample specimens.

4.2 Sample preparation

The samples used for material characterization such as scanning electron microscopy (SEM), secondary electron (SE) and 2D electron backscattering diffraction (EBSD) were cut from combustion chamber to provide several specimens; near the weldment, copper, copper alloy, alloy 718 and copper-PP-Ni interfaces, some of the PP-Ni as deposited, some before and after annealing and some before and after slow strain rate test (SSRT). These are mounted using conductive epoxy resin as shown in figure 4.2.1 (a). The mounted samples were mechanically ground using P600, P400 and P280 silicon carbide grid paper for 6 minutes depending on the sample material. The mechanically ground specimens are polished using two different techniques 1) mechanical polishing and 2) electro polishing. Mechanical polishing was done with $9\mu\text{m}$, $3\mu\text{m}$ and $1\mu\text{m}$ diamond suspension for 6 minutes, 10 minutes and 15 minutes respectively. The final polishing was done using $0.02\mu\text{m}$ colloidal silica for 25 minutes. The nickel and nickel based super alloys are electro-polished using two polishing steps, an initial step for rough polishing using 15% perchloric acid (HClO_4) in acetic acid ($\text{C}_2\text{H}_4\text{O}_2$) at 15V DC current and a subsequent step for fine polishing using 3% perchloric acid in acetic acid at 5V DC current. Electro-polishing was done after the specimens were mechanically polished for 15 minutes using a $3\mu\text{m}$ diamond suspension to remove the roughness of the sample surface. The sample preparation for 3D EBSD involves 80° edge mechanical cutting of the sample as shown in figure 4.2.1 (b) and then carefully mechanical polishing similar to 2D EBSD on top surface and side surface. Then the samples were trenched to reduce re-deposition and to avoid shadowing effect during EBSD analysis and a thin layer of platinum was deposited on the top surface for homogenization cutting as shown in figure 4.2.1 (c) and (d).

4.3 SEM/EBSD

Metallographic observations for detailed microstructural evaluation on mechanically ground and polished samples were done using a Phillips XL30 Scanning Electron Microscope at various magnifications. Both TSL and HKL EBSD systems were used for 2D EBSD characterization. An Oxford instrument channel 5 HKL system configured in a Phillips XL30 Scanning Electron Microscopy was used for EBSD characterization at 20 kV accelerating voltage with a beam spot size between 5 and 7 nm.

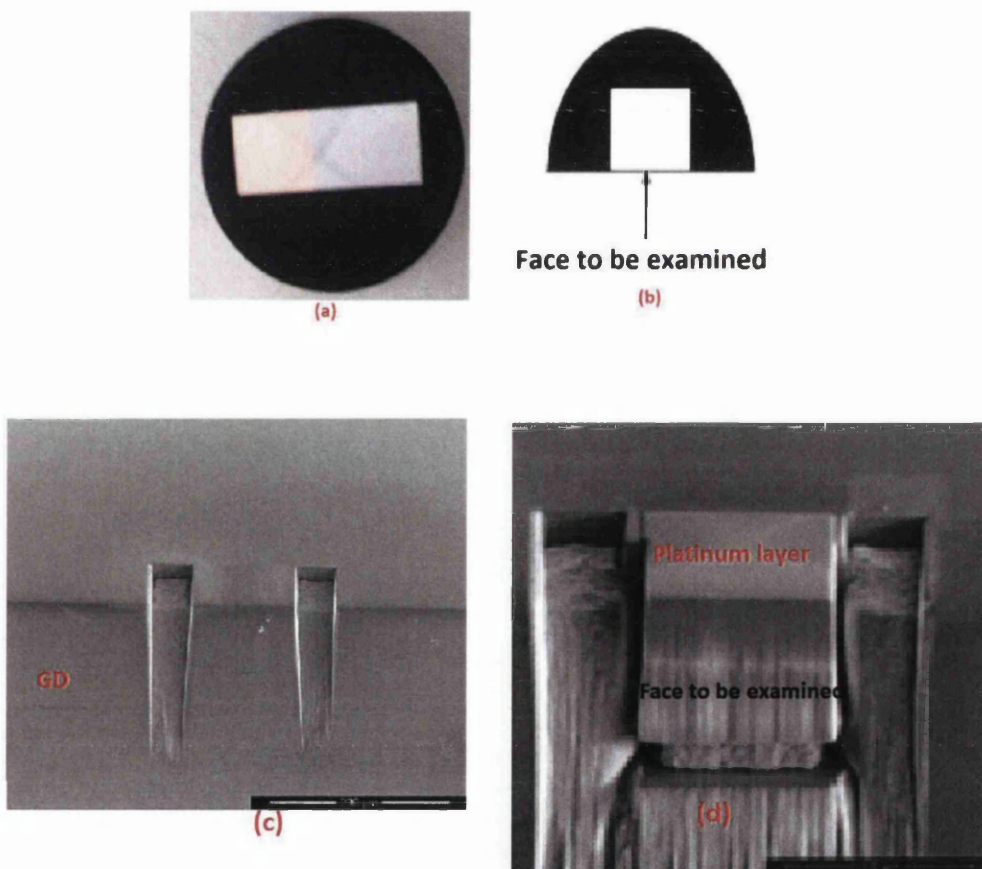


Figure 4.2.1 (a) shows the specimen mounted on conductive resin, (b) shows the 3D EBSD sample, (c) shows the 3D EBSD sample with large trenches and (d) shows 3D EBSD sample after milling and platinum layering (Note: Tranches are milled to reduce re-deposition and avoid shadowing effects and a platinum layer is deposited for homogenization of FIB cutting.).

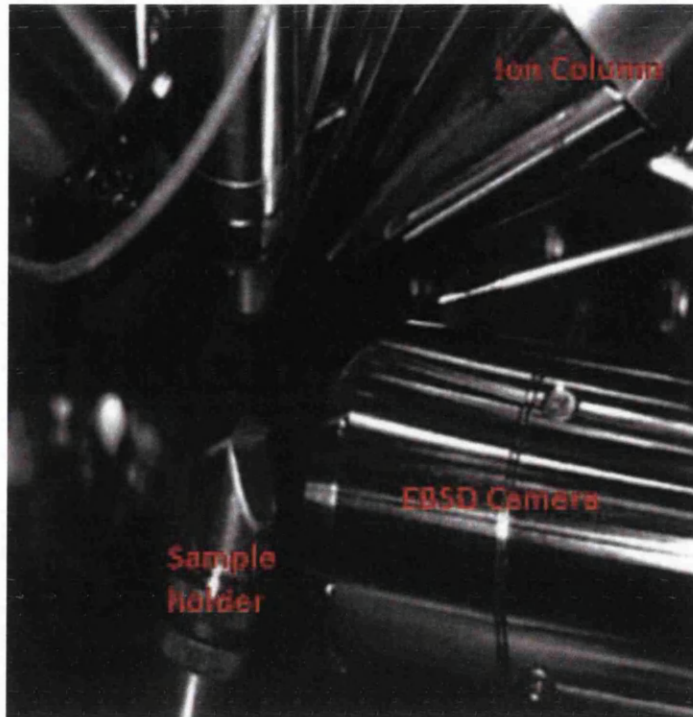


Figure 4.3.1 shows the FEG-SEM chamber.

A Nordilus Camera inserted to 164.1mm on specimen chamber and the sample specimen holder titled to 70° and then the keeping the working distance of about 20.3 for most cases. An EDAX EBSD system (EDAX, NJ, USA) combining an FEI Nova 600 Nanolab dual-beam scanning focused ion beam (FIB) field emission gun SEM (FEG-SEM) was used for 3D EBSD characterization with 20 kV electron beam and 30 kV FIB accelerating voltage and a liquid Ga^+ source. 180° rotation was done between FIB milling and EBSD acquisition with 200 nm slice thickness for 88 slices. The FEG-SEM chamber is shown in figure 4.3.1. Different step size starts from 0.05 μm to 1 μm were used in the EBSD analyses depending on the sample grain size. The camera was set to 4×4 binning, noise reduction was set to 2 frames per second and the Hough transform was set to 120 for most cases. The EBSD data was post processed using TSL EDAX Orientation image microscopy (OIM) analysis software and HKL Tango mapping software. The GB misorientation, grain orientation, grain size and CSL fraction were analysed using post processing and $\Sigma 3^n$ (i.e. $n \leq 3$ $\Sigma 3$, $\Sigma 9$ and $\Sigma 27$) GB was classified using the Brandon criterion. Grain boundary and triple

junction characteristic distributions and classifications are explained in detail in the Results sections.

4.4 Slow strain rate test (SSRT)

The slow strain rate test is one of most commonly used and accepted testing methods to determine the susceptibility of a material to hydrogen embrittlement (HE) by taking into account the interaction between a hydrogen environment and applied stress due to mechanical loading at a slow strain rate. The basic principle of this testing method is continuous constant strain rate loading in either hydrogen pre-charged samples or with continuous hydrogen charging for tests up to fracture. Material properties such as elongation to failure, yield strength and ultimate tensile strength are measured. The SSRT test is also performed in air to compare the material properties with and without a hydrogen environment to quantify the effect of hydrogen on material performance. It is important to note that the strain rate should not be too low and the generally recommended strain rates are in the range of 10^{-3} to 10^{-8} s⁻¹ depending on material. IN718 and different grades of PP-Ni SSRT are machined to the test specimen dimensions as shown in figure 4.4.1.

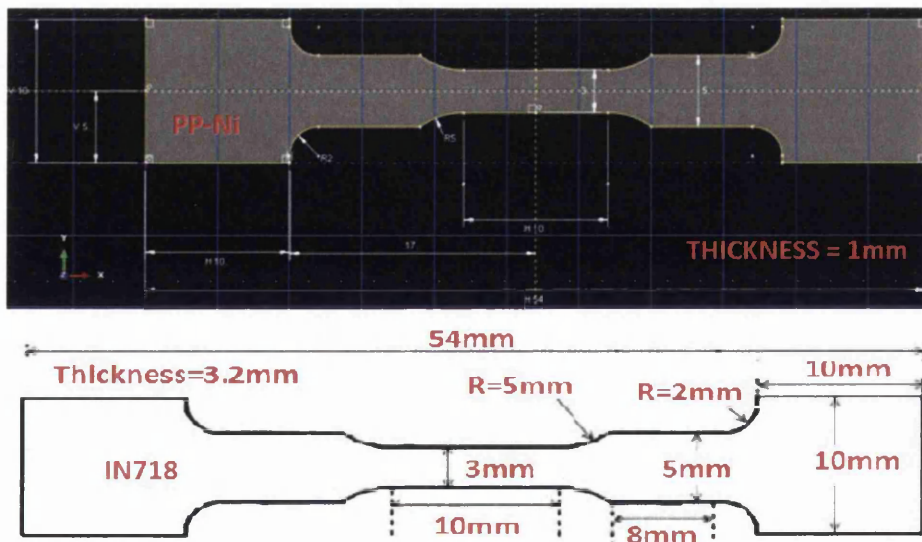


Figure 4.4.1 shows the dimension of SSRT sample specimen (i.e. PP-Ni and IN718).

Slow strain rate testing (SSRT) was conducted with two different strain rates of 10^{-4} s^{-1} and 10^{-3} s^{-1} along the rolling direction (RD) at ambient temperature (21°C) using an Instron 8511 hydraulic testing machine. SSRT tests were conducted in air and using an in-situ hydrogen charging condition. For IN718 material hydrogen was introduced into the specimens prior to tests for 4 hours and 16 hours (i.e. internal hydrogen embrittlement) and also in-situ hydrogen charging continuously was used during the SSRT (i.e. environmental hydrogen embrittlement) using cathodic charging at room temperature. In the different grades of PP-Ni hydrogen was introduced into the specimens prior to tests for 72 hours at 90°C and there was no hydrogen introduced while testing. Cathodic charging was performed in a 3% NaCl aqueous solution containing 3.0 g.dm^{-3} of ammonium thiocyanate (NH_4SCN) at a current density of 10 Am^{-2} using platinum as a counter electrode. Total hydrogen charging time is determined by addition of the pre-charging time (i.e. 4 or 16 or 72 hours) to the experimental fracture strain divided by the strain rate. Hydrogen charging was stopped when the specimen failed. Hydrogen charging during tensile testing introduces external hydrogen efficiently into the samples via hydrogen transport and stress assisted diffusion. Figure 4.4.2 shows the temperature control electrochemical charging cells and ex-situ SSRT testing machine.



Figure 4.4.2 (a) shows the electrochemical charging cells and (b) shows the ex-situ SSRT testing machine.

4.5 Heat treatment

Manufacturing techniques such as electrodeposition, welding etc. may produce residual stress and hydrogen into the materials. Heat treatments were carried out in vacuum furnaces for annealing of the material to relieve the residual stresses and effuse the hydrogen atom from material. Heat treatment was also carried out for grain boundary engineering purposes to modify grain orientations and grain boundary misorientations in an attempt to increase the fraction of particular special grain boundaries. Heat treatments are also usually carried out for precipitate strengthening in the two steps of solution heat treatment followed by age hardening. Figure 4.5.1 shows the heat treatment furnace and some of the TDS and SSRT heat treated specimens. The IN718 SSRT sample specimens were solution heat treated at 954°C for 1 hour and then furnace cooled at a rate of 20°C per minute down to 500°C followed by a normal furnace cooling to room temperature.

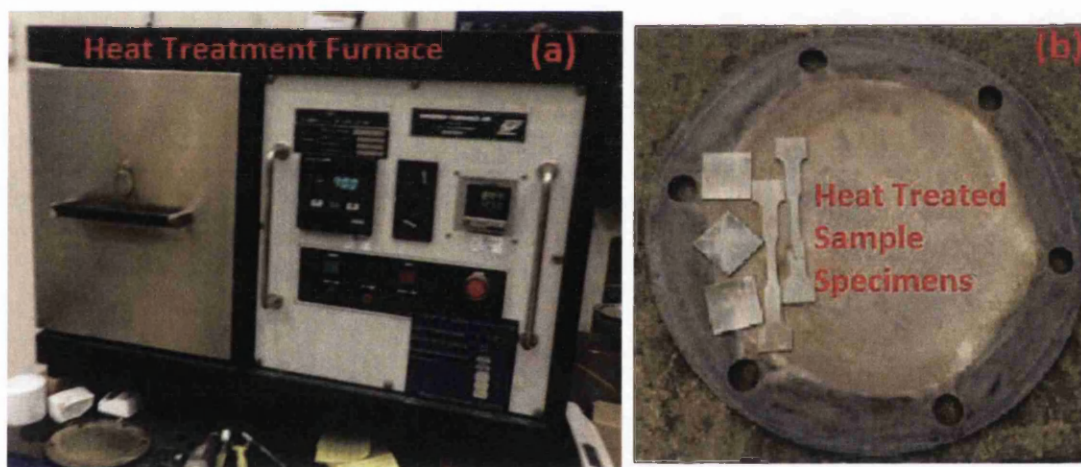


Figure 4.5.1 (a) shows the heat treatment furnace and (b) shows some of the heat treated samples.

4.6 Weldability test

Weldability test are used to assess the susceptibility of welds to hot and cold cracking. The test quantifies the cracking susceptibility for welding of the material. More than 150 weldability tests exist. The Longitudinal Vareststraint (normally called Vareststraint) test developed by Savage *et al.* is the most commonly used test method

to study hot cracking susceptibility and sensitivity of weld metals (including heat affected zone, HAZ, cracking and solidification cracking) by making real welds in the longitudinal direction on the specimen while rapidly applying strain during welding as shown in figure 4.6.1. Three different grades of PP-Ni specimens for Vareststraint test were manufactured using pulse plating techniques and machined to 40 mm width, 100mm length and 3mm and 4mm thickness, as shown in figure 4.1.2 (a). Augmented strain (i.e. the applied strain) can be varied by varying the bending die block radius as shown figure 4.6.2. The augmented strain percentage can also be varied by varying the thickness of the specimens. The augmented strain (ϵ) is calculated using equation 4.6.1.

$$\epsilon = \frac{t}{2R} \times 100 \% \quad (4.6.1)$$

Where t = thickness of the sample specimen and R =radius of the bending die block.

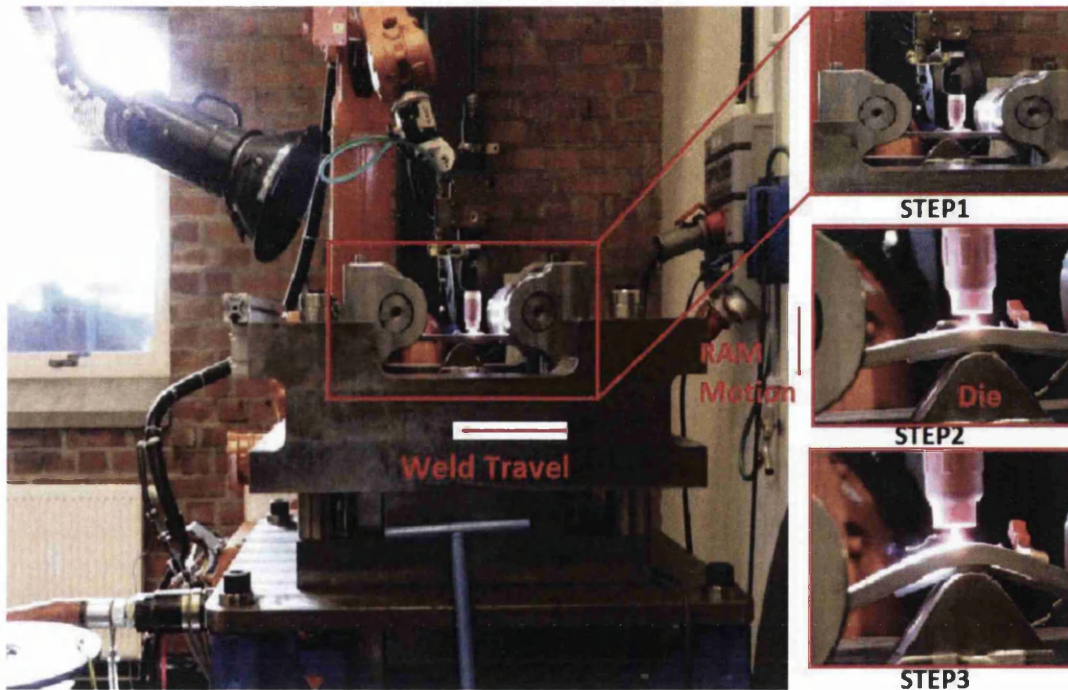


Figure 4.6.1 shows the Weldability testing machine and close view of Vareststraint test steps.

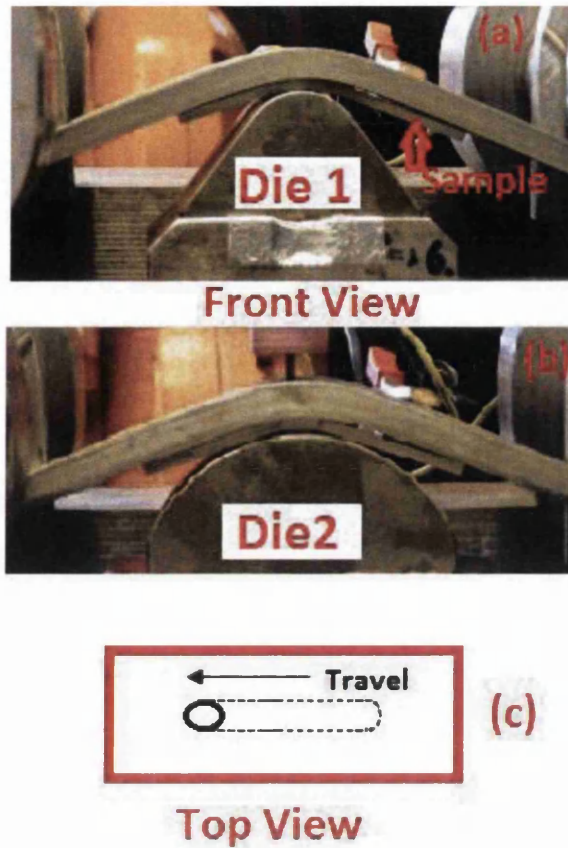


Figure 4.6.2 shows two different types of bending die blocks with two different radiuses. (a), (b) shows the side view with different die blocks [Note: The larger the die block radius the smaller the augmented strain] and (c) shows the specimen top view and weld travel direction.

Varestraint tests were conducted on the PP-Ni specimens after pulse plating under both the uncharged condition and the hydrogen charged condition to understand the weld crack susceptibility and the effect of hydrogen for established (grade 1) and newly developed (grades 2 and 3) materials.

Welding Speed (W _s)	Current (I)	Weld offset	Weld Length	Bending Speed (B _s)	Gas flow (Argon Gas)	Die block Radius 1	Die block Radius 2	Thickness 1	Thickness 2
1.0 mm/s	70 Amps	5 mm	50 mm	10 mm/s	15 l/min	20 mm	50 mm	3 mm	4 mm

Table 4.6.1 shows the weldability test parameters used.

The average total crack length (TCL) (calculated using both HAZ and Fusion Zone (FZ) of individual tests at particular augmented strains) is compared between different grades of materials and between hydrogen charged and uncharged specimens. The tested sample surfaces are examined for cracking using microscopy at low magnifications between 20x to 60x. The Varestraint testing parameters used are shown in table. 4.6.1.

4.7 Thermal desorption Analysis (TDA):

Thermal desorption analysis was used to evaluate the hydrogen content in the material by measuring the hydrogen desorption rate while heating the sample at a constant rate. The experimental setup and schematic of TDA can be found in figure 4.7.1.

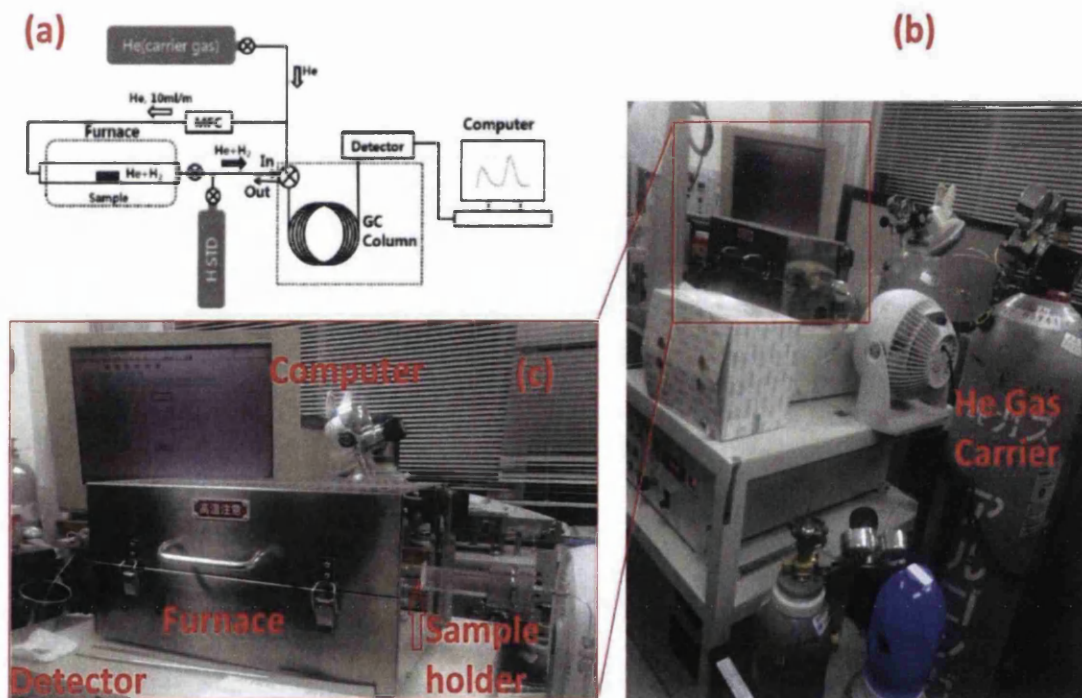


Figure 4.7.1 (a) shows the Schematic illustration of TDA with gas chromatography [271], (b) shows the real setup of TDA and (c) show the close view of TDA.

As the temperature increases the hydrogen present in the sample specimen escapes and diffuses out of the sample and desorbs to the gas chromatography unit with helium as a carrier gas. The amount of hydrogen is then measured. The

dimensions of the samples used for TDA are 1.5 cm width, 1.5 cm length with 1 mm thickness as shown in figure 4.5.1 (b).

MATHEMATICAL MODEL

5.1 Mathematical description of hydrogen diffusion

The hydrogen flux vector \mathbf{J} consists of a combination of hydrogen generated by the hydrogen concentration gradient \mathbf{J}_c . The hydrogen flux vector generated by the hydrogen concentration gradient is based on *Fick's first law of diffusion* by using the *thermodynamic formulation* based on the *Gibbs free enthalpy*.

$$\mathbf{J}(X, t) = \mathbf{J}_c(X, t) \quad (5.1.1)$$

$$\mathbf{J}_c(X, t) = -D\nabla C = -D\left(\frac{\partial C(x,t)}{\partial x} + \frac{\partial C(y,t)}{\partial y} + \frac{\partial C(z,t)}{\partial z}\right) \quad (5.1.2)$$

$$\mathbf{J}_c(X, t) = -D \frac{\partial C(X,t)}{\partial X} \quad (5.1.3)$$

Based on the *law of matter conservation*, the amount of hydrogen is expressed by the continuity equation based on a transient (time dependent) diffusion process without trapping as described by *Fick's second law*

$$\frac{\partial C}{\partial t} = -divJ \quad (5.1.4)$$

$$\frac{\partial C}{\partial t} = D\nabla^2 C \quad (5.1.5)$$

$$\frac{\partial C}{\partial t} = D \frac{\partial^2 C(x,t)}{\partial X^2} \quad (5.1.6)$$

$$\therefore \frac{\partial C}{\partial t} = D\Delta C \quad (5.1.7)$$

Where the concentration of hydrogen is C , ∇ is the gradient operator, Δ is the Laplace operator and X represents three dimensions (3D) x,y,z . The commercial software ABAQUS implements the governing equation for stress driven diffusion as

$$\therefore \frac{\partial C}{\partial t} = sD\Delta\phi \quad (5.1.8)$$

Where s is solubility, and $\phi = C/s$ is the normalized hydrogen concentration

A numerical finite element approach for stress induced hydrogen diffusion:

The standard Galerkin process is used where the element shape functions $N_j(\mathbf{r})$ serve as trial and weight residual functions, $j=1,2,3,\dots,n$ are the number of nodes of the finite element mesh.

$$[M_{ij}] \left\{ \frac{dC_j}{dt} \right\} + ([K_{ij}^l]) \{C_j\} = \{F_i\} \quad (5.1.9)$$

Where $i=1$ represents the component vector column, [...] represents components element matrices, $[M_{ij}]$ represents the concentration capacity matrix given by equation (5.1.10), $[K_{ij}^l]$ represents the diffusion matrix given by equations (5.1.11), where $l = 1$ and $[F_i]$ represents the diffusion flux vector columns given by equation (5.1.12).

$$[M_{ij}] = \int_V N_i N_j dV = \int_V [A]^T [A] dV \quad (5.1.10)$$

$$[K_{ij}^1] = D \int \nabla N_i \nabla N_j dV = D \int [B]^T [B] dV \quad (5.1.11)$$

$$[F_i] = -J_s \int_S N_i dS \quad (5.1.12)$$

The interpolation matrices $[A]$ and $[B]$ are given in equations (5.1.13) to (5.1.15).

$$C_j = [A] \{C_j\} \quad (5.1.13)$$

$$\frac{dC_j}{dt} = [A] \left\{ \frac{dC_j}{dt} \right\} \quad (5.1.14)$$

$$\nabla C = [B] \{C_j\} \quad (5.1.15)$$

The time integration in transient hydrogen concentration $\left\{\frac{dC_j}{dt}\right\}$ utilizes the modified Crank-Nicholson method given in equation (5.1.16).

$$\left\{\frac{dC_j}{dt}\right\} = \frac{1}{\Delta t} (\{C_j\}_{t+\Delta t} - \{C_j\}_t) \quad (5.1.16)$$

The final equation is given by equation (5.1.17).

$$\left(\frac{1}{\Delta t} [M_{ij}] + [K_{ij}^1]\right) \{C_j\}_{t+\Delta t} = \left(\frac{1}{\Delta t} [M_{ij}]\right) \{C_j\}_t + \{F_i\} \quad (5.1.17)$$

5.2 A mathematical description of stress assist hydrogen diffusion

The hydrogen flux vector generated by the hydrostatic stress gradient is based on a *modified Fick's first law* by taking into account the stress field where the concentration of hydrogen is C , R is the ideal gas constant equal to 8.314 J/mol K and the partial molar volume of hydrogen is V_h (2000 mm³/mol) [214],

$$J(X, t) = J_c(X, t) + J_h(X, t) \quad (5.2.1)$$

$$J_c(X, t) = -D\nabla C = -D\left(\frac{\partial C(x,t)}{\partial x} + \frac{\partial C(y,t)}{\partial y} + \frac{\partial C(z,t)}{\partial z}\right) \quad (5.2.2)$$

$$J_h(X, t) = \frac{DV_h}{RT} C \nabla \sigma_h \quad (5.2.3)$$

$$J_h(X, t) = \frac{DV_h}{RT} C \frac{\partial \sigma_h}{\partial X} \quad (5.2.4)$$

$$\therefore J(X, t) = -D \frac{\partial C(X,t)}{\partial X} + \frac{DV_h}{RT} C \frac{\partial \sigma_h}{\partial X} \quad (5.2.5)$$

Where hydrostatic stress gradient σ_h in the heterogeneous microstructural material.

Hydrostatic stresses σ_h is defined as

$$\sigma_h = \frac{1}{3} (\sigma_{xx} + \sigma_{yy} + \sigma_{zz}) \quad (5.2.6)$$

Based on the *law of matter conservation*, the amount of hydrogen is expressed by the continuity equation based on a transient (time dependent) diffusion process without trapping as described by *Fick's second law*

$$\frac{\partial C}{\partial t} = -div J \quad (5.2.7)$$

$$\frac{\partial C}{\partial t} = D\nabla^2 C - \frac{DV_h}{RT} (C\nabla^2 \sigma_h + \nabla C \nabla \sigma_h) \quad (5.2.8)$$

$$\frac{\partial C}{\partial t} = D \frac{\partial^2 C(X,t)}{\partial X^2} - \frac{DV_h}{RT} C \frac{\partial^2 \sigma_h}{\partial X^2} - \frac{DV_h}{RT} \frac{\partial \sigma_h}{\partial X} \frac{\partial C}{\partial X} \quad (5.2.9)$$

$$\therefore \frac{\partial C}{\partial t} = D\Delta C - \frac{DV_h}{RT} C \Delta \sigma_h - \frac{DV_h}{RT} \nabla C \nabla \sigma_h \quad (5.2.10)$$

The commercial software ABAQUS implements the governing equation for stress driven diffusion as shown in equation (5.2.11).

$$\therefore \frac{\partial C}{\partial t} = sD\Delta\phi - \frac{DV_h}{R(T-T_0)} s\phi\Delta\sigma_h - \frac{DV_h}{R(T-T_0)} s\nabla\phi\nabla\sigma_h \quad (5.2.11)$$

Where s is solubility, $T_0 = 0K$ and C/s is the normalized hydrogen concentration which is dependent on the hydrostatic stresses as expressed in the equation below.

$$\phi = \phi_0 \exp\left(\frac{-V_h\sigma_h}{R(T-T_0)}\right) \quad (5.2.12)$$

Where the unstressed state of the normalized concentration under the condition of hydrogen-metal equilibrium is ϕ_0 .

A numerical finite element approach for stress induced hydrogen diffusion:

The standard Galerkin process of the element shape functions $N_j(\mathbf{r})$ were used to approximate the distribution of stresses as shown in the equation (5.2.13).

$$\sigma_h(\mathbf{r}) = \sum \sigma_{hj} N_j(\mathbf{r}) \quad (5.2.13)$$

Where approximate distributions of stresses are $\sigma_h(\mathbf{r})$ and element shape functions $N_j(\mathbf{r})$ serve as trial and weight residual functions, $j=1,2,3,\dots,n$ are the number of nodes of the finite element mesh. In order to apply equation (5.2.14) in finite element analysis of stress assisted diffusion, equation (5.2.11) is converted to its discrete form given by equation (5.2.14).

$$[M_{ij}] \left\{ \frac{dC_j}{dt} \right\} + ([K_{ij}^1] + [K_{ij}^2] + [K_{ij}^3]) \{C_j\} = \{F_i\} \quad (5.2.14)$$

Where $i=1,2,3,\dots,n$, $\{\dots\}$ represents the component vector column, $[\dots]$ represents components element matrices, $[M_{ij}]$ represents the concentration capacity matrix given by equation (5.2.15), $[K_{ij}^l]$ represents the diffusion matrix given by equations (5.2.16), (5.2.17) and (5.2.18), where $l = 1,2,3$ and $[F_i]$ represents the diffusion flux vector columns given by equation (20).

$$[M_{ij}] = \int_V N_i N_j dV = \int_V [A]^T [A] dV \quad (5.2.15)$$

$$[K_{ij}^1] = D \int \nabla N_i \nabla N_j dV = D \int [B]^T [B] dV \quad (5.2.16)$$

$$[K_{ij}^2] = -\frac{DV_h}{R(T-T_0)} \int [A]^T [B] \{\sigma_h\} [B] dV \quad (5.2.17)$$

$$[K_{ij}^3] = -\frac{DV_h}{R(T-T_0)} \int [B]^T [B] \{\sigma_h\} [A] dV \quad (5.2.18)$$

$$[F_i] = -J_s \int_S N_i dS = \int_S [A]^T \phi dS \quad (5.2.19)$$

Where $\phi = D\nabla C - \frac{DV_h}{R(T-T_0)}$,

The interpolation matrices are $[A]$ and $[B]$ given in equations (5.2.20) to (5.2.23).

$$C_j = [A]\{C_j\} \quad (5.2.20)$$

$$\frac{dC_j}{dt} = [A]\left\{\frac{dC_j}{dt}\right\} \quad (5.2.21)$$

$$\nabla\sigma_h = [B]\{\sigma_h\} \quad (5.2.22)$$

$$\nabla C = [B]\{C_j\} \quad (5.2.23)$$

The time integration in transient hydrogen concentration $\left\{\frac{dC_j}{dt}\right\}$ utilizes the modified Crank-Nicholson method given in equation (5.2.24).

$$\left\{\frac{dC_j}{dt}\right\} = \frac{1}{\Delta t} (\{C_j\}_{t+\Delta t} - \{C_j\}_t) \quad (5.2.24)$$

The final equation is given by equation (5.2.25).

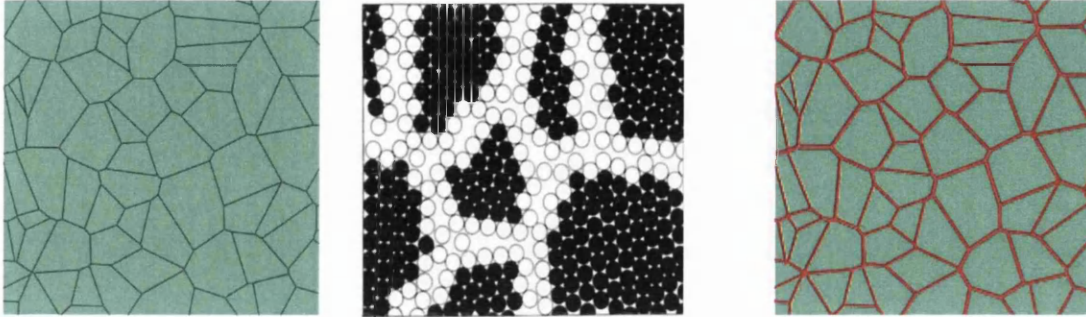
$$\left(\frac{1}{\Delta t}[M_{ij}] + [K_{ij}^1]\right)\{C_j\}_{t+\Delta t} = \left(\frac{1}{\Delta t}[M_{ij}] - [K_{ij}^2] - [K_{ij}^3]\right)\{C_j\}_t + \{F_i\} \quad (5.2.25)$$

MULTISCALE COMPUTATIONAL METHODS

6.1 Synthetic polycrystalline microstructure model

The workings of a computationally modelled heterogeneous polycrystalline microstructure and the effects of average intragranular phase size and intergranular phase are presented here. Voronoi tessellation techniques were adopted to geometrically model the polycrystalline material. The 2D polycrystalline microstructure was randomly created as polygonal intragranular phase grains surrounded by zero intergranular phase thickness in the fixed 2D plane area. The grains were generated by calling the Voronoi generation function in MATLAB. Seeds for the Voronoi polygon grains were generated using random points. Then by averaging the vertices of each cell the centre point of these random polygons grain cells were calculated. Interior Voronoi polygon grains are generated using the calculated centre points and by matrix arithmetic, as shown in equation (6.1.1), the random intergranular phase thickness was introduced into the polycrystalline microstructure as shown in the figure 6.1.1. Each polygonal intragranular region is surrounded by the intergranular phase thicknesses which are shared by adjoining polygonal grains to form a random polycrystalline microstructure with a random

intergranular phase as shown in the figure 6.1.1. The average thicknesses of the random intergranular phase are controlled by controlling the number of seeds. The average size of the intragranular polygonal phase grains and its distribution are controlled by controlling the number of seeds and their relative position in the fixed representative area element.



(a)

(b)

(c)

Figure 6.1.1 Polycrystalline microstructures (a) With zero intergranular phase thickness (b) Atomic structure of a two dimensional model of nanostructured material. The atoms in the centres of the crystals are indicated in black represented as grains. Those in the boundary core regions are drawn as open circles representing grain boundaries [32] (c) Same as (a) but with nonzero random intergranular phase thickness.

$$(ipvx, ipvy) = (1 - \delta) * (opvx, opvy) + \delta * (cmx, cmy) \quad (6.1.1)$$

In the above equation $ipvx, opvx$ are the inner and original centre polygon vertex x-coordinate values respectively, $ipvy, opvy$ are the inner and original centre polygon vertex y-coordinate values respectively, cmx, cmy is the calculated centre point of original centre closed polygon coordinates x and y coordinate values respectively and δ is the average thickness of the random polygon.

A MATLAB code was developed to determine the inner Voronoi polygon grain cells edges, vertices, and centre for each randomly generated polygon of the polycrystalline microstructures and these data were exported to the PYTHON programming language. Then PYTHON code was developed to import the inner and outer Voronoi polygon grain cells data. By using these data, lines were drawn for each polygon cells vertices to partition the faces of each polygon. An average random intergranular phase thickness was generated in MATLAB (for example 5 nm is used for an approximate average grain size of 100 μm as shown in figure 6.1.2).

The polycrystalline microstructures for different average grain size ranges from $100\ \mu\text{m}$ to $0.01\ \mu\text{m}$ were simulated. According to many reported results, the importance of triple junctions is significant when the average grain size is less than $10\ \text{nm}$ [7]. In this work the triple junction is not specified individually but is incorporated as part of the intergranular phase.

The MATLAB and PYTHON codes were used to obtain different average intragranular polygon phase grain sizes, different surface areas per unit volume of intergranular regions, different average intergranular phase thicknesses and different volume fractions of intergranular microstructures by changing the number of Voronoi seeds/scale factors and the thickness between the interior and exterior Voronoi diagrams.

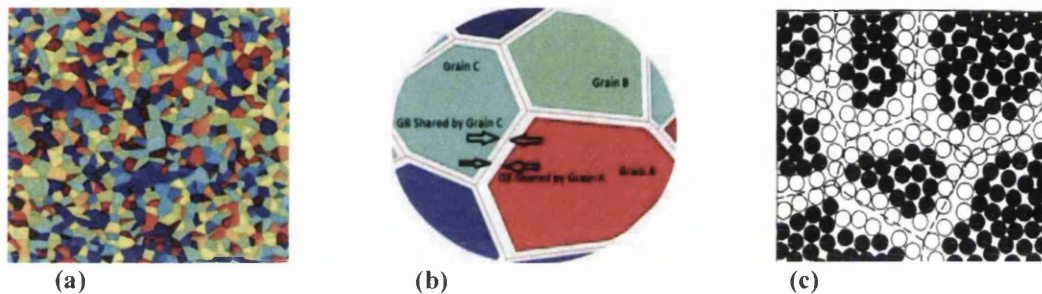


Figure 6.1.2 (a) computationally generated 2D Representative Volume Element model of heterogeneous polycrystalline microstructure with average random intergranular phase thickness of $5\ \text{nm}$ and approximate grain size of $100\ \mu\text{m}$. (b) Heterogeneous polycrystalline microstructures with random intergranular phase shared between adjoining polygonal intragranular phases. (c) Schematic cross section through a two dimensional nano-glass. The atoms are represented by circles. The material consists of small interior regions (filled circles) in which the interatomic spacings are similar to a bulk glass. In the interfacial region (broken lines, open circles) a broad spectrum of interatomic spacings exists [42].

A mesh convergence study was then performed in ABAQUS to eliminate the mesh sensitivity from results and to ensure the precision of the analysis. The number of elements used was based on the mesh convergence study. Triangular elements were generated as they were suitable for capturing the complexity of the geometry required. Intergranular and intragranular phases were given different diffusion properties according to the constitutive equations. The diffusivity parameters of intragranular and intergranular phases used in the finite element model were of the order of $9 \times 10^{-14}\ \text{m}^2/\text{s}$ and $4 \times 10^{-10}\ \text{m}^2/\text{s}$ respectively.

6.2 Microstructural homogenization Method

In the microstructural homogenization technique, it is the practice of most microstructural models to consider the representative volume element RVE of heterogeneous microstructural distribution in a periodic arrangement to reduce the complexity of the analysis and for computational efficiency. Figure 6.2.1 shows the heterogeneous macroscopic polycrystalline composite media and the intergranular and intragranular microstructural RVEs.

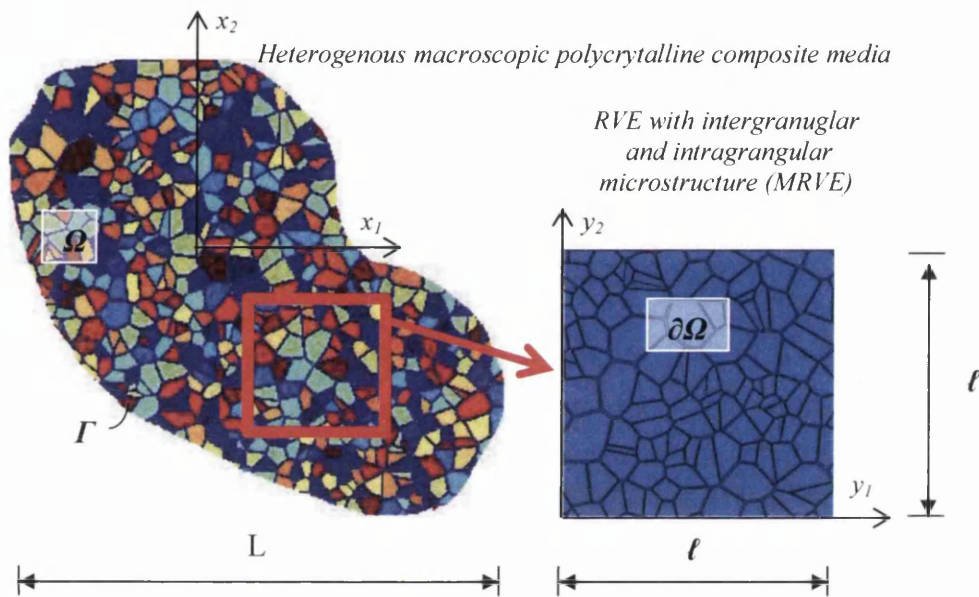


Figure 6.2.1 Heterogeneous polycrystalline composite media and microstructural representative volume element.

In a heterogeneous composite polycrystalline medium, the actual microstructural intergranular and intragranular distributions are random. The generated 2D random intergranular polygon and random intragranular microstructural distribution were taken as the microstructural representative volume element (MRVE) and implemented in the finite element model to generate the 2D finite element microstructural representative volume element model (FEMRVE). This MRVE has the same mass transport properties and intragranular volume fraction as the composite media. The heterogeneous MRVE were embedded with the homogeneous RVE (HRVE) to global RVE (GRVE) as shown in the figure 6.2.2 to make it easier to find the unknown effective composite mass transport constant. Both the

heterogeneous MRVE and HRVE have the same mass transport constants. Normally, the heterogeneous polycrystalline composite media is modelled as a homogenous media with certain effective mass transport properties that describe the average hydrogen transport properties of the heterogeneous polycrystalline phase field microstructure.

In the present work, the hydrogen transport equations are solved numerically. The macroscopic 2D domain, that is, Ω , made of heterogeneous polycrystalline composite media. The microstructural response of the material was analysed using RVEs of microscopic length scale (ℓ), where microscopic size scale is much small than the macroscopic length scale (L). The length scale ratio is represented by the small parameter $\varepsilon = \ell/L$ where ε is the small parameter $0 < \varepsilon \ll 1$. The periodic in local variable $y = x/\varepsilon$ and for each $x \in \Omega$. All the field variables are macroscopic (x), microscopic (y) and time dependent (t) as $\Phi(x, y, t) = \Phi(x, x/\varepsilon, t)$.

The steady state mass flow equilibrium of the macroscopic Ω domain is:

$$\frac{\partial J_i}{\partial x_j} = 0 \quad \text{in } \Omega \quad (6.2.1)$$

Where $\partial J_i / \partial x_i$ denotes the mass flux vector through the macroscopic unit area, the suffix i denotes the directions.

$$J_i n_i = \tilde{f} \quad \text{on } \Gamma \quad (6.2.3)$$

Where \tilde{f} is the prescribed mass flux normal to the boundary Γ , n_i is the outward vector component normal to the boundary. The constitutive equation for the mass flux at any point in macroscopic Ω domain is given by

$$J_i(x) = -D_{ij}(x) \cdot \left(\frac{\partial c}{\partial x_1} + \frac{\partial c}{\partial x_2} \right) \quad (6.2.3)$$

$$J_i(x) = -D_{ij}(x) \cdot \nabla C_j(x) \quad (6.2.4)$$

Where D_{ij} second order diffusivity tensor. The local properties are assumed to be isotropic in this work. D_{ij} is defined according to the underlying intergranular and intragranular microstructure.

For a uniform mass flux at the boundary, the mass flux at any point $x \in \Gamma$ is given by the equation below. To describe macroscopic homogeneous media, the

steady state microscale mass flows through the microscopic domain were volume averaged as shown below.

$$\overline{J_i(x)} \cdot n_i = J_i(y) \cdot n_i \tag{6.2.5}$$

$$\Rightarrow \overline{J_i(x)}(x) = \langle J_i(y) \rangle \tag{6.2.6}$$

$$\overline{J_i(x)} = \langle -D_{ij}(y) \cdot \nabla C_i(y) \rangle \tag{6.2.7}$$

Where $\overline{J_i(x)}$ is the macroscopic mass flux and $J_i(y)$ is the microscopic mass flux.

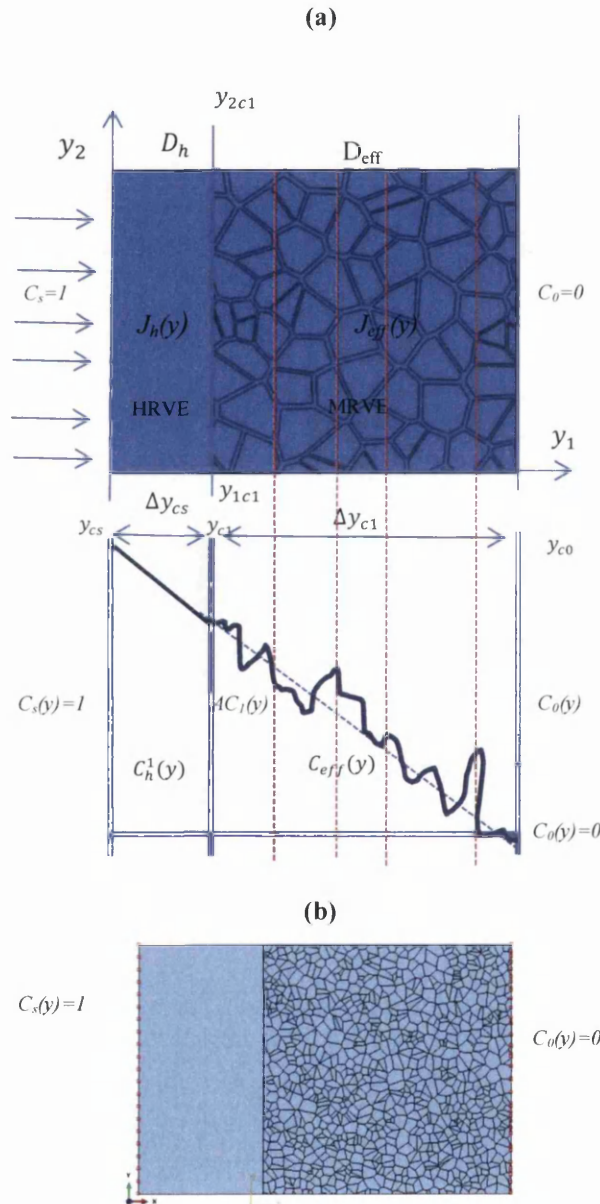


Figure 6.2.2 (a) GRVE with MRVE embedded with HRVE (b) Mass concentration profile in HRVE with increase or decrease at MRVE due to intergranular microstructures and (c) the boundary condition of the GRVE for FE analysis.

Consider the two dimensional heterogeneous polycrystalline microstructural composite media formed by periodically distributed polycrystalline intragranular and intergranular microscopic regions with the diffusion coefficient D_{ig} and D_{gb} , respectively and its effective diffusion coefficient D_{eff} shown in Figure 6.2.2 (a). The corresponding concentrations are denoted by $C_g(y)$, $C_{gb}(y)$ and $C_{eff}(y)$. According to the effective medium theory, the macroscopic heterogeneous polycrystalline composite periodic media were replaced by the MRVE consisting of randomly generated polygon grains as intragranular microstructure and randomly generated grain boundaries embedded between the polygon grains as intergranular microstructure. These are embedded into the homogeneous RVE (HRVE) with the diffusion coefficient D_h and concentration $C_h(x)$ as shown in figure 6.2.2(b). The Global RVE (GRVE) is the whole and consists of the HRVE and MRVE substructure. The direction of mass flow is from left to right through the GRVE normal to the interface of the MRVE and HRVE. The HRVE diffusion constant was taken as any value between the D_{ig} and D_{gb} microstructural diffusion constant. The driving mechanism for mass transport is the concentration gradient developing in the volume as a result of boundary conditions. Figure 6.2.2 (c) Shows the boundary condition of the GRVE for FE analysis.

Under steady state conditions the mass flux in the MRVE is equal to the mass flux in the HRVE, as shown in the equation below. The boundary conditions are

$$\therefore J_{h1}(y) = J_{eff}(y) \quad (6.2.8)$$

$$D_h \frac{\partial C_h^1}{\partial y_1^1} = D_{eff} \frac{\partial C_{eff}}{\partial y_1^2} \quad (6.2.9)$$

$$D_h^1 \frac{(AC_1 - C_s)}{(y_1^2 - y_1^1)} = D_{eff} \frac{(AC_0 - AC_1)}{(y_1^3 - y_1^2)} \quad (6.2.10)$$

Where $AC_1 = \int_{y_{2c1}}^{y_{1c1}} C_1 dy_2$, $AC_0 = 0$ and $D_{eff}(D_{ig}, D_{gb}, k_{ig}, k_{gb})$

The effective mass diffusivity of the MRVE can be calculated using the above equations.

$$D_{eff}(y) = k_{ig} D_{ig}(y) + k_{gb} D_{gb}(y) \quad (6.2.11)$$

In the above equation k_{ig} , k_{gb} are the intergranular and intragranular coefficients respectively characterizing the effective mass diffusion of the MRVE. The average

mass diffusion coefficients obtained from the simulation results were compared with the effective medium approximation analytical results which are shown in result and discussion section.

6.3 Real microstructural RVE model and virtual permeation test

The real microstructure has been extracted from EBSD analysis data. An algorithm was developed to extract data from EBSD data files and convert them into Abaqus mesoscale microstructural meshes. The Abaqus geometric model uses the following information extracted from the EBSD data:

- Grain shape, size and structure of the observed microstructure.
- Volume fractions of grains, grain boundaries and triple junctions.
- Statistical distributions of the crystal orientation and grain boundary misorientations.

In the computational model the grain boundaries were assigned a thickness of 10 Å to form “grain boundary affected zones” (GBAZ). This allows the enhanced diffusivity associated with the grain boundaries to be accounted for numerically. Figure 6.3.1 shows the flow of conversion of real microstructure into ABAQUS FE microstructure RVE model and meshes. Figure 6.3.1 (a) shows the real microstructure of electrodeposited nickel observed experimentally using EBSD analysis. Figure 6.3.1 (b), (c) and (d) shows the converted ABAQUS real MRVE model, shows the close up view of meshed model and shows the close up view near a triple junction with grain boundary affected zone (GBAZ) and grain boundary (GB) and fine mesh in GBAZ respectively.

Based on this MRVE model, virtual electrochemical hydrogen permeation tests were developed as a standard, reliable and industrially applicable micro-scale FE simulation of real permeation tests in order to calculate the effective hydrogen diffusivity in polycrystalline material by considering the microstructure morphological effects using real EBSD-derived microstructures. Experimental electrochemical permeation tests comprise two chambers, “cathodic” and “anodic”, separated by the nickel sample as shown in figure 6.3.2. In this experiment current as function of time is measured.

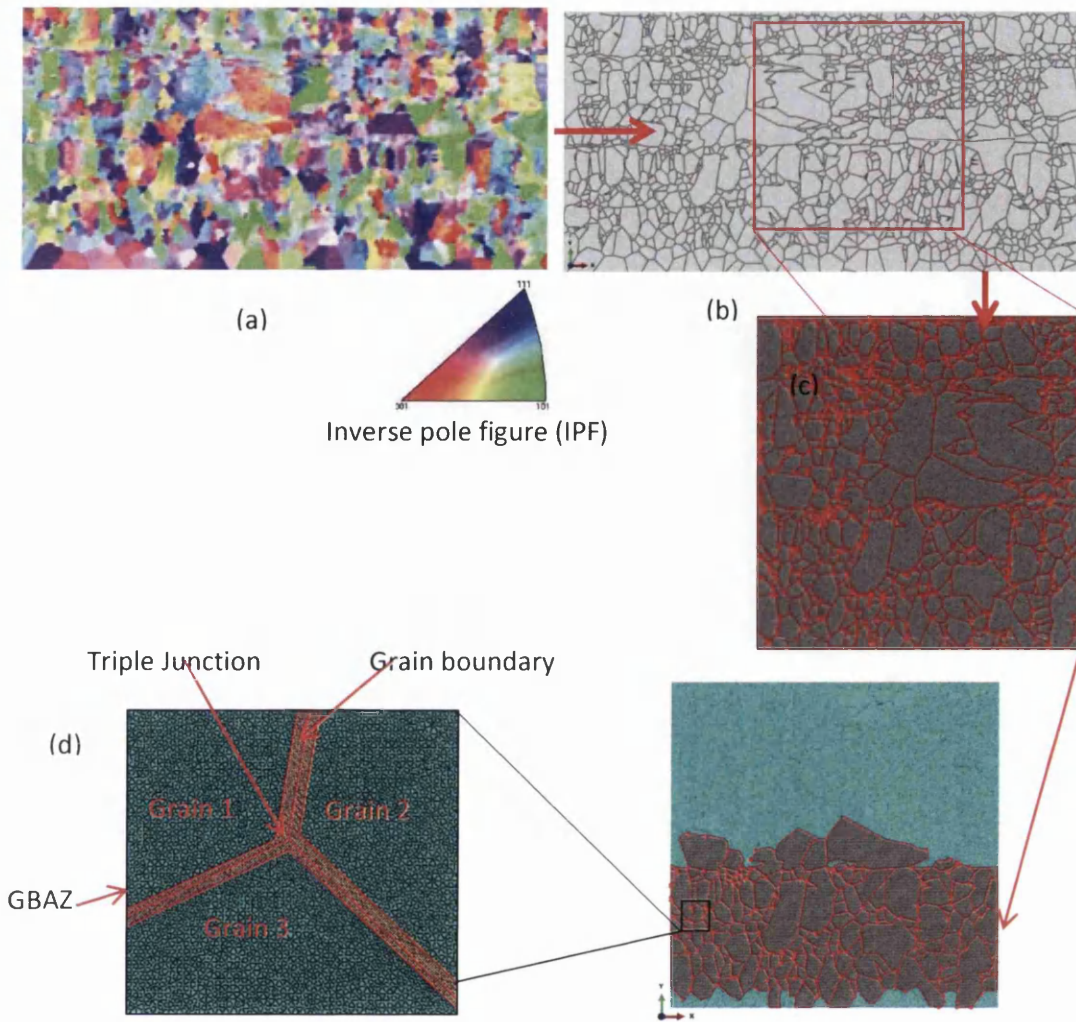


Figure 6.3.1 (a) EBSD analysis result and IPF image showing the real microstructure of electrodeposited nickel foil, (b) shows the ABAQUS 'real' microstructure RVE model (c) shows a magnified view of the meshed model (d) Shows a magnified view of the mesh near a grain boundary and triple junction.

The hydrogen diffusivity (D) and subsurface concentration (C_0) in the sample specimen can be calculated using equations 6.3.1 and 6.3.2.

$$D = (L^2)/(M \cdot t_L) \quad (6.3.1)$$

Where, L = thickness of the specimen used in experimental permeation test (m), $M = 6$ for 63% of I_{\max} related lag time (t_L) (sec), t_L = Time lag represents the time required for the anodic exit current to reach 0.63 of its steady state current (i.e. t_L can be calculated from the experimental curve) and I_{\max} = maximum current.

$$Co = [(I_{max} * L) / (A * E_c * D)] \tag{6.3.2}$$

Where A = area of the sample, Note: $A \neq L^2$, $E_c =$ elementary charge ($1.6 \times 10^{-19} C$)

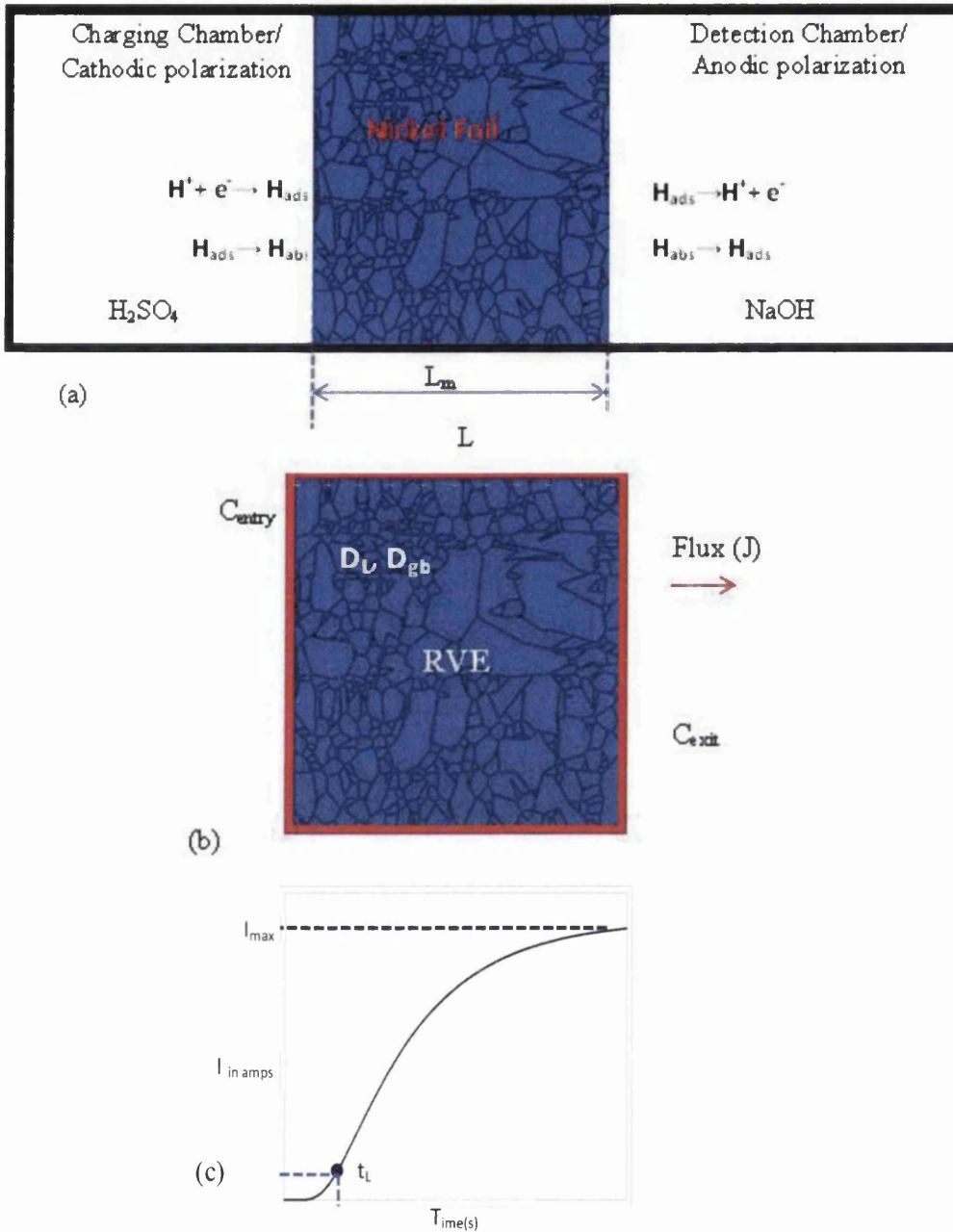


Figure 6.3.2 Experimental setup of electrochemical permeation test. Nickel sample foil with lattice (blue) and grain boundary high diffusivity path (black).

The virtual permeation test, based on multiscale FE modelling, was validated using experimental electrochemical permeation test results. This technique was also applied for PP-Ni and results are discussed in later sections.

6.4 Micro-macro coupling techniques

Prediction of hydrogen embrittlement phenomena within a component requires multiple length scales to be accounted for and has attracted research attention over a significant period [162, 147]. Some mechanisms that affect hydrogen embrittlement include hydrogen diffusion in short circuit paths such as grain boundaries and triple junctions [1, 163, 164, and 165]. The hydrogen embrittlement mechanisms of cracking are intrinsically microstructural level and have frequently been regarded as microstructural intergranular phenomena [167, 168]. So it is important to include these microstructural intergranular phenomena at the design stage to investigate the hydrogen embrittlement mechanisms and life prediction analyses of structural materials at the component level. Computational investigation of the component macro-scale hydrogen embrittlement problem, including detailed heterogeneous microstructure, usually requires the use of supercomputers. In practice, to avoid this complexity the component macro-scale hydrogen embrittlement problem is investigated by neglecting the detail of the microstructure of the polycrystalline material. But such component level macro-scale models provide limited understanding of the hydrogen embrittlement problem. In this thesis a multiscale modeling technique is proposed which accounts for the effects of the heterogeneous microstructure in an investigation of the hydrogen embrittlement phenomena at the component level. The proposed micro-macro coupled multiscale model is capable of resolving the necessary microstructural phenomena simultaneously with less usage of computer resources and decreased computational time. This section describes the method. The model is termed the coupled Microstructure and Continuum Critical Defect modelling (CMCD) method and uses substructural (Tie boundary) and submodelling (Cut boundary) techniques to investigate the hydrogen embrittlement mechanism. The CMCD technique consists of a microstructural model near critical sites such as cracks, defects and voids as a submodel which is coupled to continuum models (macro-scale) away from critical sites. The CMCD method thus replaces the continuum domain near the critical sites by including relevant microstructural features such as grains, grain boundaries, triple junctions, voids, defects and clustered grains. The component level macroscopic body is considered as a macro continuum domain (Ω_c) and modeled as a global continuum model with single or multiple pre-existing critical micro crack sites or

without any pre-existing micro cracks. The micro domain near the critical defect site contains intergranular and intragranular heterogeneous microstructural features. In the micro domain (Ω_m) region any combination of microstructural features can be included depending on the nature of the problem. Details of the model of the micro domain with heterogeneous two phase intragranular and intergranular microstructural model can be found in chapter 7.1. Initially a continuum model without pre-existing defect sites is run to find the critical defect sites in the continuum model. These critical sites are then subsequently modeled as micro domains.

The CMCD modeling technique can be employed using two methods to couple the micro domain to the continuum domain as illustrated in the Figure 6.4.1. These alternative approaches are the (i) substructure micro domains (Ω_{mss}) method and (ii) submodel micro domain (Ω_{msm}) method. The substructure micro domain (Ω_{mss}) is coupled through a tie boundary ($\partial\Omega_t$) with the continuum domain (Ω_c) and the boundary value problem is solved as a single problem. The submodel micro domain (Ω_{msm}) is coupled as a cut boundary ($\partial\Omega_c$) with the continuum domain and the boundary value problem is solved as two decomposed problems as shown in Figure 6.4.1 (d). In brief, these boundary techniques allow the creation of refined element meshes in the localized micro submodel regions with the same degree of freedom as the global macro model. The localized micro submodel reacts to the load and boundary conditions of the global macro model. The tie and cut boundary elements and nodal DOFs, load and boundary condition datasets are stored in a different data file and are handled using subroutine programs to run the localized micro substructure analyses. As a test, the proposed CMCD technique is implemented to investigate the hydrogen embrittlement mechanism. The present model will connect the hydrogen diffusion and accumulation mechanism in the microstructural region to the macroscopic hydrogen embrittlement. The model includes the heterogeneous intragranular and intergranular microstructural defects as a substructure or submodel near critical sites. This localization of the microstructural domain limits the expenditure of computational resources and allows much more detailed information to be obtained for the embrittling effects of hydrogen in structural polycrystalline materials. The information from the continuum domain can be passed to the microstructural Ω_{mss} or Ω_{msm} so that the hydrogen embrittlement

mechanism can be investigated at the microstructural level and understood better with detailed microstructural information.

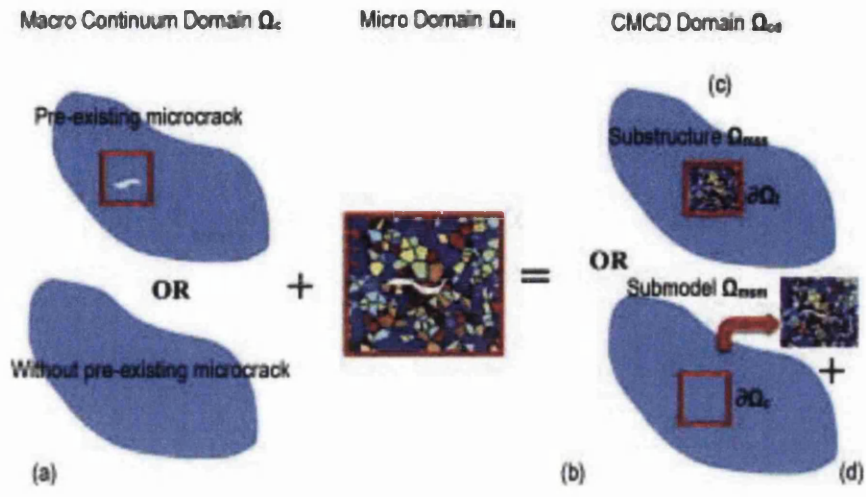


FIGURE: 6.4.1 Schematic of the coupled microstructural and continuum critical dislocation site model using heterogeneous intragranular and intergranular microstructural domain as substructures or submodels.

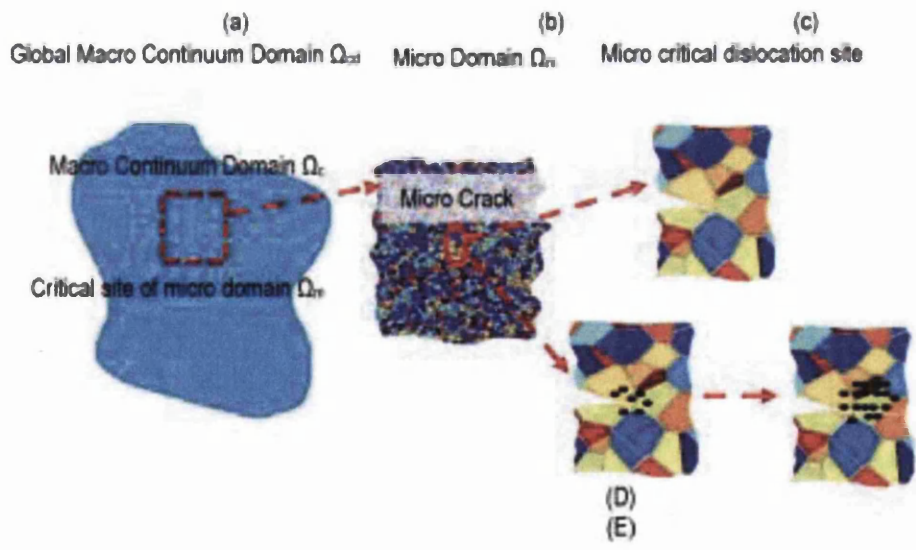


FIGURE 6.4.2 (a) Macro Continuum domain with a micro domain containing a microcrack. (b) Schematic close-up view of micro domain, a region of heterogeneous intragranular and intergranular microstructural polycrystalline material with the pre-existing microcrack (c) Close up view of critical intragranular and intergranular

microstructural dislocation site containing a microcrack tip in the absence of hydrogen. (d) Close up view of critical intragranular and intergranular microstructural dislocation site containing a microcrack tip in the presence of hydrogen accumulation near the crack tip (e) A critical amount of hydrogen concentration after a certain period of time due to stress assisted hydrogen diffusion near the micro cracks leads to catastrophic failure or premature brittle rupture.

The hydrogen diffusion boundary value problem for this CMCD model is solved using finite element method by employing the *weighted residual Galerkin method* developed within the finite element analysis software ABAQUS. PYTHON script has been developed to link the macro-micro models in the form of boundary techniques. This work tests the two methods of the CMCD modeling technique by investigating the hydrogen embrittlement mechanism using hydrogen diffusion problem based on Fick's law using two methods, initially with substructure micro domains (Ω_{mss}) method and then with a submodel micro domain (Ω_{msm}) method. Both the problems modelled are limited to traps and stress and strain assisted diffusion. Figure 6.4.2 shows the schematics of the CMCD modeling technique. These techniques were applied to both hydrogen diffusion problem as well as the multi-physics chemo-mechanical problem (i.e. stress assisted hydrogen diffusion analysis). The mechanical analysis and stress-assisted diffusion models are coupled sequentially. First the mechanical problem of the multiscale CMCD model is solved which is then used in the subsequent stress assisted hydrogen diffusion model. Thus the CMCD model attempts to bridge the gap between microstructural and continuum length scales to investigate the chemo-mechanical hydrogen embrittlement problem.

The mechanical response of the coupled domain is captured firstly using an initial static stress analysis. Initially, the stress analysis is done at the macro-structural level, assuming the material is isotropic. These results are transferred to the microstructural level sub-mesh, via the submodelling technique. This effectively maps values from the macro model to the boundaries of the micro mesh. Values calculated in the micro region are similarly mapped back onto the macro mesh at the next stress analysis. The same macro to micro coupling procedure is carried out for the hydrogen diffusion analysis as well. In the micro-scale model the material mechanical anisotropy is accounted for by assigning individual grains random crystallographic orientations (for example in FCC nickel single crystal elastic constants $C_{11}=247$ GPa, $C_{12}=147$ GPa and $C_{44}=125$ GPa). The micro-level model

also includes micro-level stress-based driving forces for hydrogen diffusion. Hydrogen diffusion without the effect of stress in an FCC single crystal is isotropic with one independent diffusion material property. However, hydrogen diffusion in grain boundaries is faster than diffusion within grains in nickel. The hydrogen diffusivity and initial hydrogen concentration values used in the micro model within grains and in grain boundary affected zones are different. The results and detailed discussion for these models are discussed in later sections.

6.5 Multi-scale specimen model:

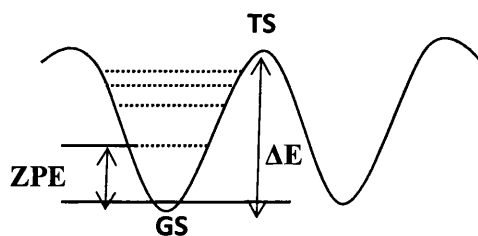
Atomic features such as local arrangements of atoms, misorientation of atoms at lattice and grain boundaries, vacancies, and grain boundaries energies also play vital roles in hydrogen diffusion and hydrogen embrittlement [145, 254-259]. The diffusivity of hydrogen also depends on the position before and after an atomic hydrogen jump, the jump length of hydrogen atoms and the jumping rate between neighbouring sites (Γ),

$$D = nL^2\Gamma \quad (6.5.1)$$

$$\Gamma = \frac{k_B T}{h} \exp\left[-\frac{\Delta E + \Delta ZPE}{k_B T}\right] \quad (6.5.2)$$

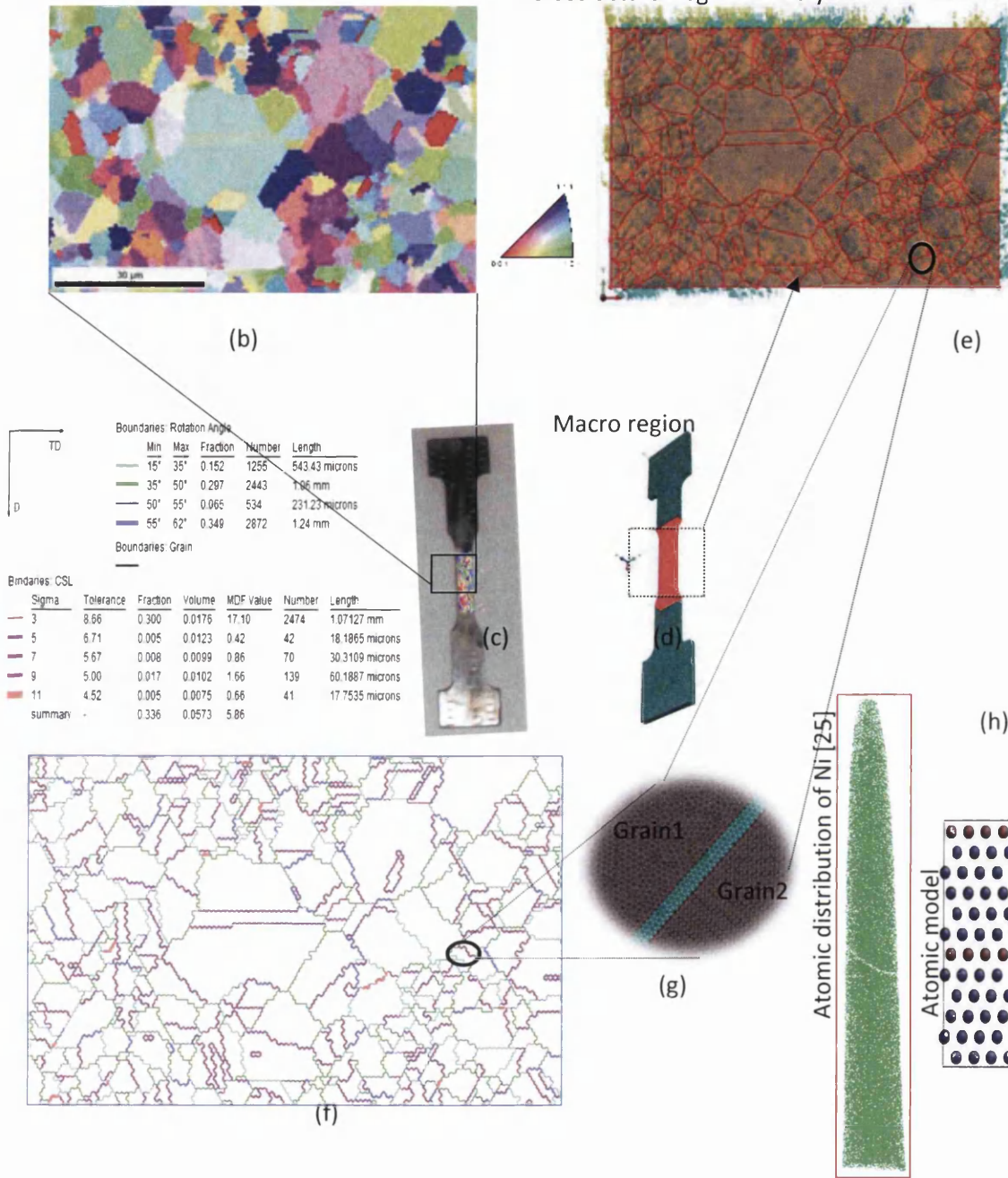
$$ZPE = \frac{1}{2} \sum_v h\nu \quad (6.5.3)$$

Where n is a numerical coefficient which depends on the initial and final position of hydrogen i.e. before and after hydrogen jumps, L is the jump length projected onto the diffusion direction and it can be calculated using the nudged elastic band (NEB) method, Γ is jump rate between neighbouring sites, ΔE is the activation energy barrier, ν is a real normal mode frequency, ΔZPE is the difference in zero-point vibrational energies between ground state and transition state as shown below and more details can be found in elsewhere [e.g. 145, 256-259].



Coupling the atomic model calculated information into MFE model allows the influence of such atomistic features to be accounted for. The grain boundary

Microstructural region and crystal orientations



$$D_{\text{Lattice}}=3.5 \times 10^{-14} [4], D_{\text{RGB}}=2.05 \times 10^{-12} [4], D_{\Sigma 3}=D_{\text{bulk}} [260], D_{\Sigma 5}=10^2 \times D_{\text{bulk}} [260], D_{\Sigma 9}=4.6 \times 10^{-13} [253].$$

Figure 6.5.1 (a) shows the SSRT specimen drawing and dimension. The SSRT specimens of VULCAIN combustion chamber PP-Ni from AIRBUS Group as shown as follows. (b) and (c) Experimental SEM/EBSD microstructure image and real SSRT sample specimen, (d) ABAQUS model with coarse mesh (e) shows the ABAQUS FE microstructural representative volume element (MRVE) model (f) shows the grain boundary characteristics of MRVE and colour code, (g) shows the fine mesh at the $\Sigma 3$ type grain boundary affected zone and associated grains and (h) shows the atomic structure $\Sigma 3$ type grain boundary [260].

RESULTS AND DISCUSSION

Hydrogen induced intergranular embrittlement has been identified as a cause of failure of aerospace components such as combustion chambers made from electrodeposited polycrystalline nickel. Accurate computational analysis and prediction of this process requires the understanding and knowledge of many factors. This chapter contains several self-contained analyses of increasing complexity which aim to build up a more detailed understanding of this problem. The specific contents of each subsection are described below.

The effect of microstructure such as intergranular, intergranular and grain size on effective hydrogen diffusion properties and bulk diffusion of hydrogen in polycrystalline nickel: This drives the author to develop a synthetic microstructural model to predict the effective diffusion coefficient based on intergranular regions and grain size effects of heterogeneous polycrystalline nickel material. Results are discussed in chapter 7.1

The effects of triple junctions (TJs), pores/voids and fine grains at TJs on the bulk diffusion of hydrogen in micro and nano polycrystalline (NPC) nickel. This

drives the author to investigate these effects in synthetic micro and nano polycrystalline nickel structures. Results are discussed in chapter 7.2.

The effective diffusion coefficient of hydrogen may be measured experimentally, though experimental measurement of the intergranular grain boundary diffusion coefficient of hydrogen requires significant effort. Therefore the author developed a finite element approach to calculate the intergranular GB hydrogen diffusivity and isotropic effective diffusivity of conventional electrodeposited nickel using real microstructures. Data from 2D electron backscatter diffraction (EBSD) measurements were used to construct 2D mesoscale microstructural representative volume elements (MRVE) including details of grain size and shape and volume fractions of grains and grain boundaries. A PYTHON optimization code was developed for the ABAQUS environment to calculate the unknown grain boundary diffusivity. The mesoscale FE simulation results are validated using experimental electrochemical permeation test results. Results from this computational approach can be found in chapter 7.3.

In order to understand the grain structure, size, shape, orientation and GB misorientation distribution of electrodeposited pulse plated nickel in the Ariane-5 Vulcain-2 combustion chamber referring to 3D EBSD analysis were used with an SEM/EBSD/FIB system. Another aim of this work is to investigate the effect of this microstructure on hydrogen permeation along the three principal directions by constructing 3D meso-microstructural RVEs based on real microstructure using 3D EBSD data. These anisotropic hydrogen permeation properties are then applied to the combustion chamber. Results and discussion can be found in chapter 7.4.

The effect of grain boundary misorientation on stress assisted hydrogen diffusion in bi-crystal and polycrystalline nickel: The author developed bi-crystal and polycrystalline models to investigate these effects. The results and discussion of these investigations can be found in chapter 7.5. Chapter 7.5 contains the results and discussion concerning computational techniques and tools developed to understand hydrogen embrittlement and hydrogen induced intergranular cracking based on grain boundary (GB) engineering with the help of computational materials engineering. This study can help to optimize GB misorientation configurations by identifying the

cases that would improve resistance to hydrogen embrittlement. In order to optimize it is important to understand the influence of misorientation angle on the atomic clustered hydrogen distribution under the impact of dilatational stress distributions. In this study, a number of bi-crystal and polycrystalline FE models with tilt grain boundary (TGB) misorientation angles (θ) ranging between $0^\circ \leq \theta \leq 90^\circ$ were developed, with rotation performed about the [001] axis. Local stress and strain concentrations generated along the TGB (due to the difference in individual neighbouring crystals elastic anisotropy response as a function of misorientation angles) were evaluated when bi-crystals and polycrystals were subjected to overall uniform applied traction. Finally, the hydrogen distribution and segregations as a function of misorientation angles were studied. In real nickel, as opposed to the numerical model, geometrically necessary dislocations are generated due to GB misorientation. The generated dislocation motion along TGBs in response to dilatational mismatch varies depending on the misorientation angles. These dislocation motions affect the stress, strain and hydrogen distribution. Hydrogen segregates along these dislocations which act as traps and since the dislocation distribution varies depending on misorientation angles the hydrogen trapping is also influenced by misorientation angles.

Prediction of hydrogen embrittlement within a component requires the influence of several length scales to be accounted for. The loads that affect the rate of hydrogen diffusion, typically thermal and structural, derive from the macro or component scale. Micro-structural analysis has an important role to play in providing accurate estimates of the typically homogenous material characteristics employed by modellers at the component scale. This inspired the author to develop the coupled microstructural and continuum including critical defect site (CMCD) techniques to couple the micro-scale and macro-scale models and to investigate hydrogen diffusion and hydrogen embrittlement in specimens and components. The results and discussion of this micro-macro CMCD coupling technique can be found in chapter 7.6. A micro-scale model is employed in critical regions of the component where resolution of the heterogeneous behaviour is necessary. A tie boundary/cut boundary technique is introduced to couple the micro-scale model to the macro-scale model. This technique offers a computationally efficient procedure to analyse the multi-scale inter-granular hydrogen embrittlement in a polycrystalline material.

In chapter 7.7, the multiscale CMCD is implemented to investigate the hydrogen embrittlement of a tensile specimen via simulation of the chemo-mechanical process (i.e. a stress assisted hydrogen diffusion analysis). Within a macro scale finite element model the macro domain is replaced at critical defect sites with a microstructural domain and as described in section 7.6. Resolution of the different microstructural material characteristics within the grain and grain boundary, including grain orientation, can be used to improve the predicted distributions of both hydrogen and stress within the microstructure. The results show that microstructural features of polycrystalline nickel play an important role in the segregation of hydrogen which may lead to hydrogen induced crack initiation and development. Computational analyses are presented to demonstrate the application of the model in an attempt to bridge the gap between the micro and macro length scales for the chemo-mechanical problem where a pre-placed micro-crack in a loaded specimen plate in a hydrogen rich environment was investigated.

AIRBUS have reported that GBs play a critical role as preferential sites for crack nucleation and propagation in hydrogen induced cracking (HIC) of polycrystalline FCC nickel materials, as shown in figure 7.1. Real microstructures from EBSD analysis of an annealed nickel specimen were simulated to investigate the localized HIC. Fractured specimens were observed using SEM/EBSD/OIM analysis to validate the FE multiscale simulation results described in chapter 7.8.

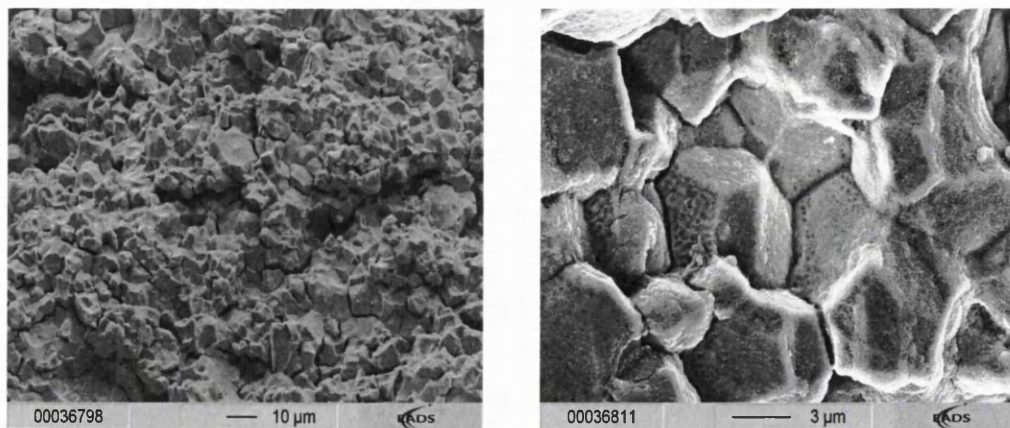


Figure 7.1 shows the fracture due to hydrogen embrittlement in the heat affected zone (HAZ) of a weld (Fracture is intergranular) [Note: Data supplied by Airbus].

The nickel-iron based superalloy Alloy 718 possesses a complex microstructure which is susceptible to ductility and delayed failure due to the presence of hydrogen through such embrittlement phenomena (Hicks et al., 1992, Lynch et al., 2003, Xu et al., 1994). Despite many studies on hydrogen embrittlement in superalloy Alloy718, very little information is reported on the relationships between the following:

- Micro-mechanisms of hydrogen induced localization slip along intergranular micro-void formation and intergranular hydrogen cracking/embrittlement.
- Micro-mechanisms of crystal lattice micro-voids and pressure for hydrogen induced transgranular cracking.
- Micro-mechanisms of microstructural grain boundary misorientations, triple junction characteristics and hydrogen induced intergranular cracking phenomena.

This motivated the author to investigate the effects of the above mentioned micro-mechanisms on hydrogen induced cracking using an in-situ hydrogen charging SSRT test and SEM/EBSD/OIM in order to explore ways of increasing the resistivity of the nickel-iron based superalloy 718 to hydrogen induced cracking/embrittlement. Results and discussion of this investigation can be found in chapter 7.9

7.1 Effect of microstructure on hydrogen diffusivity

A 2D phase field finite element microstructural representative volume element (FEMRVE) model with different intergranular and intragranular microstructures has been developed using the Voronoi tessellation technique and calculated the effective diffusivity of heterogeneous polycrystalline nickel for various intergranular and intragranular microstructures using FEMRVE model.

7.1.1 Experimental results

Heterogeneous polycrystalline microstructures are divided into intergranular phase and intragranular phase. The results of the five different synthetic heterogeneous phase field microstructures developed computationally as the function of intergranular and intergranular fraction are shown in figure 7.1.1. Magnified views are shown in figure 7.1.2. These synthetic microstructures are developed to

investigate the effect of hydrogen diffusion and its properties as a function of microstructure. Figure 7.1.3 shows the average perimeter to area of grains as a function of grain size.

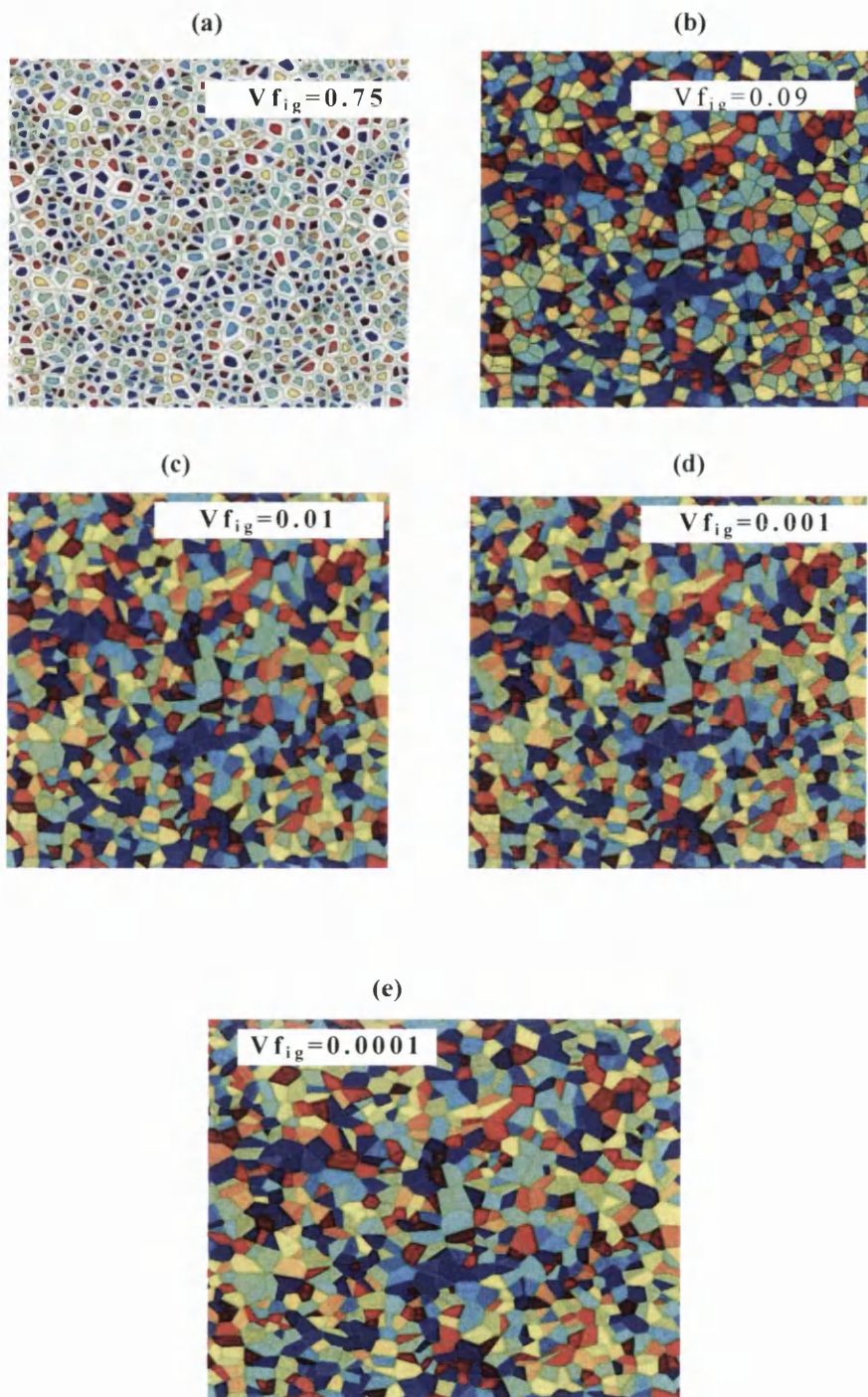


Figure 7.1.1 shows the computationally generated microstructure model as a function of intergranular fraction (Note: Decreasing intergranular phase fraction from (a-e)).

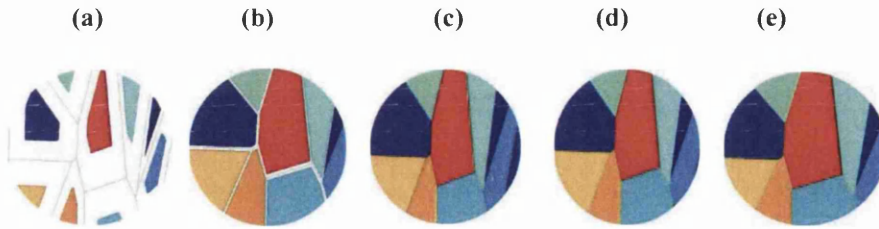


Figure 7.1.2 (a-e) shows the magnified view of the computationally generated phase field microstructure model as a function of intergranular fraction.

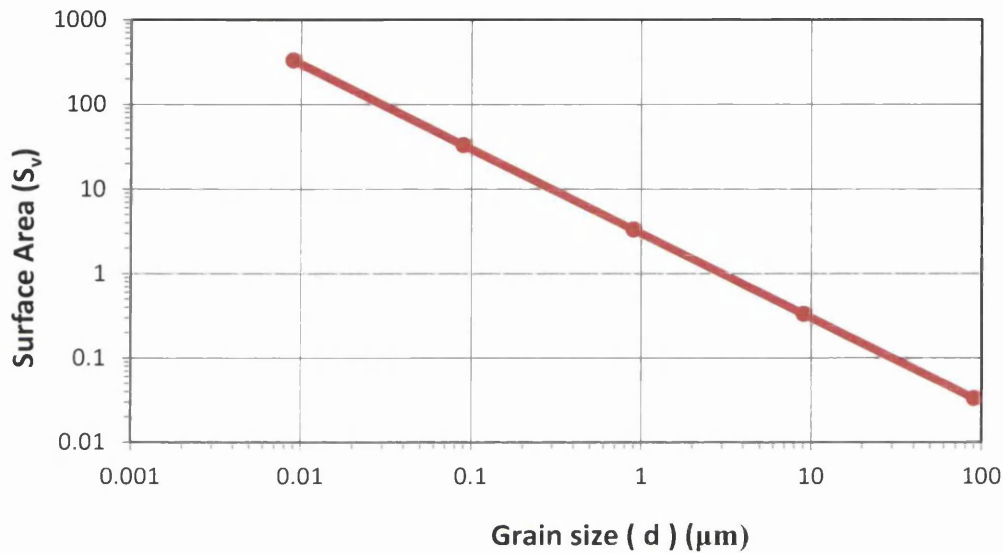


Figure 7.1.3 shows the results of computationally generated microstructure phase field model as the average perimeter to area of grains as the function of grain size.

Hydrogen diffusion coefficients for intergranular and intragranular microstructure are different and the different hydrogen diffusion properties response of the intergranular phase and intragranular phase are also incorporated. At the present stage, no attempt was made to consider anisotropic effects of hydrogen diffusion; the anisotropic effects were studied in real microstructure of PP-Ni and reported in section 7.3. The diffusion of hydrogen for five different intergranular fractions was carried out. Figure 7.1.4 shows the FE hydrogen diffusion analysis results for the computed effective concentration of hydrogen for the different microstructures. The size of the intergranular region and grain size have a significant effect on the effective diffusion of hydrogen.

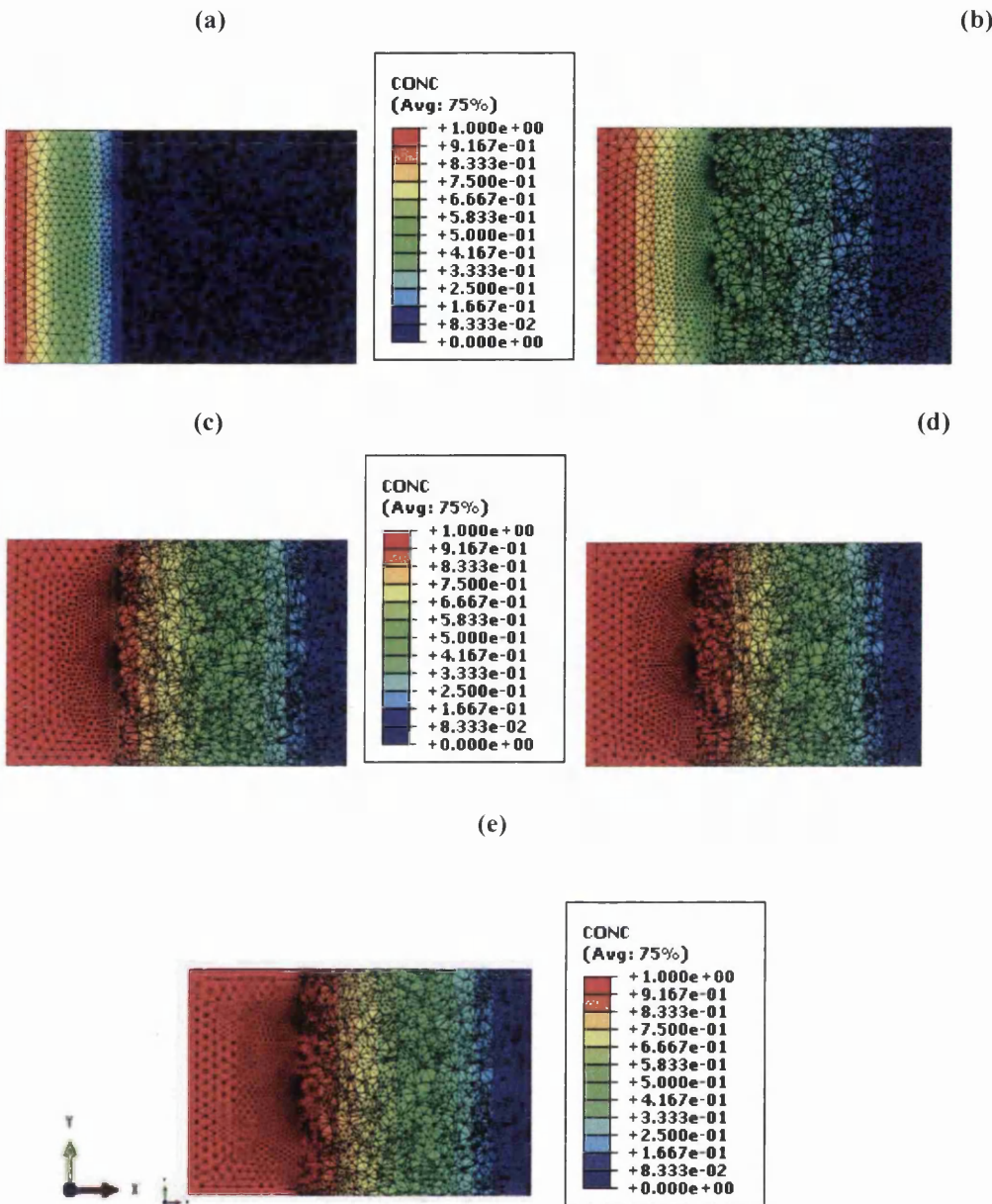


Figure 7.1.4 (a-e) Cross section in the xy plane of the steady state mass concentration of global representative volume elements with microstructural representative volume element for five different average grain sizes starts from $0.009039 \mu\text{m}$ (9.039 nm) in increasing by one order of magnitude to $90.39 \mu\text{m}$.

Figure 7.1.5 (a) shows the computational results of average surface area of intergranular phase plotted as a function of average grain size with the trend of the line found to be based on a power law as shown in the equation (7.1.1). Figure 7.1.5 (b) shows the change in volume fraction of intergranular phase as the function of average grain size.

$$S_{Aig} = k \cdot d^n \quad (7.1.1)$$

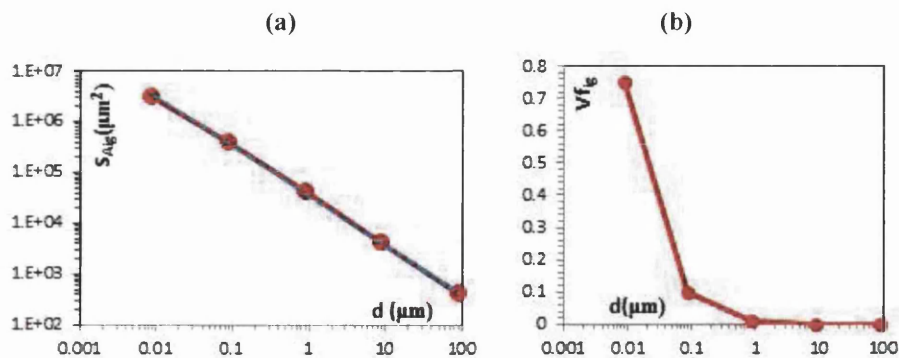


Figure 7.1.5 (a) Computational results of volume fraction of intergranular phase as a function of average grain size. (b) Computational results (solid line) and power law $A_{ig} \propto d^{-0.972}$ (dotted line) of average surface area of intergranular phase (A_{ig}) as a function of average grain size.

7.1.2 Discussion

The average surface area of intergranular phase increases when the grain size decreases as is clearly shown by the computational results in figure 7.1.5 (a). The computational results of average surface area of intergranular phase are found to be dependent on the grain size. The volume fraction of intergranular microstructure phase increases as the average grain size decreases as shown in figure 7.1. (b). In the following discussion the results are divided into three ranges corresponding to differing average grain sizes. These are (i) 1 μm to 100 μm , (ii) 100 nm to 1000 nm and (iii) 10 nm to 100 nm. In the first range the volume fraction of intergranular phase shows a very small increase, which is less than 0.01, for the 2 orders of change in average grain sizes. In the second range the variation in volume fraction of intergranular phase is high when compared to the previous range but this is very much lower when compared to the final range. In the third range the variation in the volume fraction of intergranular phase is quite high given that the average grain size changes by one order. This clearly shows that the intergranular phase dominates when the average grain size less is than 100 nm.

Figure 7.1.6 shows the evolution of effective mass diffusivity of heterogeneous polycrystalline composite media as the function of average surface area of intergranular phase. The effective mass diffusivity of the polycrystalline composite media decreases with decreasing average surface area of intergranular phase. The decrease in intergranular surface area corresponds to an increase in

average grain size. For annealed heterogeneous polycrystalline materials the increase in grain size would depend on annealing parameters such as temperature and time.

Next the effective diffusivity of hydrogen transport correlation with average grain size and intergranular phase will be discussed. Figure 7.1.7 (a) shows the evolution of effective mass diffusivity of heterogeneous polycrystalline composite media as the function of average grain size. The effective diffusion of mass in heterogeneous polycrystalline composite media increases as the average grain size become smaller which increases the mobility of mass atoms in the fine microstructure while the mobility of mass atoms decreases in the coarse microstructure. The analytical results in dotted lines from Hashin-Shktrikman upper bound coincide with the Maxwell-Garnett effective medium approximation as expected. The FE results calculated in solid lines are a good fit to these analytical results.

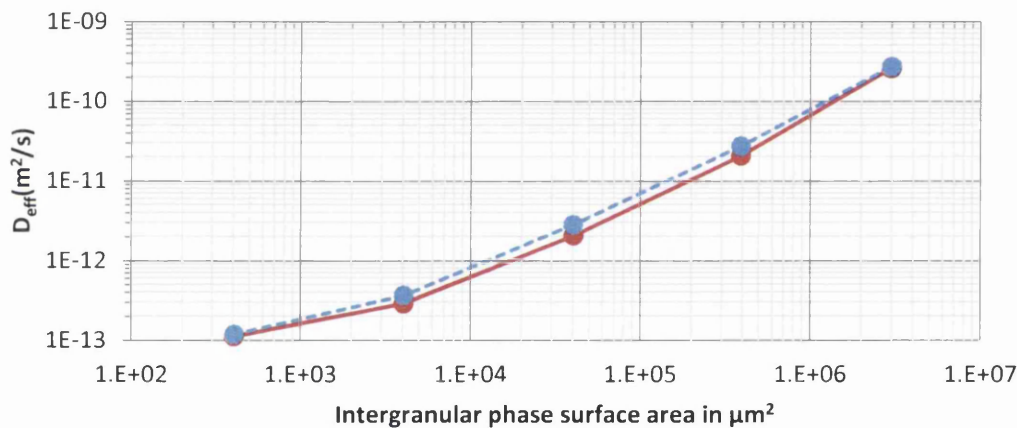


Figure 7.1.6 shows the computational results of effective hydrogen diffusivity in polycrystalline nickel as the function of average surface area of intergranular phase (solid line) and analytical results (dotted line).

Figure 7.1.7 (b) shows the evolution of effective mass diffusivity of heterogeneous polycrystalline composite media as the function of volume fraction of intergranular microstructure phase. Again, the analytical results in the dotted line match the calculated FE results.

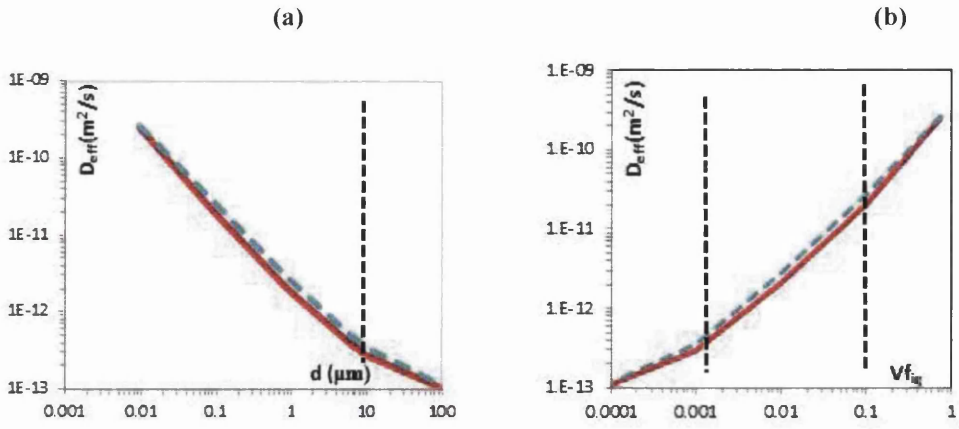


Figure 7.1.7 (a) Simulation results (solid line) and analytical (dotted line) for effective hydrogen diffusion coefficient as a function of average grain sizes (b) Simulation results (solid line) and analytical (dotted line) for effective hydrogen diffusivity as a function of volume fraction of intergranular phase.

The calculated results of the steady state normalized concentration of the GRVE, HRVE and MRVE are showed in figure 7.1.8 as a function of normalized distance for five different average grain sizes. When the normalized distance of the GRVE increases, the normalized concentration decreases. The result curves are divided into two regions due to the difference in the hydrogen diffusivity between the HRVE and the MRVE. The left hand side region shows the normalized concentration profile of HRVE and the right hand side of the normalized concentration profile of MRVE for five different grain sizes.

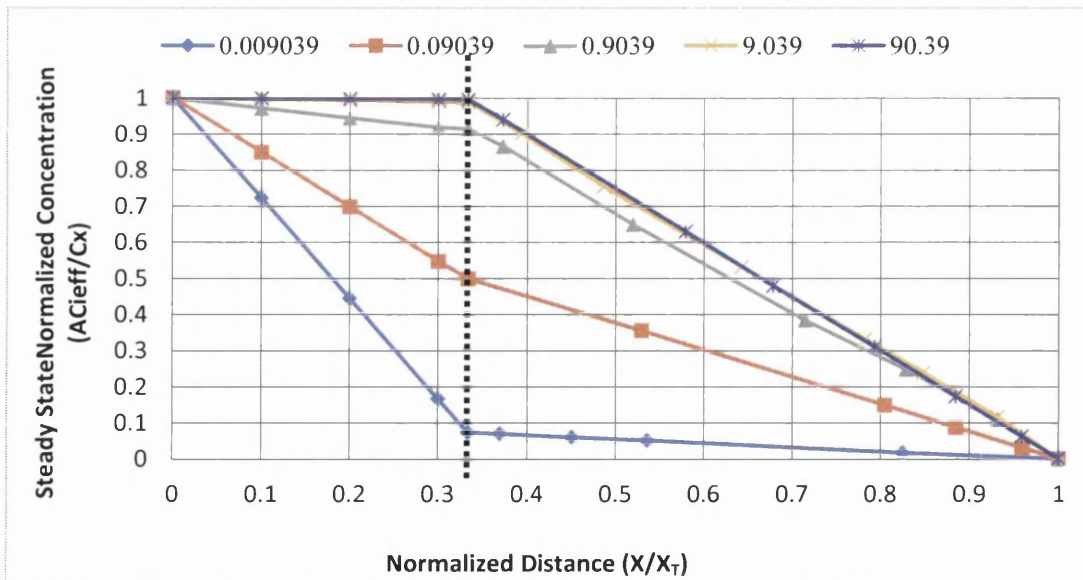


Figure 7.1.8 Computational results of normalized concentration of mass atom as the function of normalized distance of GRVE for various average grain sizes. The

Curves are divided into two regions by a dotted line, the left hand region shows the steady state normalized concentration profile of HRVE and the right hand region shows the steady state normalized concentration profile of the MRVE. The diffusion coefficients assigned to HRVE is $1 \times 10^{-11} \text{ m}^2/\text{s}$. The diffusion coefficients assigned to the intergranular and intragranular phases are $9 \times 10^{-14} \text{ m}^2/\text{s}$ and $4 \times 10^{-10} \text{ m}^2/\text{s}$ respectively.

The variation of the normalized concentration with respect to normalized distance is higher in HRVE and smaller in MRVE for GRVE with nano grains, due to the higher area fraction of the intergranular phase. The variations of the normalized concentration with respect to the normalized distance are smaller in HRVE and higher in MRVE for the coarse grained GRVE due to the smaller area fraction of the intergranular phase. Figure 7.1.9 shows the normalized steady state concentration of hydrogen as a function of average grain sizes of the microstructure for seven different normalized distances of GRVE. The normalized steady state hydrogen concentration decreases with decreasing average grain size. The resultant curves are divided into two regions by a dotted line. In the left hand region in Figure 7.1.9 for an average grain size up to $1 \mu\text{m}$, the increase in the normalized hydrogen concentration is higher with increasing grain size. In the right hand region of Figure 7.1.9 the normalized steady state concentration of hydrogen attains saturation conditions and there is very little variation for grain sizes from $1 \mu\text{m}$ up to $100 \mu\text{m}$. For the top four normalized distance curves from $(0.1 \leq X/XT \leq 0.33)$ for the HRVE there is no change in the normalized concentration for the grain sizes from $1 \mu\text{m}$ up to $100 \mu\text{m}$.

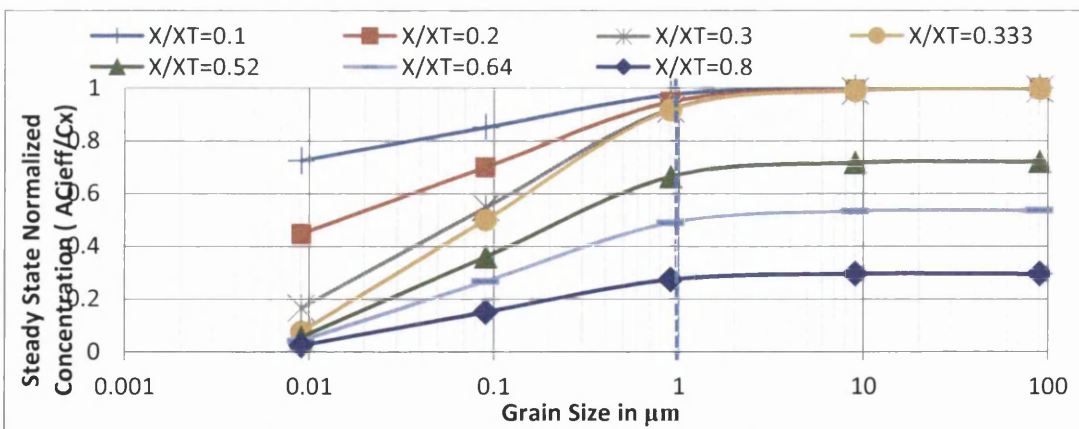


Figure 7.1.9 Calculated results of normalized steady state concentration of hydrogen atom as the function of average grain sizes for various normalized distance of GRVE.

7.2 Effect of microstructure on hydrogen diffusion in micro and nano polycrystalline nickel

In this section microstructural models were developed to investigate the following: (i) The effect of microstructural morphology such as grain size, grain boundary interface/GBAZ on hydrogen diffusion in micro polycrystalline nickel material, (ii) the effect of triple junctions on hydrogen diffusion in NPC nickel material, (iii) the effect of pores/void/fine grains in triple junctions on the hydrogen diffusion in polycrystalline nickel.

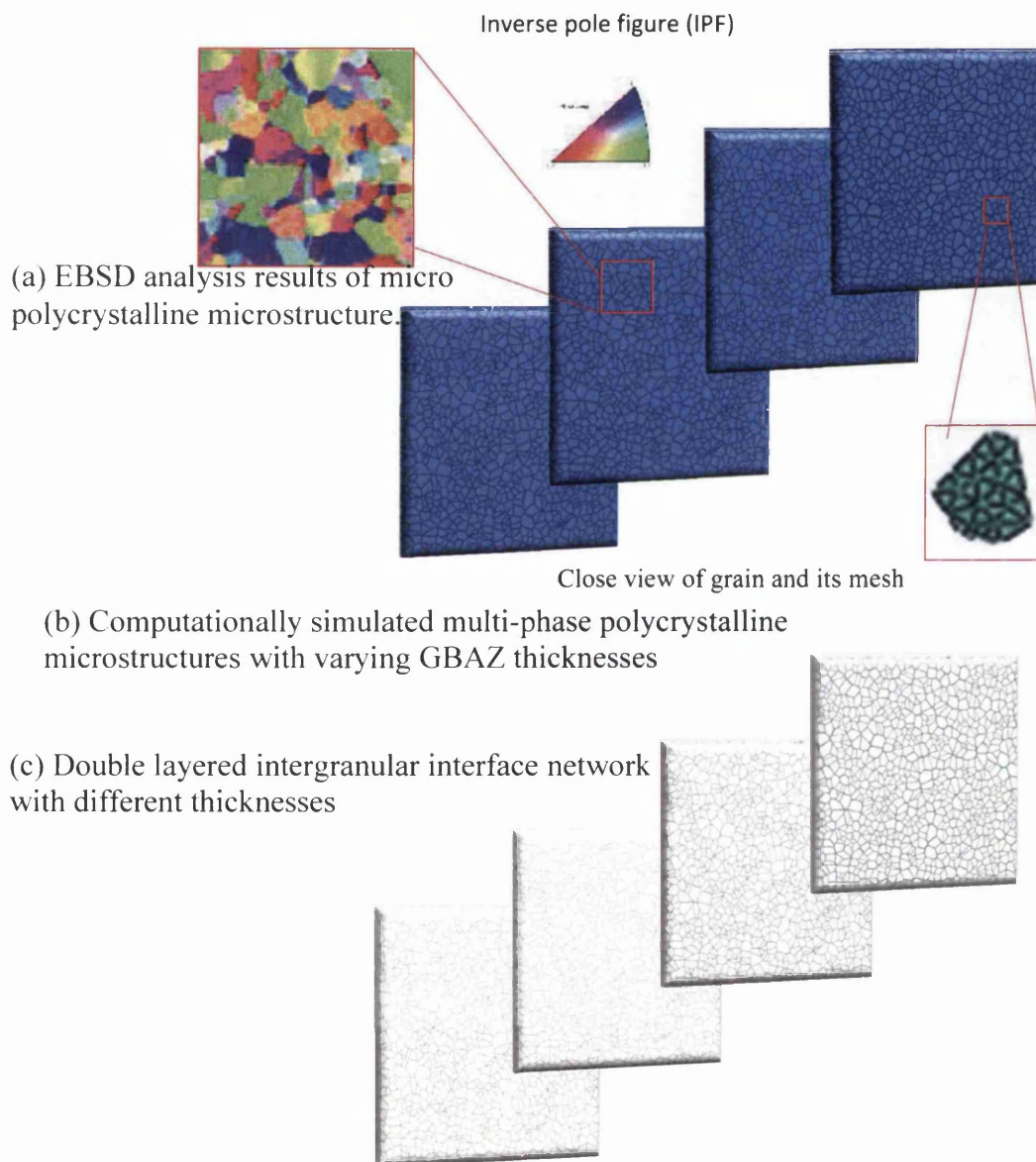


Figure 7.2.1 (a) shows the EBSD analysis of a micro polycrystalline microstructure. The computationally generated finite element ABAQUS micro polycrystalline microstructures model with (b) four different micro polycrystalline microstructures

with different grain boundary affected zone (GBAZ) and (c) double layered intergranular interface networks with different thickness.

7.2.1 Experimental results

(i) First, to investigate the effect of grain boundaries and grain sizes on hydrogen diffusion in micro polycrystalline nickel, different microstructure models with four different grain boundary thicknesses were modelled. Figure 7.2.1 shows the computationally generated micro polycrystalline microstructures with the four different grain boundary thicknesses (or grain boundary affect zones, GBAZ), the grain boundary networks, a close-up view of the FE mesh and an EBSD image. Figure 7.2.2 shows the computational hydrogen diffusion analysis results for the four different grain boundary thicknesses after 1 hour and 1 day. These simulations all used the same underlying grain structure. They differ only in the proportion of grain boundary thickness assigned at the grain boundary regions. Larger proportions of GBAZ can be seen in figure 7.2.1 as thicker lines surrounding the grains. The simulations used values characteristic of typical GBAZ thicknesses ranging from $0.005 \mu\text{m}$ to $5 \mu\text{m}$ (figures 7.2.2 (a), (b), (c) and (d) are for GBAZ thicknesses of 0.005 , 0.05 , 0.5 and $5 \mu\text{m}$ respectively). Thus GBAZ thicknesses spread over four orders of magnitude are simulated. The results show the influences of the GBAZ thickness on hydrogen transport at $25 \text{ }^\circ\text{C}$ after 1 hour (central column Figure 7.2.2) and 1 day (right column Figure 7.2.2). Figure 7.2.3 (a) and (b) show the predicted hydrogen concentrations in micro polycrystalline nickel for the four different GBAZ thicknesses. Figure 7.2.4 shows the normalized hydrogen concentration with normalized distance along a path from the hydrogen source to the hydrogen sink for various GBAZ thicknesses after diffusion times of one hour and one day. Figure 7.2.5 shows the hydrogen segregation distributions for two different micro polycrystalline nickel microstructures, one coarse grain size and one fine grain size. This clearly shows that hydrogen diffusion between the grain interior and grain boundary is inhomogeneous and diffusion of hydrogen in the intergranular grain boundary network is higher than diffusion within the polygonal grains as expected.

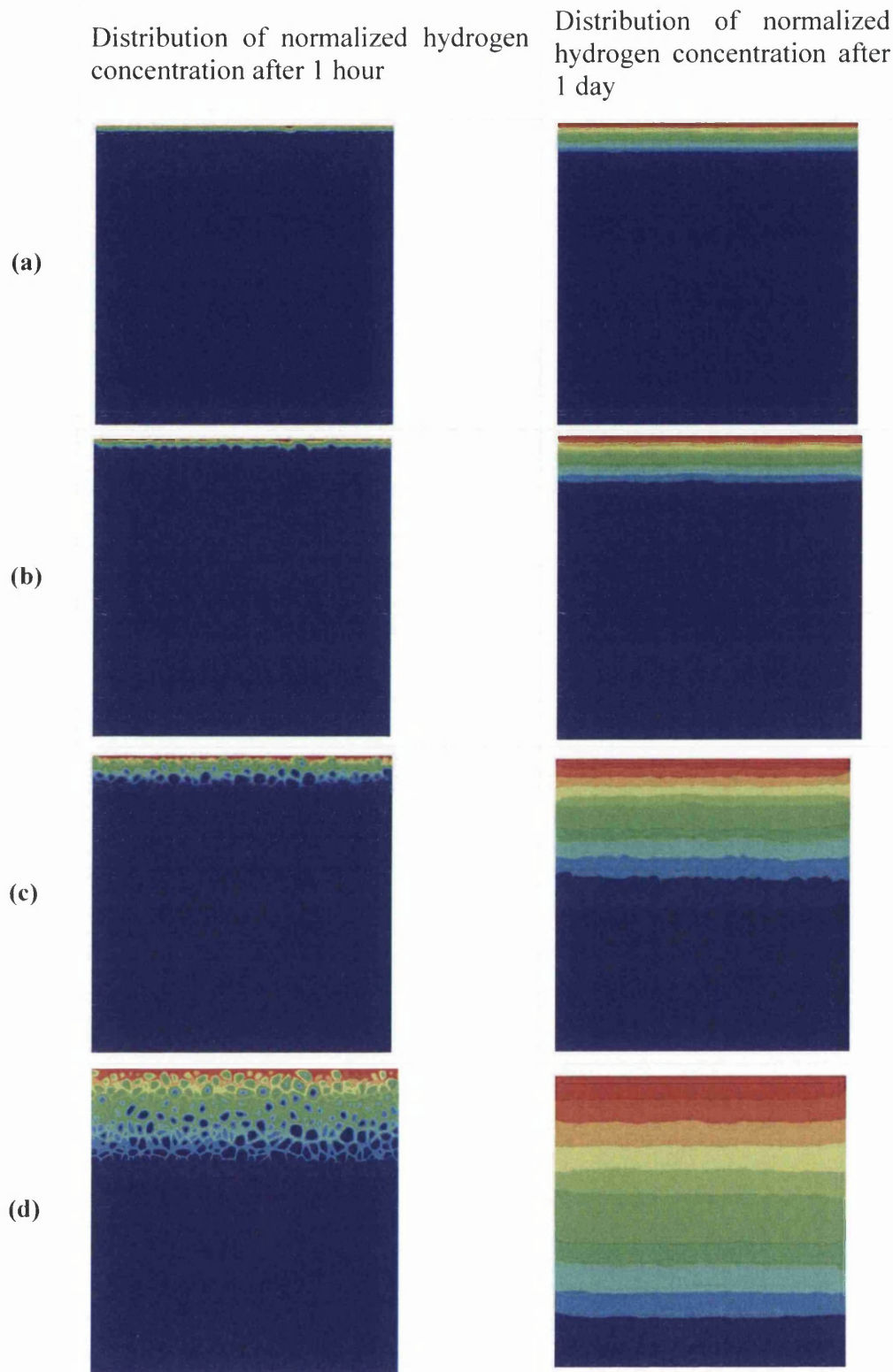


Figure 7.2.2 Contours of hydrogen concentration in a computationally simulated polycrystalline material for increasing GBAZ thicknesses (a), (b), (c) and (d) are for GBAZ thicknesses of 0.005, 0.05, 0.5 and 5 μm respectively, after 1 hour (middle) and 1 day (right). Note: GI and GBAZ diffusivities used are 9×10^{-14} and 4×10^{-12} m²/s respectively used in all simulations.

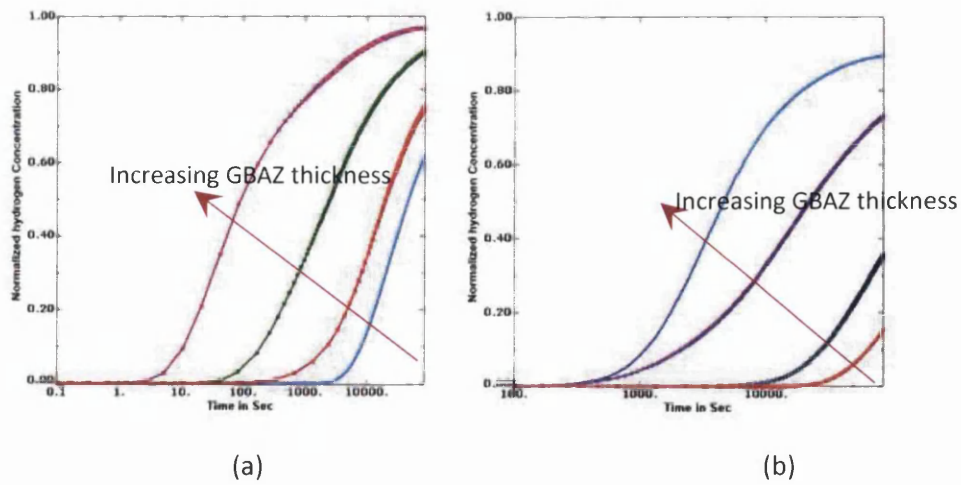


Figure 7.2.3. Normalized hydrogen concentration of polycrystalline microstructures with four different GBAZ thicknesses, 0.005, 0.05, 0.5 and 5 μm , at two different positions. (a) 70 μm and (b) 200 μm from the top surface of the computational grid.

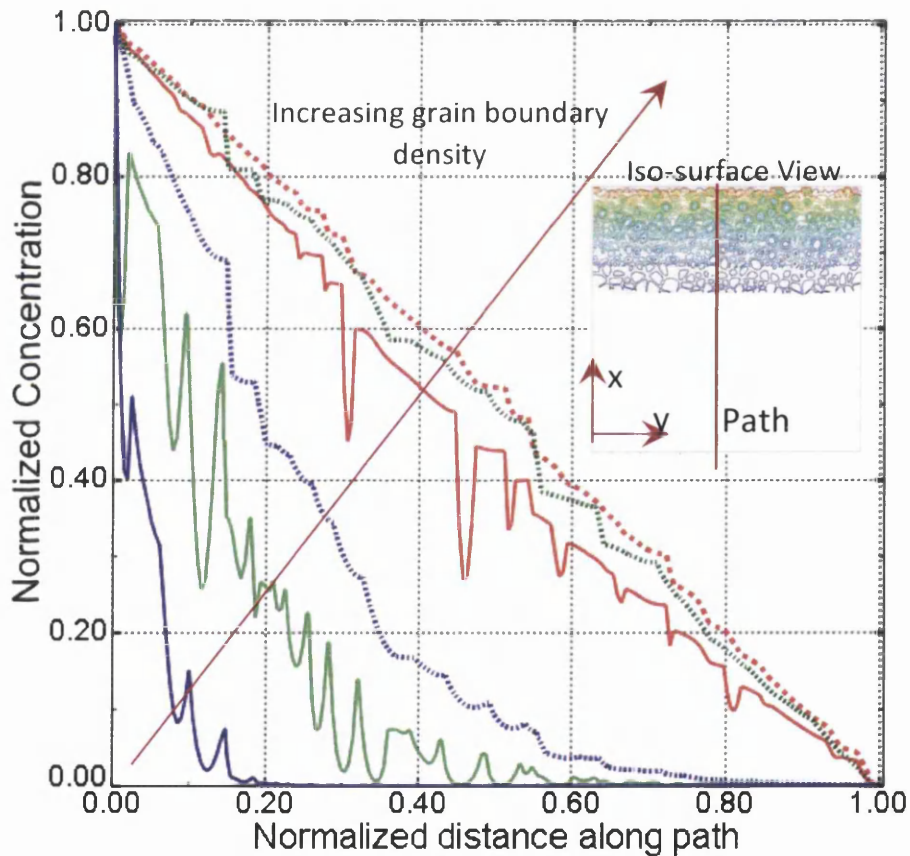


Figure 7.2.4 shows normalized hydrogen concentration along the vertical path shown above in the polycrystalline material for GBAZ thicknesses of 0.05 (blue), 0.5 (green) and 5 (red) μm after (i) one hour (solid lines) and (b) one day (dotted lines).

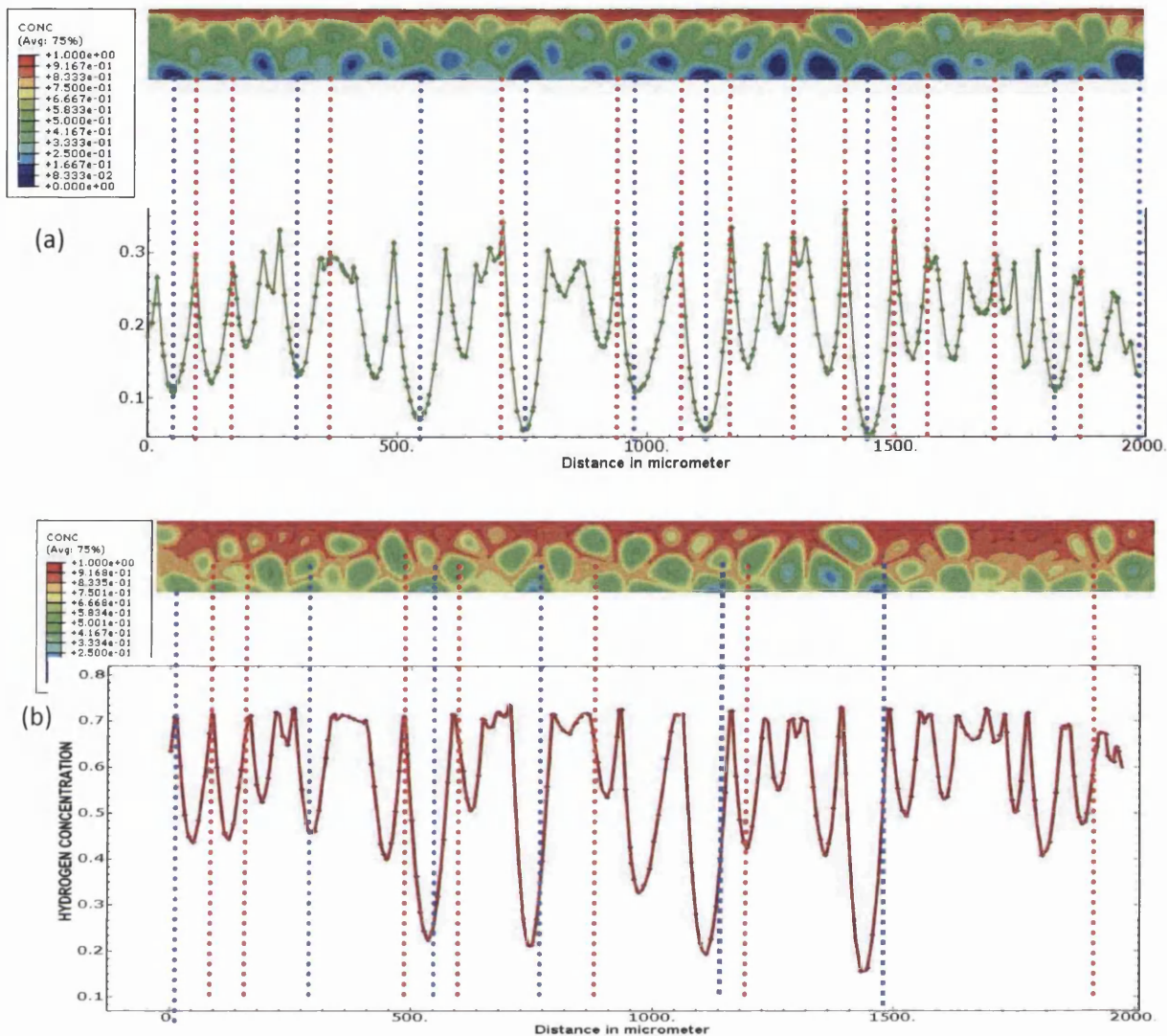


Figure 7.2.5 Segregation/Accumulation of hydrogen along intergranular grain boundaries and inhomogeneous hydrogen diffusion processes along grain boundaries and within grains for (a) micro polycrystalline nickel material with coarse grains after one hour, (b) micro polycrystalline nickel material with fine grains after 1 hour. Note: red dotted lines grain boundaries and blue dotted lines grain interiors). (Note: GBAZ diffusivity = 4×10^{-12} m²/s and GI diffusivity = 9×10^{-14} m²/s). **Note:** Colour contours are same for all results).

(ii) Secondly, the effects of triple junctions on hydrogen diffusion in NPC as a function of TJ characteristics and grain size are investigated including the influence of the shape of TJs (i.e. sharp corner shaped TJs and round corner shaped TJs). Figure 7.2.6 shows the structural contribution of TJs on NPC material using EBSD analysis and schematic diagrams. This shows the increase in the fraction of TJs when grain size decreases. The sequence in figure 7.2.6 of (a), (b) and (c) are the 2D EBSD images of NPC Nickel with decreasing average grain sizes. A decrease in average

grain size corresponds to an increase in number of triple junctions. Figure 7.2.6 (d), (e) and (f) are the schematic views of the 2D multiphase NPC model showing the increased number of triple junctions in NPC material as the grain size decreases. The blue circles, red lines and white polygons show the triple junction phases, grain boundary phases and grain phases respectively. Figure 7.2.7 shows an SEM image of nickel triple junctions and also the computational model with sharp or round corner triple junctions. These 2D synthetic microstructural geometries are generated computationally in heterogeneous form with polycrystalline aggregates composed of two phases, GI phase and Ig phase. The Ig phase is further divided into two regions to form three phase regions GI, GBAZ and TJ as shown in figure 7.2.8. The proposed finite element (FE) model accounts for the effect of triple junctions by increasing the average density of TJs as the average grain size of the NPC material decreases in the range 50nm - 5nm as shown in figure 7.2.9. Mesh sensitivity studies were performed for all samples and then sufficient elements were used in the GI, GBAZ and TJ to capture the time evolution of hydrogen concentration in the NPC nickel.

Figure 7.2.10 shows the statistical distribution of elements per grain interior for the GBAZ in the computationally developed synthetic mesoscale microstructural FE model of NPC material. This shows that the average number of elements in each grain was 6000 and the average number of elements in each GBAZ was 400. Figure 7.2.11 shows the statistical distribution of the number of elements per TJ in synthetic microstructural models for sharp corner TJs and round corner TJs. This shows an average number of 50 elements per TJ in the sharp corner TJ synthetic microstructural model and an average number of 400 elements per TJ in the round corner TJ synthetic microstructural model. The difference in the average number of elements per TJ between the sharp corner TJ and round corner TJ microstructure is due to the increase in the area fraction between them. Figures 7.2.10 and 7.2.11 show the number of elements that are placed in the three different phases of the three phase synthetic microstructural model to capture the hydrogen transport concentration in NPC material. Figure 7.2.12 shows the discretization nodes of the sharp corner TJ three phase synthetic microstructural models and finite element (FE) mesh of the model in a region with TJs, GBAZs and three adjacent neighbouring grains of NPC material. The effect of TJs on the hydrogen transport of electrodeposited NPC nickel was investigated using computationally developed NPC materials with synthetic

microstructures (of average grain size 5nm, 10nm, 50nm and single crystal). The results of these analyses for the three different average grain sizes and a single crystal of NPC material, all with the same domain area of 2.5 nm^2 at 298 K are shown in figure 7.2.13 after three different time periods of 1.3, 83.0 and 167.0 ms.

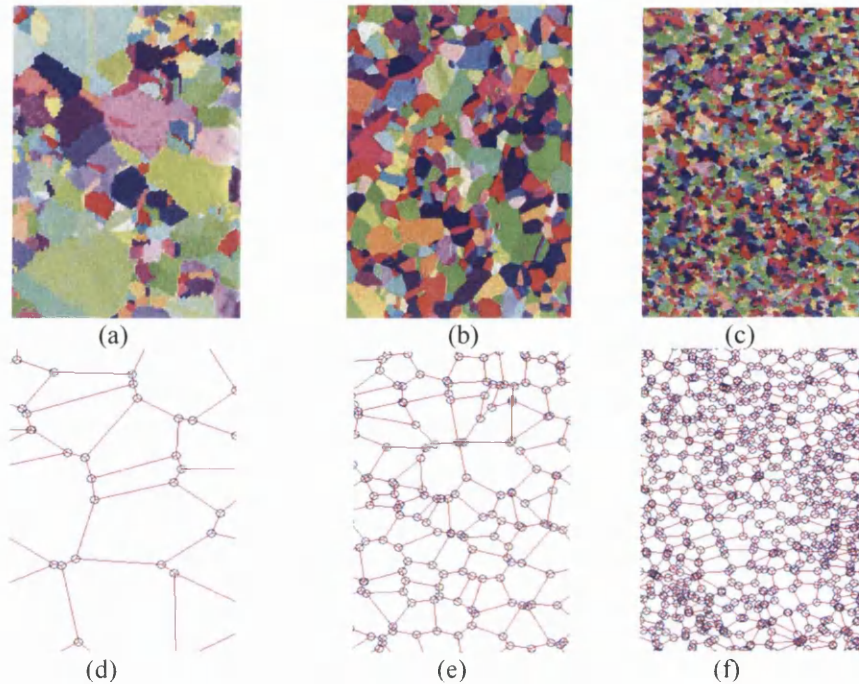


Figure 7.2.6 (a), (b) and (c) are the 2D EBSD (Electron backscattered diffraction) experimental microstructural image of NPC Nickel with decrease in average grain sizes respectively. The decrease in average grain size shows the increase in number of triple junctions. Fig. 2 (d), (e) and (f) are the schematic views of two dimensional multiphase NPC model showing the increased number of triple junctions in NPC material as the grain sizes decreases. The blue circles, red lines and white polygons show the triple junction phases, grain boundary phases and grain phases respectively.

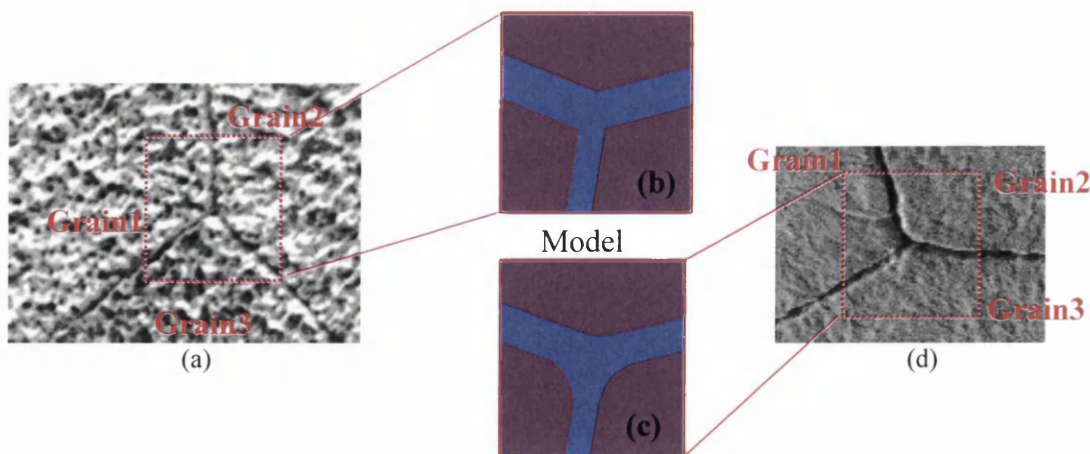


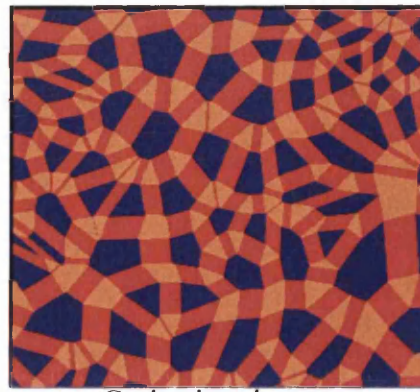
Figure 7.2.7 Actual microstructures and models with two types of TJs. (a) real microstructure of nickel with 'sharp corner' TJ and (b) close up view of modelled 'sharp corner' TJ (c) close up view of modelled 'round corner' TJ and (d) real microstructure of nickel with 'round corner' TJ.



Figure 7.2.8 (a) Synthetically developed microstructural model for NPC material based on the modified double line Voronoi (i.e. this double line area is considered as microstructural Ig phase in the model) (b) Synthetic microstructural model based on modified three phase microstructural model (i.e. the double line Ig phase is divided into two regions as GBAZ and TJ with sharp corners).

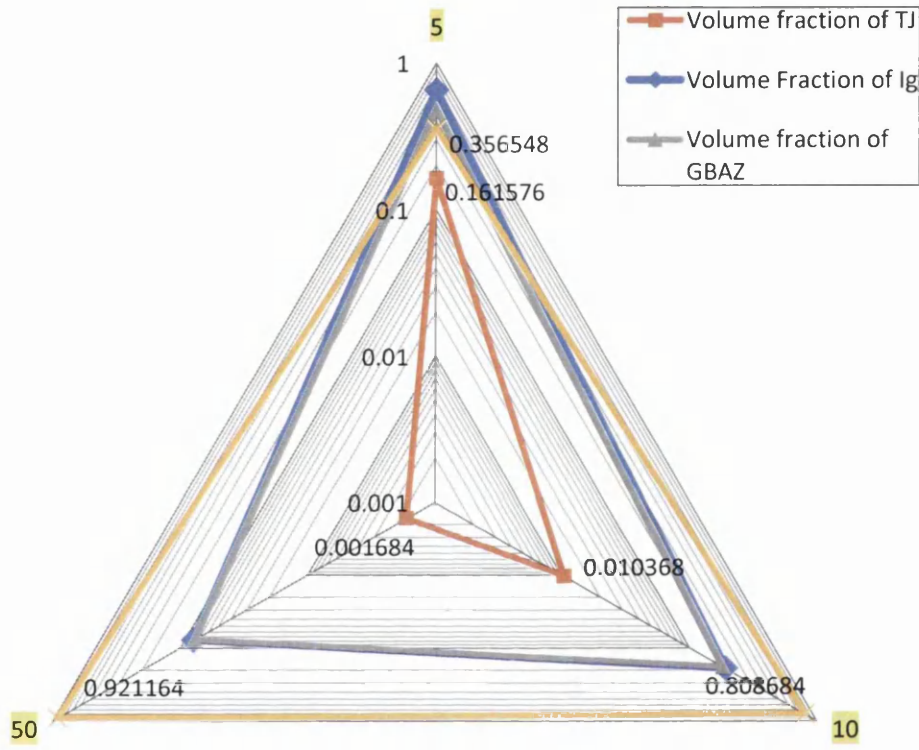
Figure 7.2.14 shows the microstructural FEA computed results of dimensionless hydrogen concentration for various different volume fractions of TJs for three different times and two different positions in NPC material. Figure 7.2.14 shows that an increase in the volume fraction of TJs increases the accumulation of hydrogen concentration in the NPC material. Figure 7.2.15 shows how the normalized hydrogen concentration varies with time for various grain sizes and the single crystal material. Figure 7.2.16 shows microstructural FEA results of normalized concentrations depend on normalized distance for various average grain sizes in NPC nickel and single crystal nickel material.

The NPC microstructure using round and sharp corner TJs based on the real microstructure is shown in figure 7.2.7. From this microstructural model for the two different TJ shapes, the statistical distribution of the grain area and the GBAZ area are computed and are shown in Figures 7.2.17 (a) and (b) respectively from which the mean value of the average grain area distribution is 34.8 nm^2 and the average GBAZ area distribution is 2.7 nm^2 . Figure 7.2.18 (a) and (b) show the computed statistical area distributions for the sharp corner TJs and round corner TJs. The total area of TJ in the ‘round corner TJ’ (187.14 nm^2) mesoscale model is approximately seven times higher than the ‘sharp corner TJ’ (25.92 nm^2). The average grain size between the round corner TJ NPC microstructural model and sharp corner TJ mesoscale model are the same but the area fractions of TJ in these two models are different. This difference in the area fraction of TJ is due to the change in the shape of the TJ.

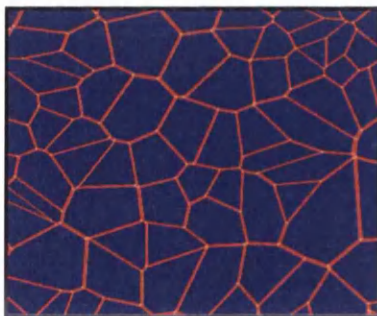


Grain sizes in nm

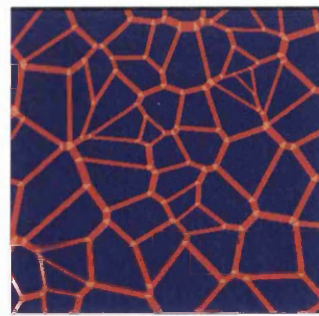
(a)



(d)



(c)



(b)

Figure 7.2.9 Mesoscale microstructure of NPC material with average grain size of (a) 5nm, (b) 10nm and (c) 50nm. (d) A radar triangle graph showing the effect of average grain sizes of NPC materials on the calculated volume fraction of GI, Ig, GBAZ and TJ.

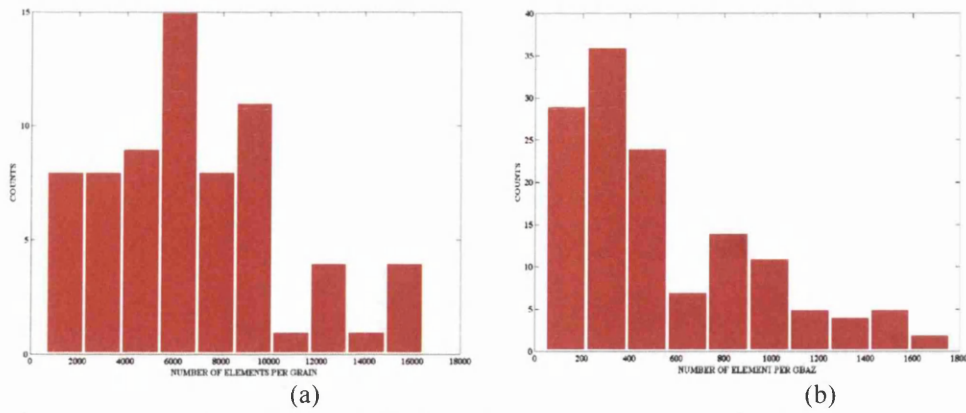


Figure 7.2.10 Statistical distribution of (a) the number of elements per grain and (b) the number of elements per GBAZ in a synthetic microstructure with sharp corner TJ model of NPC material.

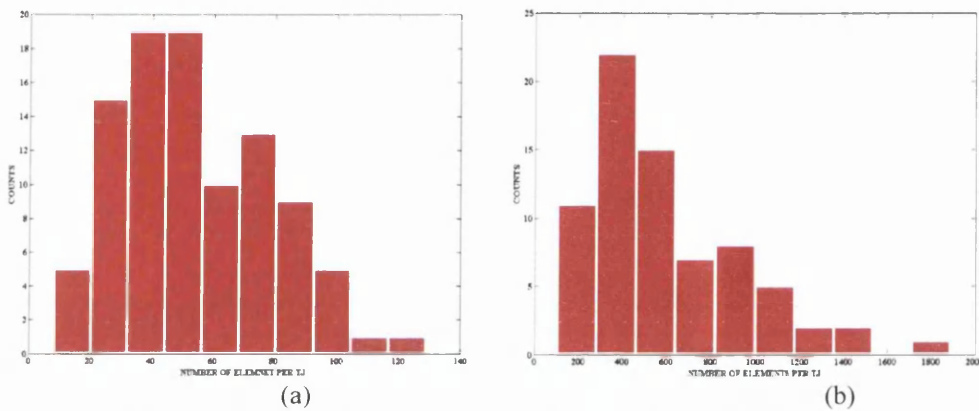


Figure 7.2.11 Statistical distribution of (a) the number of elements per TJ distribution of the sharp cornered TJ synthetic microstructural model and (b) the number of elements per TJ distribution of the round cornered TJ synthetic microstructural model of NPC material.

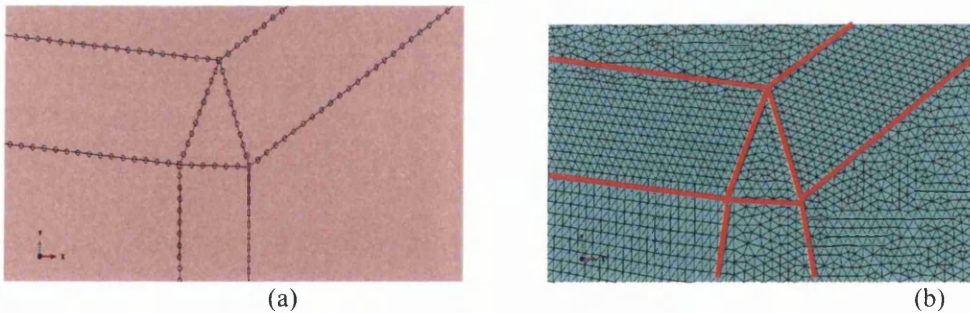

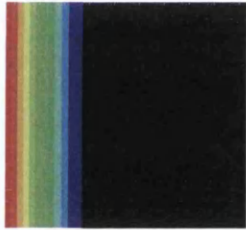
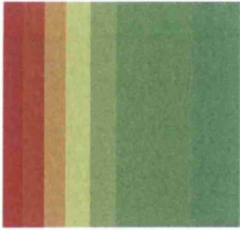
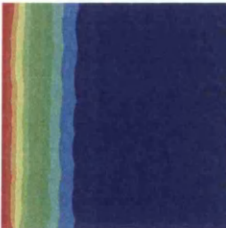
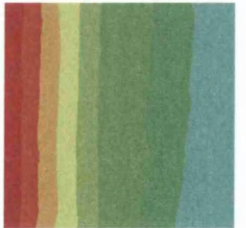
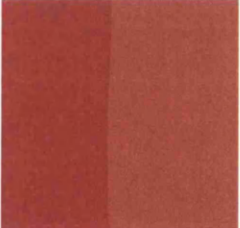
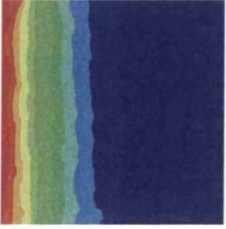




Figure 7.2.12 (a) Discretization nodes of the TJ with sharp corners, GBAZ and three neighbouring grains and (b) FE mesh of the same region as shown in the figure (a) of the NPC microstructural model.

The mean values of both of these TJ area distributions are computed as 0.2477 nm^2 and 2.552 nm^2 respectively. The mean area value of the sharp corner TJ is one order of magnitude higher than the round corner TJ microstructure. Figure 7.2.19 (a) shows the computed statistical distribution of the GBAZ thickness with a computed mean

value of 0.6957 nm. Figure 7.2.19 (b) shows the cumulative frequency of the TJ area distribution between sharp corner TJs and round corner TJs. Only 25% of the TJs are greater than 3.5nm^2 in the round corner TJ microstructural model and less than 1% of TJs are greater than 0.5nm^2 in the sharp corner TJ microstructural model.

Figure 7.2.20 shows the results of the computational analysis of hydrogen transport in NPC nickel microstructures with sharp corner TJs and round corner TJs after two different time periods of 2.6 ms and 20.97 ms in the same domain with the same grain size and with the same material diffusivity properties. The hydrogen transport is accelerated in the round corner shape TJ microstructure compared to the sharp corner shape TJ microstructure. This acceleration of hydrogen transport in round corner TJ material is due to the higher volume fraction of TJs. Figure 7.2.21 shows the normalized hydrogen concentration calculated at TJs as a function of time for three different distances X1 (15.21) , X2 (32.92) and X3 (51.80) for the sharp corner TJ and round corner TJ models.

Grain size	Time :1.3milliseconds	Time:83 milliseconds	Time: 167milliseconds
Single Crystal			
50nm			
10nm			

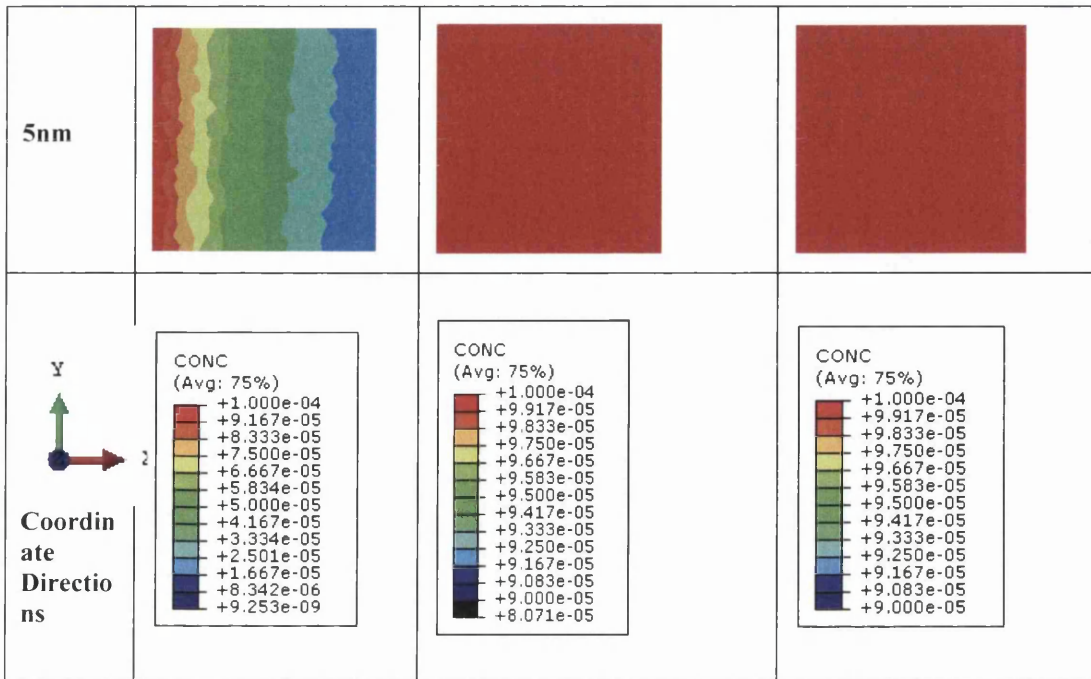


Figure 7.2.13 Results of the hydrogen transport in mesoscale microstructures with average grain size of 5nm, 10nm and 50nm in NPC material after 1.3ms, 83.0ms and 167.0ms.

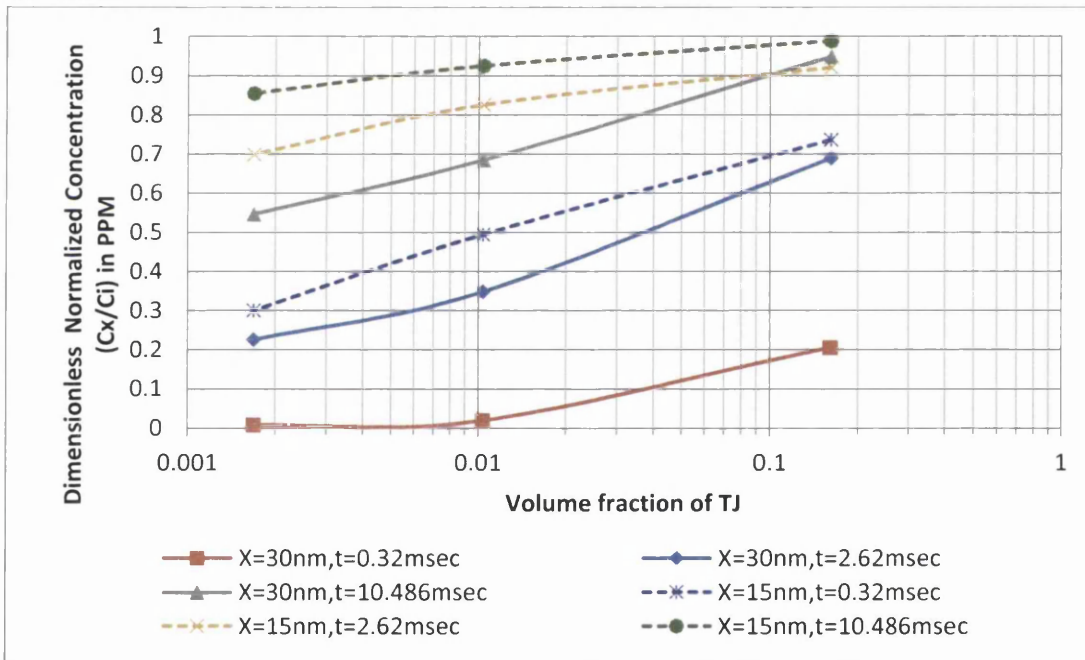


Figure 7.2.14 Results of the computed dimensionless hydrogen concentration for three different volume fractions of TJs, three different times at two different positions in the NPC material.

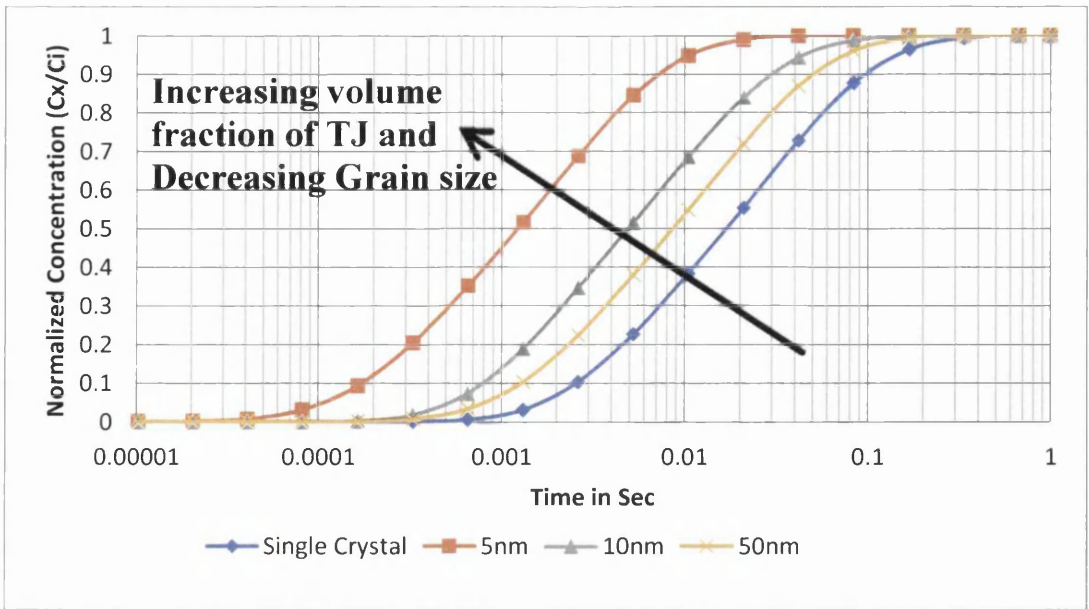


Figure 7.2.15 Computed normalized hydrogen concentration dependency on time for various average grain sizes of 5 nm, 10 nm and 50 nm of NPC material and the single crystal case (the results have been calculated at $X=30,0$).

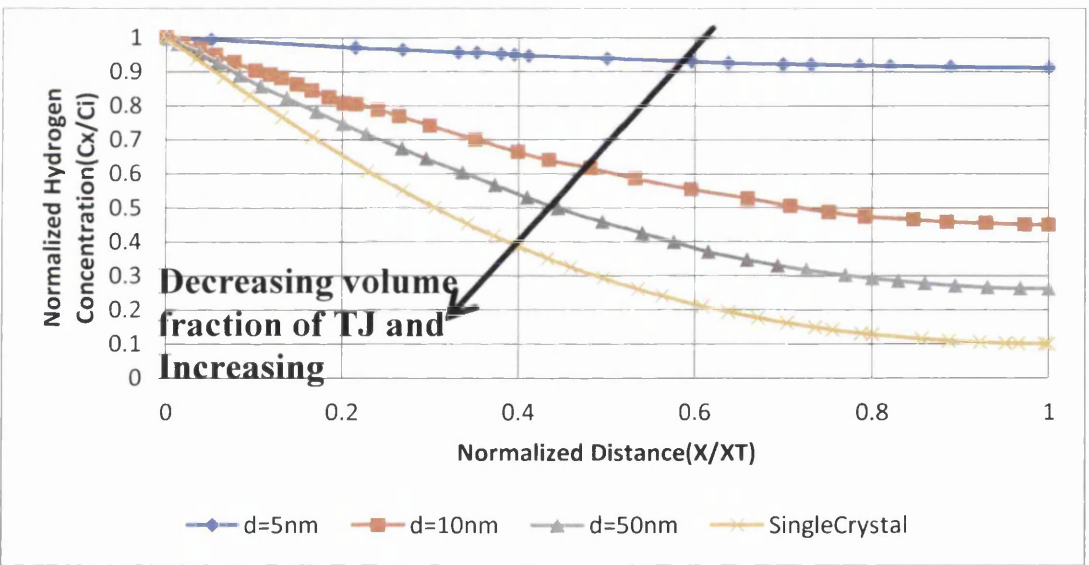


Figure 7.2.16 Computed normalized hydrogen concentration dependency on normalized distance for various average grain size 5 nm, 10 nm and 50 nm NPC material and the single crystal material. The results have been calculated at time =10 ms.

In all of the three different distance cases the size and shape of the TJs affects the hydrogen transport. The decrease in the area under the curve of the normalized hydrogen concentration in the sharp corner shape TJ microstructure compared to the round corner TJ case is due to the reduction in the density of TJs in the sharp corner TJ microstructure. Figure 7.2.22 shows how the computed normalized hydrogen

concentration depends on normalised distance with the same average grain size having two different volume fractions of TJ. The graph was plotted after 10 ms of hydrogen diffusion in the sample material. The 0.064 increase in volume fraction of TJ microstructure increases the area under the curve of normalized hydrogen concentration (i.e. the total normalised accumulated hydrogen within the sample). This demonstrates how an increase in the volume fraction of TJs (associated with much higher diffusion coefficients) enhances bulk diffusion of hydrogen.

(iii) Thirdly, the effect of pores/voids and fine nano grains (FNGs) in triple junctions on transport mechanisms in NPC nickel materials are numerically analysed. Figure 7.2.20 (a) shows the experimental SEM image of void/pores in the NPC nickel microstructure. Figure 7.2.20 shows the results of the computationally generated NPC nickel microstructure with (b) voids/pores on TJs and (c) fine grains on TJs. The volume fraction of voids considered in the model is 0.186. In the three phase (Ig, GBAZ and TJ) synthetic microstructure model, the TJs are further divided into fine grains with an average grain size of 1 nm. The results of hydrogen transport analyses of material with nano fine grain microstructure in TJs and voids in TJs for various time periods are shown in Figure 7.2.21. The 2D hydrogen transport in a microstructure with fine grains in TJs is faster than the NPC microstructure with voids in TJs. Therefore it is important to take into account microstructural features such as voids, fine grains etc. in TJs to correctly capture the hydrogen transport in NPC material. Figure 7.2.22 shows how the computed normalized hydrogen concentration depends on time for 10nm grain size material with three different microstructures (material with microstructure containing TJs, fine grains in TJs and pores in TJs). The area under the curve is greater for microstructures with normal TJs than those containing fine grains or pores in TJs. The area under the curve is smaller for microstructures containing pores in TJs than either the microstructure with fine grains in TJs or the microstructure with normal TJs. These results show that the bulk diffusion of hydrogen in NPC material with microstructures containing fine grains in TJs is slower than the microstructure with normal TJs and faster than the microstructure with pores in TJs.

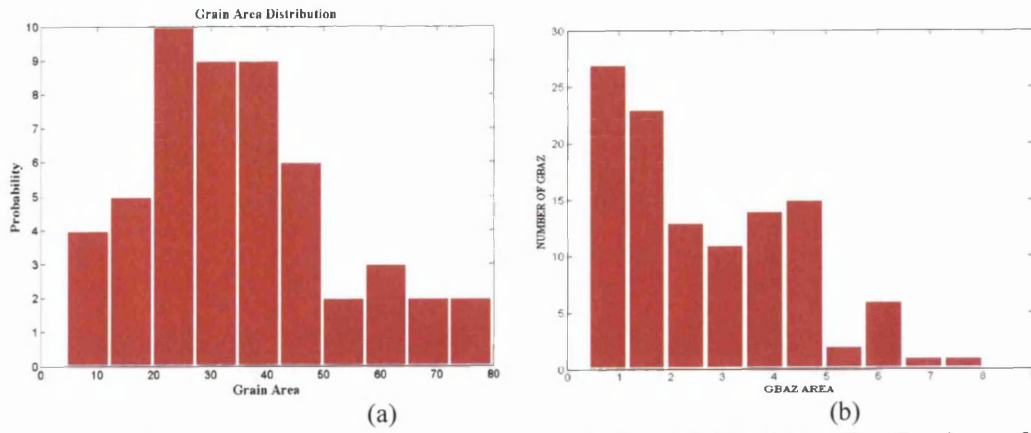


Figure 7.2.17 (a) Grain Area distribution and (b) GBAZ Area distribution of the Model

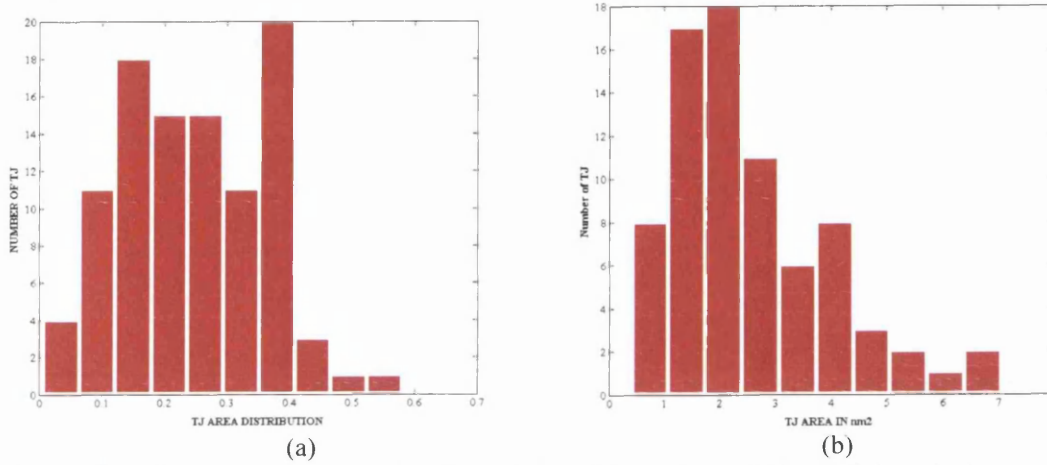


Figure 7.2.18 (a) TJ area distribution of the sharp corner TJ Model and (b) TJ area distribution of the round corner TJ model.

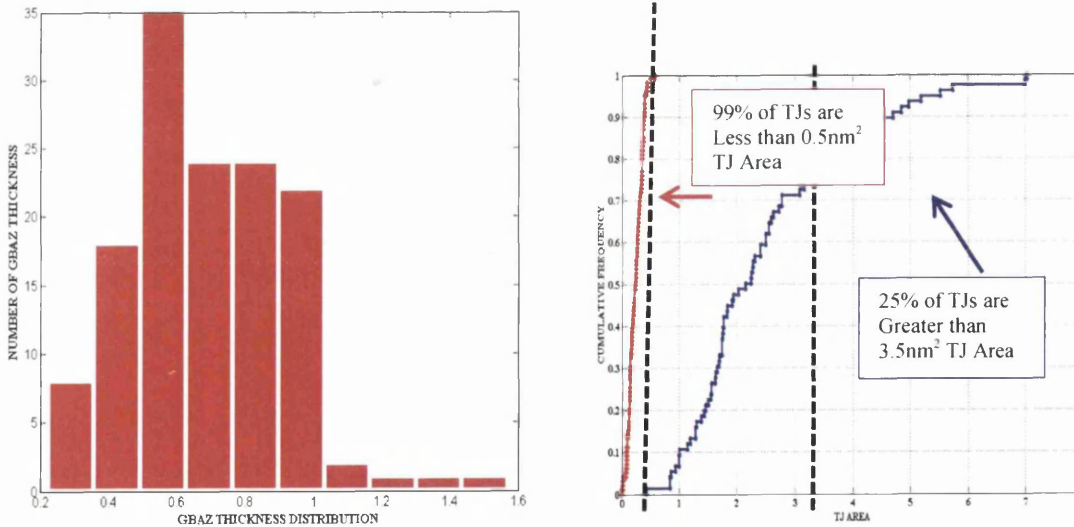
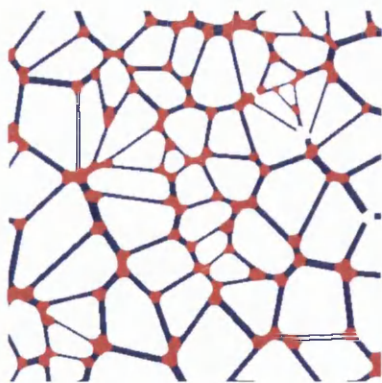
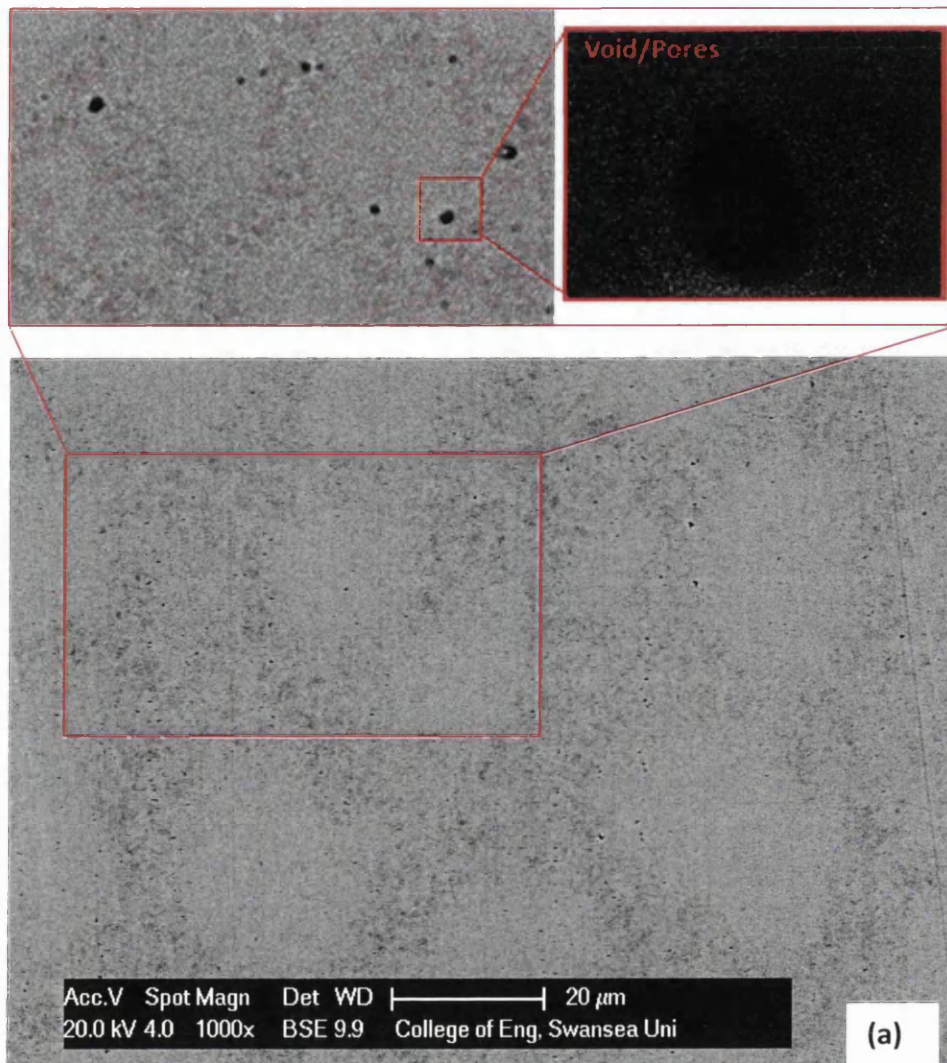
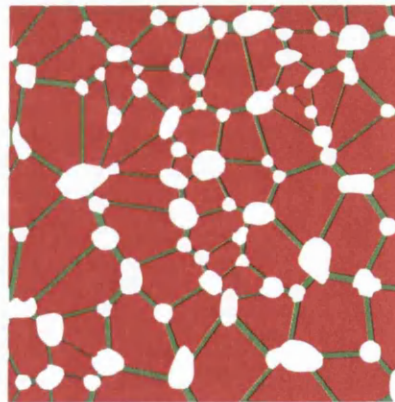


Figure 7.2.19 (a) GBAZ thickness distribution and (b) cumulative frequency of TJ area distribution of the microstructural model with sharp corner TJs (red line: area under curve is 25.92nm²) and round corner TJs (blue line: area under curve is 187.14nm²).



(b)



(c)

Figure 7.2.20 (a) shows an SEM image of NPC nickel with pores and the computationally generated NPC material microstructure with (b) pores on TJs and (c) fine nano grains on TJs.

Finally, the effect of the presence/absence of TJs on hydrogen diffusion in NPC nickel material was investigated. NPC microstructures with two phases (grain interior and grain boundary/intergranular region) and three phases (grain interior, grain boundary and triple junctions) were computationally analysed using FEA. In the three phase microstructure the TJ is considered as a separate phase. Figure 7.2.23 shows the results of microstructural FEA of hydrogen diffusion in the two phase and three phase microstructures. The results show how the computed normalised hydrogen concentration depends on the normalized distance (Y/Y_t) at a distance (X/X_t)=0.65 in the x-direction for 10nm grain size NPC material with a two phase microstructure (GI and Ig phases) without TJs and a three phase microstructure (GI, GBAZ and TJ phases) with TJs. The diffusivity value used for Ig was $6.3 \times 10^{-9} \text{ cm}^2/\text{s}$.

The hydrogen transport in the two phase and three phase microstructures is heterogeneous due to the difference in the hydrogen transport properties of microstructural GI, GBAZ, Ig, and TJ. It is interesting to note that the two curves for normalised concentration with and without TJs in Figure 7.2.23 would almost overlie one another if the lower curve was moved upwards. This highlights that the main effect is the increased flow rates within TJs compared to the Ig phase. Figure 7.2.23 also shows the computed homogenous normalised hydrogen concentration at the same place in a single crystal. The hydrogen transport in single crystal nickel is both slower than the NPC nickel and homogenous.

To aid understanding of the accumulation of hydrogen in TJs in NPC nickel the graph is plotted for accumulated normalized hydrogen concentration depending on the number of TJs in the three phase microstructure and on Ig in the two phase microstructure along the path at a normalised distance of (X/X_t) 0.045 at time 0.164 ms in figure 7.2.24. This also demonstrates that the accumulated hydrogen in TJs and Ig is heterogeneously distributed even along the same path. These results show that the hydrogen concentration in the three phase microstructure is higher than the two phase microstructure due to the faster transport of hydrogen in the three phase microstructure containing the TJs. Figure 7.2.24 also shows that even at a very small distance from the left-hand side there is a difference between a model with TJs and a model without TJs. Thus the TJ significantly affects hydrogen transport with the accumulation of hydrogen being heterogeneous. This reinforces the importance of considering TJs in modelling as well as experimental observations when investigating hydrogen transport in NPC nickel.

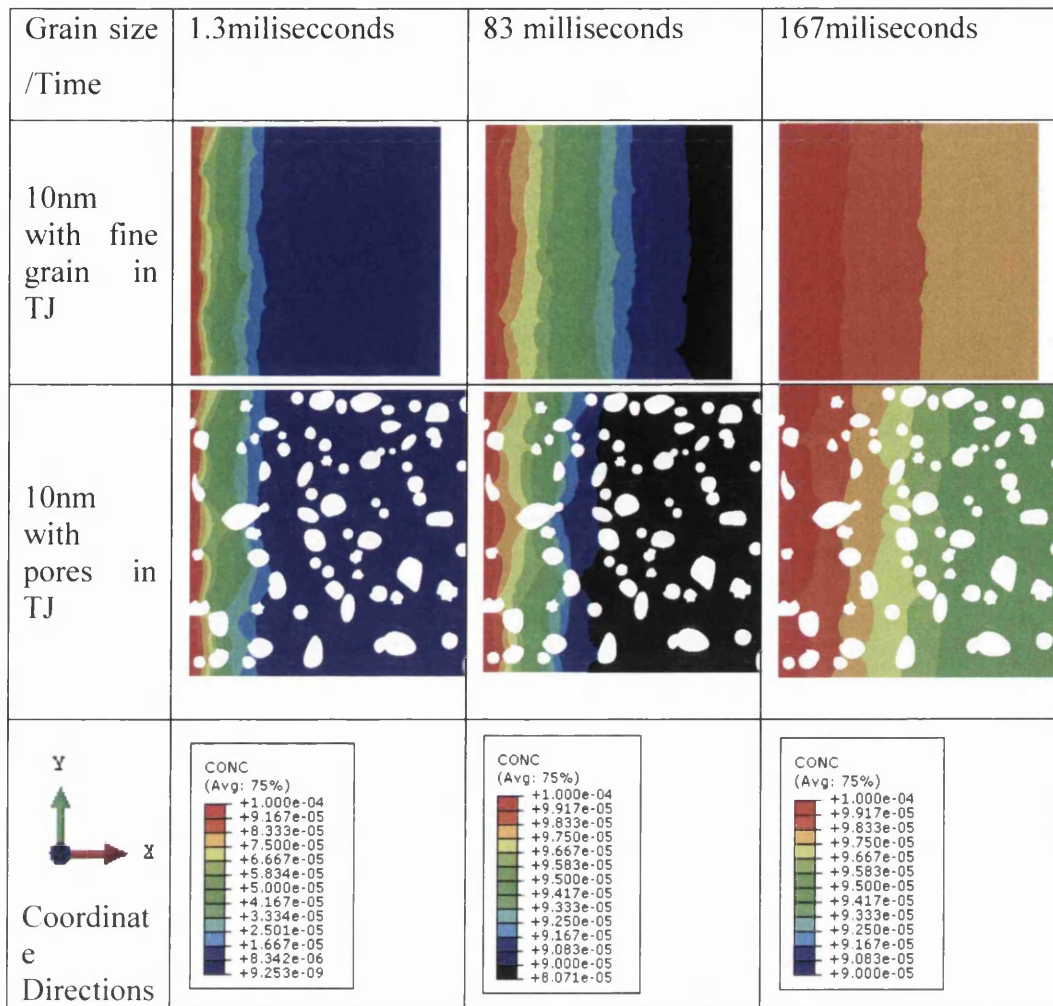


Figure 7.2.21 (a) Hydrogen transport results from the computational analysis of two different synthetic microstructures with average grain size 10nm (a) with fine grain in TJs and (b) pores in TJs after three different time intervals.

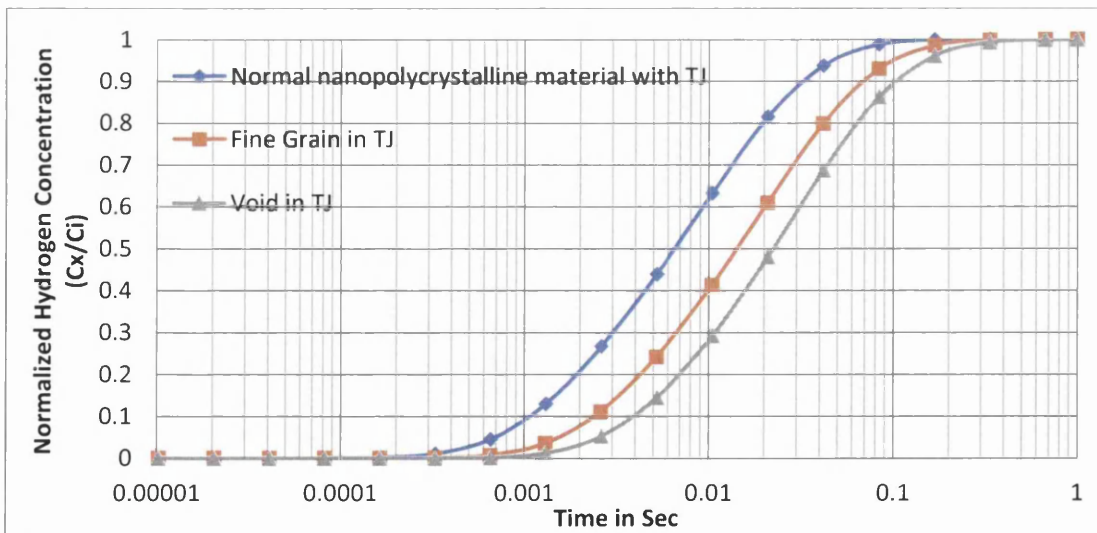


Figure 7.2.22 Computed normalized hydrogen concentration dependency on time for 10nm grain size NPC materials with three different microstructures i.e. material with a microstructure containing TJs (blue line), fine nano grains in TJs (red line) and pores in TJs (grey line).

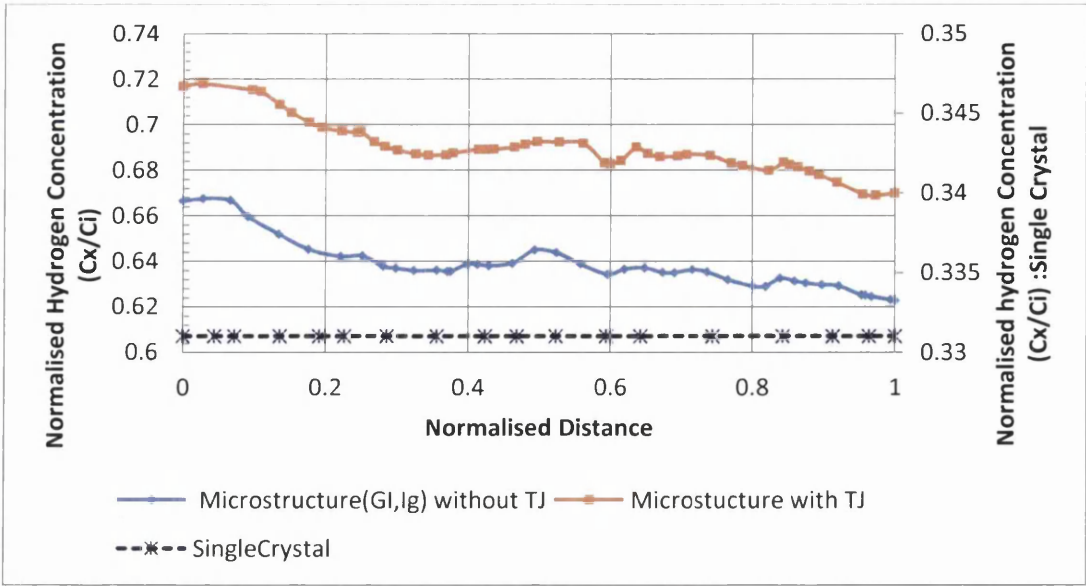


Figure 7.2.23 Computed normalized hydrogen concentration dependency on normalized (Y/Y_t) distance at a distance (X/X_t) = 0.65 for 10nm grain size NPC with a two phase microstructure (GI and Ig), a three phase microstructure (GI, Ig and TJs) and single crystal nickel. The results were obtained at time 10 ms.

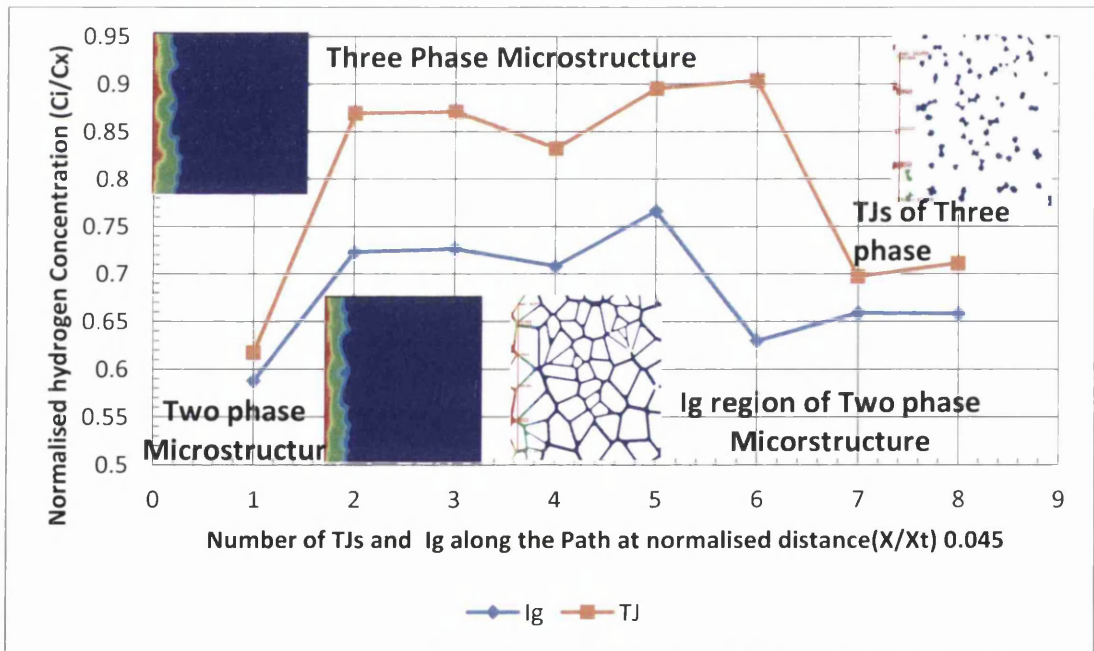


Figure 7.2.24 Computed accumulated normalized hydrogen concentration dependency on i) number of TJs in three phase microstructural NPC nickel and ii) number of Ig in two phase microstructural NPC nickel along a path at a normalised distance (X/X_t)=0.045 at time 0.164ms.

7.2.2 Discussion

(i) The hydrogen diffusion in micro polycrystalline nickel microstructures with smaller GBZ thickness is slower when compared to larger GBZ thicknesses as shown in computational result figure 7.2.2. An order of magnitude increase in GBZ thickness increases the effective hydrogen diffusion distance more than twice and a four orders of magnitude increase in GBZ thickness increases the effective hydrogen diffusion distance more than eight times. These results suggest that decreasing grain size will promote bulk diffusion of hydrogen due to the increase in grain boundary surface area in polycrystalline nickel.

The results also show the heterogeneous distribution of hydrogen in bulk polycrystalline material along GBZ and grain interiors after a time period of 1 hour. This suggests that intergranular softening of polycrystalline material (which is due to the segregation of atomic hydrogen along the intergranular microstructure) may lead to intergranular hydrogen embrittlement (as opposed to transgranular hydrogen embrittlement) at shorter times before the system attains a more steady state. This depends on the particular intergranular diffusion properties but could be an important consideration when considering hydrogen embrittlement effects.

Figure 7.2.3 (a) and (b) show the predicted hydrogen concentration in micro polycrystalline nickel for four different GBZ thicknesses. This shows that the hydrogen concentration profile attains steady state earlier for higher relative fractions of grain boundary polycrystalline material. A number of studies have already reported that the relative fraction of grain boundary in NPC nickel is significantly larger than the case of micro polycrystalline nickel while observing faster diffusion in the NPC case [Turnbull et al., 1989, Harris 1991]. These observations are in agreement with the model prediction that bulk diffusion in NPC nickel will be faster than the micro polycrystalline case. From figure 7.2.4, it is clear that hydrogen diffusion is heterogeneous between grain and grain boundary in the polycrystalline material becoming more homogenous with decreasing grain boundary thickness and/or increasing time. Even though the grain interior and grain boundary diffusion coefficients are the same for all GBZ thicknesses simulated the model predicts less diffusion of hydrogen for smaller GBZ thicknesses. This enhanced hydrogen diffusion for larger GBZ thicknesses is due to the increased contribution of the

intergranular grain boundary density as shown in the figure 7.2.4. The increased density of grain boundary in smaller grained polycrystalline materials greatly increases the hydrogen diffusion along the grain boundary thus increasing the effective bulk hydrogen diffusion. These results show the significant influences of intergranular grain boundaries on the bulk hydrogen diffusion process in micro polycrystalline nickel materials. Hydrogen flux increases along grain boundaries and hydrogen accumulates more in the grain boundaries than grain interior, as shown in the figure 7.2.5. These results also show that the inhomogeneous diffusion and segregation of hydrogen along grain boundaries becomes more homogeneous when moving towards steady state. Hydrogen diffusion in fine grain size micro polycrystalline material becomes homogenous much earlier compared coarse micro polycrystalline materials. And the coarse grained micro polycrystalline materials need more time to attain steady state. This suggests that hydrogenated fractures occurring before steady state in micro polycrystalline materials may be intergranular in nature due to embrittlement along grain boundaries interface.

(ii) Figure 7.2.9 (d) shows how the volume fraction of the intergranular region increases by one order of magnitude as the average nano grain size decreases from 50 nm to 5 nm. At the same time, when decreasing the average nano grain size from 50 nm to 5 nm, the volume fraction of GI decreases from 92.12 % to 35.65 %, with the major decrease in volume fraction of 45 % from 80.87 % occurring when the grain size decreases from 10 nm to 5 nm as shown in Table 1. The result of the computationally developed synthetic NPC material shows that a decrease in average size from 50 nm to 10 nm increases the volume fraction of TJ by one order of magnitude with less than a 1 % increase in the density of TJs from 0.16 %. A decrease in the average grain size from 10 nm to 5 nm increases the volume fraction of TJs by 15.12 % from 1.03 %. The decrease in average grain size of NPC material from 50 nm to 5 nm increases the volume fraction of TJs by 2 orders of magnitude, increases the volume fraction of GBAZ by one order of magnitude and decreases the volume fraction of GI by less than one order of magnitude. Palumbo et al. [43] found a similar trend relating the volume fraction and density of TJs with changes in nano grain size in 3D NPC materials.

Grain Size in nm	Volume fraction of GI	Volume fraction of TJ
5	35.65 %	16.18
10	80.87 %	1.03 %
50	92.12 %	0.16 %.

Table 7.2.1 Calculated volume fractions of GIs and TJs from computationally developed synthetic nano polycrystalline models for three different grain sizes.

Figure 7.2.13 shows the effect of TJs on hydrogen diffusion in NPC nickel based on FEA results. These show that hydrogen transport after 1.3 ms in 50 nm grain size NPC material is slower than that for the 10 nm average grain size at the same time in the same domain. The hydrogen transport in the bulk microstructure of 5 nm grain size material is more than twice as fast as the material with a grain size of 10 nm and much faster than the 50 nm grain size material. The much faster bulk hydrogen transport in NPC material of 5 nm grain sizes when compared to 50 nm is due to the 16 % higher volume fraction of TJ between the 50 nm and 5 nm grain size microstructures. The hydrogen transport in 5 nm grain size NPC material attains steady state earlier than 83 ms and the 10 nm grain size NPC material attains steady state at 163 ms, but the 50 nm grain size NPC material does not attain steady state even after 167 ms. The results clearly show that a major increase in the density of TJs is found when the average grain size is less than or equal to 10nm in NPC materials. This transports the hydrogen in bulk NPC material much further and faster and attains steady state much earlier than the microstructure of NPC material with an average grain size greater than 10 nm. Since the TJs play a vital role in NPC material of ≤ 10 nm it is important to consider the effects of TJs on NPC material with hydrogen embrittlement problems experimentally as well as via modelling. Figure 7.2.14 shows how an increase in the volume fraction of TJs increases the accumulation of hydrogen concentration in the NPC material. From figure 7.2.15 it is clear that hydrogen transport in the single crystal material is slower than the hydrogen transport in NPC material. The normalized hydrogen concentration is smaller in microstructures with average grain sizes of 50 nm and higher compared to the 5 nm NPC material due to the lower volume fraction of TJs in larger grain size NPC material. Figure 7.2.16 shows how the normalized concentrations depend on the normalized distance for various average grain sizes and single crystal material. The area under the normalized hydrogen concentration curves increases from the single

crystal material to smaller grain sizes. The difference in the area under the normalized concentration curve (i.e. the total normalised accumulated hydrogen within the samples) is greatest between the 5nm vs 10nm cases compared to the difference in the area under the normalized concentration curve between the 10nm vs 50nm and the single crystal vs 50nm cases. This is because the increase in the volume fraction of TJs is higher when the grain size is less than 10nm. From the results the difference in size and shape of TJs is shown to affect bulk hydrogen transport. They also show that the effective diffusion of hydrogen in NPC nickel with round corner TJs is faster than NPC nickel with sharp corner TJs. This effect is due to the reduction in the density of TJs in the sharp corner TJ microstructure. This also demonstrates how an increase in the volume fraction of TJ (associated with much higher diffusion coefficients) enhances diffusion of hydrogen in bulk NPC nickel material.

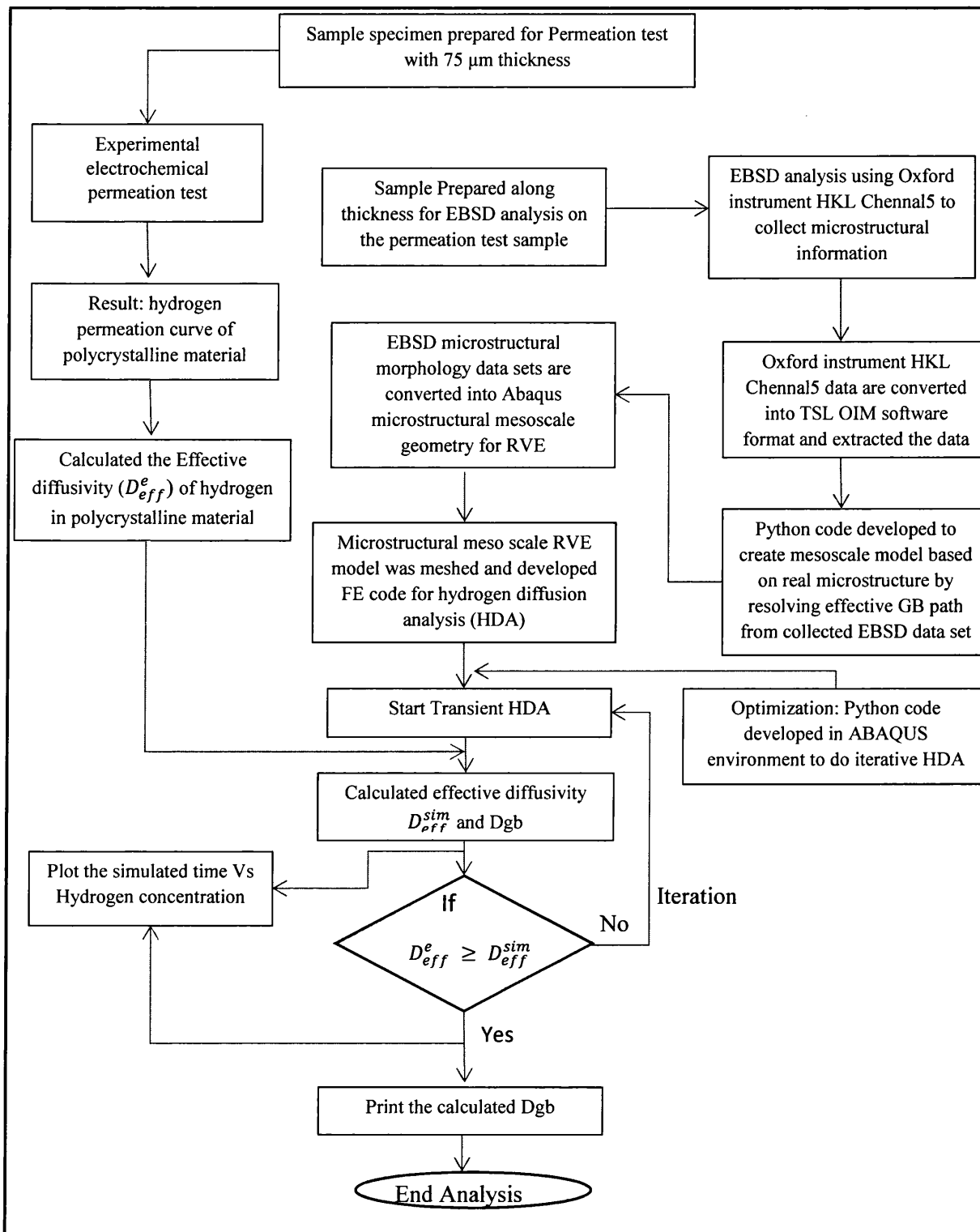
(iii) From the results of nanostructural hydrogen diffusion FEA on NPC nickel material with pores/voids and fine grains in the TJs it is clear that the bulk diffusion of hydrogen in a nanostructure with fine grains in TJs is faster than the NPC nickel nanostructure with voids in TJs. These results also show that the bulk diffusion of hydrogen in NPC material with nanostructures containing fine grains in TJs is slower than the nanostructure with normal TJs and faster than the nanostructure with pores in TJs. Therefore it is important to take into account such microstructural features to correctly capture the hydrogen diffusion and hydrogen embrittlement in NPC material. These results reinforce the importance of considering TJs in modelling as well as experimental observations when investigating hydrogen transport in NPC nickel. Detail information about the trap model and its results can be found in Appendices.

7.3 Real microstructural based 2D mesoscale FE simulation to predict intergranular hydrogen diffusivity and isotropic effective bulk diffusion of hydrogen in conventional electrodeposited nickel.

Computational analysis of the hydrogen induced intergranular embrittlement failure process requires accurate calculation of the differential hydrogen transport in intergranular and intragranular regions. An effective hydrogen diffusion coefficient may be measured experimentally although experimental measurement of the intergranular grain boundary diffusion coefficient of hydrogen requires significant effort. Therefore an approach to calculate the intergranular GB hydrogen diffusivity using 2D microstructural FEA was developed which was also used to calculate the effective diffusivity of hydrogen in conventional electrodeposited polycrystalline nickel as measured using electrochemical permeation tests. Data from 2D EBSD measurements were used to construct 2D microstructural representative volume elements including details of grain size and shape and volume fraction of grains and grain boundaries. A PYTHON optimization code was developed for the ABAQUS environment to calculate the unknown grain boundary diffusivity.

7.3.1 Experimental results

The material used in this study was conventional electrodeposited polycrystalline pure nickel in the form of 75 μm thick thin foil with a 3 μm average grain size. The detailed computational approach to calculate the intergranular diffusivity of hydrogen using real microstructures by coupling experimental techniques is shown in flowchart 7.3.1. The orientation mapping was done on the cross-section of the nickel foil used for the electrochemical permeation test to determine several metallurgical parameters. The microstructural geometric features were extracted to develop a meso-microstructural RVE for subsequent simulation. The EBSD analysis results of crystallographic orientations within the cross section of the nickel foil are shown in figure 7.3.1(a). Figure 7.3.1(b) shows the inverse pole figure of the crystallographic orientation map. The grain diameter distribution is shown in Figure 7.3.1(c). The majority of grains have diameters between 1 and 4 μm . The total length of the GB was calculated to be 12015.2 μm .



Flowchart 7.3.1 shows the detail about the computational approach developed in this study to calculate the effective GB diffusivity of hydrogen in conventional electrodeposited polycrystalline nickel.

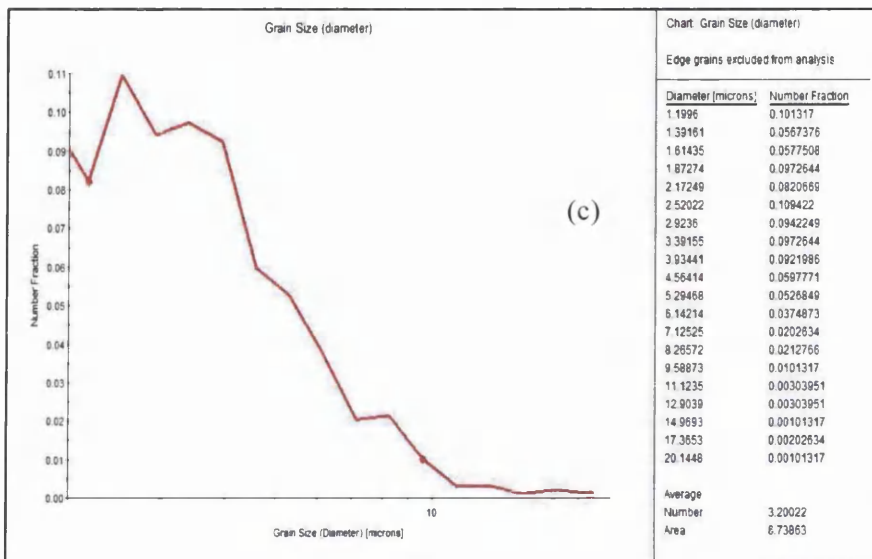
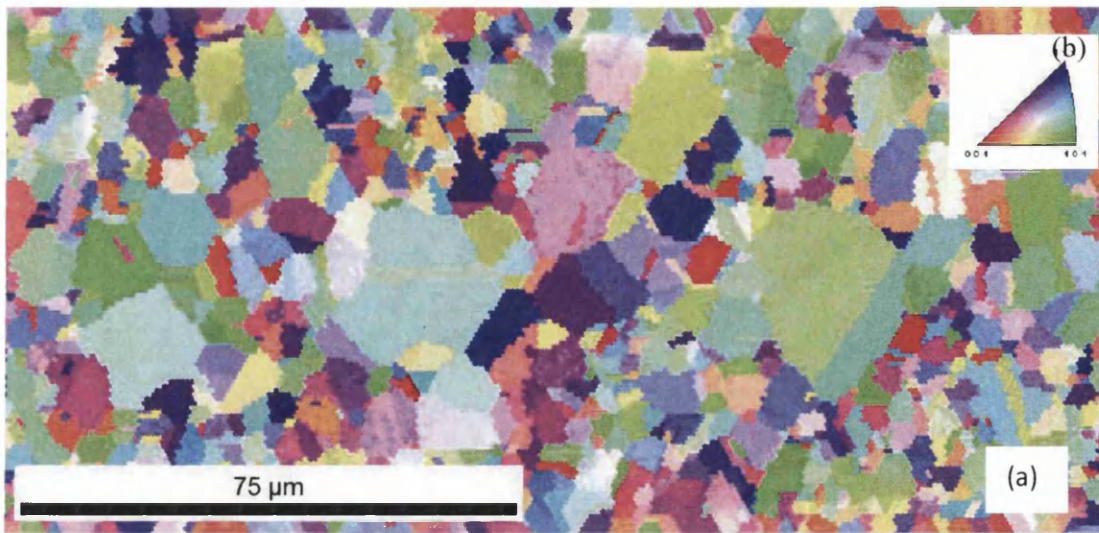


Figure 7.3.1 (a) Experimental EBSD analysis results for the cross-section of the nickel foil (b) inverse pole figure, (c) grain size distribution.

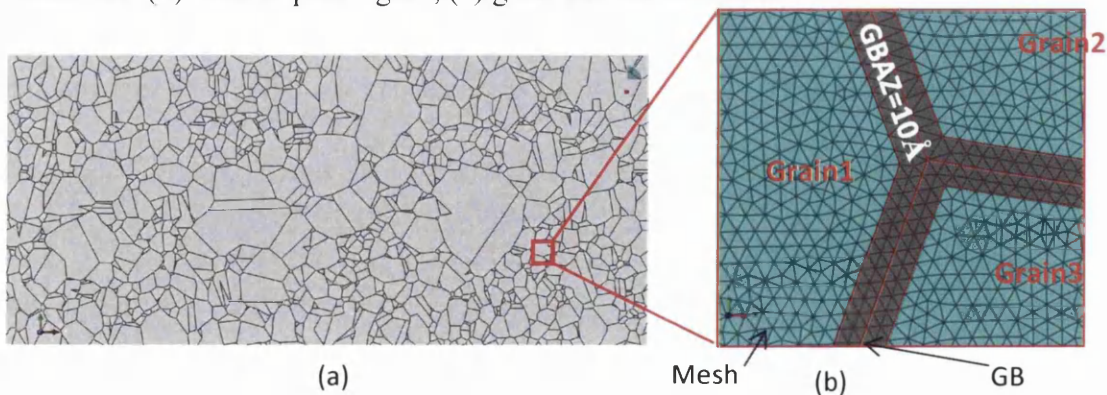


Figure 7.3.2 (a) ABAQUS FE meso scale microstructural model based on the EBSD data shown in Figure 7.3.2. (b) Detail of the FE mesh near a triple junction of three neighbouring grains showing the GBAZ (red/grey region) with a thickness of 10 Å.

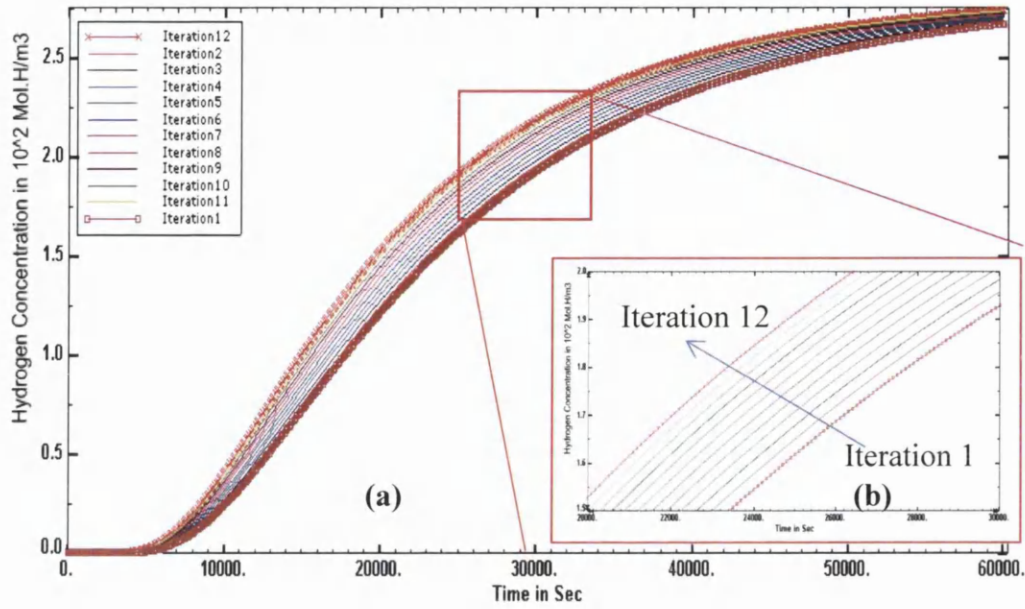


Figure 7.3.3: (a) ABAQUS meso-microstructural polycrystalline nickel FE simulation results of transient hydrogen diffusion for various iterations. (b) Magnified view.

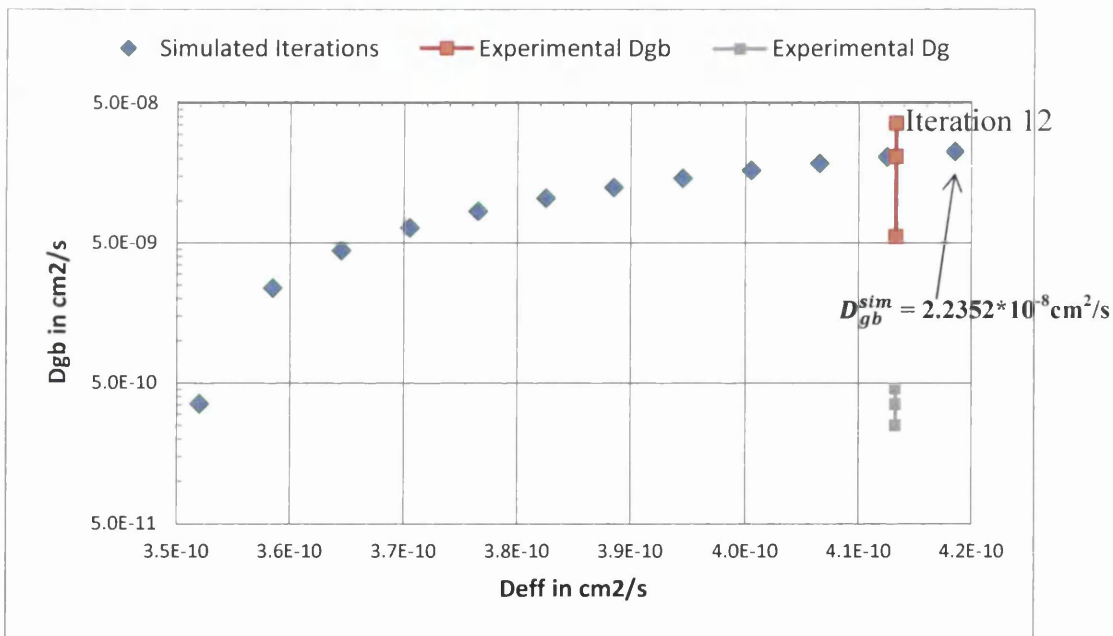


Figure 7.3.4 Results of the ABAQUS meso-microstructural FE simulations for effective grain boundary diffusivity and effective bulk diffusivity for polycrystalline nickel over 12 iterations and experimentally measured results of D_{gb} [4,101,160], lattice diffusivity (D_g) from literature [4, 160] and experimentally determined effective diffusivities from electrochemical permeation tests [101,160].

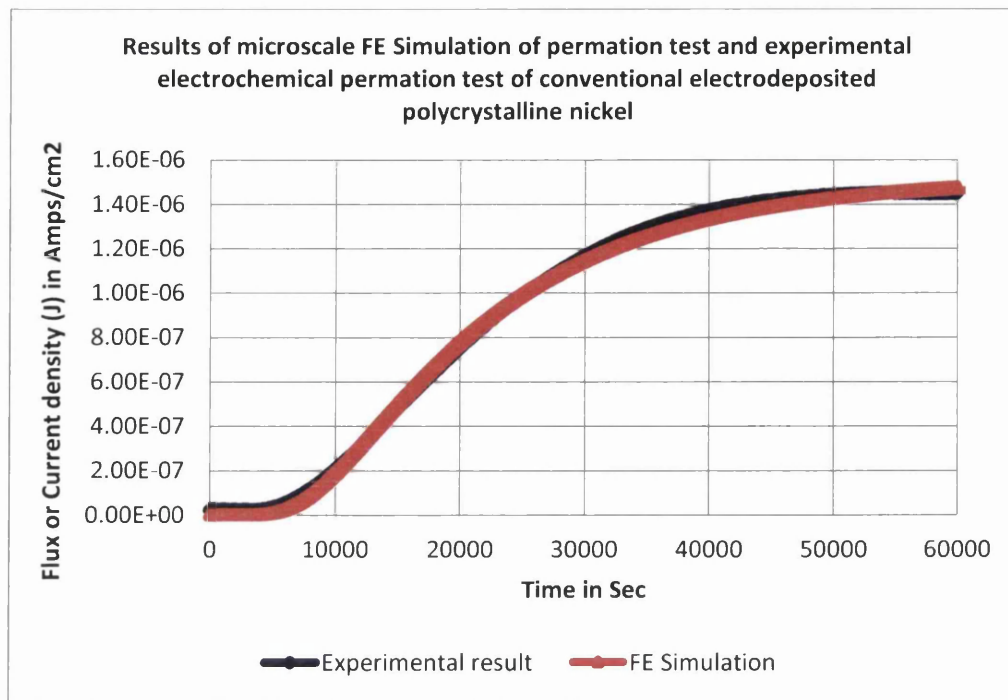


Figure 7.3.5 Experimental and simulated permeation rates (current density or hydrogen flux) of conventional electrodeposited polycrystalline nickel. (Measured and FE-calculated hydrogen diffusivity values are $D_{eff}^e = 4.1333 \times 10^{-14} \text{ m}^2/\text{s}$ and $D_{eff}^{sim} = 4.1327 \times 10^{-14} \text{ m}^2/\text{s}$ respectively).

The RVE model is shown in figure 7.3.2(a). Figure 7.3.2(b) shows a magnified view of the FE model near a triple junction with three neighbouring grains, GBs and GBAZs. In the initial FE simulation, it was assumed that $D_{gb} = D_g \cdot D_{eff}^{sim}$ as calculated from the theoretical plot of the hydrogen flux versus time. D_{gb} was then systematically increased and the simulation repeated until D_{eff}^e and D_{eff}^{sim} converged. A total to 12 iterations were needed for the results to converge. In the final solution D_{gb} was equal to $2.2 \times 10^{-8} \text{ cm}^2/\text{s}$, which is two orders of magnitude higher than the standard lattice diffusivity. The hydrogen concentration as function of time is shown in figure 7.3.3 (a) and figure 7.3.3 (b) shows a magnified view. The results are plotted in Figure 4 and show good agreement with results published by Tsuru and Latanision [4].

7.3.2 Discussion

A meso-scale real microstructure FE computational technique was developed to calculate the diffusivity of hydrogen along grain boundaries in a polycrystalline

material. The microstructural model is based on features such as grain size, grain shape and grain boundary volume fractions extracted from EBSD data. The predicted grain boundary diffusivity is two orders of magnitude higher than the lattice diffusion of hydrogen in conventional electrodeposited nickel. The results are in good agreement with experimental measurements as shown in figure 7.3.4 and 7.3.5. Understanding the intergranular diffusion of impurity atoms aids understanding, control and solution of engineering problem such as hydrogen embrittlement. This method could potentially be used to design new polycrystalline materials with improved resistance to material degradation and failure.

7.4 Real microstructural based 3D mesoscale FE simulation to calculate effective anisotropic hydrogen diffusivity of Ariane 5 combustion chamber pulse plated nickel

7.4.1 Experimental results and discussion

An Ariane-5 Vulcain-2 combustion chamber electrodeposited pulse plated nickel material was characterised using 3D EBSD experiments together with SEM/FIB techniques to understand the anisotropic distribution of grains size, grain shape, GB type and GB fraction. (Note: Although different grades of PP-Ni are used in Ariane-5 combustion chambers only one grade was accounted for in this investigation due to AIRBUS commercial confidentiality.)

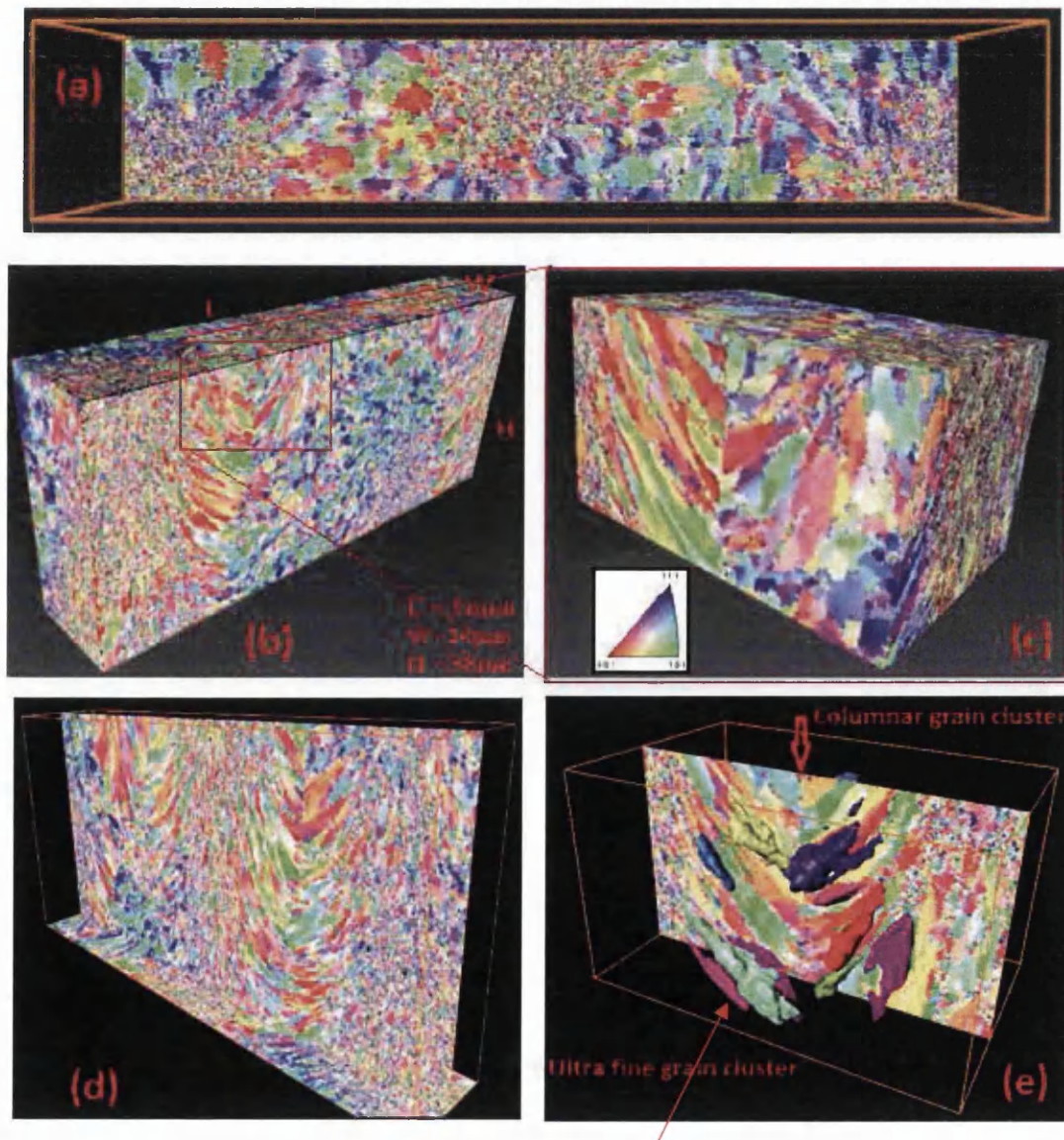


Figure 7.4.1 3D EBSD analysis of Ariane-5 combustion chamber electrodeposited pulse plated nickel microstructure. (a) Shows crystallographic orientation map of microstructure perpendicular to growth direction (TD). (b) Shows the 3D isometric side view and dimensions. (c) Shows the close up view near a columnar grain cluster and IPF. (d) Isometric cut view showing the internal distribution of grains and orientations. (e) 3D iso-surface view plus EBSD slice near a columnar grain cluster.

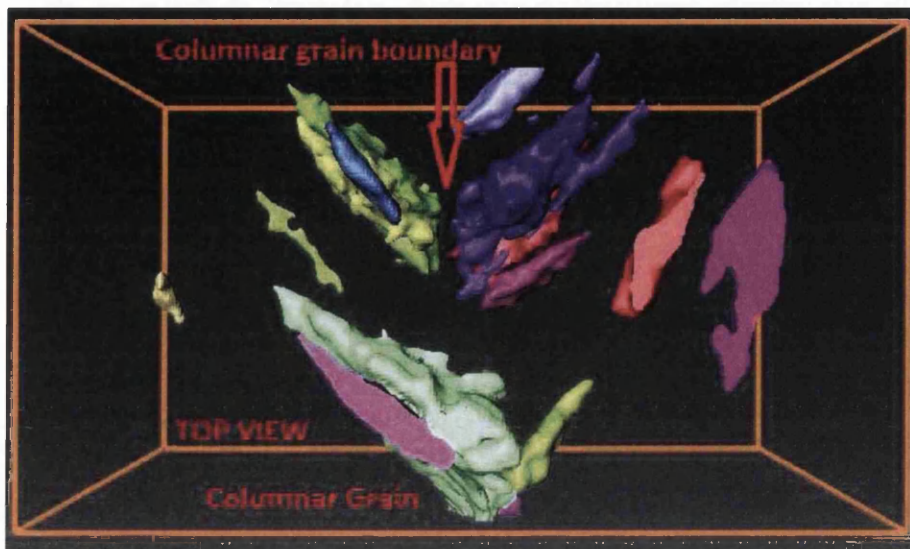


Figure 7.4.2 shows the close up view of a 3D iso-surface of the electrodeposited PP-Ni microstructure near a columnar grain boundary.

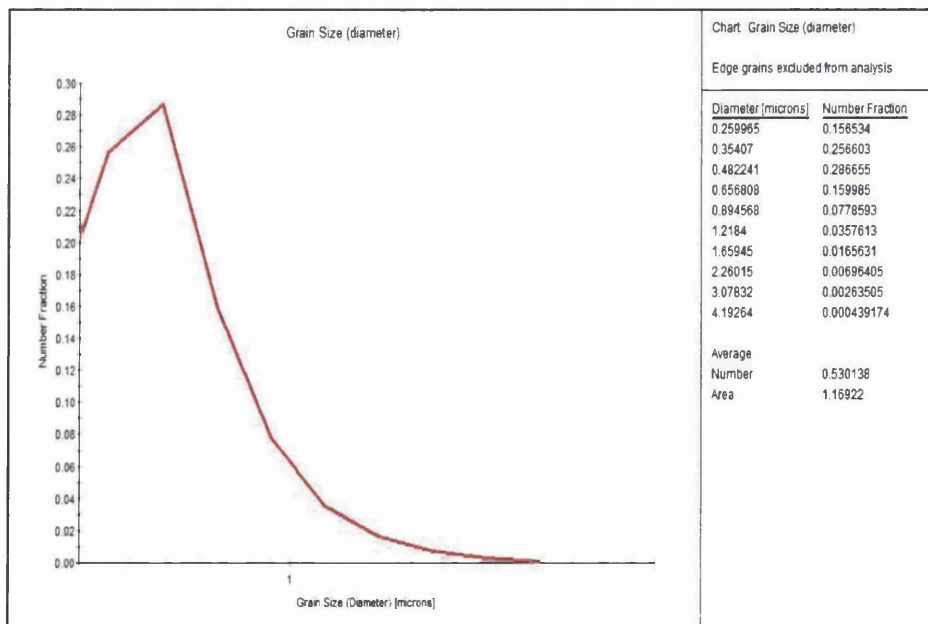


Figure 7.4.3 Grain size distribution of PP-Ni microstructure.

Figure 7.4.1 shows the 3D microstructure of the Ariane-5 combustion chamber electrodeposited PP-Ni from 3D EBSD (80 slices of EBSD results observed every 200nm toward the growth direction and merged using TSL OIM software).

The close up view near a columnar boundary was carefully converted into a 3D iso-surface using Avizo advanced 3D analysis software, figure 7.4.2. This shows that PP-Ni microstructures contain clusters of columnar grains and clusters of ultrafine grains. The grain size distributions and volume fractions of grain boundary were calculated using TSL OIM software. The calculated grain size distributions are plotted in figure 7.4.3. Table 7.4.1 shows the calculated grain boundary volume fraction and average grain size of the PP-Ni. A binary image in the PP-Ni microstructure along the Growth Direction (GD), Normal to the GD (ND) and perpendicular to the growth direction (TD) are shown in figure 7.4.4. The PP-Ni microstructures were observed using SEM along the growth plane and perpendicular to the growth plane (i.e. the TD plane) as shown in figure 7.4.5. This clearly shows that the ultrafine grains clusters are present in elliptical shapes. Cluster of ultrafine grains are observed as dark regions and clusters of coarse grains are observed as lighter region as shown in figure 7.4.6 (a).

EBSD/OIM calculated result	PP-Ni
Volume fraction of GB	0.0429
Average Grain size (nm)	300

Table 7.4.1 Calculated values from EBSD analysis result data.

Figure 7.4.6 shows the EBSD binary scan image observed on the growth plane of PP-Ni and shows elliptical fine grain clusters and an extruded 3D MRVE geometry of the PP-Ni material and a mesh for FE computational hydrogen diffusion analysis. Figure 7.4.7 shows the results of the hydrogen permeation test along the three principal directions. Figure 7.4.8 shows the good agreement between experimental and simulation results of the hydrogen permeation along the growth direction in PP-Ni. Figure 7.4.9 shows the results of the hydrogen permeation along the three principal directions (i.e. growth direction, perpendicular to growth direction and normal to GD). Table 7.4.2 shows the calculated anisotropic diffusivity of hydrogen

along three principal directions. These properties were then implemented in the model of a section of space launcher combustion chamber and compared with the use of effective isotropic hydrogen diffusivities. Figure 7.4.10 and figure 7.4.11 shows the effect of this choice of parameters on two different types of space launcher component. These results highlight the importance of using the correct hydrogen diffusivity values to accurately predict hydrogen embrittlement in aerospace combustion chambers.

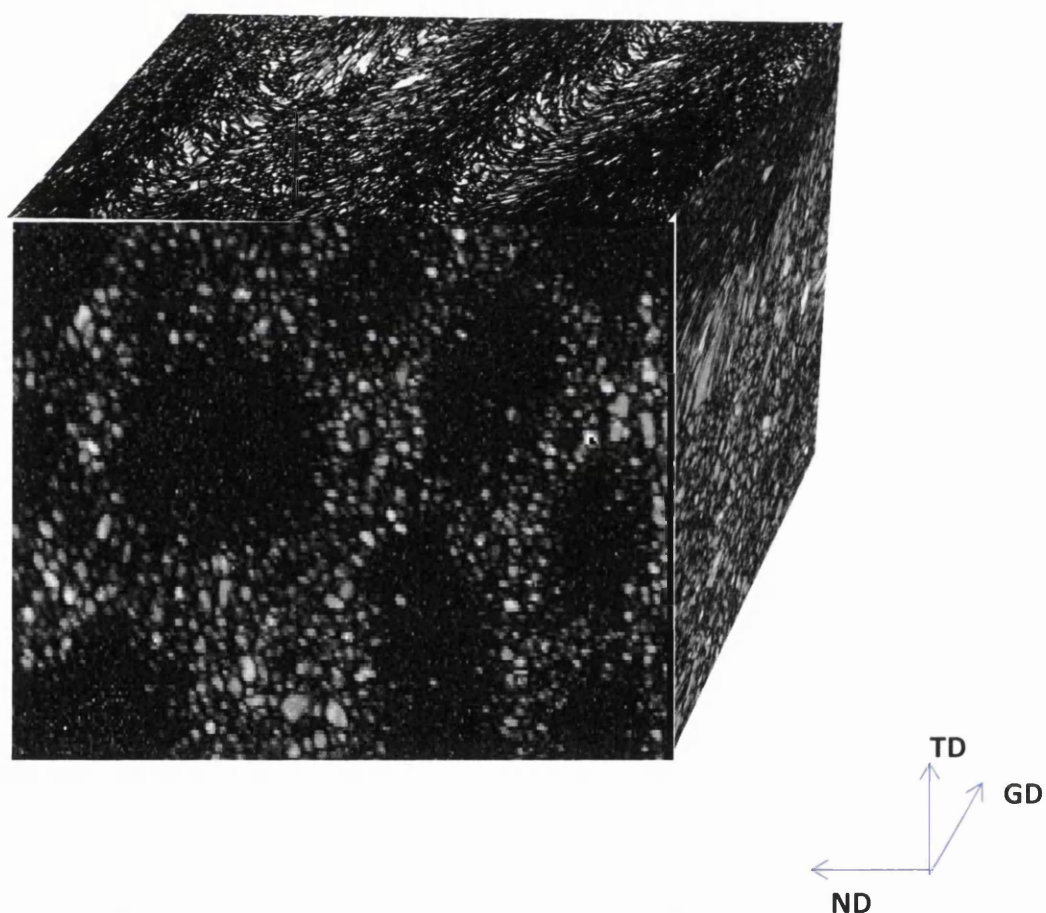


Figure 7.4.4 SEM image shows the PP-Ni microstructure observed on TD plane (i.e. plane perpendicular to growth direction) and on the growth plane.

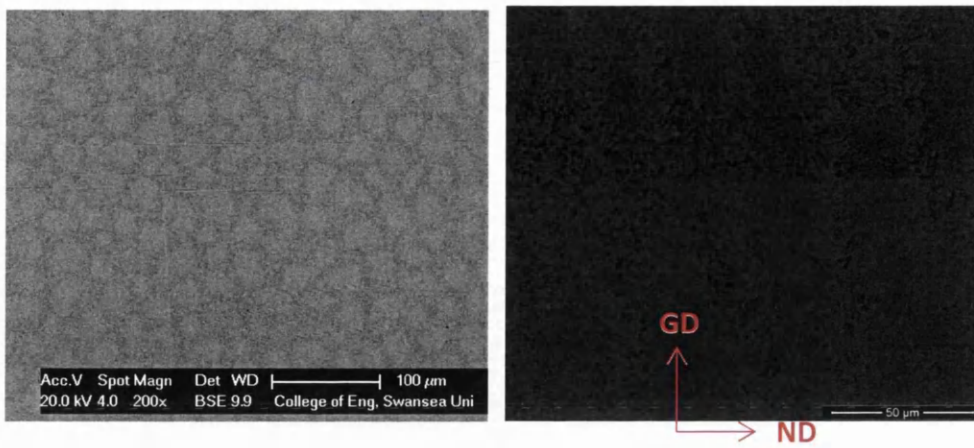


Figure 7.4.5 SEM image shows the PP-Ni microstructure observed on TD plane (i.e. plane perpendicular to growth direction) and on the growth plane.

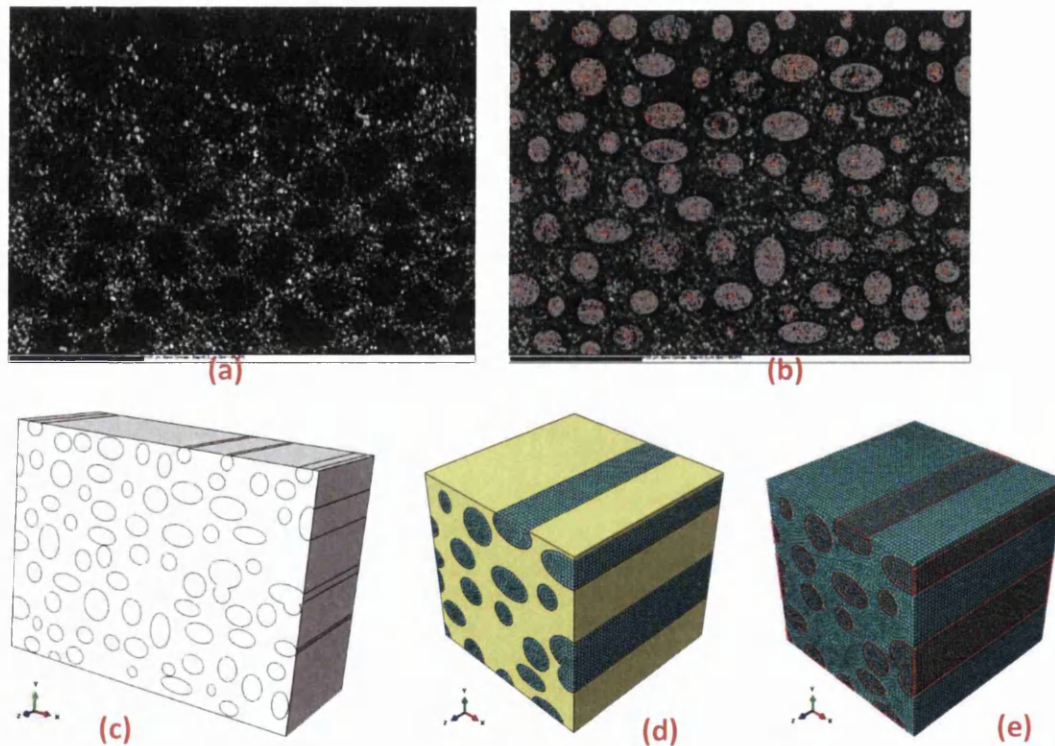


Figure 7.4.6 (a) EBSD binary scan image observed on growth plane of PP-Ni. (b) Elliptical fine grain clusters. (c) - (e) show 3D RVE geometries of PP-Ni with ultrafine grains clusters along the elliptical region and FE mesh.

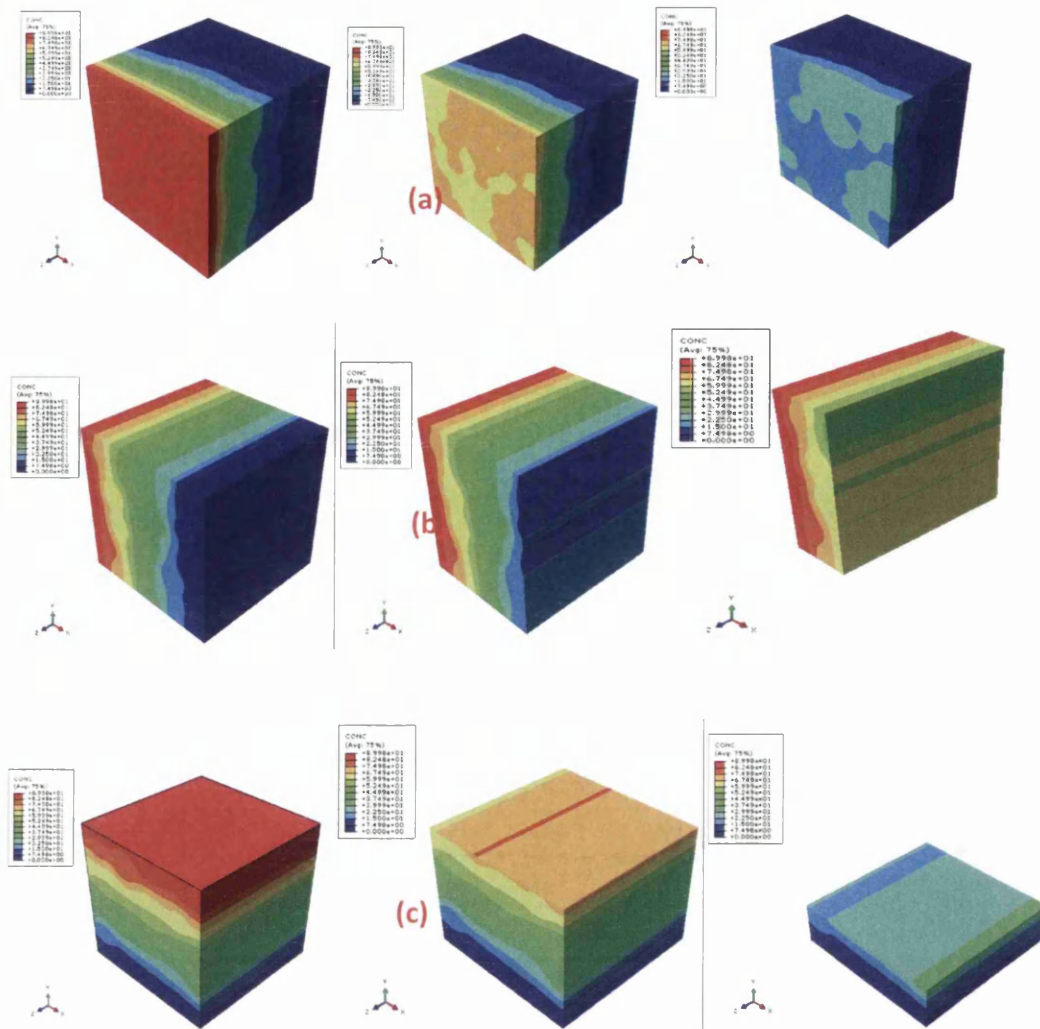


Figure 7.4.7 Results of the simulated hydrogen permeation test in the three principal directions (a) Growth direction (b) Normal to growth direction and (c) Perpendicular to growth direction.

	Experimental results (m ² /s)	FE simulation Results (m ² /s)
Conventional electrodeposited polycrystalline nickel	4.1333×10^{-14}	4.1327×10^{-14}
PP-Ni along GD	4.18287×10^{-13}	5.885×10^{-13}
ND	XX	1.84316×10^{-13}
TD	XX	1.61116×10^{-13}

Table 7.4.2 Calculated anisotropic diffusivity of hydrogen in the three principal directions.

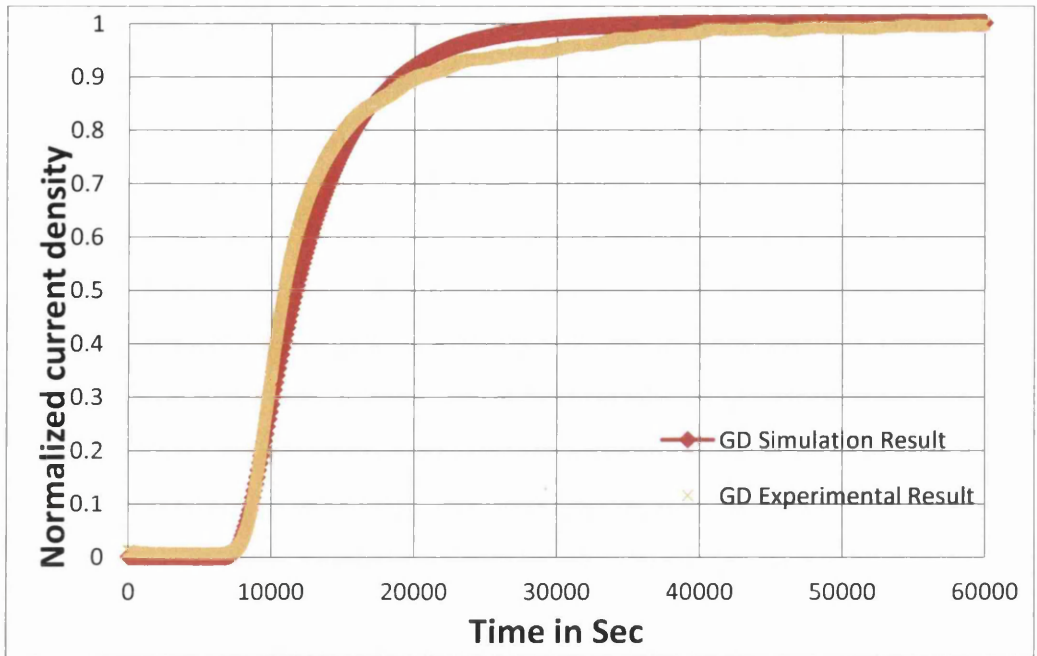


Figure 7.4.8 Experimental and FE simulation results of hydrogen permeation along the growth direction.

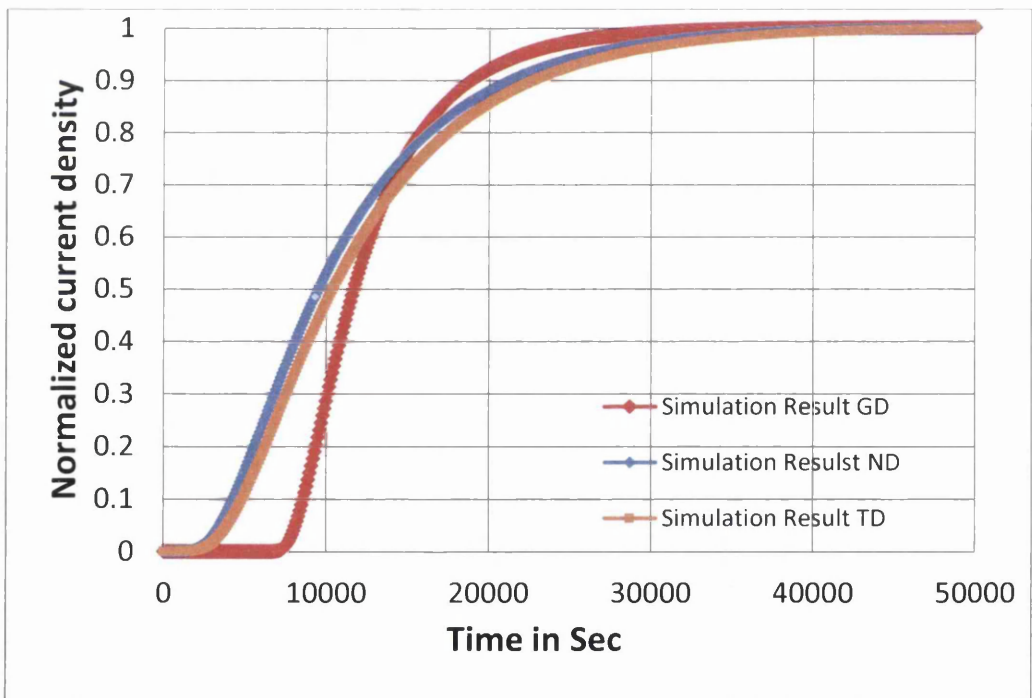
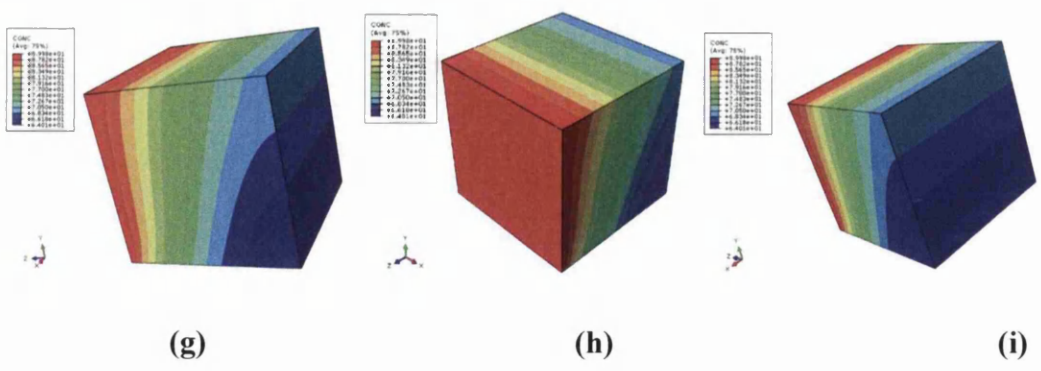
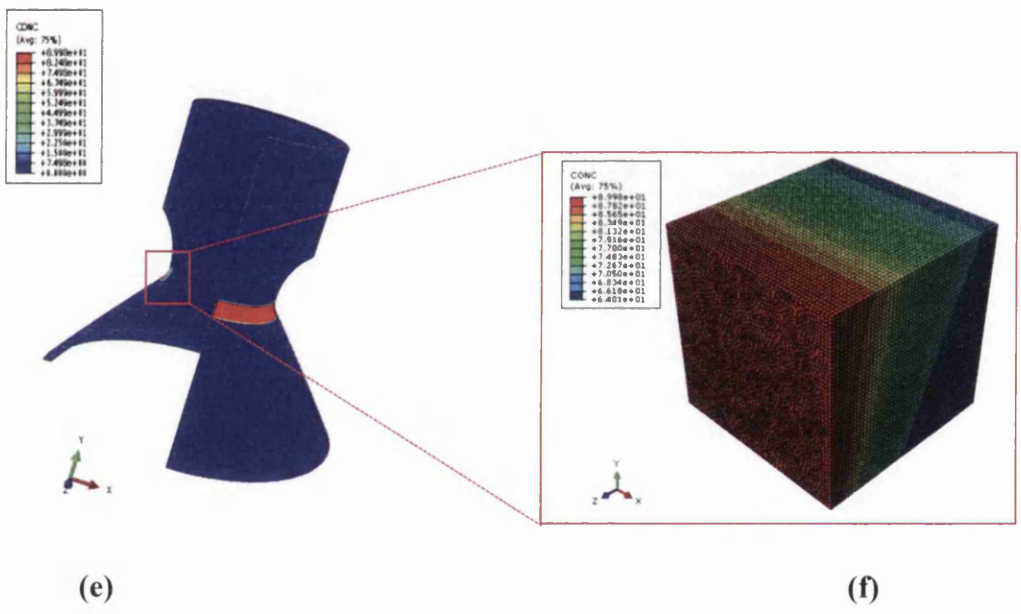
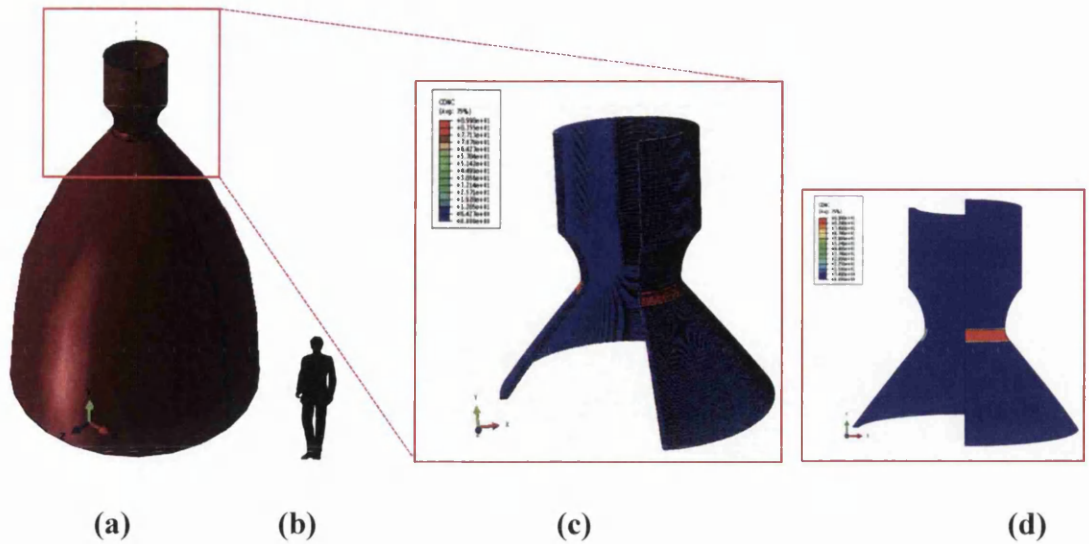


Figure 7.4.9 Results of simulated hydrogen permeation test in the three principal directions (growth direction, normal to growth direction and perpendicular to growth direction.)



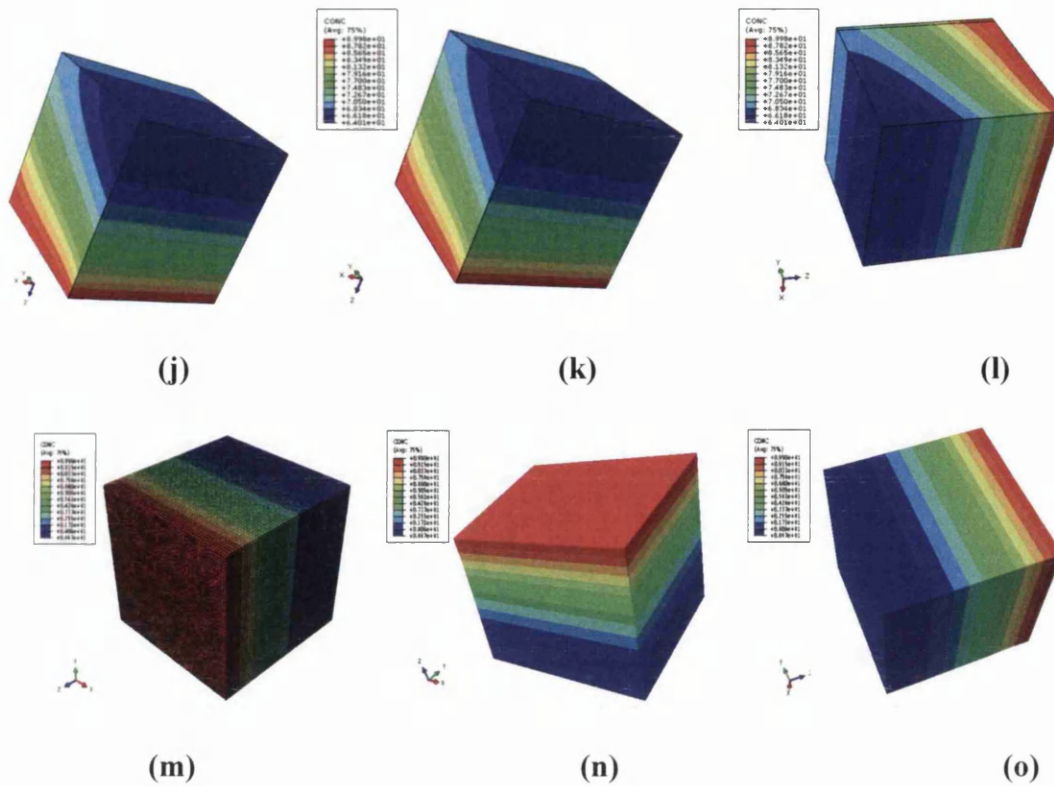
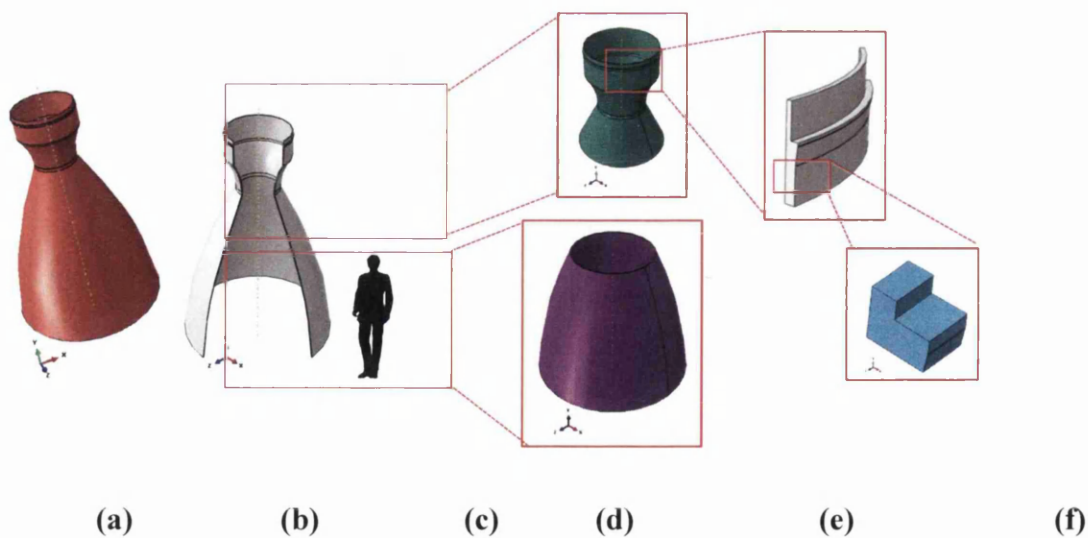


Figure 7.4.10 The effect of isotropic and anisotropic diffusion of in one type of space launcher thrust chamber. (a) The space launcher thrust chamber (i.e. combustion chamber and nozzle). (b) Man standing (to show scale). (c) Anisotropic diffusion of hydrogen on the PP-Ni layer of the thrust chamber section with mesh (d). (e) Anisotropic diffusion of hydrogen on the PP-Ni layer of thrust chamber section without mesh with (f) showing a close up view. (g)-(l) show the close up views of anisotropic diffusion on the section without the mesh. (m) Close up view of isotropic diffusion on the section with mesh. (n) and (o) show the close up views of isotropic diffusion on the section without the mesh. (Time = 13.9hr).



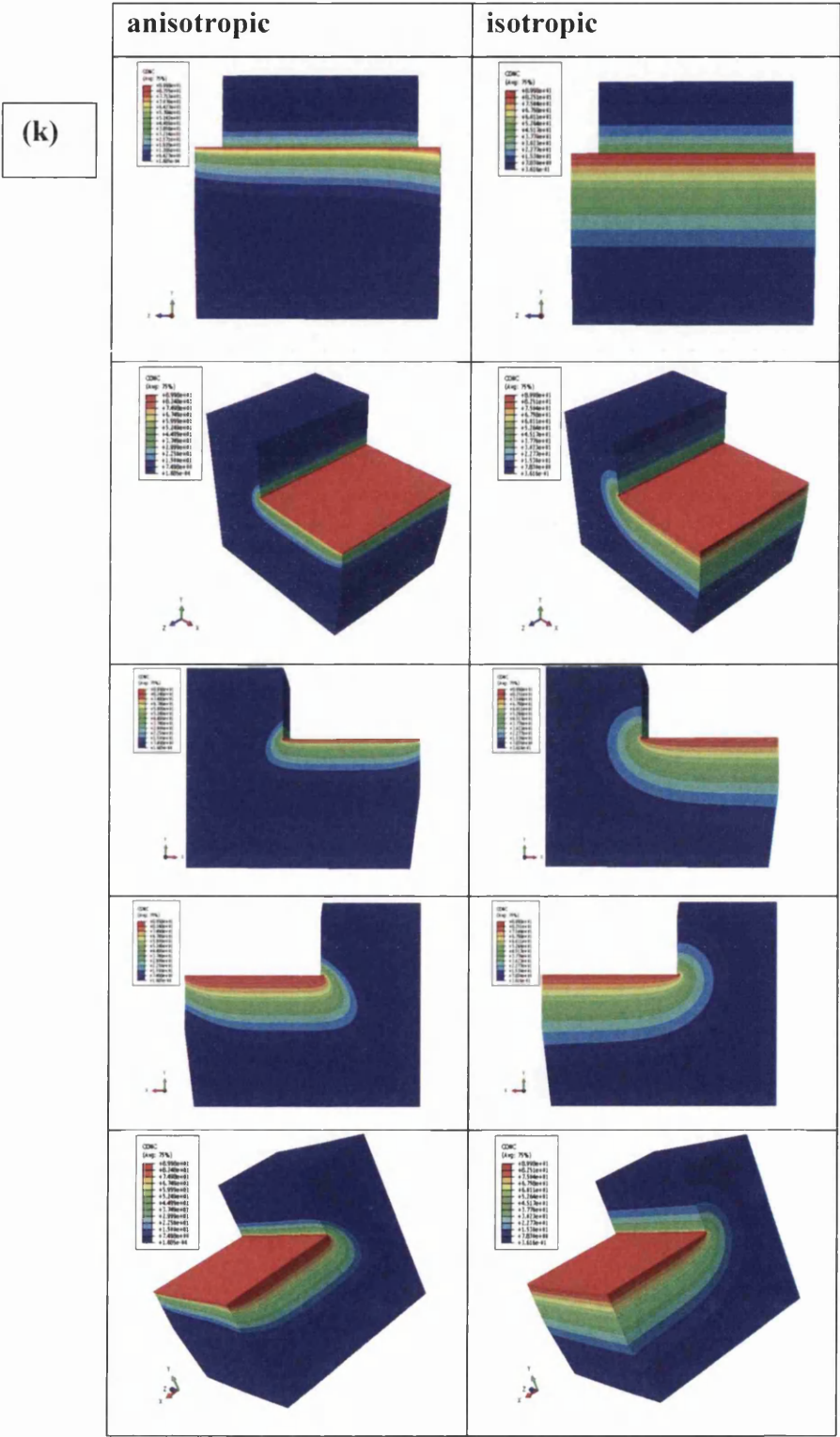
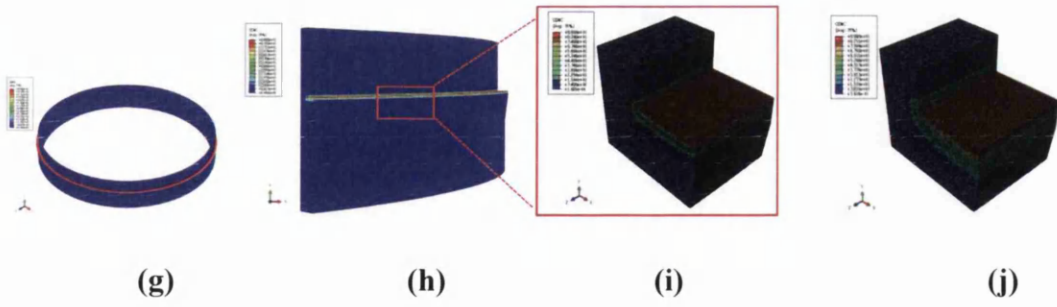


Figure 7.4.11 Effect of isotropic and anisotropic hydrogen diffusion on another type of space launcher thrust chamber. (a) and (b) show the space launcher thrust chamber Type 2 (i.e. combustion chamber and nozzle). (c) Man standing (to show scale). (d)-(f) show sections of the thrust chamber. (g)-(h) Anisotropic diffusion of hydrogen on the PP-Ni layer of the thrust chamber section. (i) Close up view of anisotropic diffusion of hydrogen on the PP-Ni layer in the thrust chamber section, including mesh. (j) Close up view of isotropic diffusion of hydrogen on the PP-Ni layer in the thrust chamber section including mesh. (k) Anisotropic and isotropic diffusion of hydrogen on the PP-Ni layer of thrust chamber section in close up view without the mesh.

7.5 Effect of GB misorientation on hydrogen embrittlement in bi-crystal and polycrystalline nickel

7.5.1 Experimental results

Initially, the bi-crystal model comprises crystal1 and crystal2 separated by a GB and GBAZ. The GBAZ is used to simulate hydrogen diffusion along the GB. The lattice misfit between the crystals accommodates the GB misorientation. The orientation of crystal1 is fixed and the orientation of crystal2 is tilted along the traction direction to form geometric tilt grain boundaries (TGBs) for various misorientation angles 0° , 5° , 15° , 30° , 35° , 40° , 45° , 60° , 75° , 85° and 90° as shown in figure 7.5.1. Next, the polycrystal model comprises 2D polygonal crystals separated by GBs and GBAZs. Similar to the bi-crystal model, the lattice misfit between the crystals accommodates the GB misorientation on the polycrystal model. The orientation of the polygonal crystals in green is fixed and the orientations of the red polygonal crystals (termed grainset1) are tilted along the traction direction to form geometric TGBs for various misorientation angles 0° , 5° , 30° , 45° , 60° , 75° , 85° and 90° as shown in figure 7.5.1 (d).

Initially, the results on the effects of TGB misorientation angle on hydrostatic stress in bi-crystal and polycrystal 2D models are discussed. Figures 7.5.2 (a), (b) and (c) show the calculated microscopic hydrostatic stress (σ_h) normalized by the applied uniform macroscopic stress (σ_0) parallel to the traction direction for various TGB misorientation angles in bi-crystal nickel along the paths x1, x2 and x3 respectively. In figure 7.5.2 the normalized distance at a point is defined as the y-coordinate divided by the total height ($2h$) of the crystal as shown in figure 7.5.1, assuming the origin is at the bottom edge of the bi-crystal. Thus, if the normalized distance at a point is zero then it is at the extreme bottom side of the bi-crystal, a value of 0.5 is the centre of the bi-crystal and a value of 1 is at the top of the bi-crystal along the y-direction, irrespective of the actual width of the crystal. The Path x1 is near the left hand corner of the crystals, path x2 is in the middle of the crystals and path x3 is near the right hand corner of the crystals as shown in figure 7.5.1 (a). The path x1 is plotted along the blue arrow line on the surface of bi-crystal nickel as shown in figure 7.5.2 (a) in order to understand the influence of the boundary on

various misorientation angles. The path x2 is plotted along the blue arrow line on the surface of bi-crystal nickel as shown in figure 7.5.2 (b) (i.e. middle of the nickel bi-crystal) in order to investigate the influence of misorientation angles under externally applied stress conditions at a region away from the boundary conditions which are applied at the left hand side of the mesh along path x1. Similarly, path x3 is plotted along the blue arrow line on the surface of bi-crystal nickel as shown in figure 7.5.2 (c) (i.e. the side of the mesh opposite to path x1) in order to investigate the influence of misorientation angle on the hydrostatic stress developed under externally applied stresses away from the boundary conditions applied at the left hand side of the mesh along path x1 and to investigate the variation of the developed hydrostatic stresses inside the crystal and grain boundary due to the deformation constraint caused by the adjacent crystal misorientation. The computed results in figure 7.5.2 show the hydrostatic stress distribution is uniform and homogenous for TGB misorientations 0° and 90° for each path. In contrast the hydrostatic stress distribution tends to be heterogeneous and non-uniform between the crystals for TGB misorientation angles of 15° , 30° , 35° , 40° , 45° , 60° and 75° (i.e. orientations $> 0^\circ$ and $< 90^\circ$).

Figure 7.5.2 (a) shows the influence of misorientation angles on hydrostatic stress along the path x1. The path x1 is plotted in order to understand the influence of the boundary on various misorientation angles. The normalized hydrostatic stress distribution between the crystals tends to be smaller near the traction side and increase moving towards the TGB attaining a maximum value close to the TGB along path x1 for misorientations between 15° and 45° . In reality, as opposed to the numerical model, the difference in the mechanical elastic properties of crystal1 and crystal2 due to misorientation would affect dislocations near the TGB due to the applied load. Varying hydrostatic stresses along the TGB and near to the TGB arise depending on the misorientation angles. The maximum accumulated local hydrostatic stress values on the TGB are tensile and are 80% of the applied uniform tensile stress for a misorientation angle of 30° . For misorientation angles greater than 45° and less than 90° the hydrostatic stress values between the crystals starts to decrease along the path x1 when moving from the traction side towards the TGB reaching a minimum close to the TGB. The minimum local accumulated hydrostatic stress values on the boundary are compressive with the highest normalized

compressive stresses less than 20% of the normalized stresses observed in the model with a misorientation of 60° .

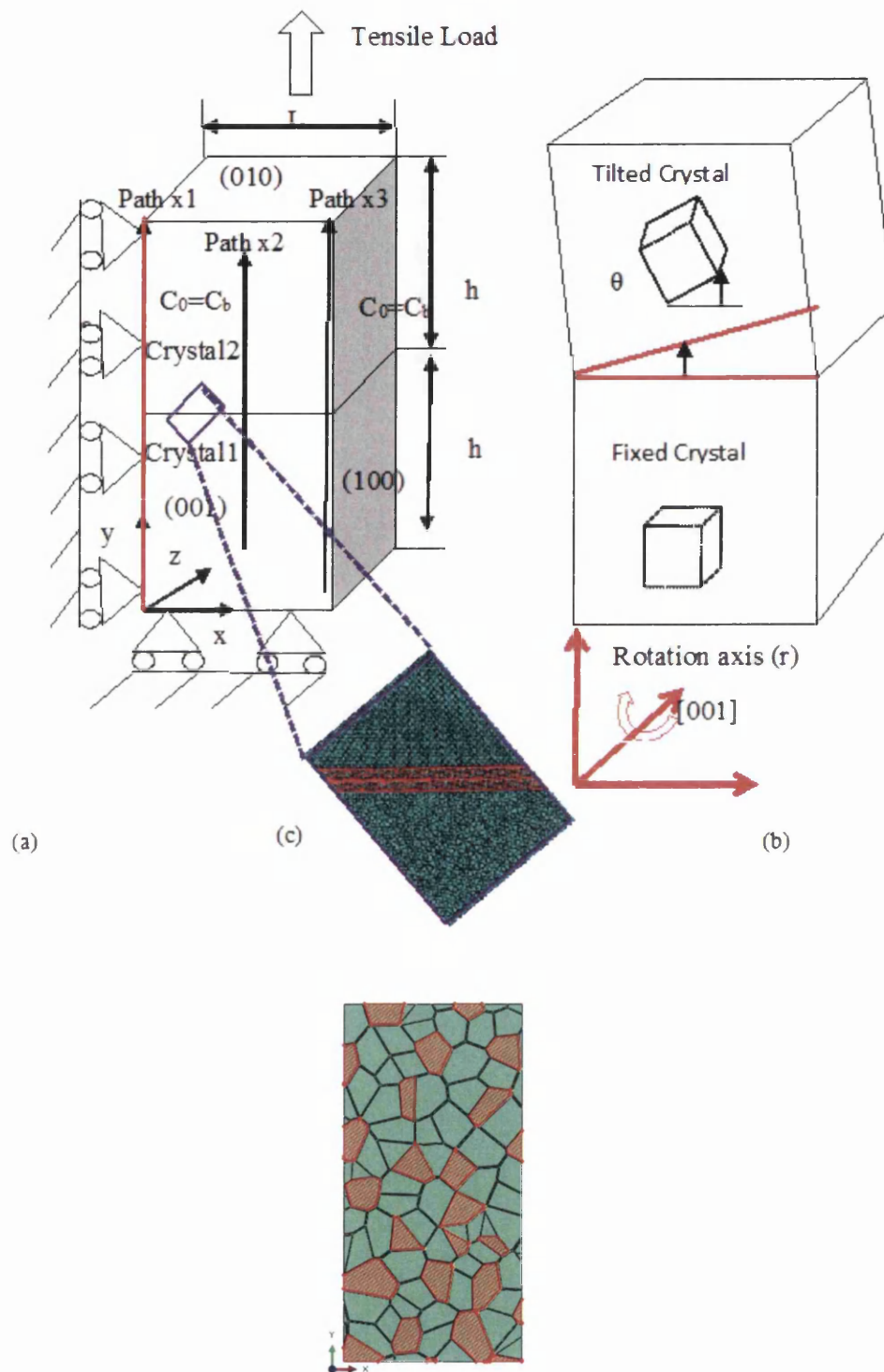


Figure 7.5.1 (a) Geometry and boundary conditions of the Bi-Crystal model and paths x1, x2 and x3 along the traction direction. (b) TGB based on fixed and tilted crystal to form various misorientation angles (θ) (0° , 5° , 15° , 30° , 35° , 45° , 60° , 75° , 85° , 90°) to the rotation axis [001]. (c) Close-up view of FE mesh of crystal (blue) and grain boundary affected zone (red). (d) shows the polycrystal model and the set misorientation grains (red) and fixed grains (green).

The compressive stresses are due to the effects of boundary and misorientation angle. *These results show that the localized hydrostatic stress concentrations inside the crystals and near to the TGB are governed primarily by the TGB misorientation.*

Figure 7.5.2 (b) shows the normalised hydrostatic stress distribution between the crystals and TGB along the path x2 for various misorientation angles. Path x2 was plotted along the blue arrow line on the surface of bi-crystal nickel as shown in figure 7.5.2 (b) (i.e. middle of the nickel bi-crystal). The path x2 results are plotted in order to understand the influence of misorientation angles on hydrostatic stresses without the effects of boundaries. The maximum normalized hydrostatic stress value is observed on the fixed crystal near to the TGB for misorientation angle 45° and the minimum normalized hydrostatic stress value is observed near to the TGB on the tilted crystal of the bi-crystal model with 45° misorientation angle. The minimum hydrostatic stress value is observed on the crystal1 near to the TGB with misorientation angle 75° and the maximum hydrostatic stress value is observed on the crystal2 near the TGB of the model with misorientation angle 15° . *The highest accumulation of hydrostatic stress concentrations are near to the TGB on the fixed crystal (i.e. Crystal1) and lowest values of local hydrostatic stress concentrations are observed near to the TGB on the rotated crystal (i.e. crystal2) along path x2.*

Figure 7.5.2 (c) shows the normalised hydrostatic stress distribution between the crystals and boundary along the path x3 for various TGB misorientations. Higher stress gradients are observed near the GB. *Low values of localized hydrostatic stress concentration are observed near the boundary on the fixed crystal and high values of localized hydrostatic stress concentration are observed near the boundary on the tilted crystal.* The minimum localized hydrostatic stress values are observed on the fixed crystal near the boundary for misorientation angles 30° and 35° and the maximum localized hydrostatic stress value is observed in crystal2 along the TGB of misorientation angle 60° . However, the difference between the maximum and minimum values of localized hydrostatic stress concentration along the TGB are observed to be highest for the misorientation angles of 45° and 40° and the lowest differences are observed for misorientation angles of 15° and 75° .

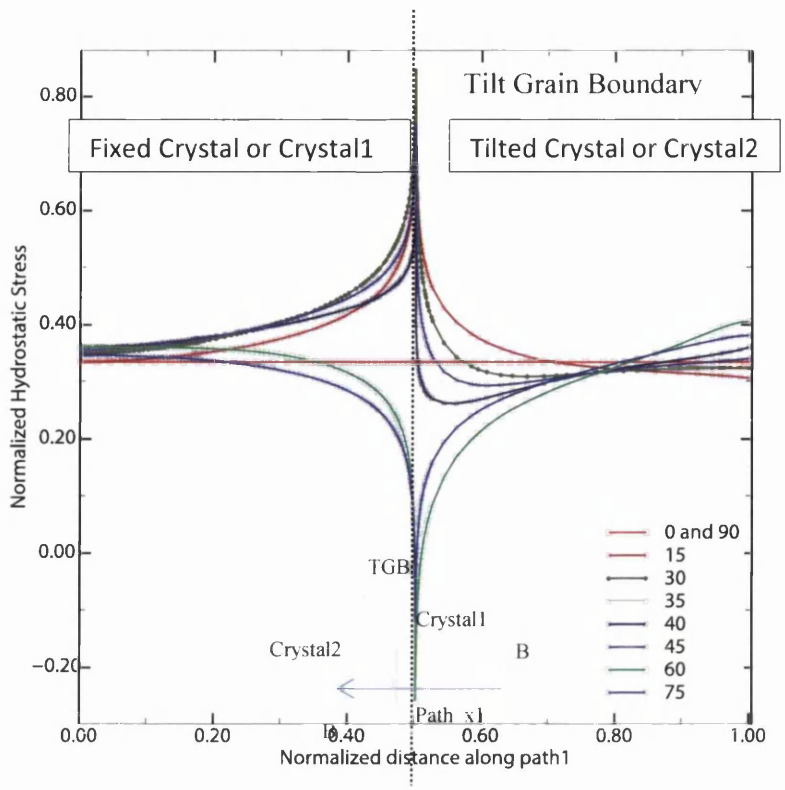


Figure 7.5.2 (a) Normalized hydrostatic stress (σ_H/σ_0) due to the boundary effect along the normalized path x1 (y/h) parallel to the traction direction for various misorientation angles in degrees.

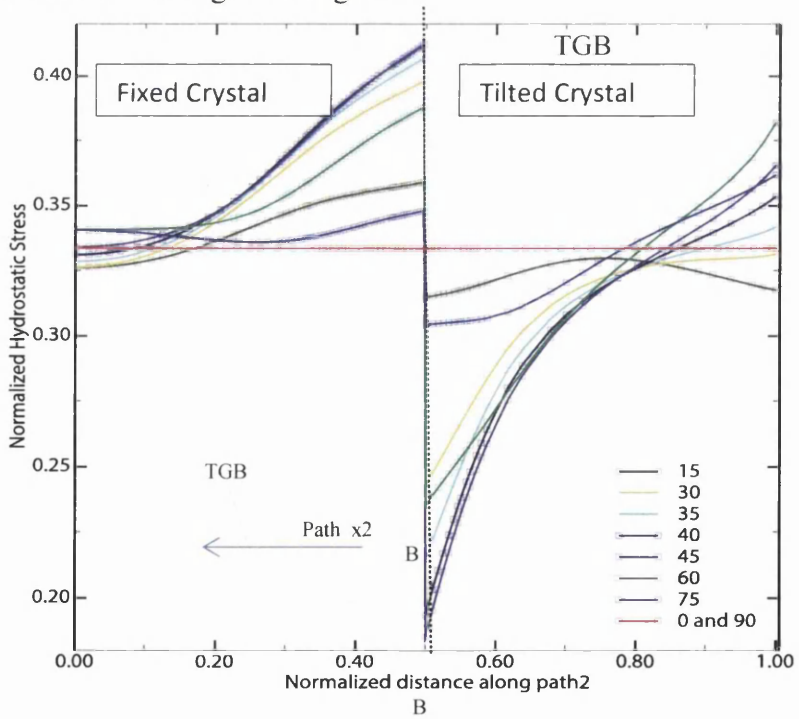


Figure 7.5.2 (b) Normalized hydrostatic pressure (σ_H/σ_0) along the normalized path x2 (y/h) parallel to the traction direction for various misorientation angles in degrees.

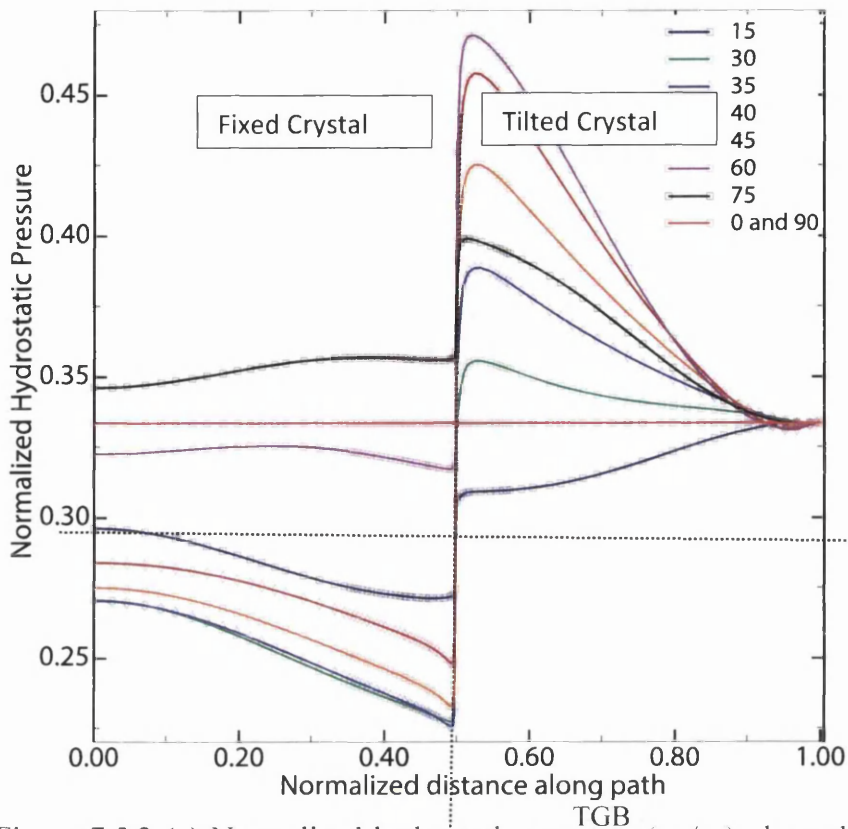
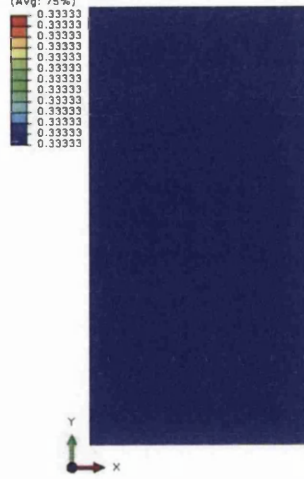


Figure 7.5.2 (c) Normalized hydrostatic pressure (σ_H/σ_0) along the normalized path $x_3 (y/h)$ parallel to the traction direction for various misorientation angles in degrees.

On the other hand, the computational results of the polycrystal model for various GB misorientations are shown in figure 7.5.3. Figure 7.5.3 shows the calculated microscopic hydrostatic stress (σ_h) normalized by the applied uniform macroscopic stress (σ_0) for various TGB misorientation angles in polycrystal model. It shows that the microscopic hydrostatic stresses are distributed heterogeneously for uniformly applied stress. The high and low concentrations of hydrostatic stress are observed along grain boundary and triple junctions and they vary depending on GB misorientations.

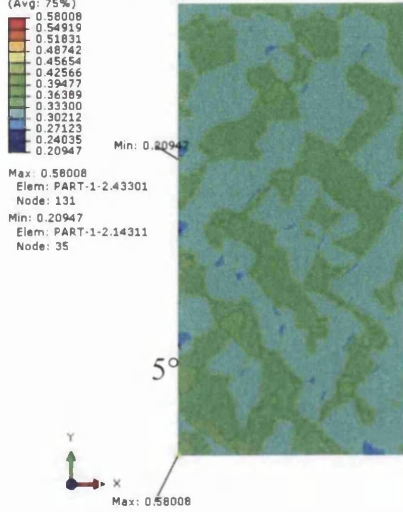
Figure 7.5.4 (a) and (b) show the normalized hydrostatic stress distribution along the path near to the tilt boundary on the GBAZ of crystal1 (fixed crystal) and crystal2 (tilted crystal) perpendicular to the traction direction for various TGB misorientation angles. This shows the influence of TGB misorientation angles due to applied boundary conditions.

Normalized Hydrostatic, Pressure



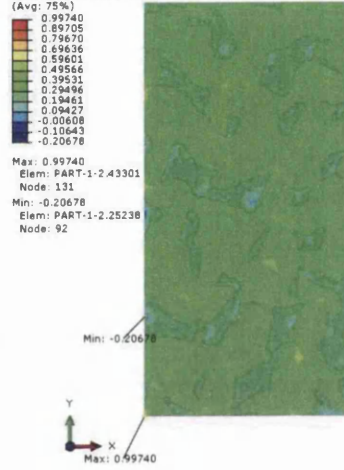
0°

Normalized Hydrostatic Stress, Pressure



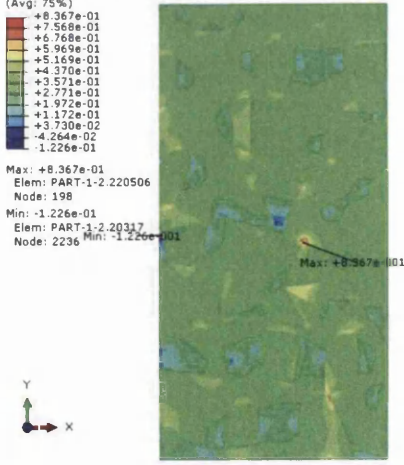
5°

Normalized Hydrostatic, Pressure



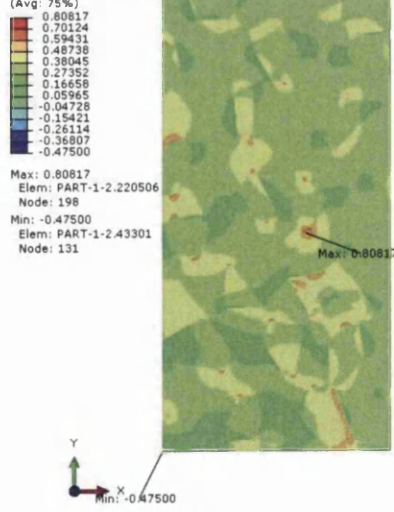
30°

Normalized Hydrostatic, Pressure



45°

Normalized Hydrostatic, Pressure



60°

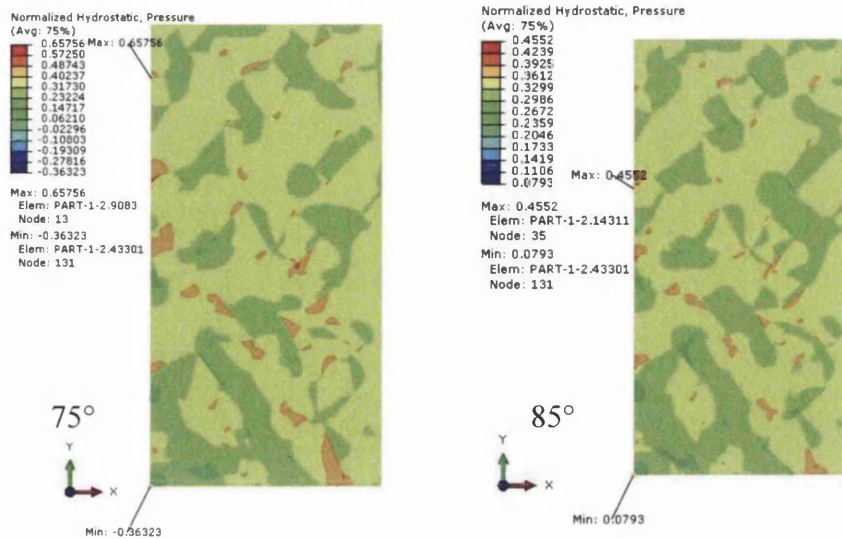


Figure 7.5.3 All other figures show the normalized hydrostatic stress for misorientations of 0°, 5°, 30°, 45°, 60°, 75° and 85°.

The normalized hydrostatic stresses accumulated near to the tilt boundary of crystal1 and crystal2 for misorientation angles in the range $0^\circ < \theta < 45^\circ$ are in the form of tensile stresses with values higher than those obtained with misorientation angles of 0° and 90° . The normalized hydrostatic stress accumulated near the tilt boundary on the left hand side of crystal1 and crystal2 for a misorientation angle 85° are in the form of tensile stresses with (i) lower values than those obtained with misorientation angles 0° and 90° and (ii) higher values on the right hand side of crystal1 and crystal2 (but still < 0.4). The normalized hydrostatic stresses accumulated near the tilt boundary on the left side of crystal1 and crystal2 for GB misorientation angles $45^\circ < \theta < 85^\circ$ are in the form of compressive stresses due to the applied boundary condition whereas the right side of crystal1 and crystal2 are in the form of tensile stresses, these tensile normalized hydrostatic stresses values are not higher than 0.5. *These results show that the areas closest to the left corner of the tilt boundary are accumulating both the tensile and compressive localized hydrostatic stress concentrations due to the effect of the applied boundary condition. Thus applied boundary conditions with the deformation constrained by the neighbouring crystal orientations also play an important role in stress*

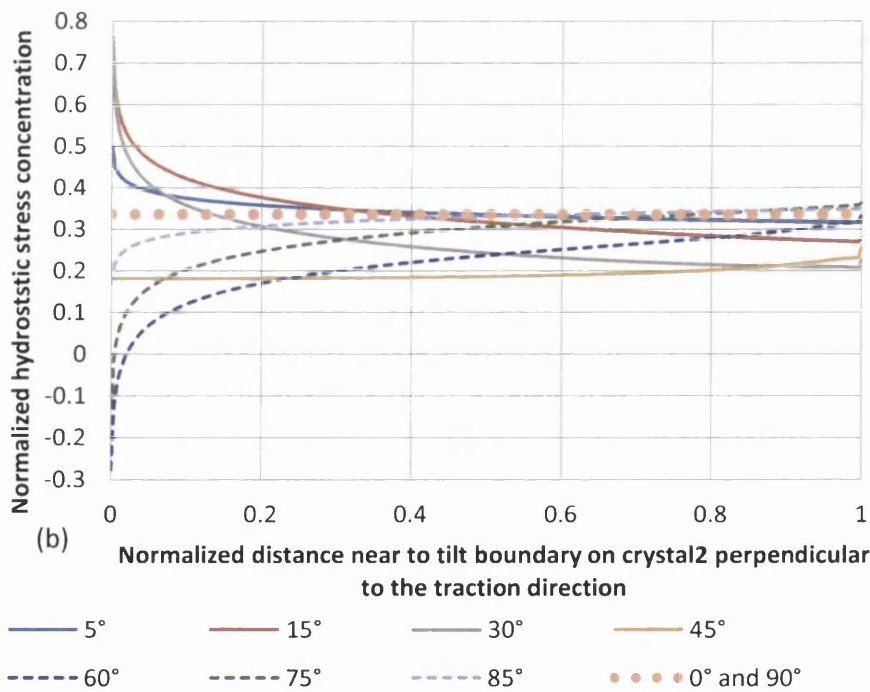
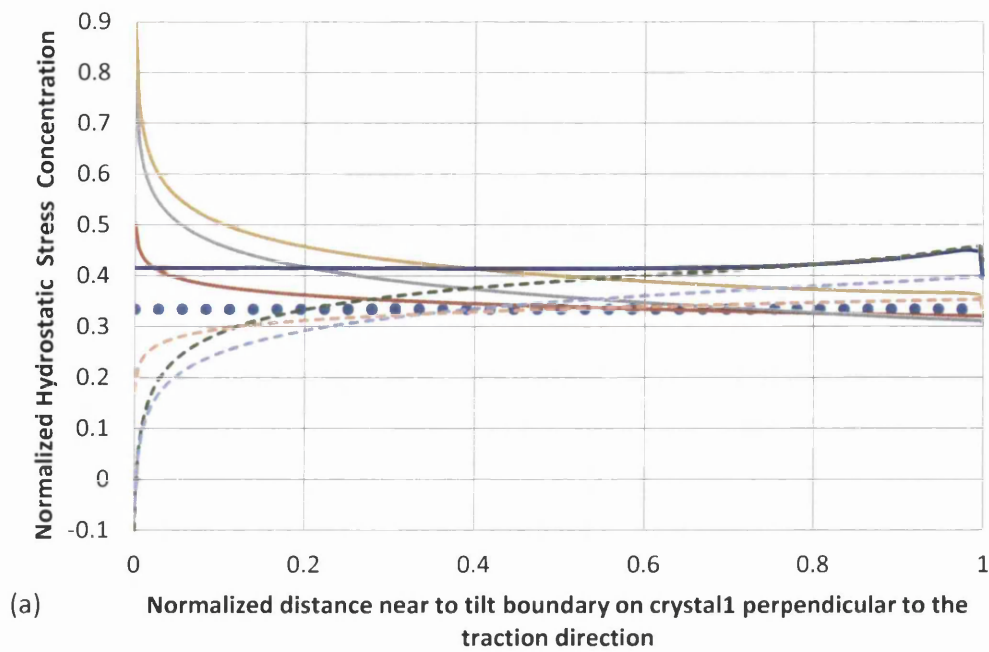
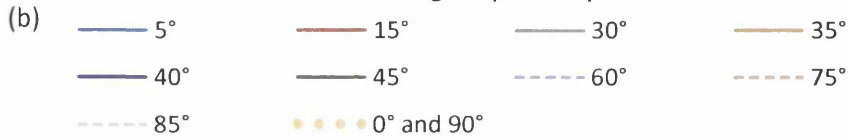
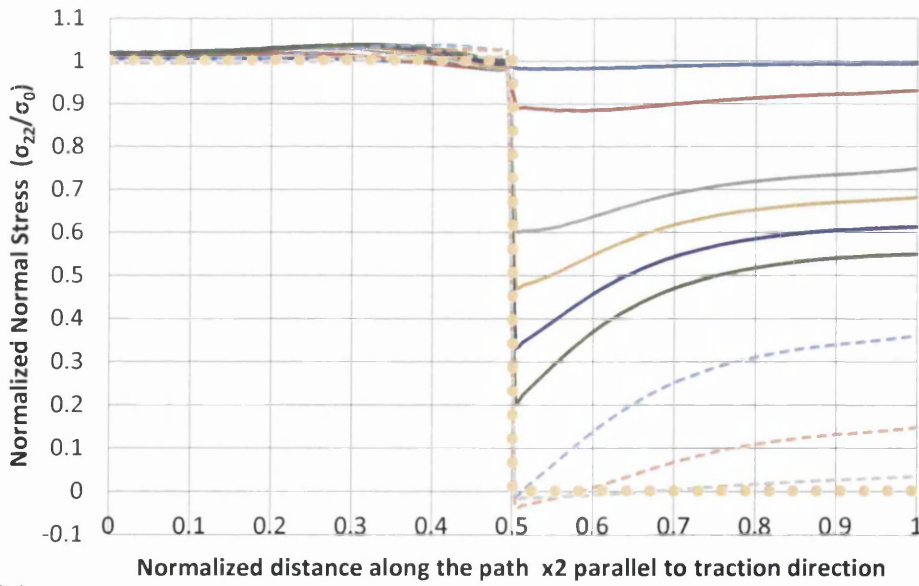
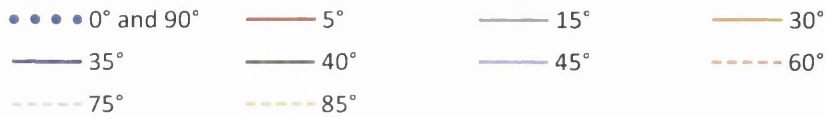
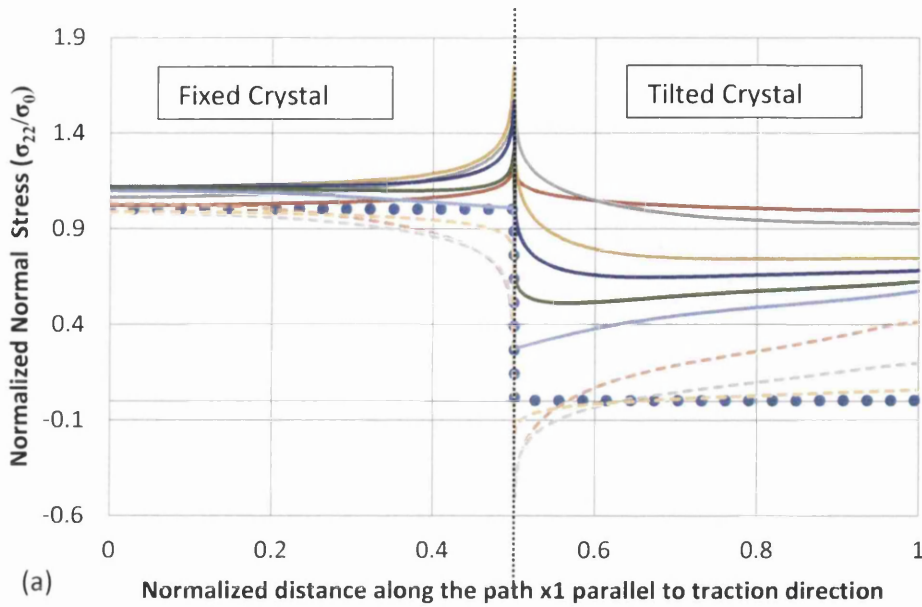


Figure 7.5.4 (a) Normalized hydrostatic stress concentration (σ_H/σ_0) along the normalized path on the GBAZ on the fixed crystal perpendicular to the traction direction for various misorientation angles. (b) Normalized hydrostatic stress concentration (σ_H/σ_0) along the normalized path on GBAZ on crystal2 perpendicular to the traction direction for various misorientation angles.

distributions related to TGB misorientation angle. These results also suggest that the generated hydrostatic stresses are low on misorientation angles $45^\circ < \theta < 90^\circ$ when compared to misorientation angles $0^\circ < \theta < 45^\circ$. The misorientation angles ranging between $45^\circ < \theta < 85^\circ$ generate compressive stresses which may increase resistance to hydrogen embrittlement as explained by Takakuwa al, [212]. The highest normalized hydrostatic tensile stress with a value of 0.9 is found in crystal1 (fixed crystal) for the TGB misorientation angle 30° and the highest normalized hydrostatic compressive stress with a value of -0.3 is found in crystal2 (tilted crystal) for the misorientation angle 60° .

Figures 7.5.5 (a), (b) and (c) show the results of microscopic normal stress (σ_{22}) normalized by the applied uniform macroscopic stress (σ_0) parallel to the traction direction along the paths x1, x2 and x3 respectively for various TGB misorientation angles in bi-crystal nickel. The high and low normalized normal stresses accumulate near the tilt boundary. The highest tensile stress with a value of 1.9 is found on the left hand side of the crystals near the tilt boundary with misorientation angle 30° . The highest compressive stress is found on the left hand side of the crystals near the tilt boundary with a value of -0.6. The left hand region in the bi-crystal model, near the tilt boundary, is where the highest normalized normal stresses are found for TGB misorientation angles $0^\circ < \theta < 45^\circ$ while the lowest normalized normal stresses are found for TGB misorientation angles $45^\circ < \theta < 90^\circ$. The right hand side of the bi-crystal model near the tilt boundary is where the highest and lowest normalized normal stresses are found for TGB misorientation angles $45^\circ < \theta < 90^\circ$. Figure 7.5.6 shows the results of microscopic normal stress normalised by the applied uniform macroscopic stress for various TGB misorientation angles in polycrystal nickel. *These results suggest that the tensile, compressive and highest/lowest values of normal stresses accumulate near the tilt boundary with values dependent on TGB misorientation angles. Since hydrostatic stress depends on the normal stress, then highest and lowest tensile and compressive hydrostatic stresses accumulate near the tilt boundary with values also dependent on misorientation angle. Thus stress gradients near TGBs are dependent on misorientation angles.*

Figure 7.5.7 shows the maximum local normal stress, maximum hydrostatic stress and maximum von Mises stress normalized by the applied uniform



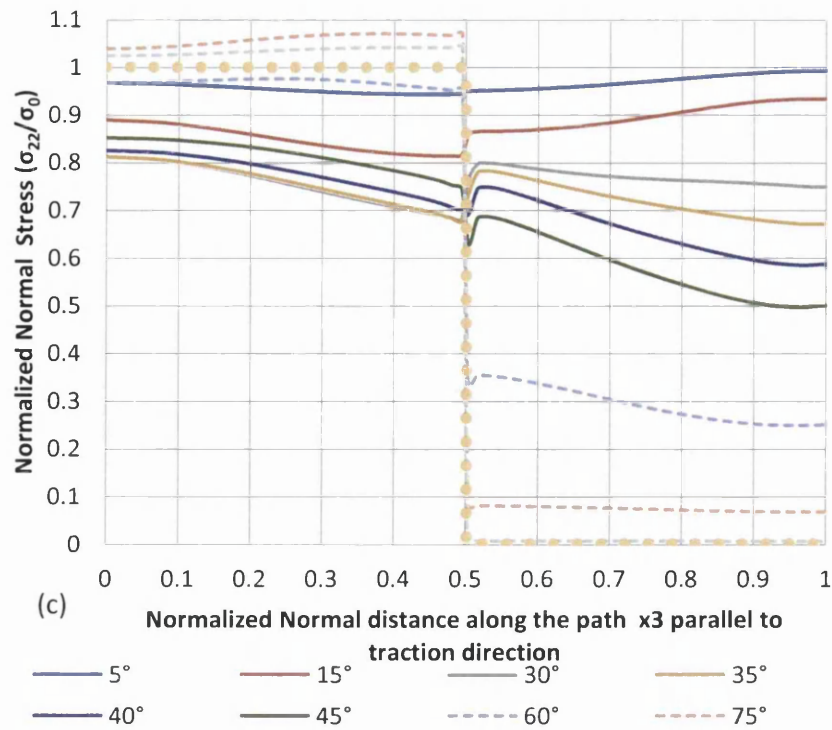
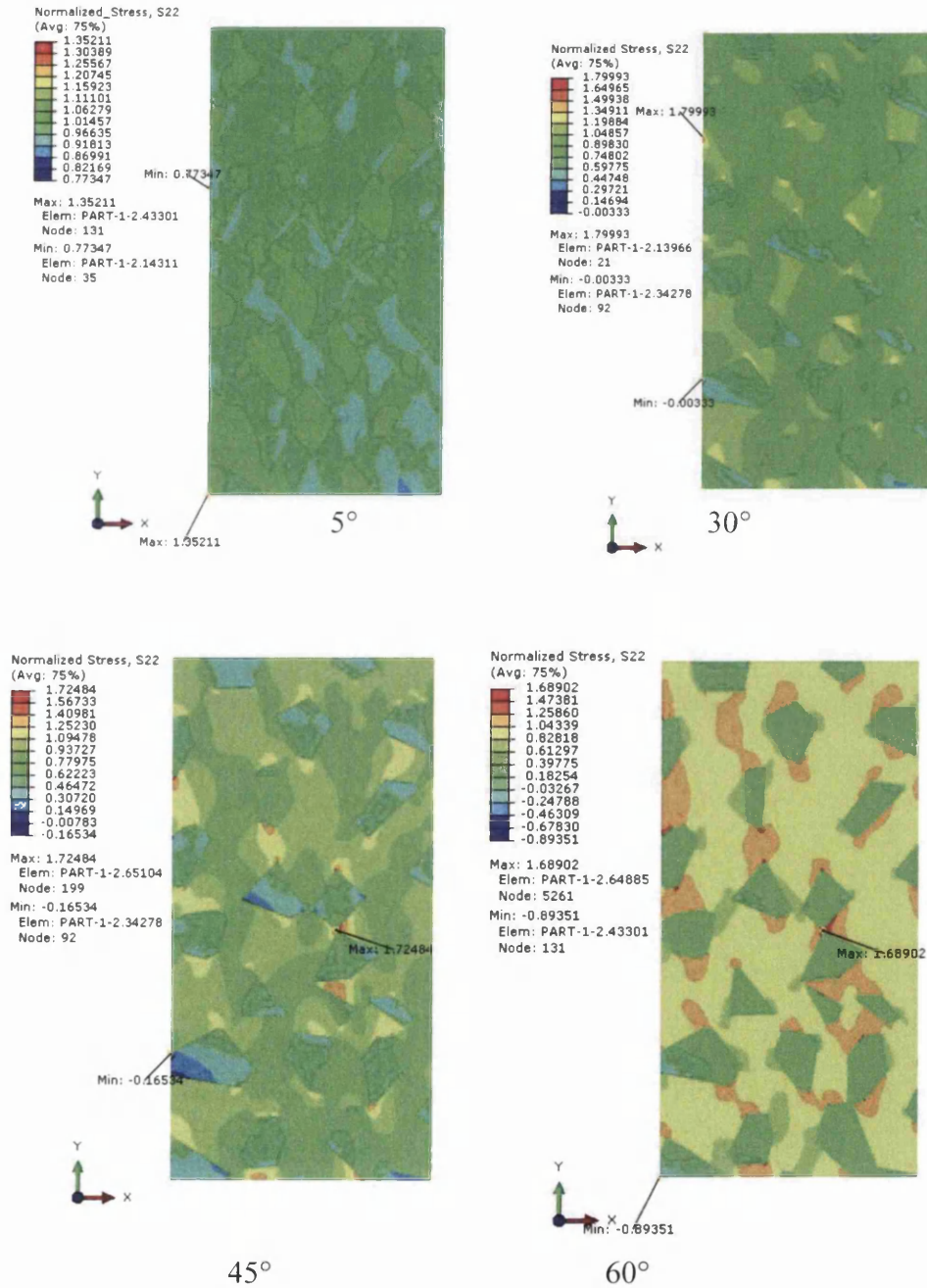


Figure 7.5.5 (a) Normalized normal stress concentration (σ_{22}/σ_0) along the normalized path x_1 parallel to the traction direction for various misorientation angles. (b) Normalized normal stress concentration (σ_{22}/σ_0) along the normalized path x_2 parallel to the traction direction for various misorientation angles. (c) Normalized normal stress concentration (σ_{22}/σ_0) along the normalized path x_3 parallel to the traction direction for various misorientation angles.

macroscopic stress for various TGB misorientation angles in bi-crystal nickel. The values of the maximum normalized normal stress and the maximum normalized von Mises stress vary approximately in the range 1 – 1.8 for various TGB misorientation angles. The values are 1.0 for TGB misorientations 0° and 90° due to zero dilatational mismatches produced along the TGB. Values greater than 1.0 are for misorientation angles $0^\circ < \theta < 90^\circ$ with high magnitudes of stress observed for misorientation angles $15^\circ < \theta < 45^\circ$. High stresses appear near GBs. Figure 7.5.8 (a), (b) and (c) show the local shear strain (ϵ_{12}) normalized by applied strain ($\epsilon_0 = L_0/L$) along the paths x_1 , x_2 and x_3 parallel to the traction direction for various TGB misorientation angles. The magnitudes of shear stress appear low in the fixed crystal and high in the tilted crystal. The shear strain jumps from lower to higher values near the TGB with the highest shear strain appearing along the TGB. Figure 7.5.9 shows the maximum local normal stress and maximum hydrostatic stress normalized by the applied uniform macroscopic stress for various TGB misorientation angles in polycrystalline nickel. *These results suggest that the local stress and strain*

distribution in the nickel bi-crystal case are governed primarily by the TGB misorientation angles.

Next the effects of GB misorientation on hydrogen distribution in the bi-crystal and polycrystal simulation results are discussed. Figure 7.5.10 shows the normalized hydrogen concentration along the normalized path x1 parallel to the traction direction for various TGB misorientation angles in bi-crystal nickel. The figure shows higher hydrogen concentration gradients along the TGB.



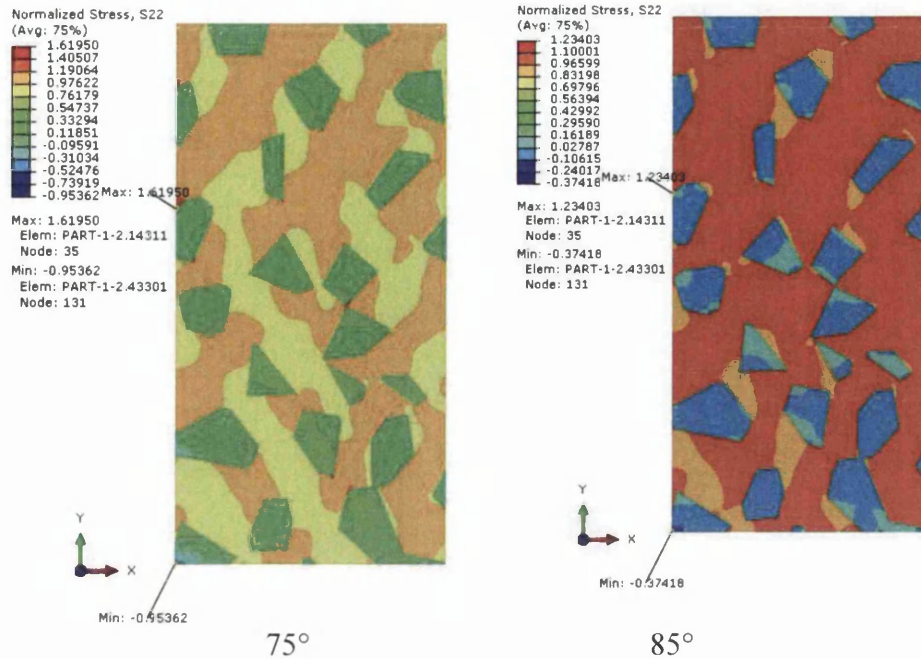


Figure 7.5.6 Normalized normal stress for various orientations of grainset1 rotated along loading direction by 5°, 30°, 40°, 45°, 60°, 75°, 85°.

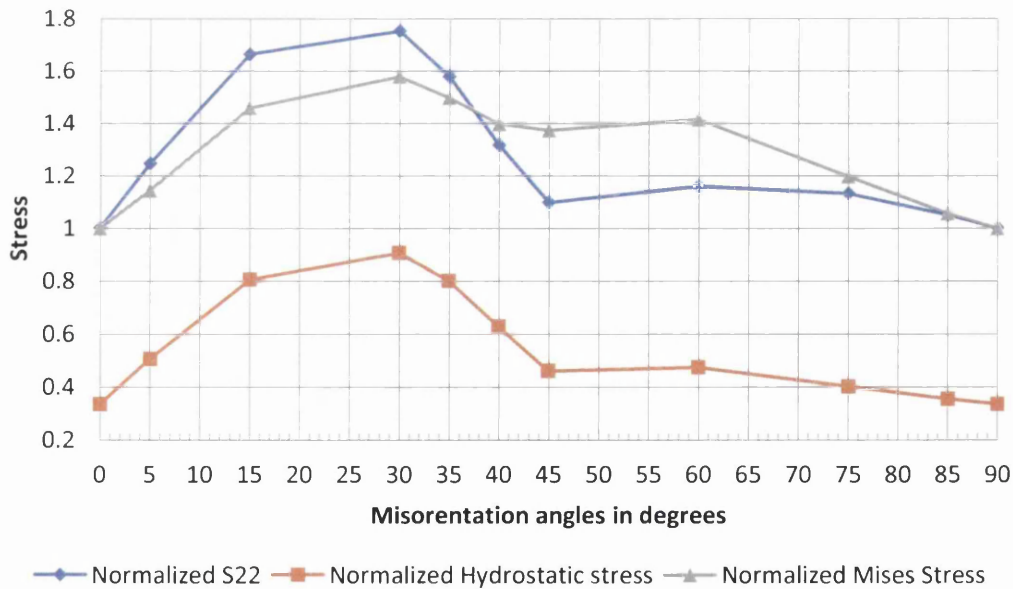
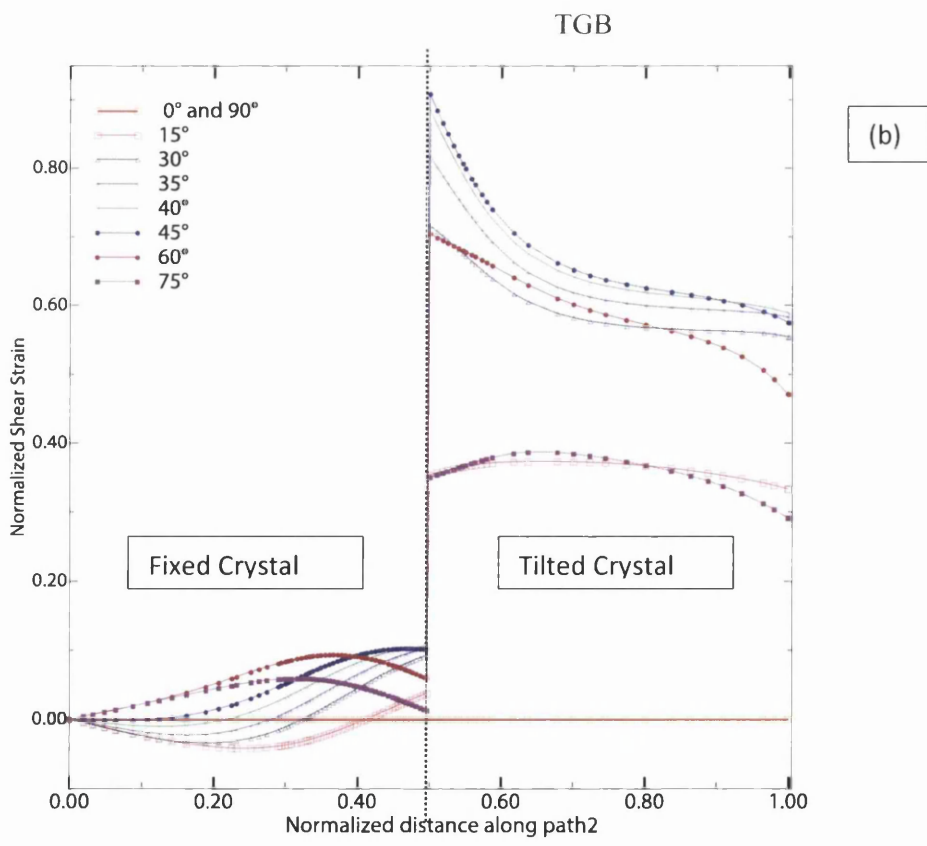
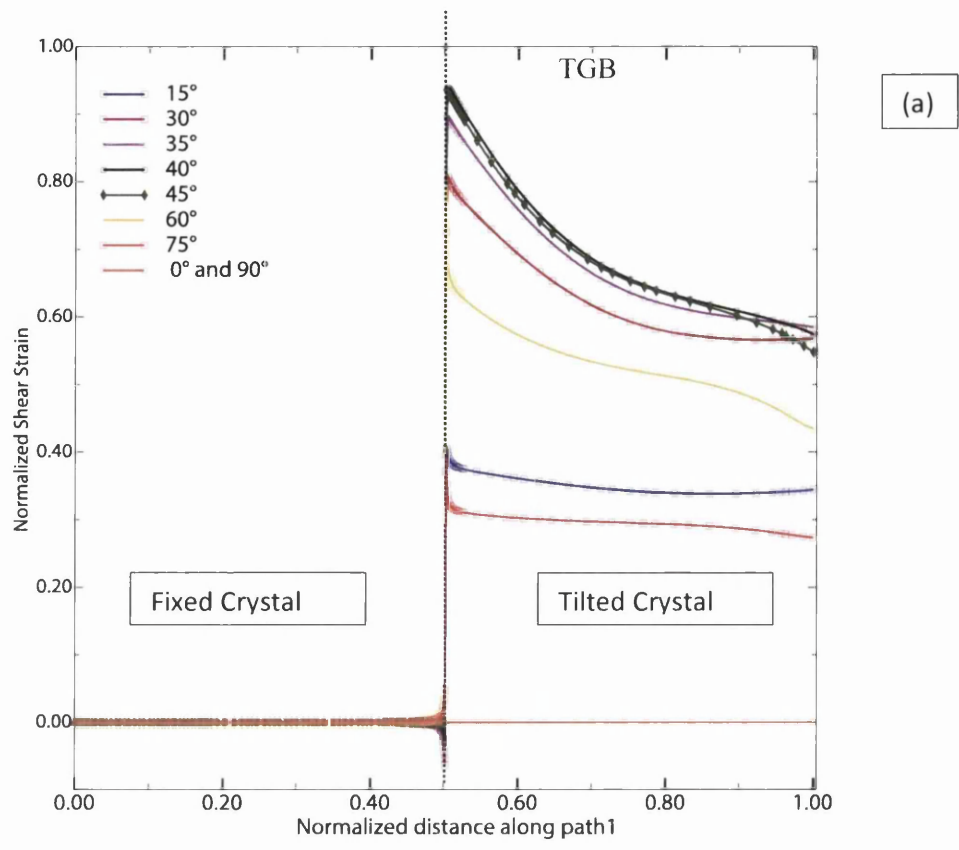


Figure 7.5.7 Maximum normalized normal stress S22 (blue), maximum normalized hydrostatic stress (orange) and maximum normalized Von Mises stress (grey) as a function of GB misorientation in bi-crystal nickel.



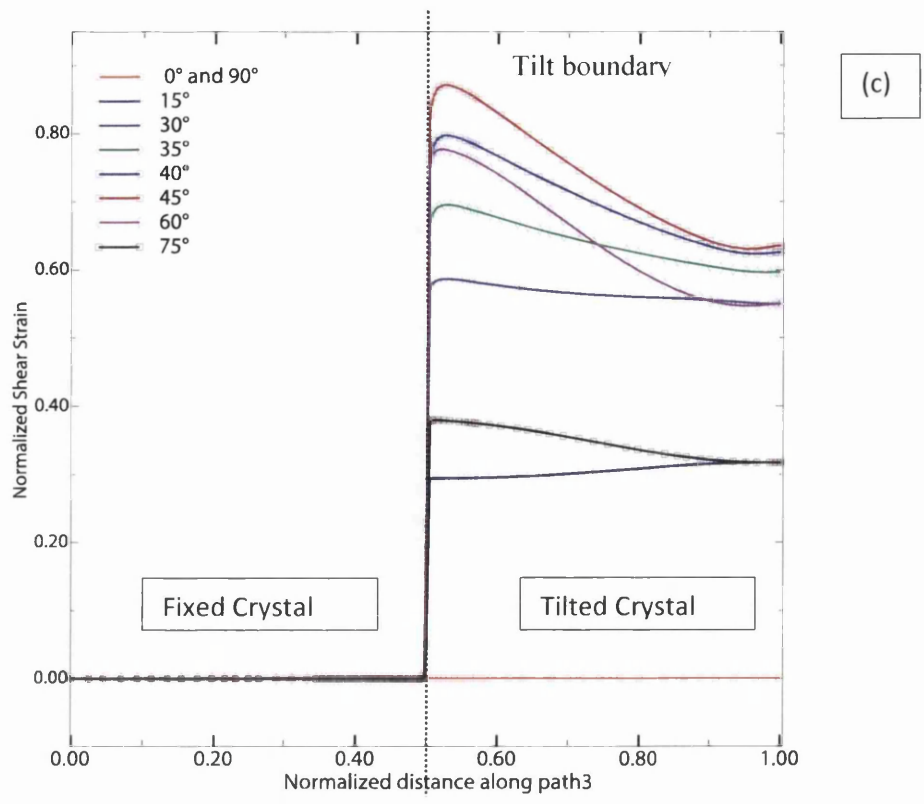


Figure 7.5.8 (a) Normalized shear strain (ϵ_{12}/ϵ_0) along the normalized path x1 (y/h) parallel to the traction direction $[010]$ for various misorientation angles. (b) Normalized shear strain (ϵ_{12}/ϵ_0) along the normalized path x2 (y/h) parallel to the traction direction for various misorientation angles. (c) Normalized shear strain (ϵ_{12}/ϵ_0) along the normalized path x3 (y/h) parallel to the traction direction for various misorientation angles in bi-crystal nickel.

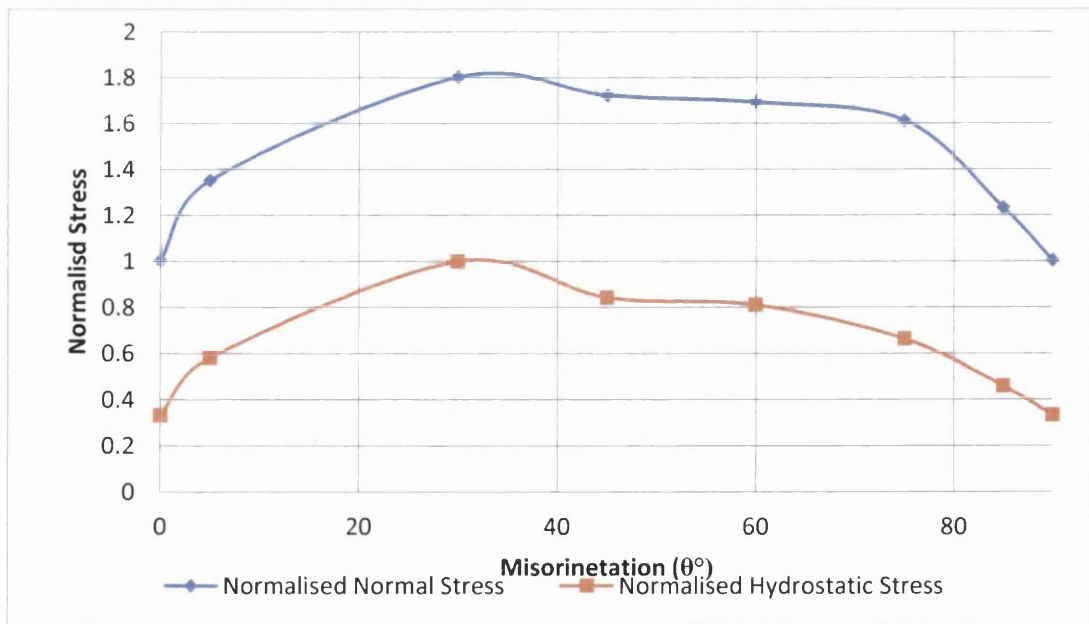


Figure 7.5.9 Maximum normalized normal stress and maximum normalized hydrostatic stress as a function of GB misorientation in polycrystalline nickel.

In the numerical model this effect is explained by the fact that i) the elastic constants in the modelled crystals are a function of orientation, ii) these differences directly affect the calculated hydrostatic stresses which iii) directly affect diffusion and the evolution of the hydrogen concentration field. The effect in real material, as opposed to the numerical model, is the same but the explanation would proceed along the following lines, i) the overall uniform applied elastic stress on the bi-crystal generates dislocations along TGB due to the dilatational mismatch produced by differences in the mechanical responses arising from the differences in anisotropic elasticity between tilted crystal and fixed crystal ii) the dislocations developed along TGB act as hydrogen trap sites which segregate and accumulate hydrogen concentrations in the form clustered atomic hydrogens along TGB iii) where the amount of dislocation generation is governed by the GB misorientation angle and the variation in the amount of dislocations generated depends on the misorientation angle between the two adjacent crystals.

The hydrogen concentrations are heterogeneously distributed in the bi-crystal nickel model for TGB misorientations $0^\circ < \theta < 90^\circ$ due to the change in stress gradients i.e. the heterogeneous distribution of normalised hydrostatic stresses (σ_h/σ_0) whose values are greater or lower than 0.33 and normalised normal stresses (σ_n/σ_0) greater or less than unity. In contrast the hydrogen concentration is homogeneously distributed for GB misorientations 0° and 90° because the homogeneous distribution of normalised hydrostatic stresses (σ_h/σ_0) are equal to 0.33 and the normalised normal stresses (σ_n/σ_0) are equal to 1. The normal hydrostatic tensile and compressive stresses are acting as the driving forces for higher and lower local accumulations of hydrogen respectively. The hydrogen concentrations near the TGB can be higher or lower depending on the misorientation angle. The accumulated hydrogen concentrations are higher near the TGB for misorientation angles $0^\circ < \theta < 45^\circ$ and lower for misorientation angles $45^\circ < \theta < 90^\circ$. Increased hydrogen concentrations along the TGB are observed for tensile normalised normal stress and normalised hydrostatic stresses (σ_h/σ_0) whose values are greater than 1 and 0.33 respectively. Lower accumulations of hydrogen along the TGB misorientation are observed with compressive normalised normal stress and normalised hydrostatic stresses whose values are less than 1 and 0.33 respectively. Tensile stresses with higher stress gradients segregate higher concentration of hydrogen.

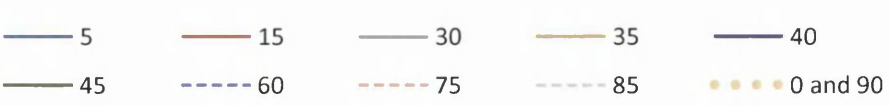
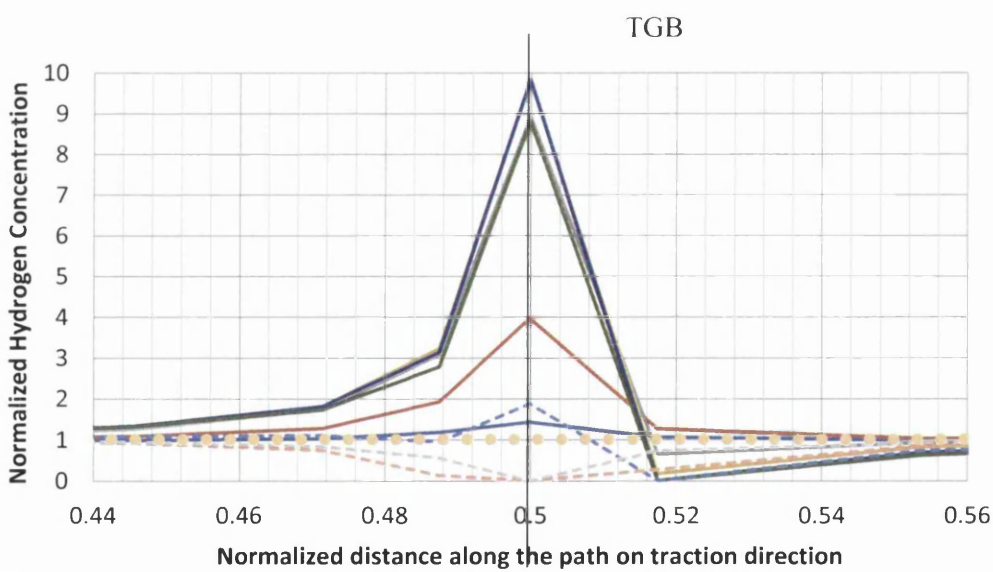
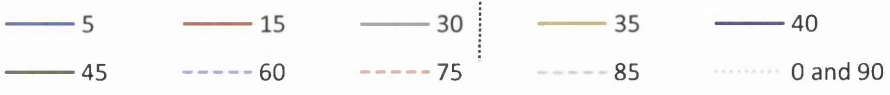
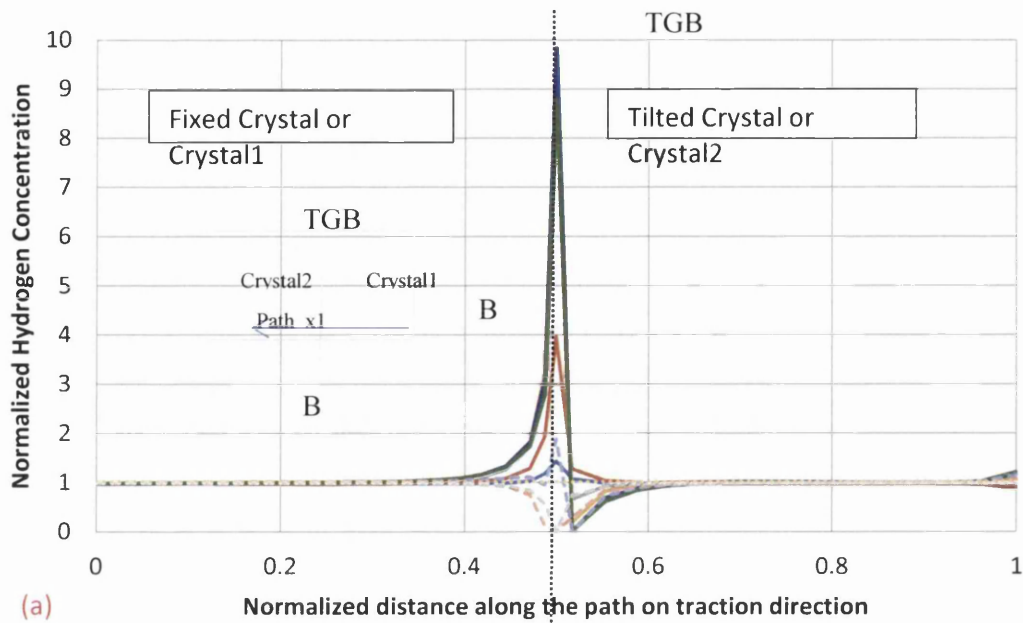


Figure 7.5.10 Normalized hydrogen concentration along the normalized path x1 (y/h) parallel to the traction direction for various misorientation angles in bi-crystal nickel. (b) Close up view of normalized hydrogen concentration along the normalized path x1 (y/h) parallel to the traction direction for misorientation angles in degrees in bi-crystal nickel.

Higher accumulation of hydrogen is observed with misorientation angles $0^\circ < \theta < 45^\circ$ due to high tensile stresses acting with these misorientation angles. Lower segregations of hydrogen concentration are observed on misorientation angles $45^\circ < \theta < 90^\circ$ due to high compressive stresses. *This numerical prediction suggests that TGBs act as trap sites as well as non-trap sites depending on the type of stresses acting on the TGB i.e. tensile or compressive.*

Figure 7.5.11 shows the normalised hydrogen concentration along the normalized path x2 parallel to the traction direction for various GB misorientations in bi-crystal nickel. Figures 7.5.12 and 7.5.13 show the normalized hydrogen concentration along the normalized path near the TGB on crystal1 (i.e. fixed crystal) and crystal2 (tilted crystal) respectively perpendicular to the traction direction for various misorientation angles. Figure 7.5.14 shows the corresponding plot of normalised hydrogen concentration for various GB misorientations in bi-crystal nickel. Figure 7.5.15 shows the normalised hydrogen concentration for various GB misorientations in polycrystalline nickel.

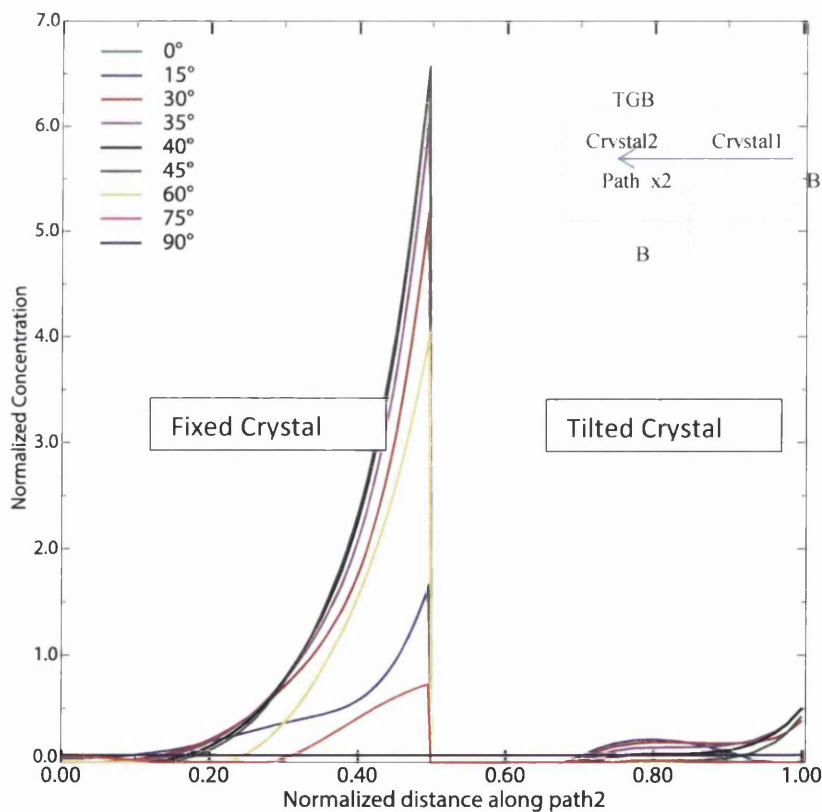


Figure 7.5.11 Normalized hydrogen concentration along the normalized path x2 (y/h) parallel to the traction direction for various misorientation angles in bi-crystal nickel.

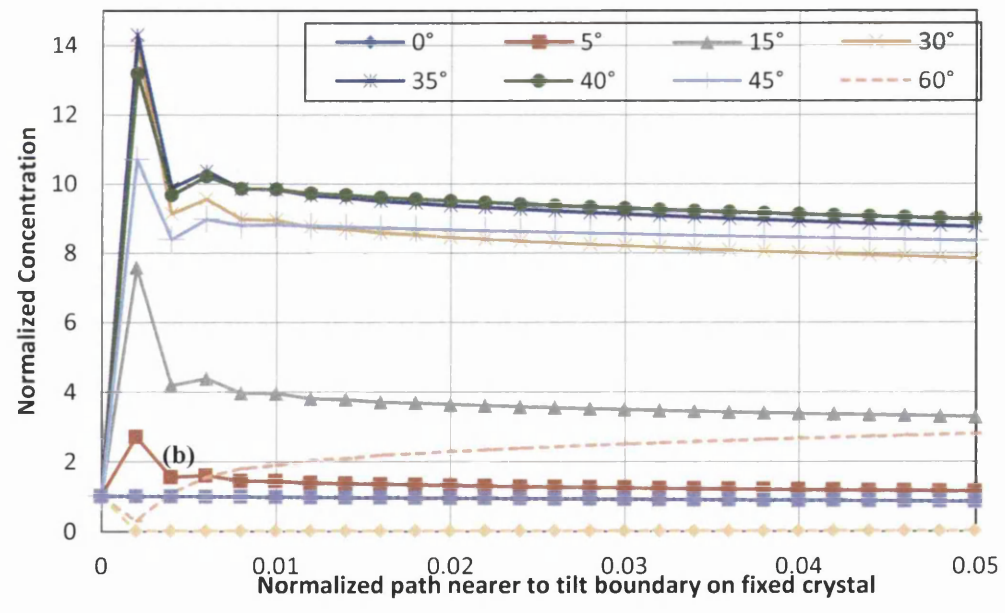
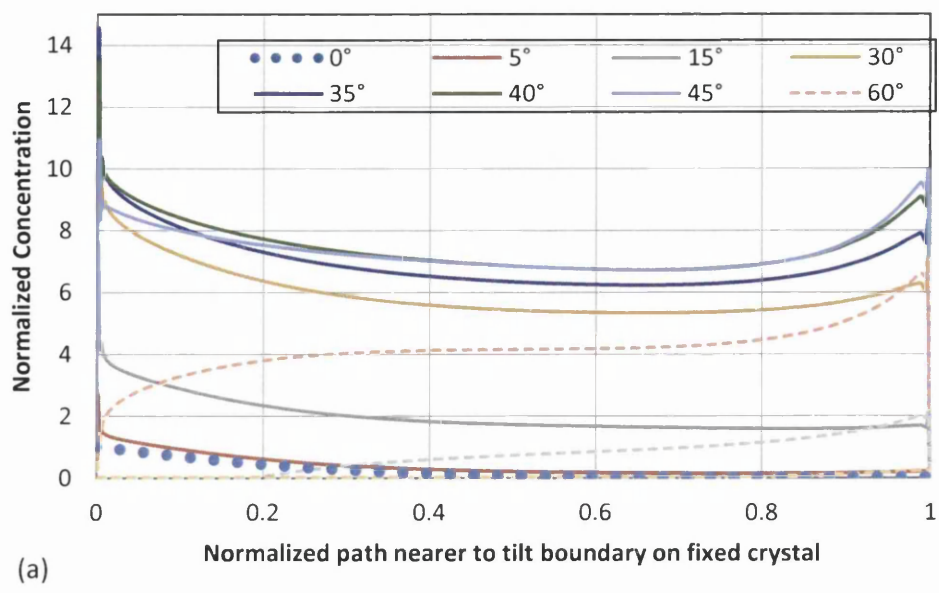


Figure 7.5.12 (a) Normalized hydrogen concentration along the normalized path nearer to the TGB on the fixed crystal perpendicular to the traction direction for various misorientation angles in bi-crystal nickel. (b) Close up view of normalized hydrogen concentration along the normalized path nearer to the TGB on the fixed crystal perpendicular to the traction direction for various misorientation angles in bi-crystal nickel.

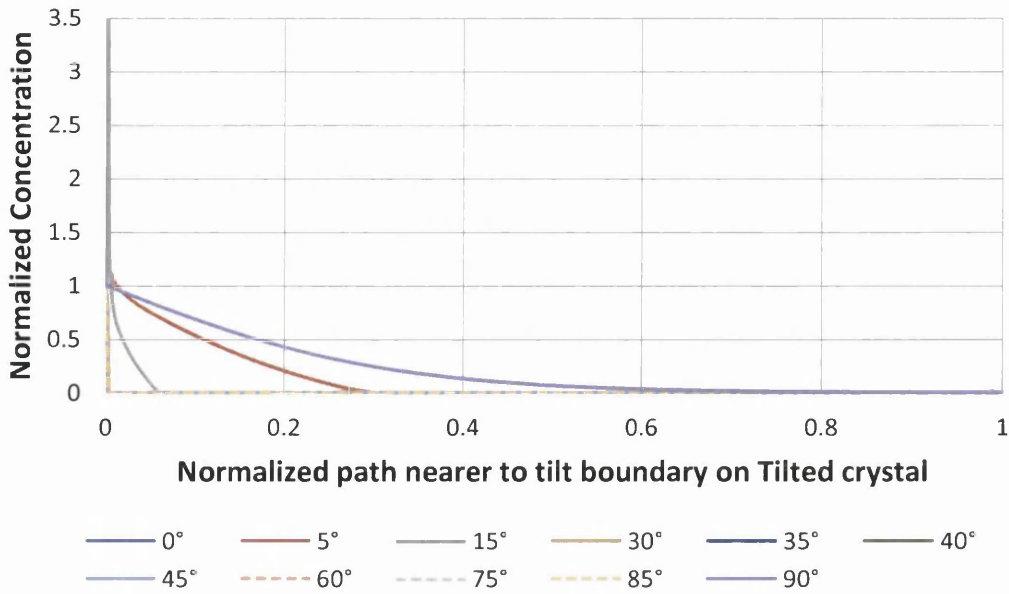
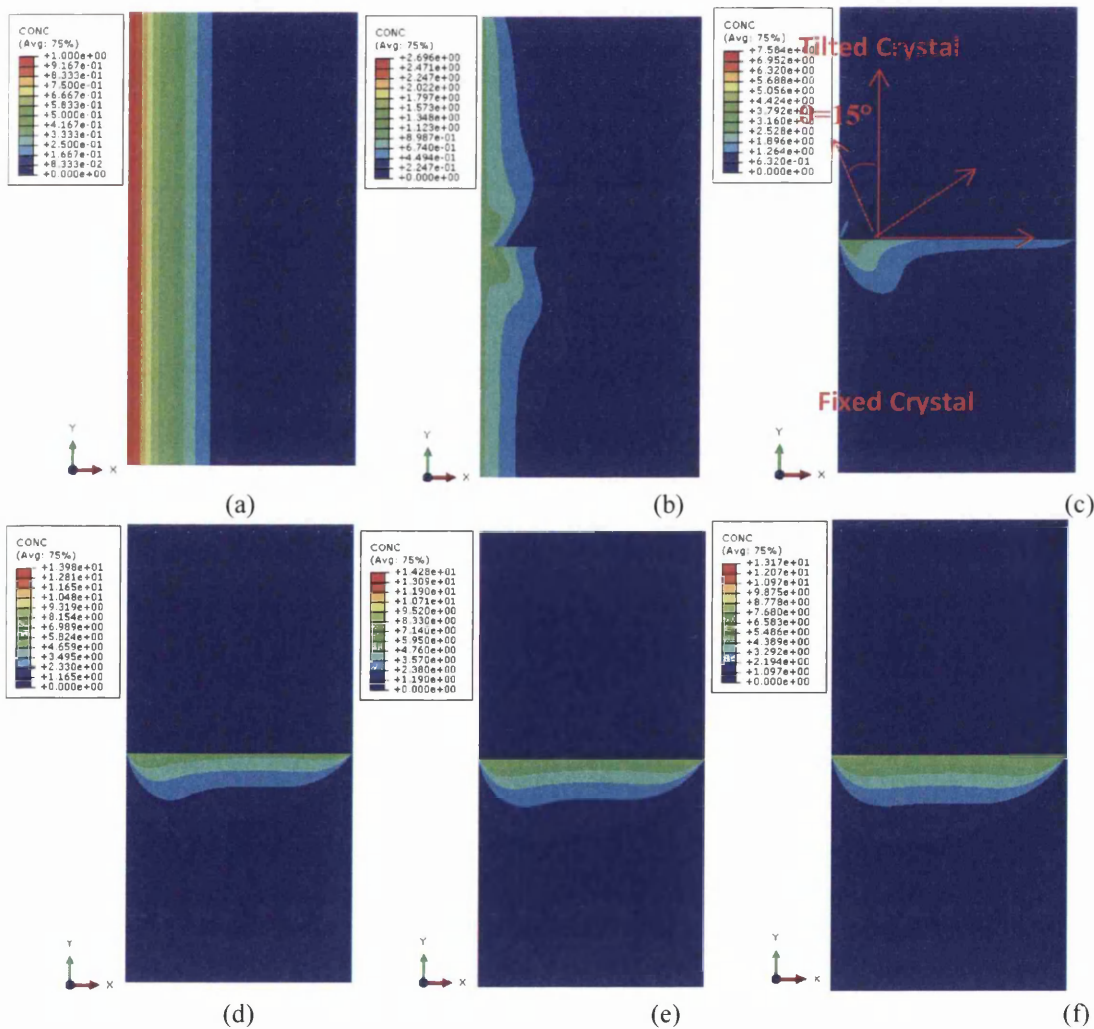


Figure 7.5.13 Normalized hydrogen concentration along the normalized path nearer to the TGB on crystal2 perpendicular to the traction direction for various misorientation angles in bi-crystal nickel.



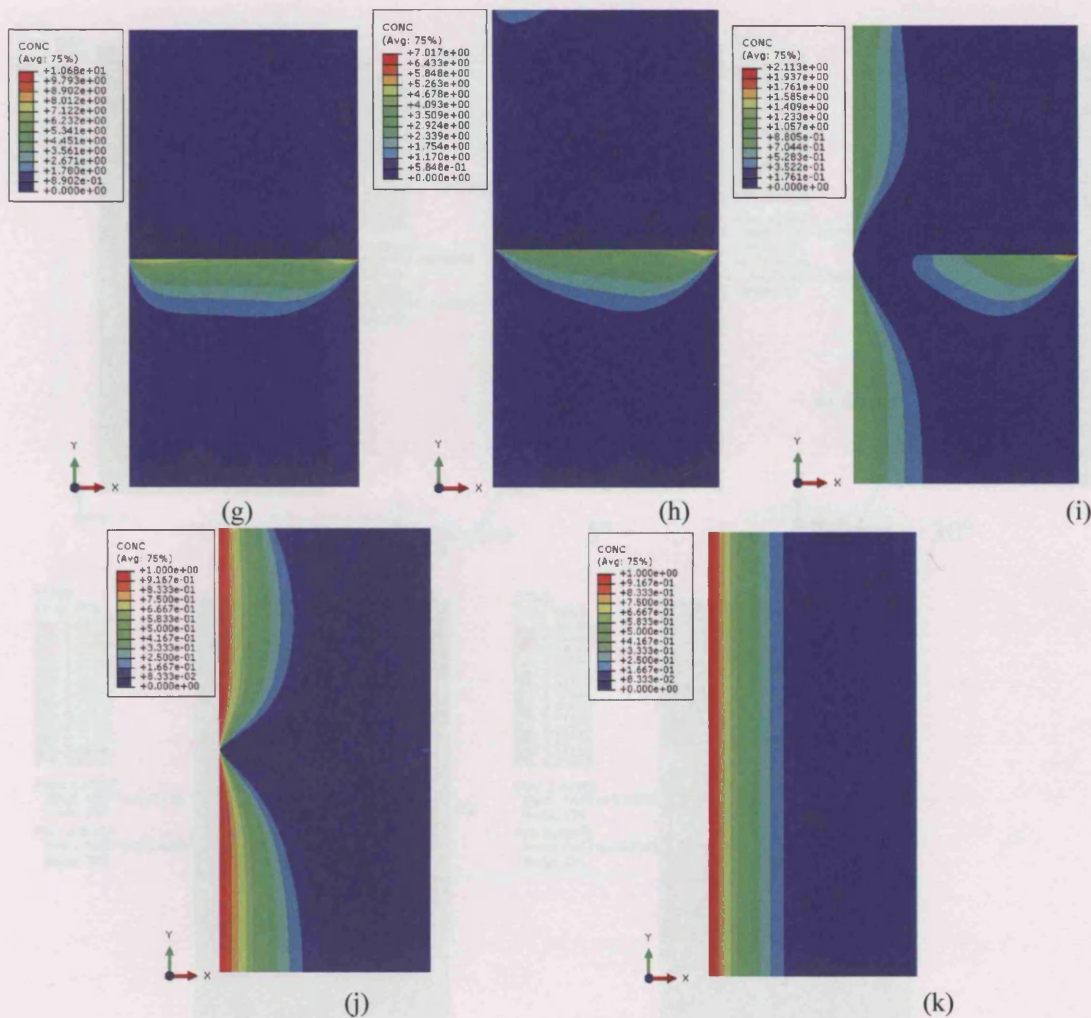


Figure 7.5.14 Contour plot of normalized hydrogen concentration for various misorientation angles in bi-crystal nickel (a) 0° (b) 5° (c) 15° (d) 30° (e) 35° (f) 40° (g) 45° (h) 60° (i) 75° (j) 85° (k) 90° .

In a real material the amount of hydrogen traps would increase along the TGB as the tensile stress increases. An increase in dilatational mismatch between crystals increases the tensile stress. The amount of hydrogen traps would correspondingly decrease along a TGB as the compressive stress increases due to a decrease in the dilatational mismatch between crystals.

In the case of the model, figure 7.5.16 shows the maximum normalized hydrogen concentration as a function of TGB misorientation angles in bi-crystal nickel. Figure 7.5.17 shows the maximum normalised hydrogen concentration as a function of misorientation angles in polycrystal nickel. Maximum hydrogen segregation increases as the TGB misorientation angle increases above 0° attaining a maximum for the TGB misorientation angle of 35° then it decreases, attaining a steady state after the TGB misorientation angle of 85° . Thus the model predicts

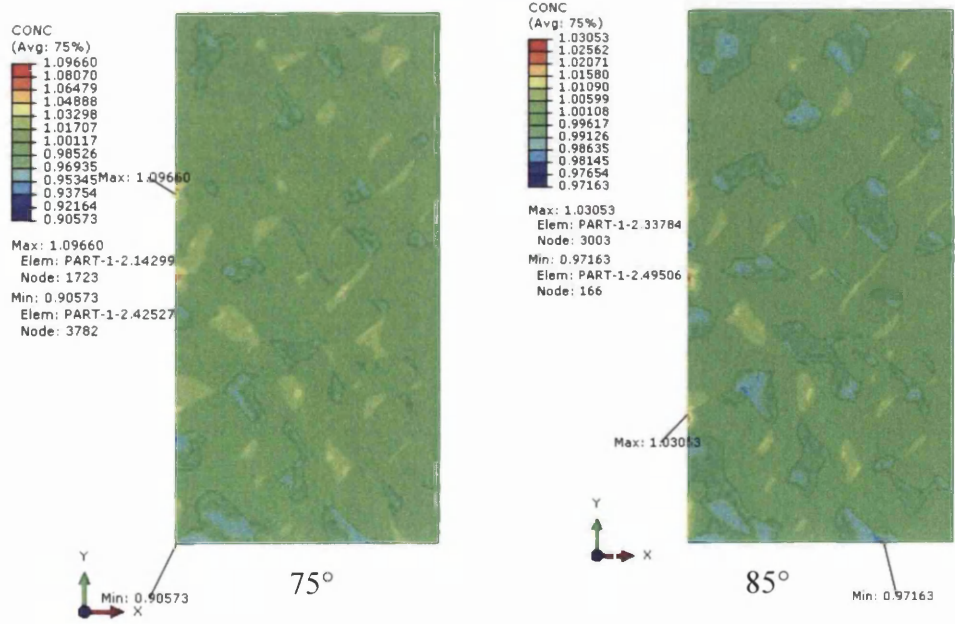
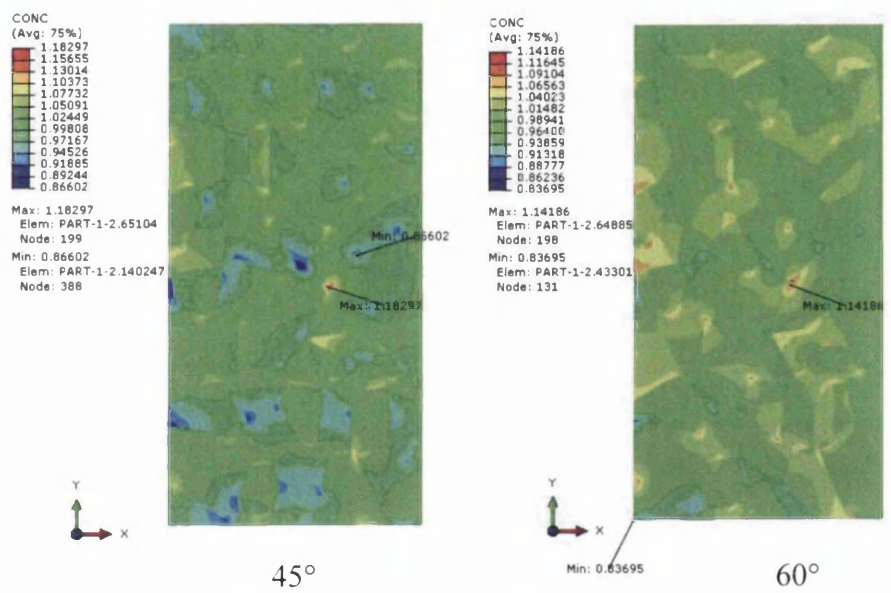
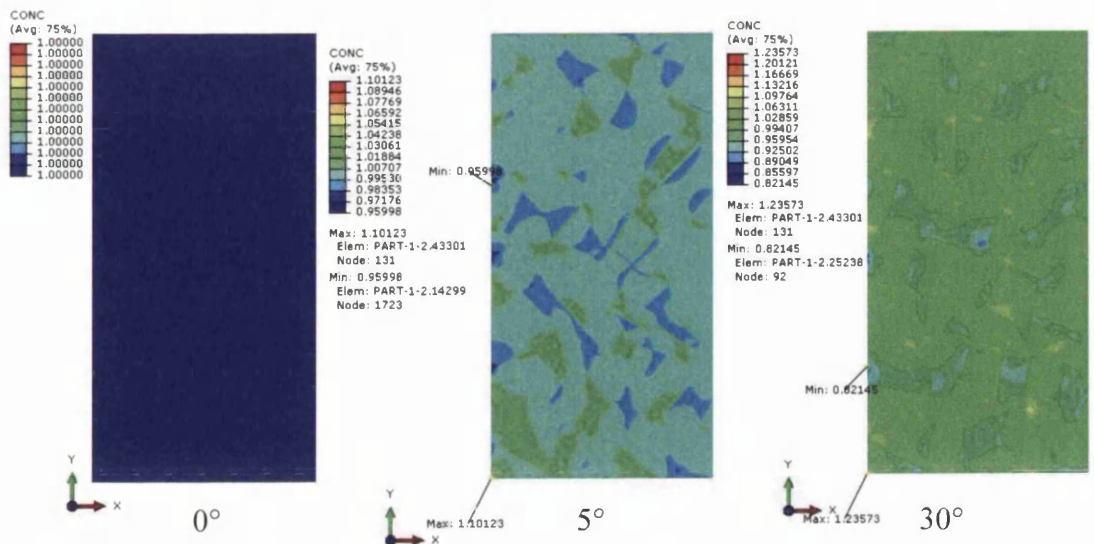


Figure 7.5.15 Normalized hydrogen concentration for various orientations of grainset1 rotated along loading directions 0, 5°, 30°, 45°, 60°, 75°, 85° in polycrystalline nickel.

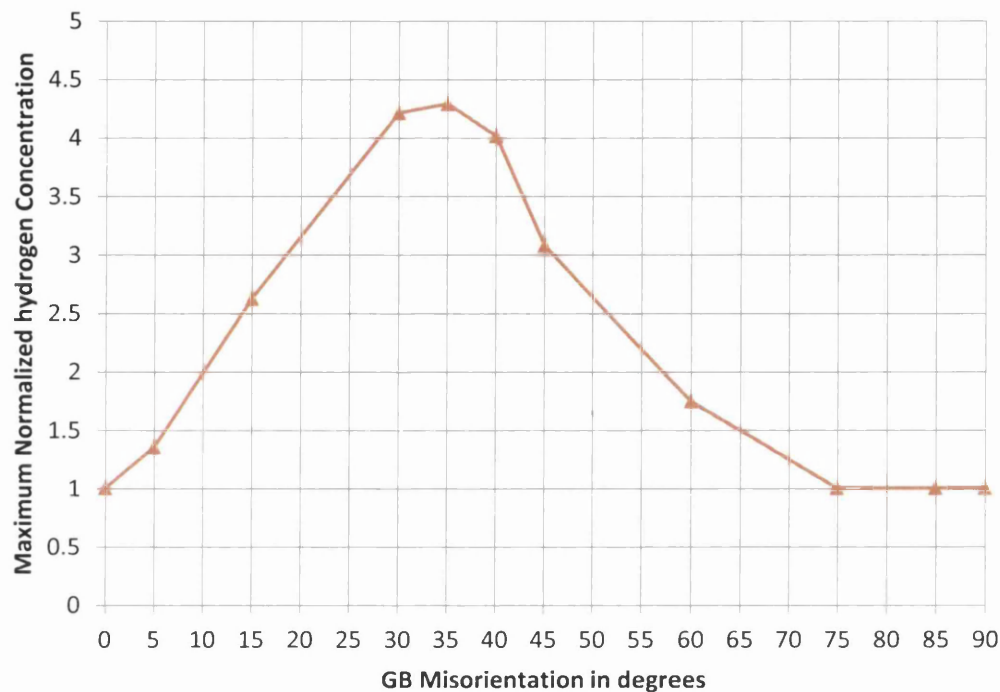


Figure 7.5.16 Maximum normalized hydrogen concentration as the function of misorientation angles in bi-crystal nickel.

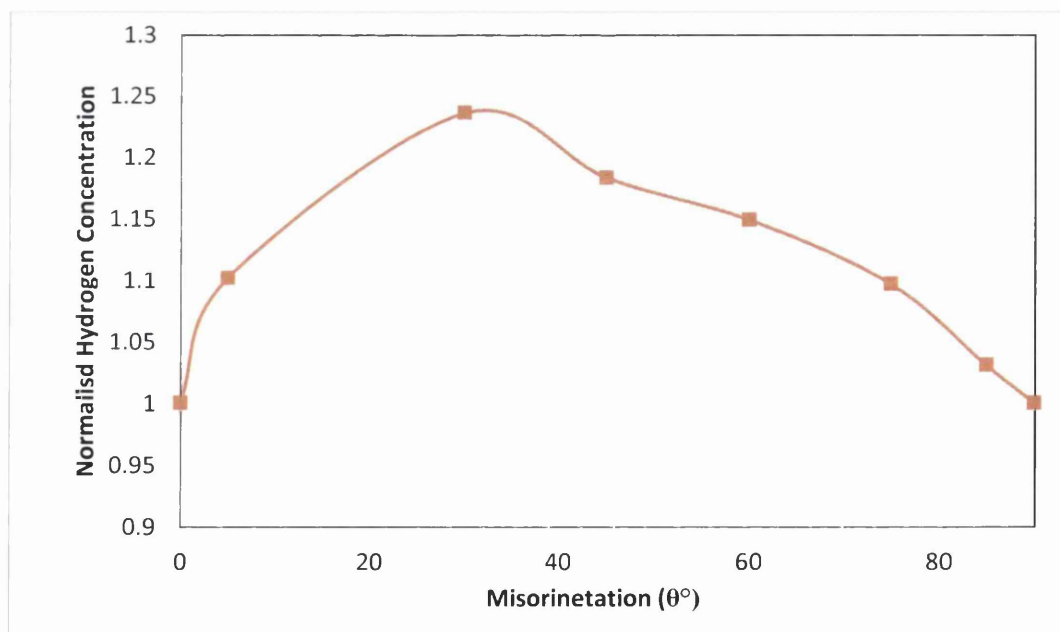


Figure 7.5.17 Maximum normalized hydrogen concentration for various misorientations in the polycrystalline model.

maximum highly segregated hydrogen concentrations are found on TGB misorientation angles in the range $15^\circ < \theta < 45^\circ$.

7.5.2 Discussion

The results of numerical modelling in this investigation indicate that the TGB misorientation angle affects the followings factors: neighbouring crystal boundary conditions, changes in stress gradients and types of stress developed (i.e. tensile/compressive) depending on the applied boundary condition and neighbouring crystal orientations. The effect of stress induced hydrogen diffusion in the meso-scale bi-crystal and polycrystalline nickel models would indicate that TGB misorientation angles are one of the key factors significantly influencing hydrostatic stress, normal stress, strains and hydrogen distributions. This result illuminates the problem of how TGB misorientation angles influence hydrogen segregation and trapping in bi-crystal and polycrystal nickel specimens and the effects of TGB misorientation on stress induced hydrogen evolution. This knowledge could be beneficial for optimization of TGB misorientations in materials in order to reduce hydrogen traps and segregations sites which would lead to improvements in resistance to hydrogen induced intergranular cracking and hydrogen embrittlement.

From the results of this computational numerical modelling it has been observed that the local stress, strain and hydrogen distributions are inhomogeneous and are affected by misorientation angles, orientations of neighbouring crystals and boundary conditions. In a real material, as opposed to the numerical model, the clustered atomic hydrogens are segregated in traps near to the TGB due to the influence of dislocations developed under the effects of applied mechanical stress. The numerical model predicts maximum hydrogen concentrations are accumulated on the TGB with misorientation angles ranging between $15^\circ < \theta < 45^\circ$. This investigation reinforces the importance of GB engineering for designing and optimizing these materials to decrease hydrogen segregation arising from TGB misorientation.

7.6 Coupled micro-macro model for hydrogen diffusion

The proposed multi-scale model is capable of resolving the necessary microstructural phenomena with less usage of computer resources and decreased computational time. In this section such a method is described using coupled microstructural and continuum approaches including critical defect site (CMCD) modeling method with sub-structural and sub-modelling techniques to investigate the hydrogen embrittlement mechanism. The CMCD technique consists of a microstructural model (micro scale) near critical sites such as cracks, defects and voids as a sub-structure or a sub-model coupled to macro-scale continuum models away from critical sites. The CMCD method thus replaces the continuum domain near the critical sites by including microstructural phenomena such as grain, grain boundaries, triple junction, voids, defects, and clustered grains. Initially the CMCD model is implemented in hydrogen diffusion analysis and then this technique is extended to solve multi-physics (i.e. coupled chemo-mechanical) problems.

7.6.1 Experimental results

Initially, the developed CMCD model was tested by simulating hydrogen diffusion in two example problems in a 2D system. The initial problem is crack free and the second problem includes a single micro crack in the form of sharp notch in the round test piece. The geometry and boundary conditions for hydrogen entry are sketched in figures 7.6.1 and 7.6.2 respectively for each of the models. Figures 7.6.1 and 7.6.2 show the CMCD model micro domains embedded within the continuum macro domain, without a crack and with a crack respectively. Note all the material properties used in the analysis are given in the appropriate figure captions. Figures 7.6.1 (a) and (b) show the space shuttle launcher thrust chamber geometry on the metre scale and in close-up view respectively. Figure 7.6.1 (c) shows the close-up view of the thrust chamber macro domain cross section coupled to the micro domain.

In the CMCD without a crack model, the micro domain is coupled with the homogenised continuum domain using a tie boundary as shown in figure 7.6.1 (d).

The area of the micro domain is $36 \mu\text{m}^2$ and the average grain size is $6 \mu\text{m}$. Figure 7.6.1 (e) shows the boundary conditions for hydrogen entry into the surface of the material as an environmentally controlled concentration of hydrogen. Figure 7.6.1 (f) shows the tie boundary (in yellow) coupling the macro and micro domains of the CMCD model. The diffusion properties used in the intragranular region, intergranular region and macro domain are $9 \times 10^{-14} \text{ m}^2/\text{s}$, $4 \times 10^{-10} \text{ m}^2/\text{s}$ and $2 \times 10^{-12} \text{ m}^2/\text{s}$ respectively. The effective diffusion property used in the macro domain for average grain size of $1 \mu\text{m}$ is calculated based on a FEA microstructure homogenization method developed by authors and detailed descriptions of this technique can be found chapter 7.1. The reader should refer to the respective figures for the diffusion property values used in the models. In the CMCD with a crack model, the micro domain is confined to a small domain in the critical region near the corner of notch in the test piece. The remaining region is considered as a homogenized continuum domain as shown in figure 7.6.2 (a). Cortés *et al.* consider the 3D round sharp notch test piece as a 2D axisymmetric model to analyse the hydrogen embrittlement problem by examining the effect of a crack starting from the root of the sharp notch. The 2D sharp notch geometry considered here is used to test the hydrogen transport mechanism of the CMCD model with a crack (i.e. the sharp notch is considered as a crack as shown in figure 7.6.2 (a)). Figure 7.6.2 (b) shows the axisymmetric boundary condition and the boundary condition of hydrogen concentration entering into the surface of the structural polycrystalline material. Figure 7.6.2 (c) shows the coupling of the micro domain and homogenised continuum domain via the tie boundary. The mesh used for the CMCD model without a crack and with a crack and the close-up view of the meshed micro domain region are shown in figures 7.6.3 and figure 7.6.4 respectively.

The simulations of the CMCD model with a crack and without a crack were performed to investigate the hydrogen embrittlement mechanism of a polycrystalline material using a 2D hydrogen diffusion simulation. Figure 7.6.3 shows contours of the hydrogen concentration within the intragranular and intergranular heterogeneous microstructure in the CMCD without a crack model where the subscale micro domain and the homogenous behaviour of the hydrogen diffusion mechanism at the macro scale continuum level are solved using a substructure micro domain method.

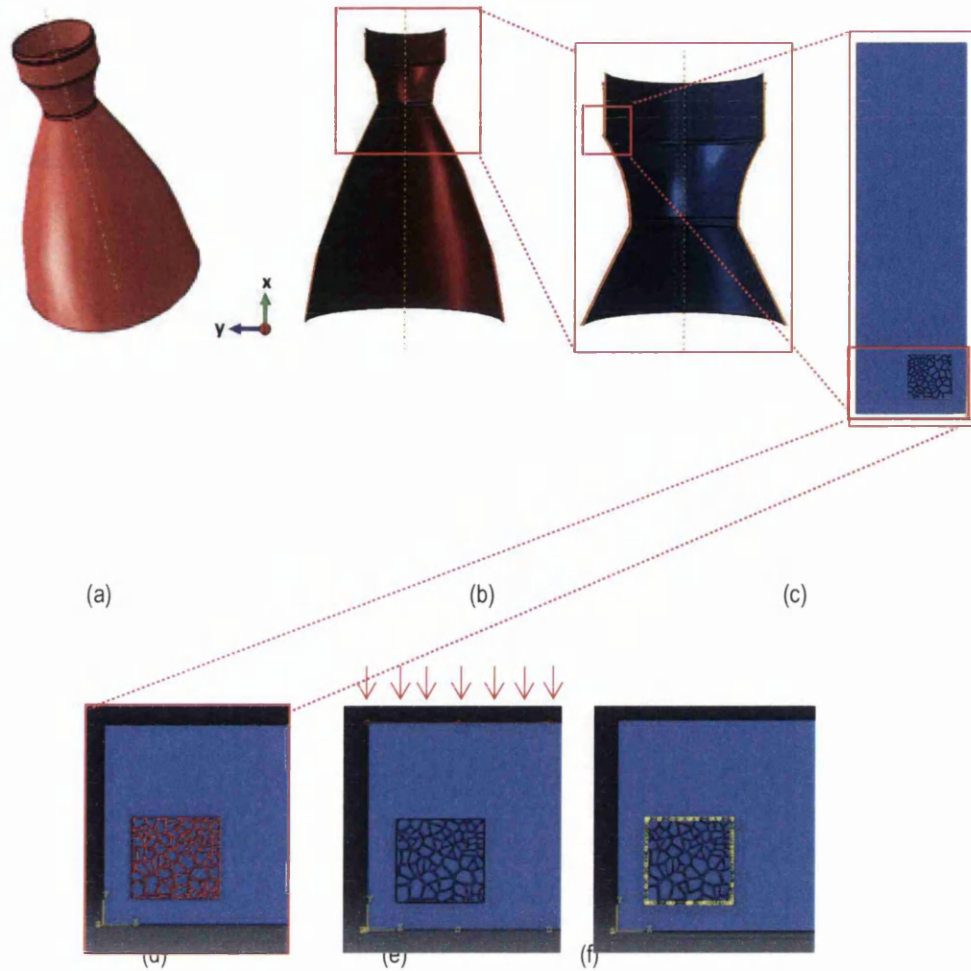


Figure 7.6.1 (a) & (b) Space shuttle launcher thrust chamber geometry on the metre scale and a close-up view. (c) Close-up view of the nickel layer of a thrust chamber cross section macro domain coupled with the micro domain. (d) CMCD model without any cracks: Geometry with coupled continuum domain and micro domain and its close-up view. (e) Boundary condition with hydrogen from environment entering into the material from outer surface to inner surface. (f) Tie boundary in yellow couples the micro and continuum domains.

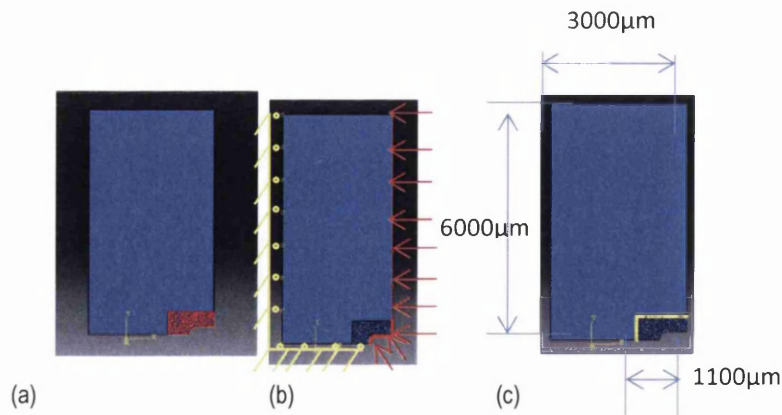
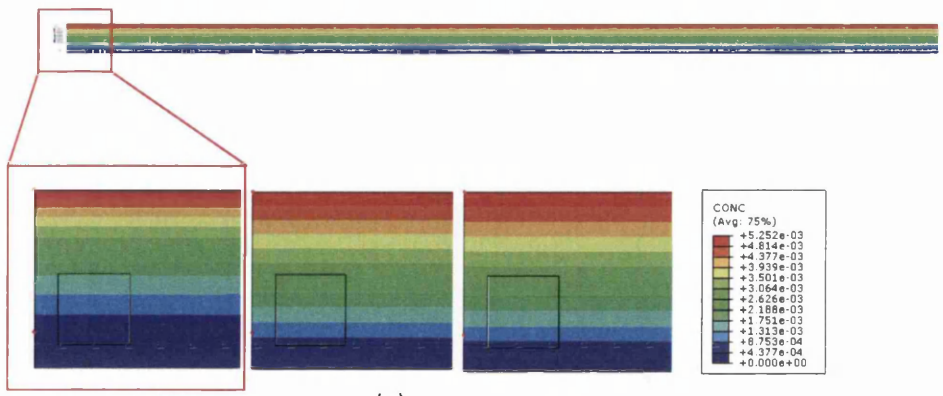
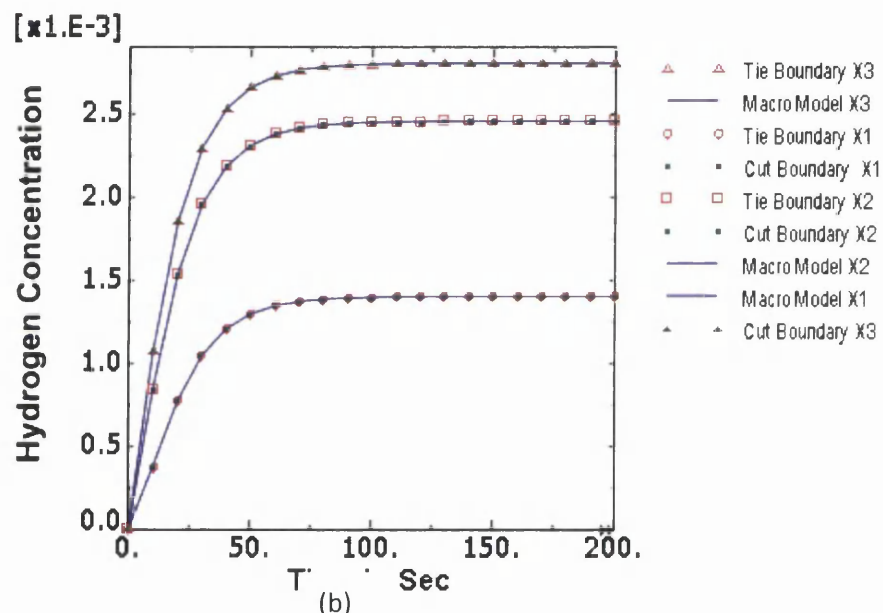


Figure 7.6.2 2D axisymmetric CMCD model with a crack in the form of sharp notch, the micro domain geometry is embedded within the homogenized continuum domain near the critical site of sharp notch test piece. (Note: Notch radius 200µm, crack

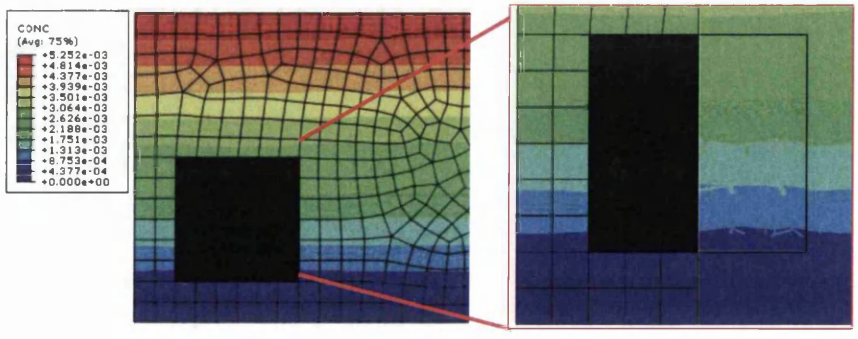
length = 500 μ m and average grain size = 70 μ m). (b) Coupling the micro domain with the continuum domain with a tie boundary in yellow. (c) Boundary condition showing the hydrogen entry surface of the material from the environment.



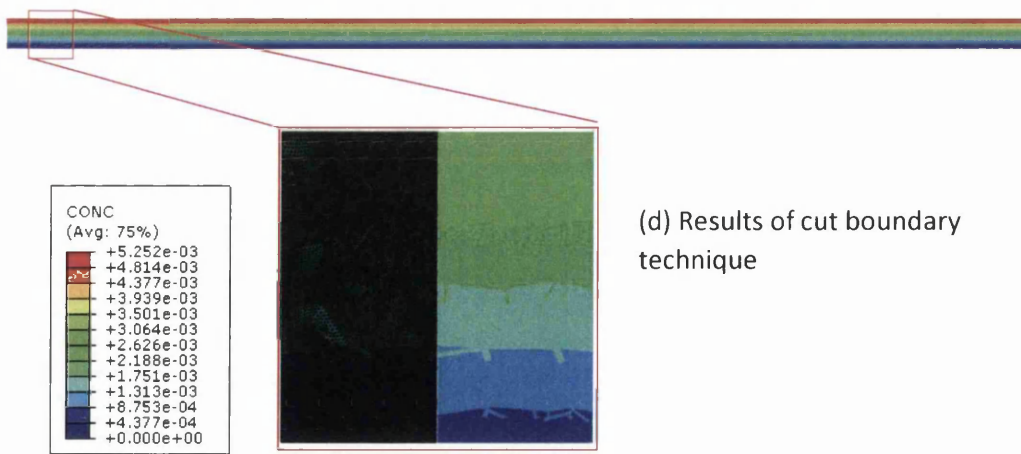
(a)



(b)



(c) Results of tie boundary technique



(d) Results of cut boundary technique

Figure 7.6.3 Contours of hydrogen concentration on a coupled two scale CMCD model without any crack. (a) Shows the hydrogen diffusion results of boundary technique at three different elapsed times of 20s, 60s and 400s respectively. Note: To validate the tie and cut boundary technique the CMCD model without crack has been analysed using the effective diffusion property in both macro and micro models. (b) Validation of the micro boundary technique model. The results shows the hydrogen diffusion concentration profile between macro model and micro model with the tie boundary and cut boundary techniques at three different distances from top to bottom ($X_1=7\mu\text{m}$, $X_2=8\mu\text{m}$ and $X_3=11\mu\text{m}$, the same colour legend is used for all figures. (c) and (d) show the hydrogen distribution in the CMCD model based on a tie boundary technique and cut boundary technique respectively after an elapsed time of 400s. Homogeneous distribution of hydrogen in the macro model and heterogeneous distribution of hydrogen in the micro model are observed. On the sub-scale the diffusion through grains and grain boundaries is resolved using the sub-structure and sub-model micro domain boundary method. The area of the micro domain is $36\mu\text{m}^2$ and the average grain size of polycrystalline material in the micro domain is $1\mu\text{m}$.

In order to validate the developed CMCD model with both “tie boundary” and “cut boundary” technique, initially the hydrogen diffusion analysis has been done using single diffusion property in both micro and macro domain as well in intergranular and intragranular domain. The diffusivity used in the model is $2 \times 10^{-12} \text{ m}^2/\text{s}$. The results of this analysis are shown in figure 7.6.3 (a) for three elapsed times of 20s, 60s and 400s.

In order to validate the CMCD model with both tie boundary and cut boundary techniques a preliminary hydrogen diffusion analysis was done using a single diffusivity in both micro and macro domains as well as in the intergranular and intragranular domains. The diffusivity used was $2 \times 10^{-12} \text{ m}^2/\text{s}$. The results of this analysis are shown in figure 7.6.3 (a) for elapsed times of 20s, 60s and 400s. In order to validate the CMCD model based on tie and cut boundary techniques, the hydrogen diffusion

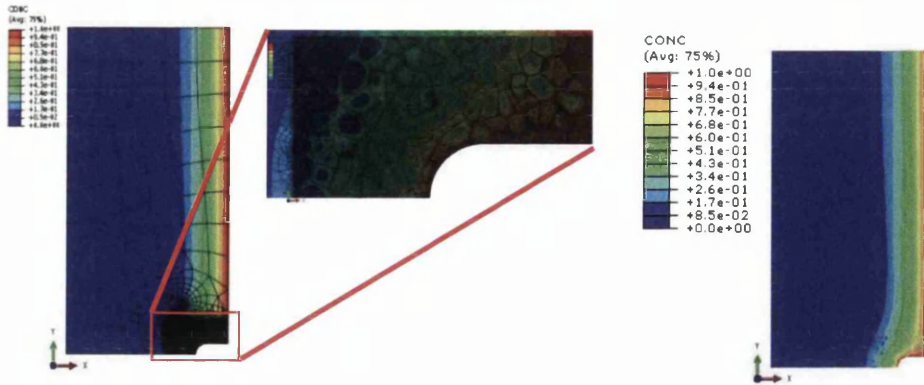


Figure 7.6.4 Contours of hydrogen concentration in a coupled two scale CMCD model with crack after 1×10^7 s. On the sub-scale the diffusion through intergranular and intergranular heterogeneous microstructure is resolved at two different time scales using a substructure micro domain method. Macro-scale assumptions, homogeneous behaviour, are assumed at the larger scale. Note: the diffusion properties used in grains, grain boundaries and the macro domain are 9×10^{-14} m²/s, 4×10^{-10} m²/s and 1×10^{-13} m²/s respectively.

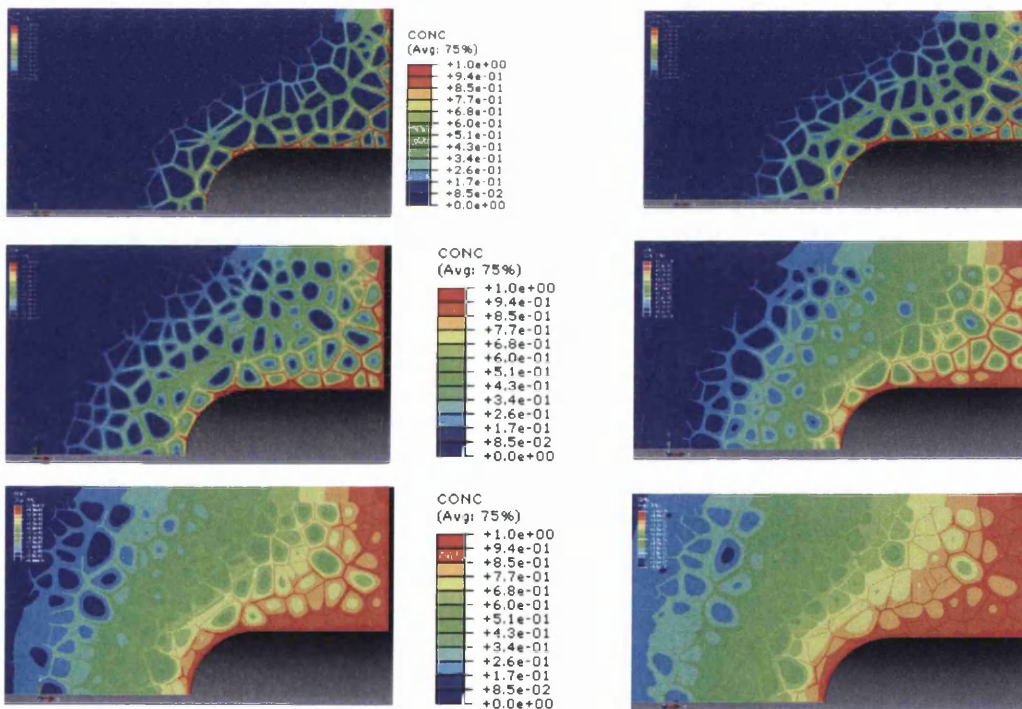


Figure 7.6.5 Close up view of the heterogeneous hydrogen diffusion and accumulation mechanism in the micro domain for various increasing elapsed times of $t_1=2.29 \times 10^5$ s, $t_2=4.9 \times 10^5$ s, $t_3=1.13 \times 10^6$ s, $t_4=4.1 \times 10^6$ s, $t_5=6.1 \times 10^6$ s, $t_6=1 \times 10^7$ s in the CMCD model with a crack.

analysis results are plotted for three different positions X1, X2 and X3 (i.e. in the cross section of the outer nickel layer of the thrust chamber from outer surface to

inner surface at distances of $X_1=7\mu\text{m}$, $X_2=8\mu\text{m}$ and $X_3=11\mu\text{m}$) in both the micro and macro domains). These plots are shown in the figure 7.6.3 (b). The tie and cut boundary micro domain results are in good agreement with the macro domain results. Two test cases were analysed using the CMCD model without a crack model using different diffusion properties in the micro domain and macro domain to show the effective application of the techniques. The homogenous effective diffusivity (i.e. the diffusivity used in the macro domain) is $2 \times 10^{-12} \text{ m}^2/\text{s}$. An average grain size of $1\mu\text{m}$ has been used in the macro domain with different diffusion properties in grains and grain boundaries in the micro domain (diffusivities used in the intragranular region and intergranular regions are $9 \times 10^{-14} \text{ m}^2/\text{s}$ and $4 \times 10^{-10} \text{ m}^2/\text{s}$ respectively). Figure 7.6.3 (c) shows the results of the CMCD model without a crack using the tie boundary technique and figure 7.6.3 (d) shows the results of the CMCD model without a crack using the cut boundary technique.

In order to show the application of CMCD model in the cracked domain another test case was analysed. The hydrogen diffusivity used in the macro domain is $1 \times 10^{-13} \text{ m}^2/\text{s}$, in the micro domain the diffusivities used in the intragranular region and intergranular region are $9 \times 10^{-14} \text{ m}^2/\text{s}$ and $4 \times 10^{-10} \text{ m}^2/\text{s}$ respectively. Figure 7.6.4 shows the equivalent plots for the test case of the CMCD model which includes the crack. Figure 7.6.5 shows the resolved hydrogen concentration and accumulation for the intergranular and intragranular microstructural micro domains at various elapsed times ($t_1=2.29 \times 10^5 \text{ s}$, $t_2=4.9 \times 10^5 \text{ s}$, $t_3=1.13 \times 10^6 \text{ s}$, $t_4=4.1 \times 10^6 \text{ s}$, $t_5=6.1 \times 10^6 \text{ s}$, $t_6=1 \times 10^7 \text{ s}$) for the CMCD crack model based on a substructure micro domain method. This simulation shows detailed information about the modelled hydrogen diffusion, aggregation and accumulation in the heterogeneous polycrystalline structural material.

7.6.2 Discussion

The predicted hydrogen concentrations obtained through representing the micro scale intragranular and intergranular geometry and physics within the current CMCD model demonstrates how microstructure plays an important role in the aggregation of hydrogen concentration near critical sites and interfacial areas. These critical and interfacial areas accumulate hydrogen more than elsewhere. This detailed local microstructural interfacial information about the hydrogen diffusion, accumulation,

and aggregation gives a better understanding about intergranular hydrogen transport mechanisms. The model also has the potential to study and understand crack nucleation, propagation, critical hydrogen concentration and debonding of materials along the interfacial critical region of a structural polycrystalline material. The proposed multi scale CMCD model couples the microscopic details to the macroscopic region using tie boundary and cut boundary techniques. It can be used for modelling the location of critical sites providing more detailed information. The incorporation of microstructural details into the macroscopic continuum region may help to predict hydrogen embrittlement at the design stage providing a better understanding of hydrogen diffusion phenomena and much more detailed local microstructural information of the hydrogen transport.

7.7 Coupled micro-macro model for hydrogen embrittlement

7.7.1 Experimental results and discussion

The multiscale multiphysics hydrogen embrittlement problem is solved by using pre-cracked specimen embedded with microstructure features. The chosen problem in this section is a cracked polycrystalline nickel plate subjected to loading in a hydrogen rich environment where a simulated crack is deliberately introduced into the mesh. The commercial finite element program ABAQUS was employed for a sequentially coupled stress-assisted hydrogen diffusion analysis consisting of repeating steps of a stress analysis followed by a hydrogen diffusion analysis. A very fine mesh is used in the microstructural model to accurately capture the gradients of stress and hydrogen concentration near the artificial crack tip and a coarser mesh is used in the more distant (and assumed homogeneous) macro region. The procedure to couple the chemo-mechanical analysis is as follows:

a) The mechanical response of the coupled domain is captured firstly using an initial static stress analysis. Initially, the stress analysis is done using boundary condition as shown in figure 7.7.1, assuming the material is isotropic with a modulus of elasticity of 200 GPa and Poisson's ratio of 0.3 and implementing the anisotropic properties in the microstructural model. These results are transferred to the microstructural level sub-mesh, shown in figure 7.7.1 (c), via the submodelling technique as explained in section 7.6. This effectively maps values from the macro model to the boundaries of the micro mesh. Values calculated in the micro region are similarly mapped back onto the macro mesh at the next stress analysis. The same macro to micro coupling procedure is carried out for the hydrogen diffusion analysis as well.

b) In the micro-scale model the material mechanical anisotropy is accounted for by assigning individual grains random crystallographic orientations using the FCC nickel single crystal elastic constants $C_{11}=247$ GPa, $C_{12}=147$ GPa and $C_{44}=125$ GPa [81, 205]. The elastic constants of grain boundaries are assumed as $C_{11}=247$ GPa, $C_{12}=147$ GPa and $C_{44}=125$ GPa.

c) The micro-level model also includes micro-level stress-based driving forces for hydrogen diffusion. Hydrogen diffusion without the effect of stress in an FCC single crystal is isotropic with one independent diffusion material property [210].

However, hydrogen diffusion in grain boundaries is faster than diffusion within grains in nickel. The hydrogen diffusivity and initial atomic hydrogen concentration values used in the micro model are $3.52 \times 10^{-10} \text{ cm}^2/\text{s}$ (within grains) and $2.05 \times 10^{-8} \text{ cm}^2/\text{s}$ (in grain boundary affected zones) [81,99] and $1 \times 10^{-4} \text{ mol.nm}^{-3}$ respectively. Thus the model uses a relatively straightforward coupling from macro to micro scales, assuming isotropic mechanical/diffusivity behaviour in the former and mechanical anisotropy and varying hydrogen diffusivity values in the latter.

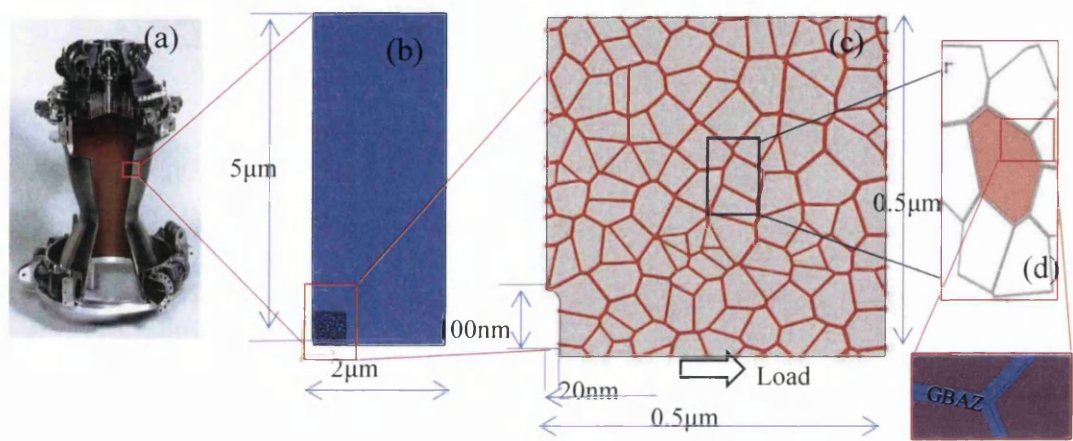


Figure 7.7.1 (a) Macro scale combustion chamber of a rocket [74]. (b) Geometry of 2D CMCD macro model domain. (c) Microstructural polycrystalline model composed of grains and grain boundary affected zones (darker) with a pre-placed nano crack at bottom left. (d) Close-up view of nano grain (shaded), grain boundaries and below a higher magnification showing grain boundary affected zones (GBAZ).

Figure 7.7.2 (a) shows the von Mises stress distribution in the microstructural domain under a $1 \times 10^{-11} \text{ N/nm}^2$ applied uniform load. The stresses observed near the defect are high as expected and they are heterogeneous near and along the grain boundary. The stresses in the rest of the microstructural region are also heterogeneous between grains and grains boundaries for the uniform applied stress. These heterogeneous stress distributions show high stresses near grain boundaries and triple junctions when compared to grain interiors due to the anisotropy arising from the random crystallographic orientation constraints and deformation constraints caused by the grains and adjacent neighbouring grains as reported in the previous research [81, 91, 213, 223, 225].

Figure 7.7.2 (b) shows the shear stress in the microstructural domain. High shear values are observed near and along GBs and TJs (highlighted in dotted circles) and also shear gradients are typically higher between neighbouring grains. Stress

analysis has also been done using isotropic material parameters (i.e. no crystal orientation effects). The results, contained in figure 7.7.2 (c), show a homogeneous stress distribution across grains and GBs as expected.

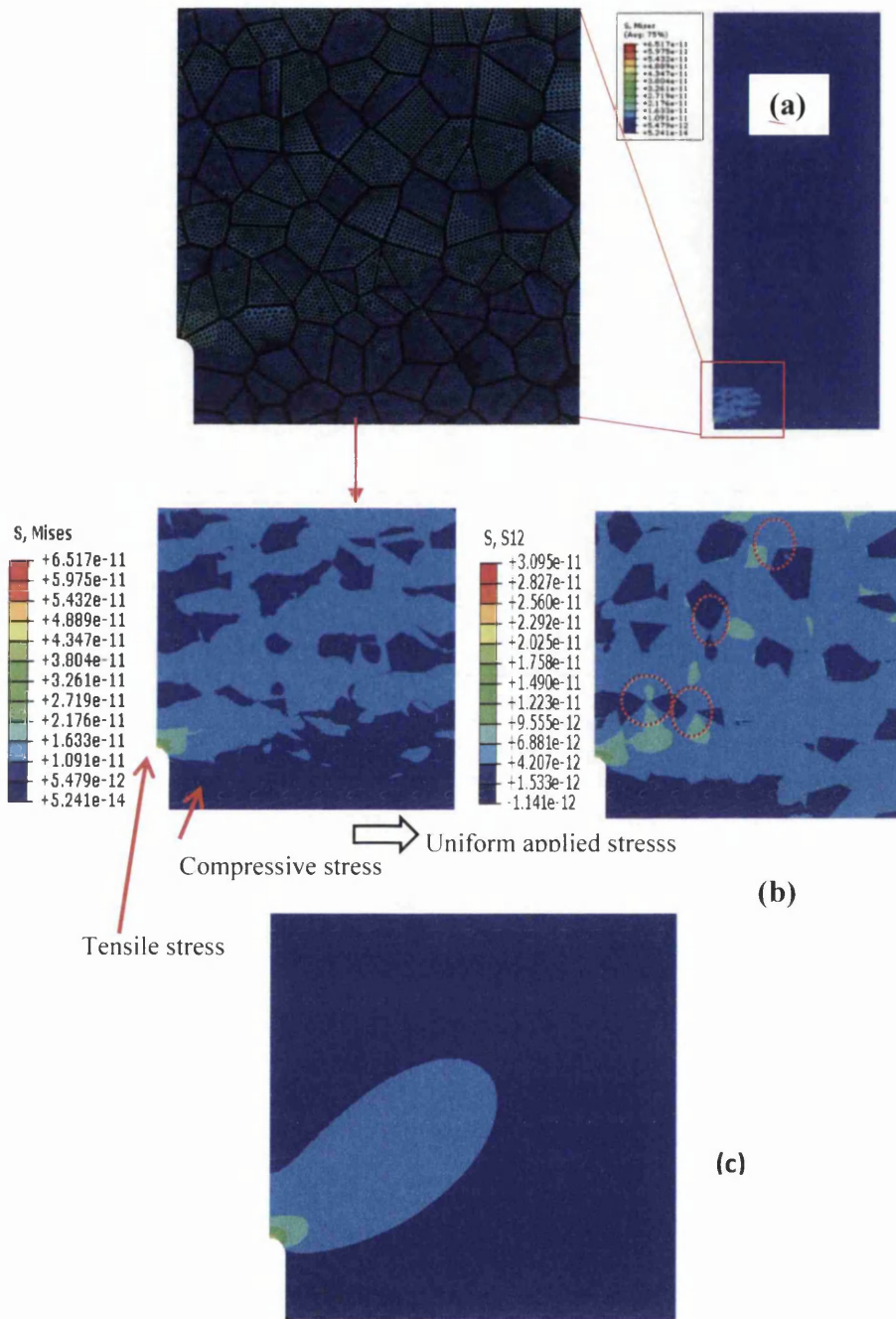


Figure 7.7.2. Mechanical response in the microstructural region for uniform applied stress. (a) von Mises stress (N/nm^2). (b) Shear stress (N/nm^2). (c) Predicted von Mises stress (N/nm^2) without microstructural anisotropy effects.

It should be noted that stresses in the vicinity of the crack tip are higher when microstructural inhomogeneity is included (i.e. stress with microstructural

inhomogeneity (S^m) = 65.17×10^{-12} N/nm²), Figure 7.7.2 (a) and lower for the homogeneous case (i.e. stress without microstructural inhomogeneity (S^h) = 53.44×10^{-12} N/nm²) in Figure 7.7.2 (c).

Figure 7.7.3 shows the multiphysics chemo-mechanical response in the form of a hydrogen distribution with associated hydrogen accumulation in the microstructural region ahead of the defect tip after (a) 1 second (b) 1 week of elapsed time. It also shows significant hydrogen accumulation along GBs and TJs due to high tensile stresses induced in the microstructure. The rapid diffusion paths along GBs and TJs combined with high tensile stresses leads to accumulations of hydrogen atoms forming clusters of high hydrogen concentration. Lower hydrogen accumulation is observed along GBs and TJs near regions of compressive stress. Compressive stresses coupled with faster diffusion along GBs and TJs effectively pushes the hydrogen atoms out from GB and TJ zones. Figures 7.7.3 (b) and (c) show the chemo-mechanical response in the micro domain without the mesh and with the mesh respectively. Figure 7.7.3 (d) shows the purely mechanical response as well the chemo-mechanical response along the normalized distance in the micro domain along the arrow line shown in Figure 7.7.3 (c). “G” represents grain and “GB” represents GB in this figure. The dotted line curve shows the stress concentration in N/nm² and the solid line curve shows the hydrogen concentration in mol.H/nm³.

Changes in local stress and hydrogen concentration at the grain scale are observed when moving from one grain to another grain. At GBs a peak value is often observed. The triple junctions display high accumulations of hydrogen compared to grains and other grain boundaries. These effects are due to neighbouring grain shapes and orientations. TJs are a meeting point of three or more GBs. Figure 7.7.3 (e) shows the variation in hydrogen concentration with distance moving along various GBs towards various TJs. These data are 130 data points along 18 GBs leading to 5 TJs plotted in the figure. This shows that when moving towards a TJ along a GB the predicted hydrogen concentration values (i) increase moving towards some TJs and (ii) decrease moving towards other TJs. Whether a high or low accumulation of hydrogen at triple junctions occurs is dependent on whether tensile or compressive stress is present in addition to the orientation of the grains and neighbouring grains as well as grain shape in the vicinity of the TJ.

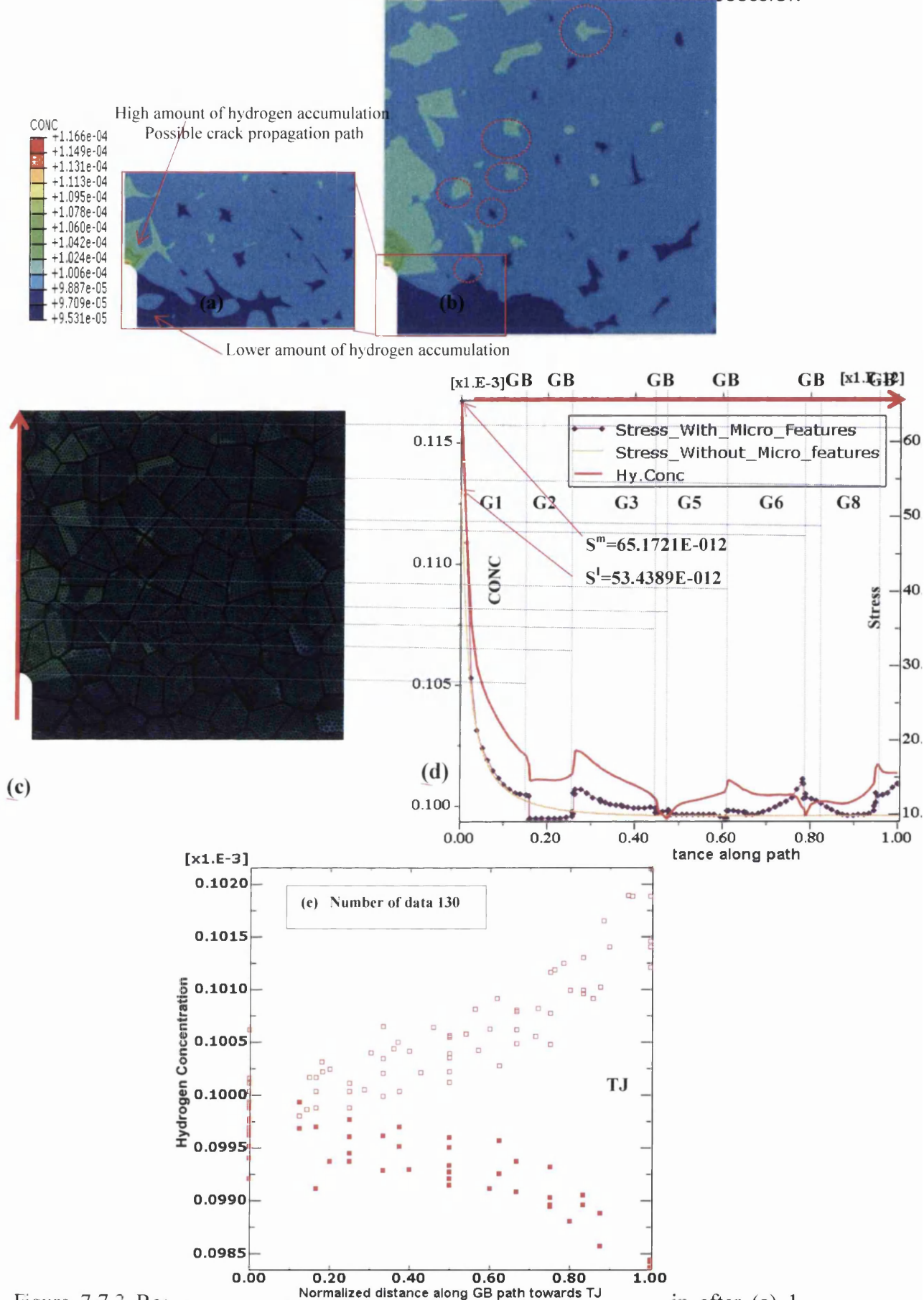


Figure 7.7.3 Reorganisation of hydrogen in the microstructural domain after (a) 1 seconds. (b) 1 week and (c) show hydrogen distributions without mesh and with mesh respectively (dotted circles show the accumulation of hydrogen on triple

junctions. (d) Hydrogen distribution (solid line, mol.H/nm³) and stress distribution (dotted line) along the normalized path along arrowed line shown in (c) also showing the stresses in the vicinity of the crack tip are higher in model with microstructural feature (i.e. $S^m=65.17 \times 10^{-12}$ N/nm²) and lower in model without microstructure feature (i.e. $S^l=53.44 \times 10^{-12}$ N/nm²). (e) Change in hydrogen concentration with normalized distance along various GB paths towards TJs (where the value of 1 on the x-axis is the TJ). The hydrogen concentration values for 130 data are collected along 18 GBs belonging to five TJs (among the five TJs, three TJs have four GBs per TJ and two TJs have three GBs per TJ).

The prediction of tensile or compression stress at GBs and TJs depends on the orientation of grains and their neighbouring grains as well as grain shape in the vicinity of the TJ. The results here show it is important to consider the microstructural features of the material to better capture local stresses and the accumulation of hydrogen when investigating hydrogen embrittlement in polycrystalline materials.

7.8 Multiscale model for localized hydrogen induced cracking

7.8.1 Experimental results and discussion

The multiscale FE model has been used to simulate stress assisted hydrogen diffusion using real microstructures extracted from EBSD analysis as described in section 6.5. The fractured sample specimens were experimentally analysed using EBSD to collect the grain boundary character distribution (GBCD) and triple junction character distributions (TJCD) related to the crack initiation and propagation path. The multi-scale FE simulation results of high and low stress concentrations, hydrogen concentration regions related to GBCD and TJCD were correlated with experimental results. The experimental and simulation results follow in the next section. First, the grain boundary character is described as follows.

- Special $\Sigma 3$ twin boundaries were defined as $\Sigma 3$ grain boundary.
- Coincidence site lattice (CSL) boundaries with $\Sigma \leq 11$ other than $\Sigma 3$ twin boundary were defined as special CSL (SCSL) grain boundaries.
- Grain boundary misorientations $0^\circ \leq \theta \leq 15^\circ$ were defined as low angle grain boundary (LAGB).
- Grain boundary misorientations $50^\circ \leq \theta \leq 62^\circ$ other than $\Sigma 3$ and $\Sigma 11$ were defined as special random grain boundary (SRGB)
- CSL grain boundaries other than SCSL and $\Sigma 3$ twin boundaries, and grain boundary misorientations other than SRGB, were defined as random grain boundaries (RGB).

The knowledge gained from GB misorientation microstructure FE simulation results in section 7.5 and 7.7 throw lights to characterize the grain boundary type and triple junction type in this chapter. Figure 7.8.1 (a) shows the SSRT fractured annealed nickel specimen and (b) shows the FEA simulated macro scale von Mises stress distribution of the SSRT specimen. Cut boundary techniques have been used in this simulation to minimize the computation time and resource. The macro scale coarse mesh FE analysis results show the macro-scale distribution of von Mises stress and the critical high stress accumulation site has been identified using this

simulation result. The critical site was replaced by a real microstructural RVE as a sub model and a micro scale FE analysis was done using the cut boundary technique. The micro scale fine mesh sub model simulation results show the local anisotropic grain and grain boundary scale distribution of Von Mises stress at the critical site of the specimen arising from the effects of crystallographic orientation as shown in figure 7.8.1 (c). Figures 7.8.1 (d) and (e) show the local distribution of stress along the traction direction and perpendicular to the traction direction, the von Mises stress and the hydrostatic stresses on a $\Sigma 3$ grain boundary and random grain boundary (RGB) respectively. These results show that there are high accumulations of hydrostatic stress along the RGB and a much lower accumulation of hydrostatic stress along $\Sigma 3$ GB. There is a large jump in hydrostatic stress between neighbouring grains of RGB and small or zero jumps in hydrostatic stress between neighbouring grains of $\Sigma 3$ GB. So, the RGBs may act as hydrogen trapping sites which may lead to crack initiation and propagation along these boundaries. This can be evaluated by using multi-scale FE stress assist hydrogen diffusion analysis.

These multiscale FE simulation results are compared with EBSD crystallographic orientation results on the hydrogen induced intergranular fractured specimen. Figure 7.8.2 shows the SSRT fractured annealed nickel specimen and the FE simulation results. Figure 7.8.2 (a) shows the real SSRT tested fractured specimen. Figure 7.8.2 (b) shows the hydrogen distribution on the macro scale FE simulation results for the SSRT specimen. Stress assisted hydrogen diffusion analyses were carried out using cut boundary techniques to minimize the computation time and resource. Figure 7.8.2 (c), from results of the microstructural FE coupled chemo-mechanical analysis, shows the localized micro scale anisotropic distribution of hydrogen along various GBCD and triple junction characteristic distributions (TJCD). The figure also shows the crack initiation point and crack propagation path, which is along random grain boundary. The hydrogen segregation along RGB is greater than the critical hydrogen concentration so a crack would initiate at this point. This has been validated from the fracture analysis of EBSD results which can be found in Figure 7.8.2 (f). Figure 7.8.2 (d) shows the effect of random GBCD and TJCD on hydrogen segregation. This RGB and its TJ connectivity is a high hydrogen segregation/trapping zone.

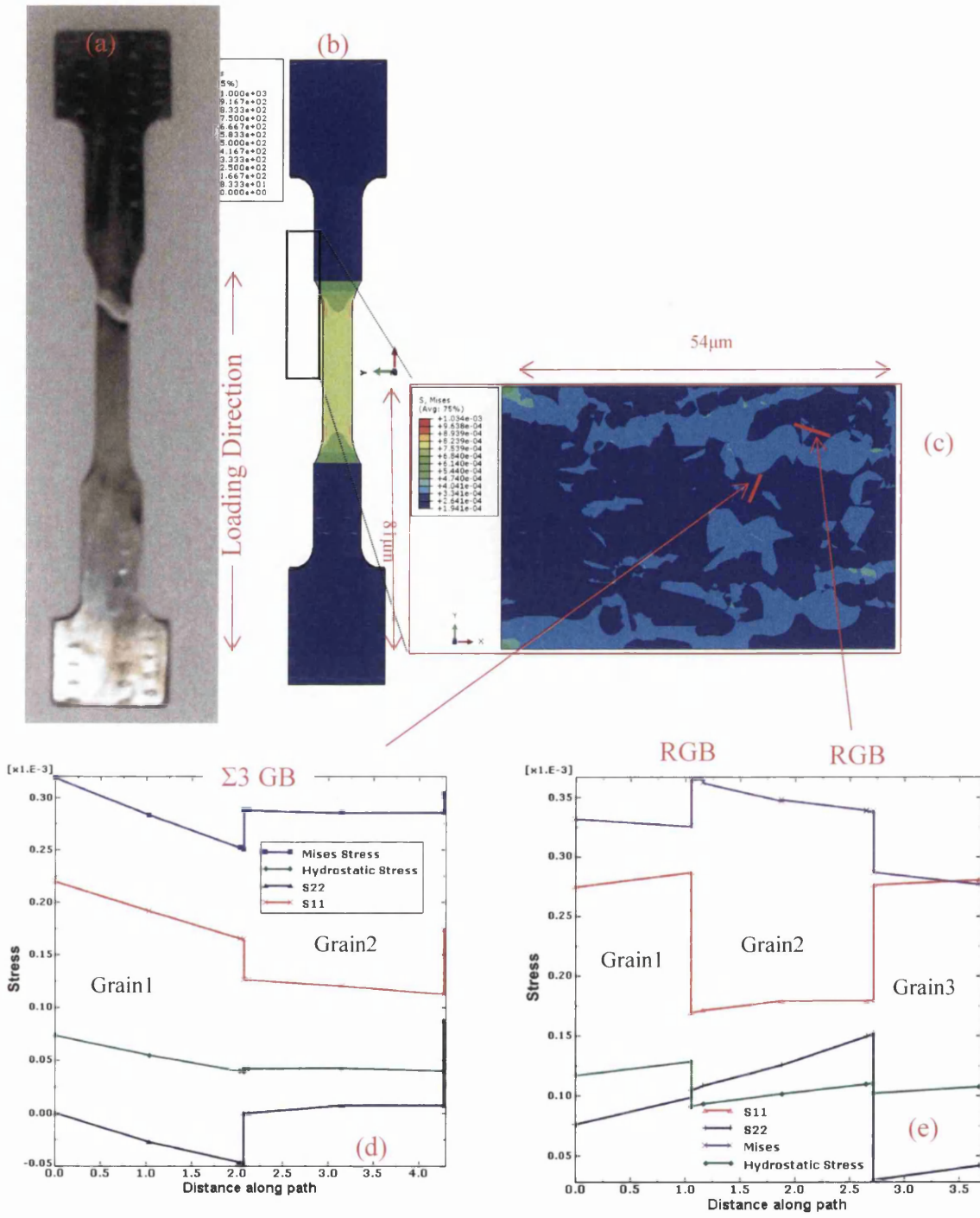


Figure 7.8.1 Multiscale finite element simulation results using cut boundary techniques. (a) The SSRT tested fractured PP-Ni specimen. (b) Macro scale coarse mesh based finite element analysis result. (c) Close up view showing the high stress accumulation critical site and local micro scale Von Mises stress distribution in the MRVE based FE simulation result [Note: macro and micro stress units are in N/mm^2 and $N/\mu m^2$ respectively]. (d) and (e) show the localised stress distributions plot along $\Sigma 3GB$ and RGB respectively.

The segregated/trapped hydrogen in this RGB exceeds the critical limit in nickel (the critical hydrogen concentration for fracture criteria was experimentally determined to be 33 ppm - Airbus confidential report). This means cracks initiate at the RGB as shown in experimental result in Figure 7.8.2 (f). The initiated crack propagated along RGB as shown in Figure 7.8.2 (f). As shown by the multiscale simulation and the experimental results, hydrogen induced grain boundary cracking seems to be driven by local random grain boundary tractions and RGB-RGB-RGB triple junction connectivity tractions arising from stress incompatibilities between neighbouring grains and by the segregated hydrogen in these zone exceeding the critical level. The multiscale FE analysis results also shows that RGB-RGB-RGB connected TJs are more susceptible to hydrogen induced cracking than RGB and $\Sigma 3$ - $\Sigma 3$ - $\Sigma 3$ connected TJs. Cracks on RGB-RGB-RGB connectivity TJs propagate along high hydrogen content intergranular RGBs as shown in Figure 7.8.2 (f). The multiscale model predicts this hydrogen induced crack initiation and propagation at a local grain scale level. Figure 7.8.2 (e) shows the effect of $\Sigma 3$ GBs, SCSL GBs and SRGBs and TJ connectivity on hydrogen segregation/distributions. This observation reveals that $\Sigma 3$ twin grain boundaries, CSL GBs and SRGBs segregate less hydrogen (less than critical level) and so the crack does not necessarily initiate in these grain boundaries. These special GB connectivity TJs are also observed as less hydrogen segregated zones with the amount of hydrogen being less than the critical level. The multi-scale finite element simulation correctly predicts the hydrogen induced crack initiation and propagation path as validated by EBSD as shown in Figure 7.8.2. Detailed EBSD analysis was conducted in the hydrogen induced SSRT fractured specimen on the fracture surface as shown in figures 7.8.3 (a) and (b). Although most of the hydrogen induced intergranular cracks were observed at RGBs, there were very few observed at SRGB and SCSL. On the other hand, hydrogen induced intergranular cracks were observed at low angle GBs and $\Sigma 3$ twin grain boundaries. Moreover, cracks also nucleated at RGB-RGB-RGB connectivity TJs. The effects of GBCD on experimental hydrogen induced intergranular cracks and predicted intergranular hydrogen segregations above the critical level are quantitatively examined as follows. Figure 7.8.3 (c) shows the relationship between (i) the frequencies of hydrogen induced intergranular cracking (ii) the frequencies of multiscale FE predicted intergranular hydrogen concentrations above the critical level and (iii) the grain boundary character.

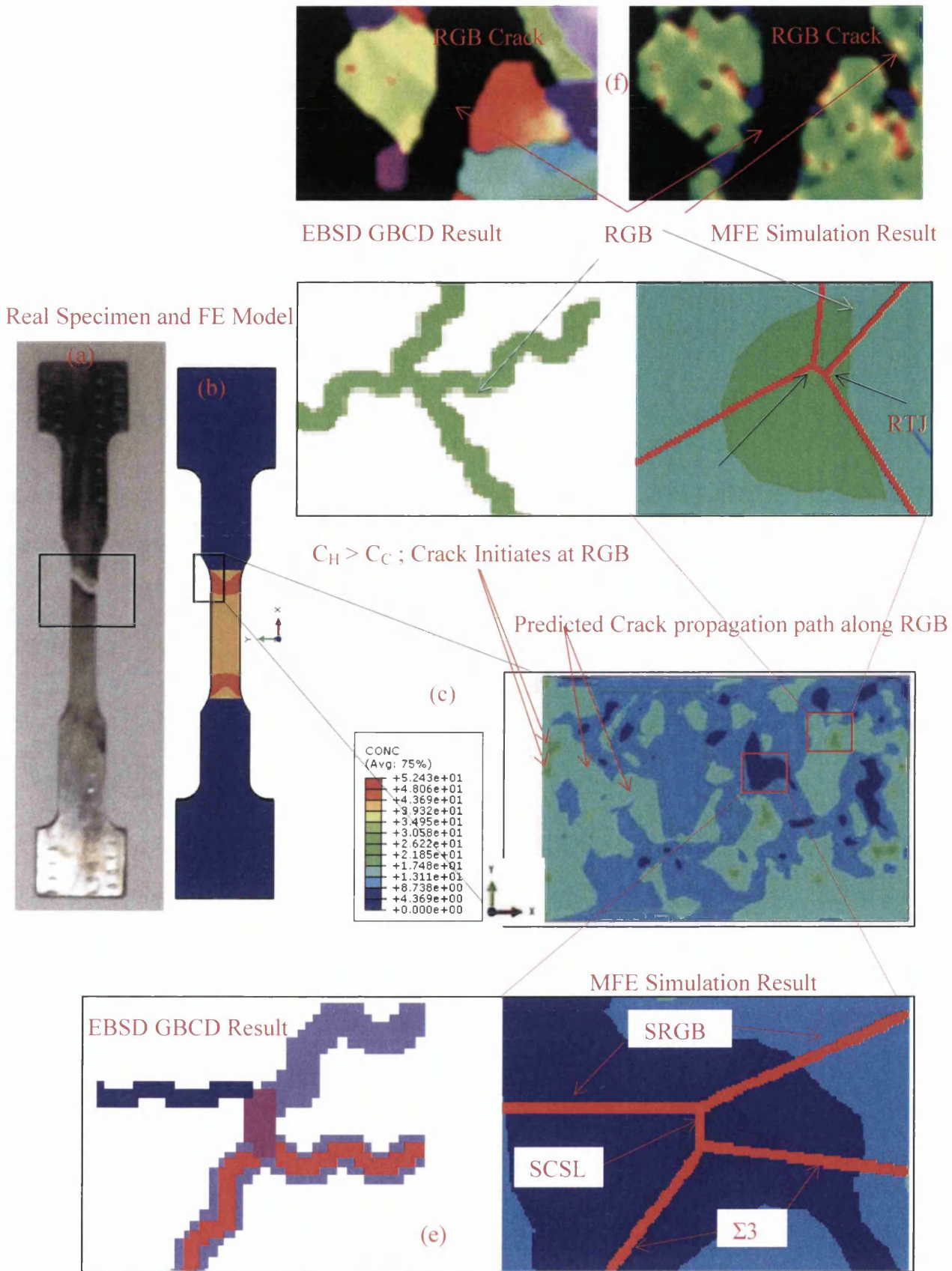


Figure 7.8.2 Multiscale FE stress assisted hydrogen diffusion (FESAD) simulation results based on cut boundary techniques. (a) The SSRT tested fractured PP-Ni specimen. (b) Macro scale coarse mesh based FESAD result. (c) Close up view of

local hydrogen distribution (ppm) at the critical site. Localised hydrogen distributions at two different zones (d) high hydrogen accumulated zone (Random GBCD) and (e) Low hydrogen accumulated zone (Special GBCD) and grain boundary information from EBSD. (f) Experimental EBSD characterization results of hydrogen induced SSRT fracture specimen showing crack initiation and propagation along RGB. Note: C_H is segregated hydrogen concentration; C_C is critical hydrogen concentration, 33 ppm.

The data were obtained from the fracture surface of the SSRT specimen using EBSD. The hydrogen induced intergranular cracks were observed at 37 grain boundaries on the fracture surface. 83.78 % of cracks within GBs were RGB, 10.81 % were SRGBs and 5.4 % were SCSL. No hydrogen induced intergranular cracks were observed at low angle GBs or $\Sigma 3$ boundaries. GB segregated hydrogen concentrations above the critical level were observed at 53 GBs at the critical site from the FEA prediction. In percentage terms GBs with predicted hydrogen concentrations above the critical value were 84.9 % RGB, 9.43 % SRGB and 5.67 % SCSL. No GBs with hydrogen concentrations above critical level were observed at low angle GBs or $\Sigma 3$ boundaries. These experimental and multiscale FE results enhance the understanding of the grain boundary engineering relationships between GBCD and HIC/IHE and localized fracture criteria. This investigation also reveals that an increase in the fraction of $\Sigma 3$, SCSL, low angle GB and SRGB grain boundaries and a reduction in the fraction of RGB in polycrystalline nickel will increase the resistance to hydrogen induced cracking and intergranular hydrogen embrittlement. Both experimental and multiscale modelling analysis results show that the random grain boundaries are susceptible to hydrogen induced crack initiation which leads to fracture. If possible, reducing the random grain boundary fraction and increasing special grain boundary fractions using grain boundary engineering techniques would likely increase ductility and minimise premature unexpected hydrogen embrittlement (HE) failure in polycrystalline nickel.

Crack resistant $\Sigma 3$ Grain boundary

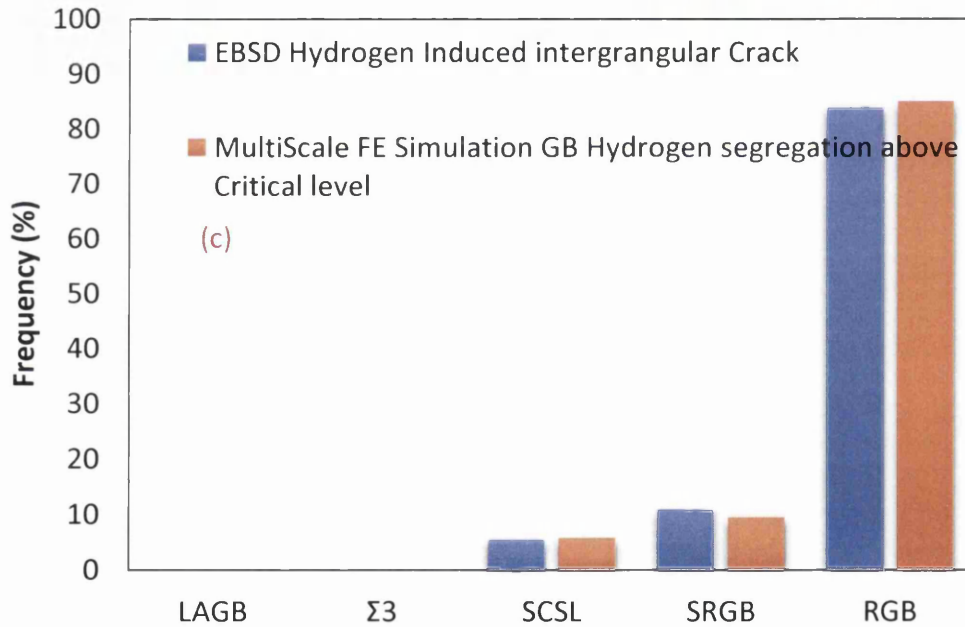
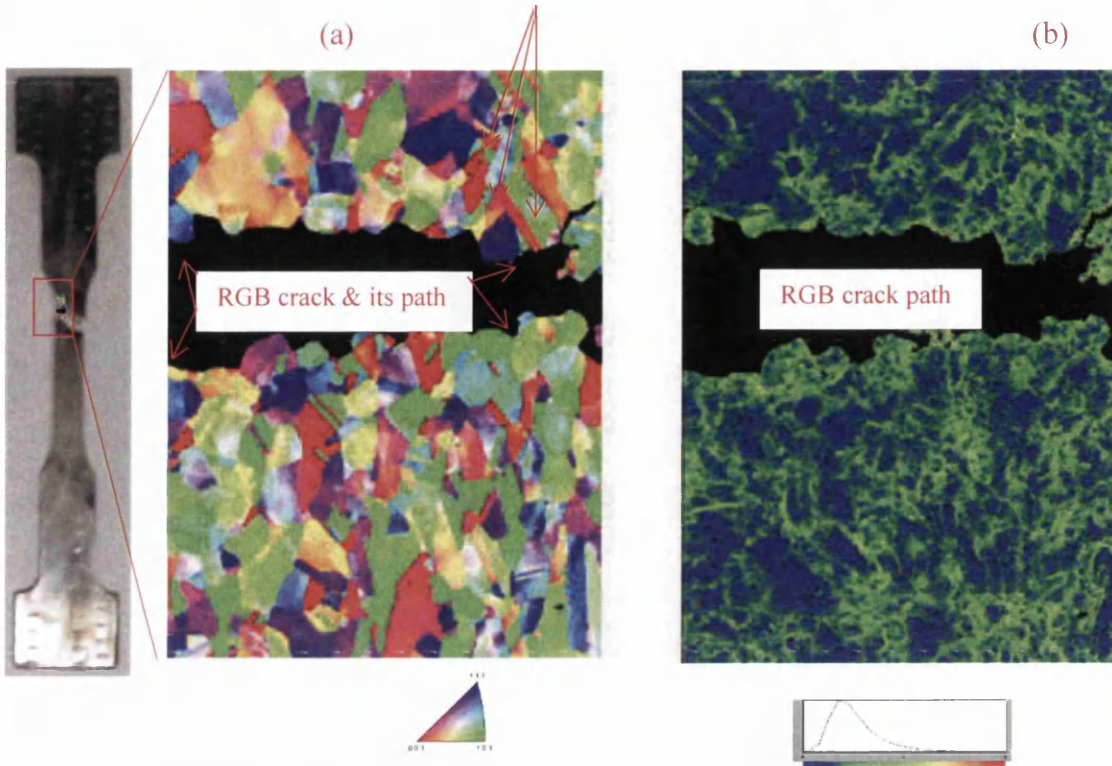


Figure 7.8.3 EBSD image showing intergranular hydrogen induced cracks on the fractured SSRT specimen surface. (a) IPF map showing crystallographic orientations and GBCD on the crack path. (b) Local misorientations on the fracture surface which qualitatively corresponds to geometric necessary dislocation density [148]. (c) Relationship between experimental hydrogen induced intergranular cracks, simulated GB segregated hydrogen above the critical level and grain boundary character.

7.9 Hydrogen Embrittlement in Nickel based superalloy 718

7.9.1 Experimental results

Figure 7.9.1 shows the microstructure of the undeformed solution heat treated Alloy 718. Figures 7.9.1 (a) and (b) shows the results of EBSD analysis, crystallographic orientation distribution maps of grain structures as an inverse pole figure (IPF) and Euler angle distribution along the rolling direction (RD) of the undeformed material microstructure respectively. Figure 7.9.1 (c) and (d) show the Special Coincidence Site Lattice (CSL) GBs (GB misorientations $\Sigma < 29^\circ$) of the undeformed microstructure and the relative statistics respectively. Table 7.9.1 gives the percentage values of CSL SGBs for the statistical distribution shown in figure 7.9.1 (d). This data shows that 33.3% of grain boundary lengths are $\Sigma 3$ SGBs (twin boundaries). 10.32% of GB lengths are found to be other SGBs. For the solution hardened Alloy 718 a total of 43.62% of grain boundaries are found to be SGBs. Figure 7.9.1 (e) shows the backscattering electron (BSE) SEM image of the undeformed microstructure. The average grain size is 8.17 μm without twin boundaries and this distribution is shown in figure 7.9.1 (f). The average grain size was evaluated from 1447 grains within an area of 179830 μm^2 . This study shows that the microstructure of the material prior to testing is free from porosity with grain sizes and shapes that are relatively homogeneous.

GB Misorientation angle(θ°)	60	36.87	38.94	50.48	61.93	51.68	46.31
CSL / GB Sigma(Σ)	3	5	9	11	17b	25b	29a
Percentage (%)	33.3	0.37	1.9	3.3	0.59	0.42	3.74

Table 7.9.1 Special CSL GBs ($\Sigma < 29^\circ$) and percentages in the undeformed solution heat treated superalloy alloy 718.

Figure 7.9.2 (a) shows the macroscopic engineering stress-strain curves obtained from SSRT conducted in air and hydrogen charging (4 hours and 16 hours pre-charging as well hydrogen charging during the SSRT). All tests were conducted at ambient temperature (21°C). This shows that there is no significant change in yield

strength and 0.2% offset yield strength if samples are tested in air, pre-charged with hydrogen or tested at strain rates of 10^{-3} s^{-1} or 10^{-4} s^{-1} .

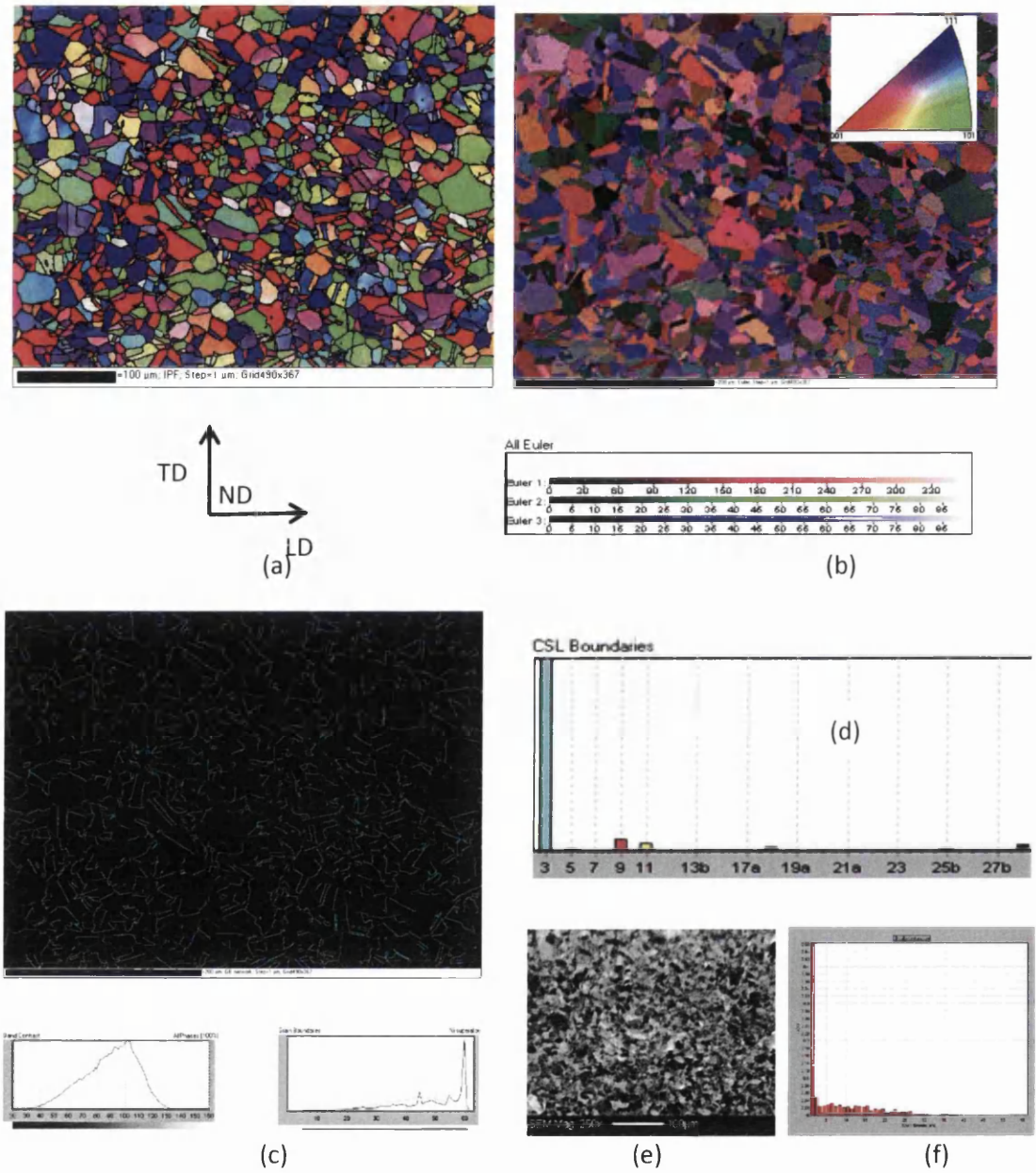
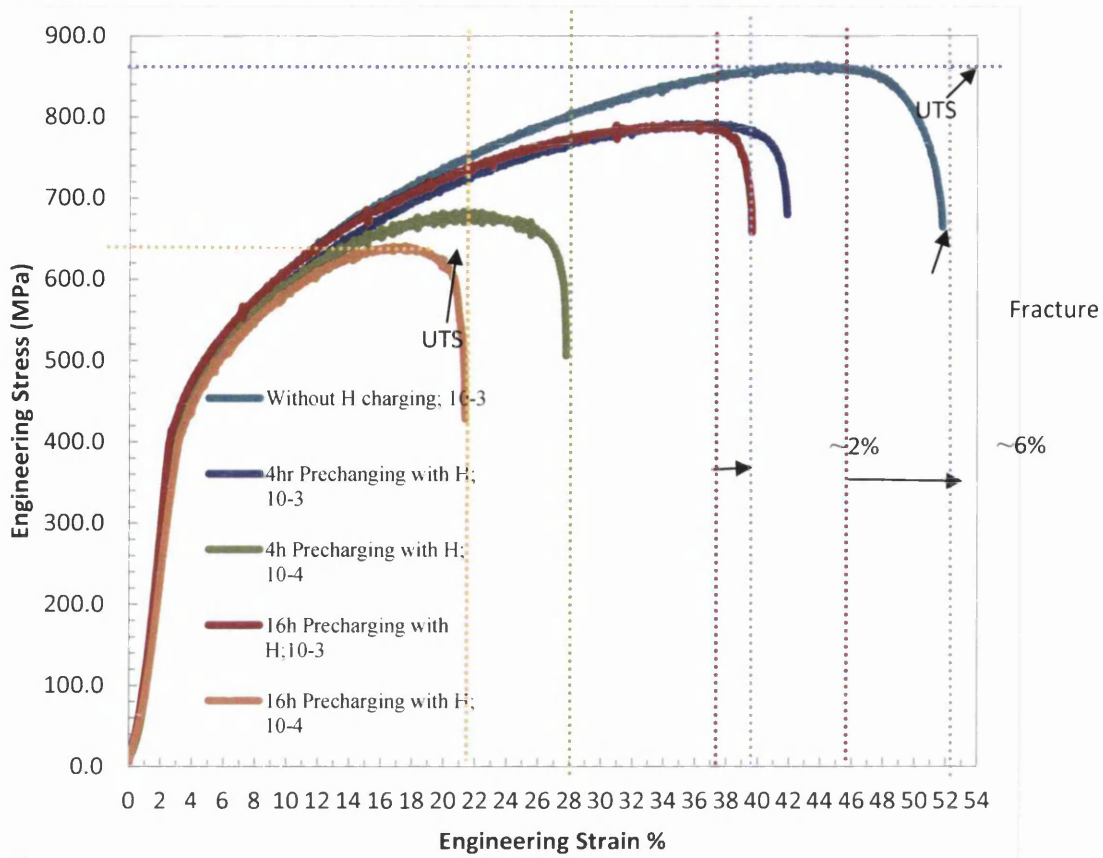
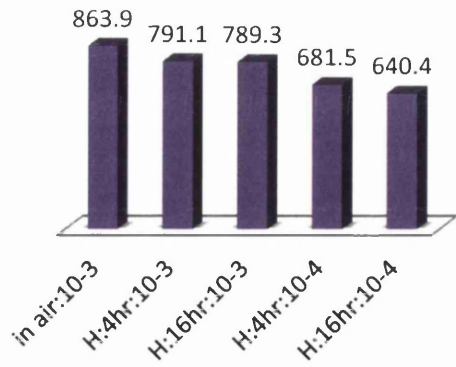


Figure 7.9.1 Shows the microstructure of the undeformed solution heat treated Alloy 718. (a) IPF figure of the undeformed material microstructure and grain morphology. (b) Crystal orientations in Euler angle. (c) Special Coincidence site lattice (CSL) GBs (GB misorientations Σ less than 29°) of the undeformed microstructure and the corresponding statistics in figure (d). (d) GB CSL (c.f. Table 7.9. for corresponding percentages). (e) SEM back scattering electron (BSE) image showing the undeformed microstructure.

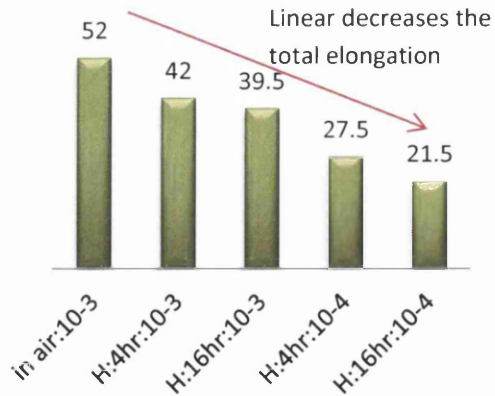


(a)

(b) UTS (Mpa)



(c) Total Elongation (%)



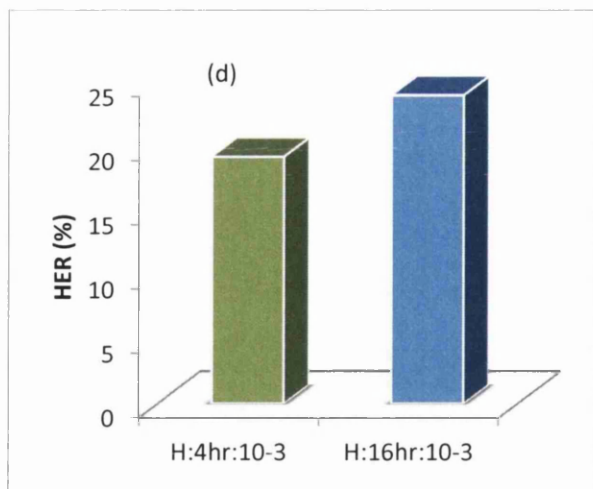


Figure 7.9.2 (a) Results of the slow strain rate test of solution heat treated superalloy Alloy 718 tested in air and with 4 hours and 16 hours in-situ hydrogen charging condition at two different cross head speeds of 10^{-3} s^{-1} and 10^{-4} s^{-1} . (b) and (c) show the hydrogen embrittlement effects of hydrogen charging times and strain rates where (b) shows ultimate tensile strength and (c) shows total percentage elongation to fracture. (d) The effect of hydrogen charging time on the hydrogen embrittlement ratio.

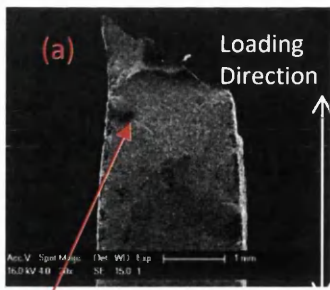
As shown in figure 7.9.2 (a) the measured UTS values for hydrogen charged specimens were significantly lower compared to the specimen tested in air. Ductility was also reduced when decreasing the strain rate from 10^{-3} s^{-1} to 10^{-4} s^{-1} for the hydrogen charged specimens. In terms of strain, the UTS values measured for samples tested with 16 hours hydrogen charging, 4 hours hydrogen charging and without hydrogen charging (i.e. tested in air) occurred at engineering strains of $\sim 37.5\%$, $\sim 39\%$ and $\sim 45.5\%$ respectively for a strain rate of 10^{-3} s^{-1} . For a strain rate 10^{-4} s^{-1} the UTS of samples tested with 16 hours and 4 hours of hydrogen charging occurred at engineering strains of $\sim 17.5\%$ and $\sim 23\%$ respectively. The curves show that sample failure begins at lower strains in the hydrogen charged specimens compared to the specimen tested in air. The increase in charging time increases the uptake of hydrogen in the samples and decreases ductility. The strain from UTS to failure in the non-hydrogen charged sample tested at strain rate 10^{-3} s^{-1} is $\sim 6\%$, which is greater than the equivalent strain in the hydrogen charged specimen tested at 10^{-3} s^{-1} of $\sim 2\%$. Figure 7.9.2 (b) shows the UTS of specimens tested with and without hydrogen charging for two different strain rates. These results illustrate the effects of various parameters on HE.

Hydrogen charging time, for the same strain rate, did not significantly alter measured UTS values. However, the specimens charged for 4 hours tested at strain rates of 10^{-3} s^{-1} and 10^{-4} s^{-1} showed a significant drop in UTS for the material tested at the lower strain rate. This is attributed to the increase in testing time for the strain rate of 10^{-4} s^{-1} . This would increase the time for hydrogen trapping at dislocations, which raises the local stress and this (i) increases local hydrogen diffusion further and (ii) leads to increased dislocation movement. This deformation also leads to incompatibility stresses along grain boundaries arising from elastic and plastic crystal anisotropy as a function of grain boundary misorientations. This dilatational mismatch between crystals generates further dislocation motion and also increases the mobility and segregation of hydrogen to trap sites (mainly intergranular) as previously reported [Wilcox et al., 1965, Mills et al., 1999]. Segregation of hydrogen atoms occurs preferentially at trap sites along highly stressed tensile regions and high stress gradient regions. For longer test durations these hydrogen induced effects are more significant leading to greater embrittlement and lower UTS values for tests extending over longer times, in this case 10^{-4} s^{-1} .

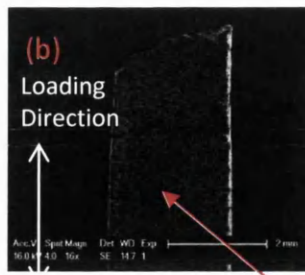
The strain to failure is used to assess the hydrogen embrittlement resistance as shown in figure 7.9.2 (c). Failure strains for samples tested with 16 hours hydrogen charging, 4 hours hydrogen charging and without hydrogen charging were $\sim 39.5\%$, $\sim 42\%$ and $\sim 52\%$ respectively for a strain rate of 10^{-3} s^{-1} . Failure strains for samples tested by 16 hours and 4 hours hydrogen charging were $\sim 27.5\%$ and $\sim 21.5\%$ respectively for a strain rate of 10^{-4} s^{-1} . The increase in hydrogen charging time increases the total amount of hydrogen uptake which decreases plastic flow. This reduces ductility leading to a more brittle failure.

Figure 7.9.2 (d) shows the percentage hydrogen embrittlement ratio (HER) of the hydrogen charged specimens tested at a strain rate of 10^{-3} s^{-1} . The percentage hydrogen embrittlement ratio (HER) is a measure of the susceptibility of metallic materials to hydrogen embrittlement. Lower HER values imply lower susceptibility to HE. The HER value (units: %) is calculated using equation (7.9.1).

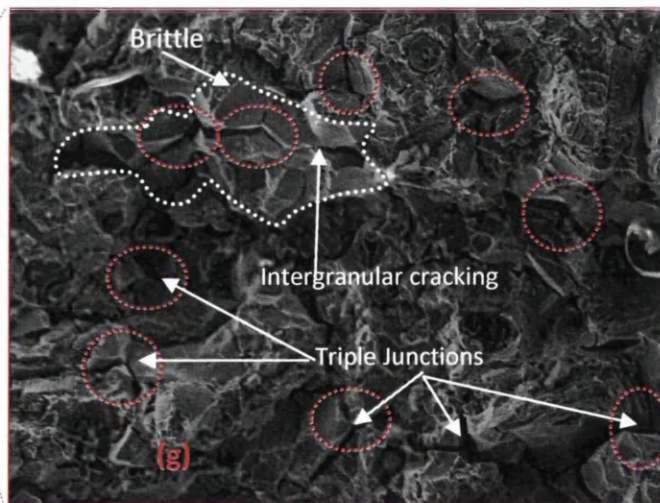
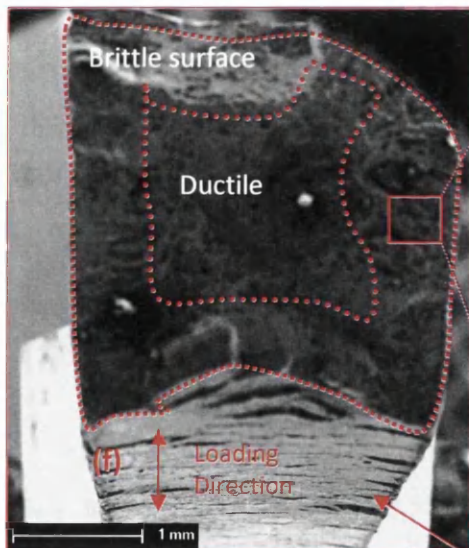
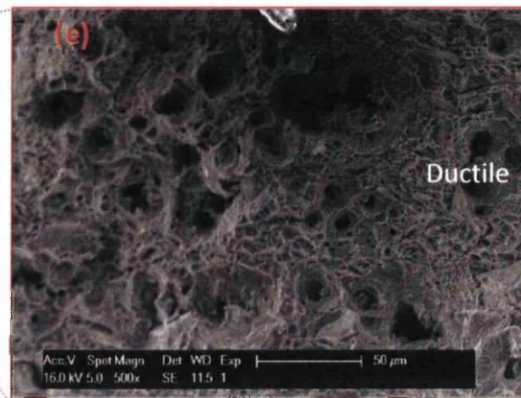
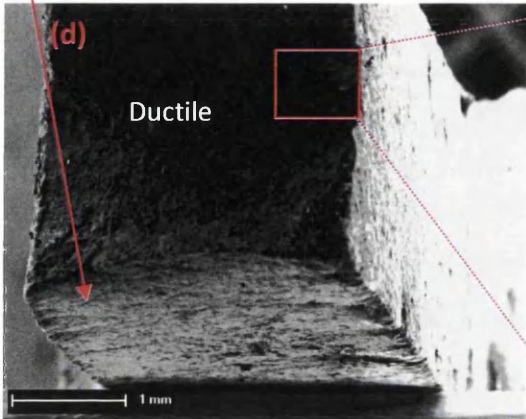
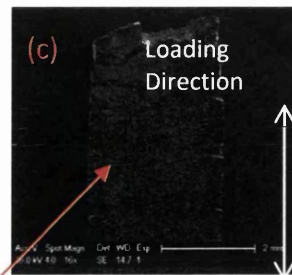
$$HER = \left(\frac{\epsilon_{air} - \epsilon_{hydrogen}}{\epsilon_{air}} \right) \times 100 \quad (7.9.1)$$



No secondary surface cracks are observed perpendicular to loading direction on sample tested in air



Numerous secondary surface cracks perpendicular to loading direction on a sample tested in a hydrogen environment



Numerous secondary surface cracks are observed perpendicular to loading direction

Figure 7.9.3 Scanning electron microscope (SEM) secondary electron (SE) images of fracture surface morphologies along the loading direction (a) samples tested in air, (b) & (c) samples tested in the 16 hours pre-charged condition with in-situ hydrogen charging during tests at strain rates of 10^{-3} s^{-1} and 10^{-4} s^{-1} respectively. (d) & (e) show secondary electron images of the fracture specimen normal to the loading direction of the sample tested in air (NB No secondary cracks are observed). (e) shows a typical ductile fracture mode. (f) & (g) show the fracture specimen tested in the hydrogen charging condition normal to the loading direction (NB numerous

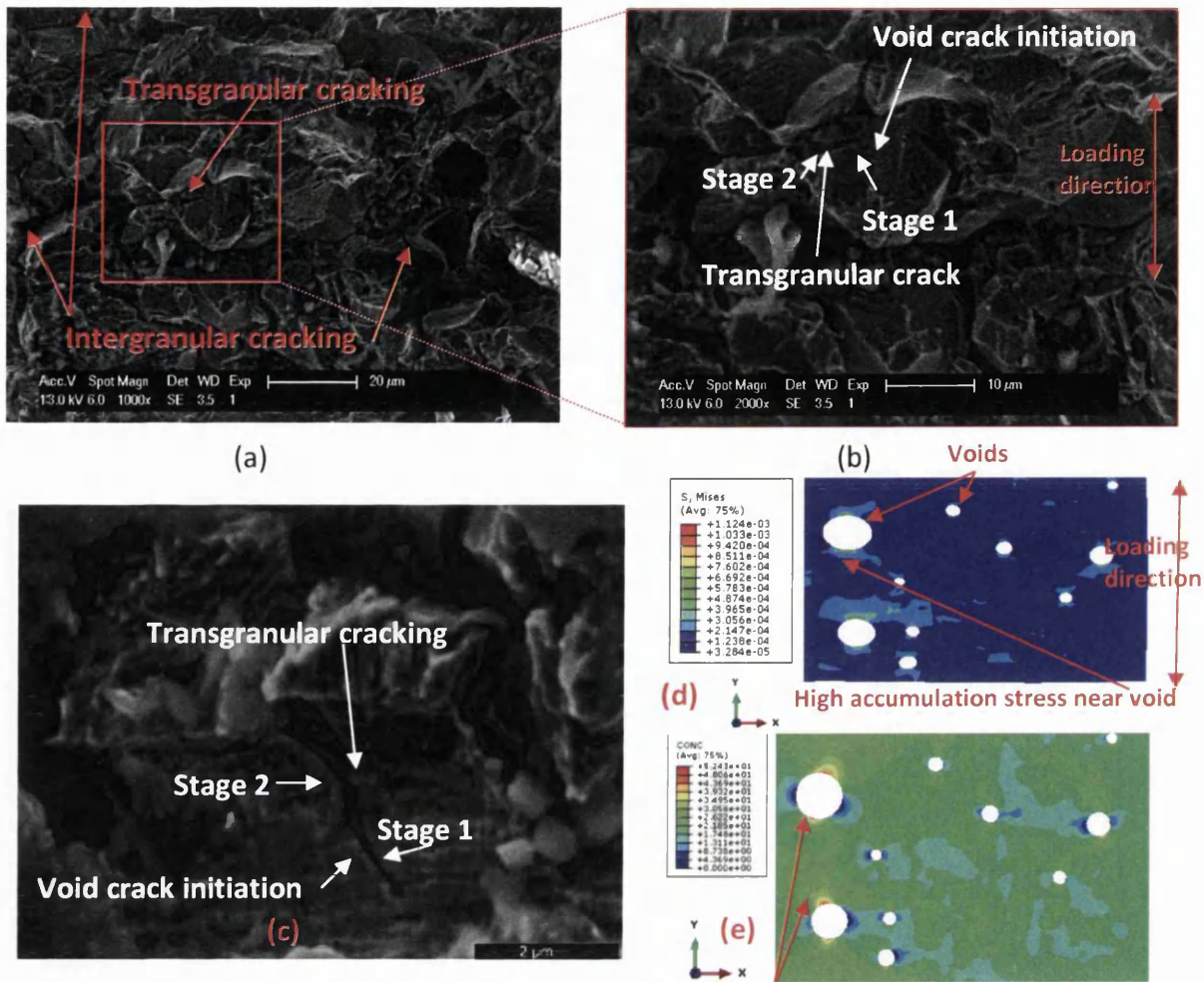
secondary surface cracks are observed perpendicular to the loading direction). (g) shows a typical brittle fracture mode in the hydrogen charged sample displaying intergranular cracking and indicating triple junctions are more susceptible to hydrogen induced cracking and appear to be crack initiation points (dotted red circles).

Here ϵ_{air} is the failure strain for a specimen tested in air and $\epsilon_{hydrogen}$ is the failure strain of a specimen tested under hydrogen charging conditions.

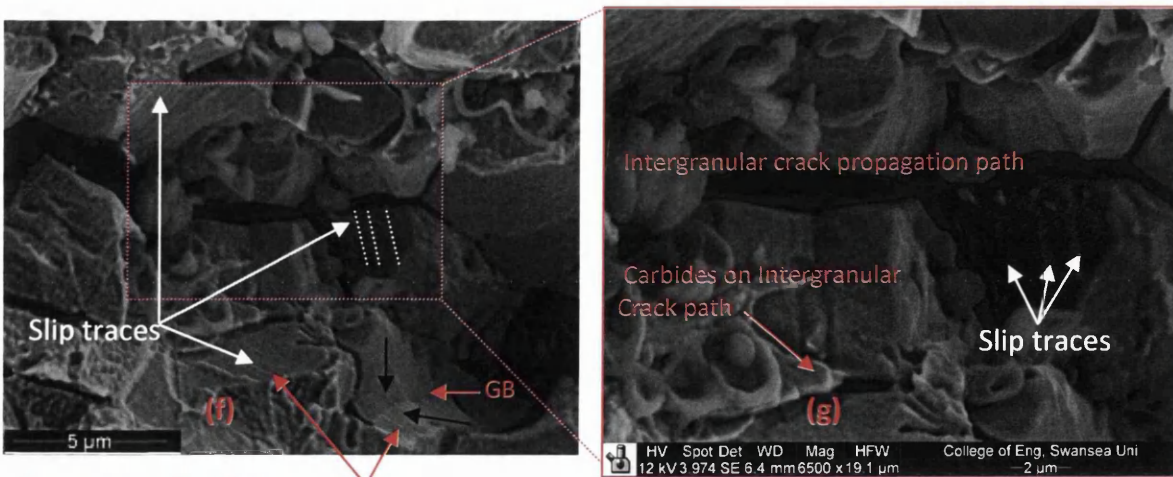
The results in figure 7.9.2 (d) show the effect of hydrogen in reducing the ductility of solution heat treated superalloy Alloy 718 with the longer charging time resulting in a higher HER. In summary, the sample without hydrogen is most ductile and samples charged with hydrogen display lower failure strains.

Figure 7.9.3 (a) shows the secondary electron (SE) image obtained from SEM of the fractured samples of the SSRT test conducted in air. One primary crack has led to failure and no secondary cracks were observed in the specimen tested in air. Figure 7.9.3 (b) & (c) show the fractured specimens from SSRT tests with 16 hours hydrogen pre-charging for strain rates of 10^{-3} and 10^{-4} s^{-1} respectively. In contrast there are many secondary surface and subsurface cracks visible in these specimens. The observed secondary cracks are largely perpendicular to the loading direction. Larger secondary cracks are observed on the surface of samples tested at strain rate 10^{-4} s^{-1} compared to samples tested at strain rate 10^{-3} s^{-1} . A decrease in strain rate increases the time duration of the test which will increase the amount and depth of hydrogen diffusion into the sample specimen and this corresponds to the amount of subsurface cracks observed.

Figures 7.9.3 (d) and (e) show the macro-scale cross section of the fracture sample and micro-scale fracture surface of the sample tested in air. Figure 7.9.3 (e) shows a typical ductile fracture surface. Figures 7.9.3 (f) and (g) show the fracture surface of the specimen tested with 16 hours hydrogen pre-charging at the macro and micro scales respectively. The fracture surface shows outer regions of brittle fracture and inner regions of ductile fracture. Brittle fracture surfaces were observed near the edge of specimen and ductile fracture surfaces were observed towards the centre of the specimen.

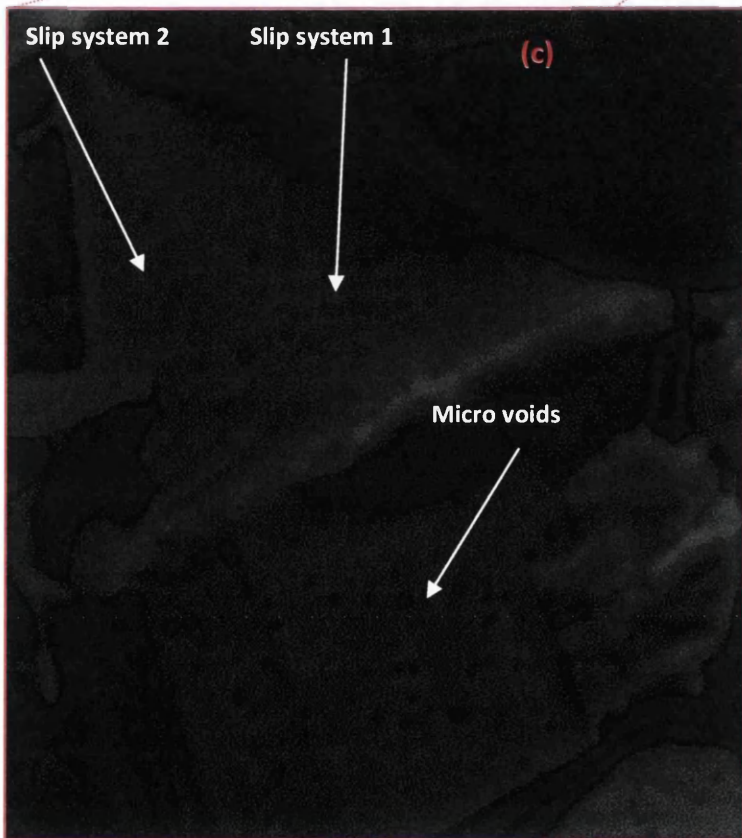
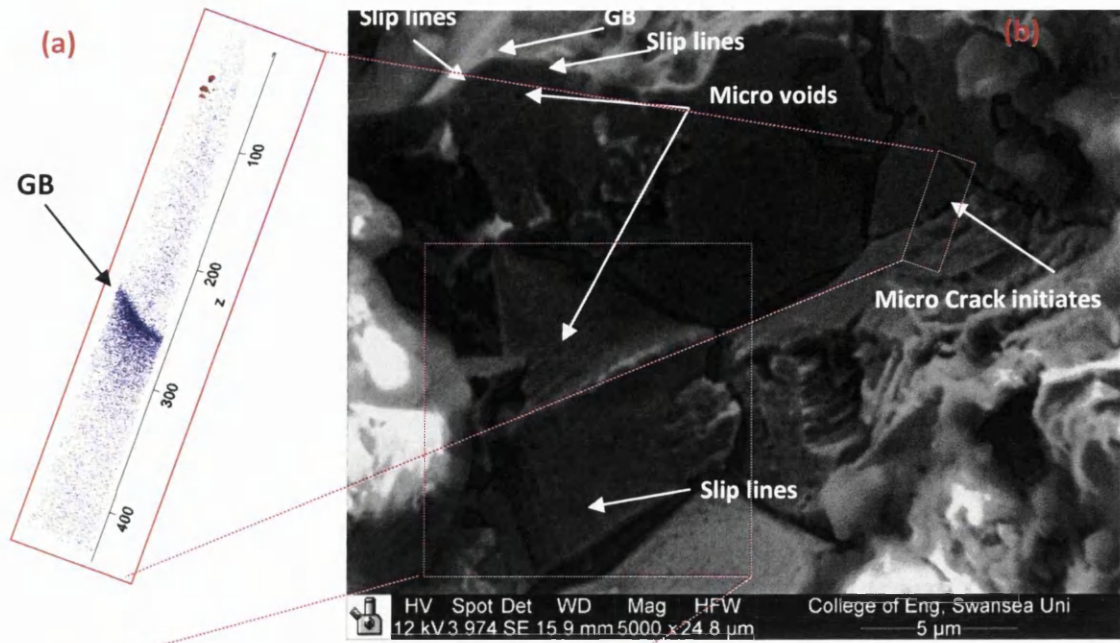


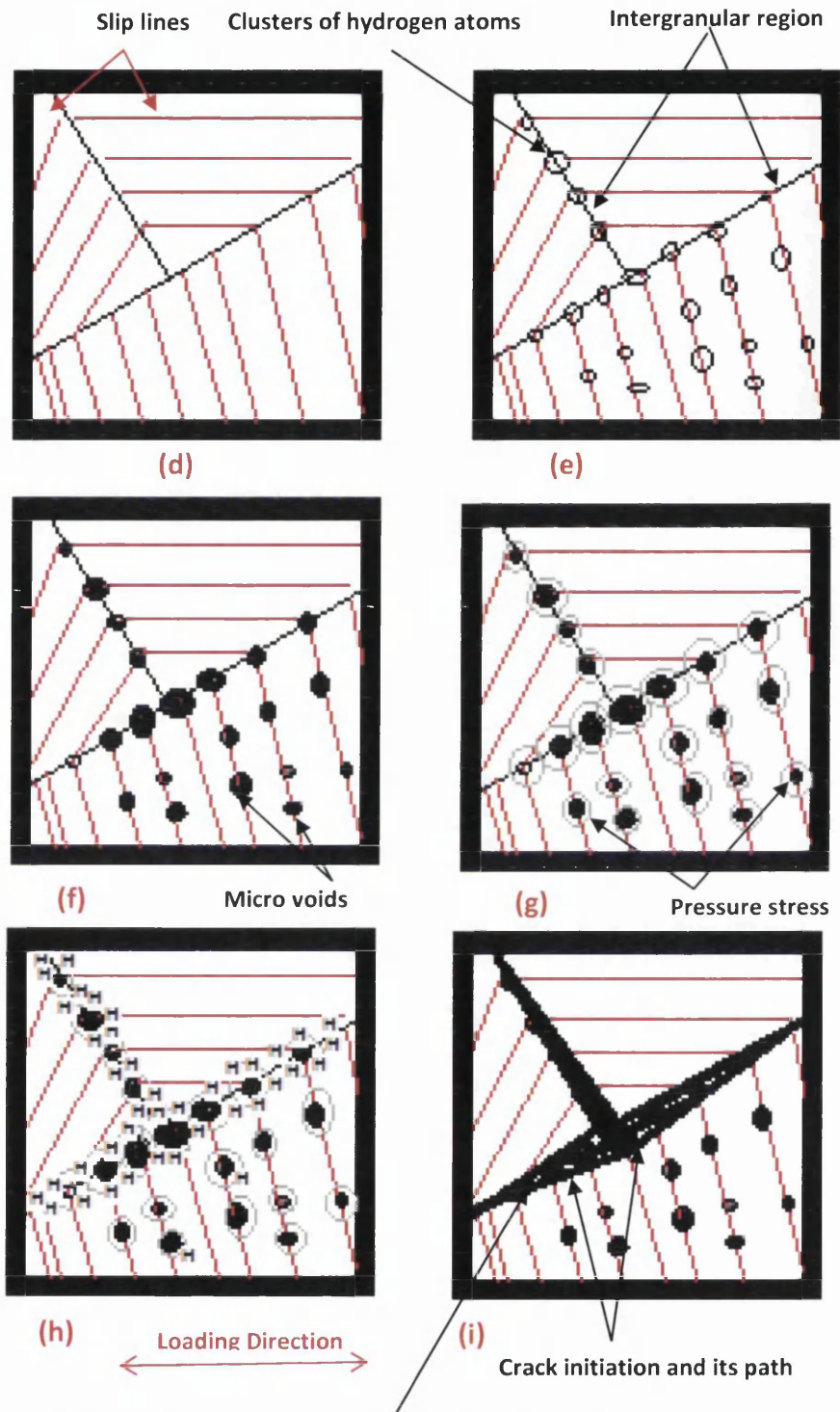
Multi-scale FE simulation predicting of crack initiation i.e. if segregation of hydrogen in void edge perpendicular to traction direction exceeds a critical level a crack initiates at this point.



Densely packed Slip traces

Figure 7.9.4 SEM fractography images showing hydrogen induced cracking of nickel alloy 718 which have been embrittled by hydrogen charging. (a) Intergranular and Transgranular cracking. (b) & (c) show magnified views of transgranular cracking, (d) shows a micro scale finite element (FE) predicted of stress distribution ($N/\mu m^2$), (e) multiscale FE stress assisted hydrogen diffusion analysis showing predicted hydrogen distribution at the micro-level predicting potential crack initiation sites near void edges perpendicular to the traction direction consistent with experimental results. (f) & (g) show fracture surface features, the intergranular crack propagation path, carbides on the intergranular crack path and slip traces on surfaces.





Hydrogen uptake increases and diffusible hydrogen segregation near micro void edges due to high pressure stresses along intergranular regions, decreasing the cohesive energy leading to crack initiation and propagation along the intergranular region.

Figure 7.9.5 (a) segregation of carbon atom to the grain boundary in alloy 718 using atom probe tomography, (b) micro crack initiation along grain boundary, (c) slip traces, micro voids along grain boundaries and strain localization consistent with

HELP mechanism. The series of schematic diagrams propose hydrogen induced localized plastic process arising from slip traces based on HELP mechanism. (d) shows the relationship between slip traces (red lines) and intergranular region (black lines), (e) shows the segregation of hydrogen clusters (black open circles) on slip lines, (f) shows the formation of micro voids (black filled circles) on the hydrogen clusters forming at slip band sites, (g) shows the developing high pressure stresses around void edges (grey circles around black filled circles), (h) trapping of hydrogen (H-symbols) around micro-voids due to tensile stresses and the high gradient of pressure perpendicular to the loading direction. (i) Crack initiation at triple junctions and/or near larger micro-void edge regions perpendicular to the traction direction, propagating by coalescence of micro-voids along intergranular regions due to the increase in pressure in micro voids.

Considering the diffusivity of hydrogen in the alloy, there is not enough time for hydrogen to fully diffuse to the centre of the specimen. Thus central regions of the specimen fracture in a ductile mode. The fractography secondary electron (SE) images in figure 7.9.3 reveal that the central region of the specimens display ductile fracture characteristics whereas and near-surface regions down to a depth of ~1 mm display brittle fracture characteristics. The hydrogen induced brittle modes of fracture appear to be intergranular supporting the idea that grain boundaries and triple junctions are more susceptible to hydrogen induced cracking compared to the grain interior lattice.

Figures 7.9.4 (a-c) show a series of fracture surface images at increasing magnification. Figure 7.9.4 (a) shows both transgranular and intergranular cracking. Most of the crack paths observed are intergranular with only very few transgranular cracks. Figures 7.9.4 (b) and (c) show the hydrogen induced transgranular crack propagation path. From a previous multi-scale FE stress assisted hydrogen diffusion numerical model it was observed that the presence of voids or pores in the grain lattice leads to high stress concentrations which act as a driving force for the segregation of hydrogen near the edges of these voids, perpendicular to the traction direction. This leads to crack initiation at the edges of the void and these cracks propagate in a transgranular manner.

The numerical model mentioned above is a microstructural coupled multi-scale FE model and multi-scale FE chemo-mechanical analysis of void/pores microstructures.

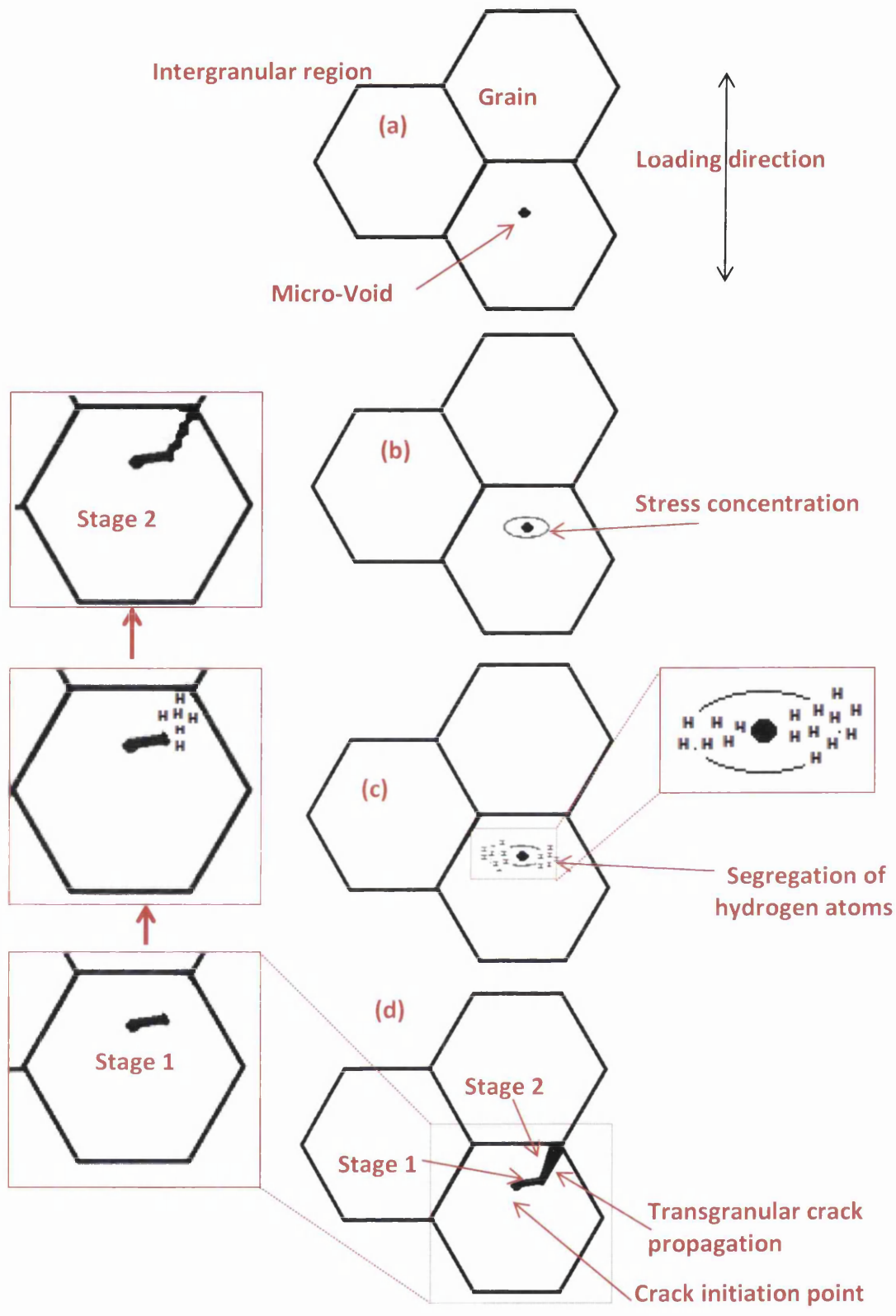


Figure 7.9.6 Schematic illustration of possible pore/void dependent hydrogen induced transgranular cracking in polycrystalline alloy 718. (a) Polycrystalline material with micro-pores before transgranular cracking. (b) Stress concentration greater perpendicular to the traction direction as opposed to parallel. (c) The tensile stress concentrations around deformed pores/voids increases the mobility of hydrogen atoms which become trapped in these tensile stress concentration sites. The

amount of trapped hydrogen will be greater in near void regions perpendicular to loading direction. (d) Illustrates a proposed model of a transgranular crack initiation site and two stage propagation path.

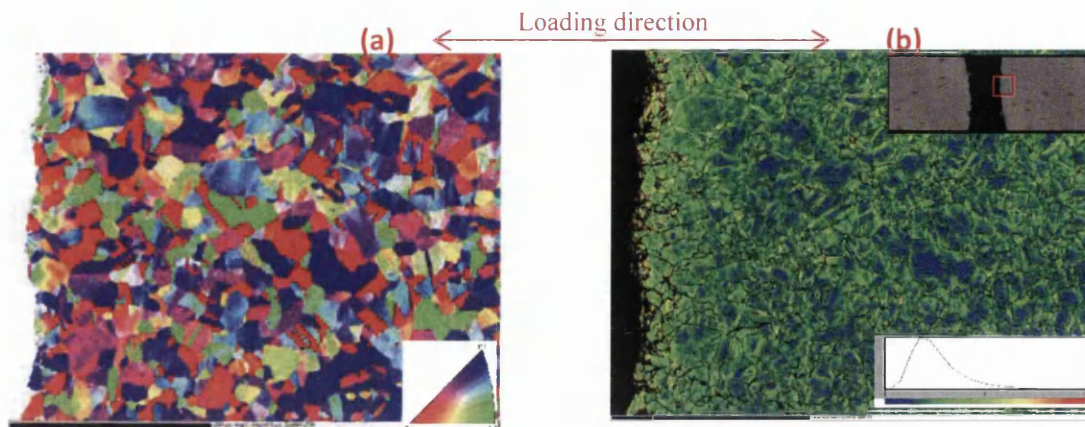


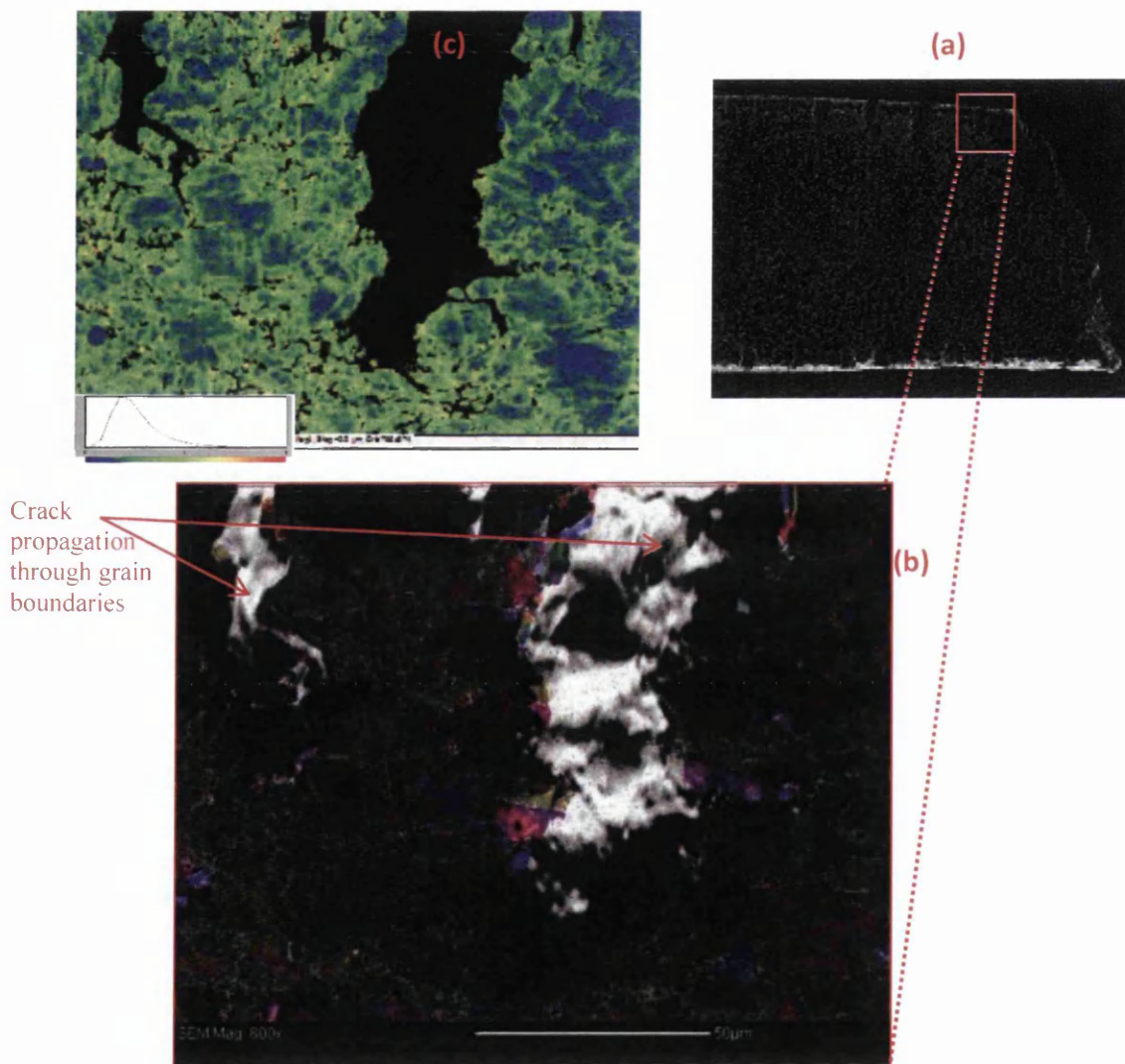
Figure 7.9.7 EBSD results for uncharged SSRT fractured specimen. (a) Crystallographic orientation and IPF image in loading direction. (b) Local misorientation map and colour contour (red colour regions have the largest misorientations and blue colour regions the smallest).

A simulation using this model is shown in figures 7.9.4 (d) and (e). Figure 7.9.4 (d) shows the predicted stress field in a representative 2D micro-scale region containing pre-existing voids in the microstructure. In this figure tensile stresses at void surfaces perpendicular to the loading direction are formed. Figure 7.9.4 (e) shows the predicted hydrogen segregation occurring preferentially in these same regions of tensile stress. Regions under high tensile stress possessing higher hydrogen concentrations would represent likely crack initiation sites. Tensile stresses around voids/pores could act as a mechanism to drive pore growth through the crystal lattice forming transgranular cracks and promoting the type of failure shown in figures 7.9.4 (b) and (c).

Figure 7.9.4 (f) and (g) show an intergranular crack propagation path (with slip traces, some highlighted with white dotted lines) and the presence of carbides in the crack path. The two black arrows figure 7.9.4 (f) show two different slip systems acting across a grain boundary very similar to previous observations in pure nickel (Martin et al., 2012).

Figure 7.9.4 (g) shows a magnified view of slip traces on a fracture surface on an intergranular crack propagation path. The majority of the crack propagates along the intergranular region where hydrogen trapping will be greater indicating that

the intergranular region and voids are the preferential sites for hydrogen trapping when compared to lattice sites. Intergranular sites provide routes of higher hydrogen mobility as they are a lower energy barrier to hydrogen diffusion and would possess lower activation energy of hydrogen desorption compared to hydrogen lattice sites. Such segregation and trapping of hydrogen along grain boundaries has previously been observed using secondary ion mass spectroscopy (SIMS) for hydrogen diffusion in pure nickel (Fukushima et al., 1984, Ladna et al., 1987). The slip traces on both sides of two crystals intersecting across grain boundary means the presence of dislocations that can also act as trapping sites for hydrogen. This causes intergranular plasticity leading to intergranular brittle cracking often referred to as the hydrogen enhanced localized plasticity (HELP) mechanism of hydrogen embrittlement.



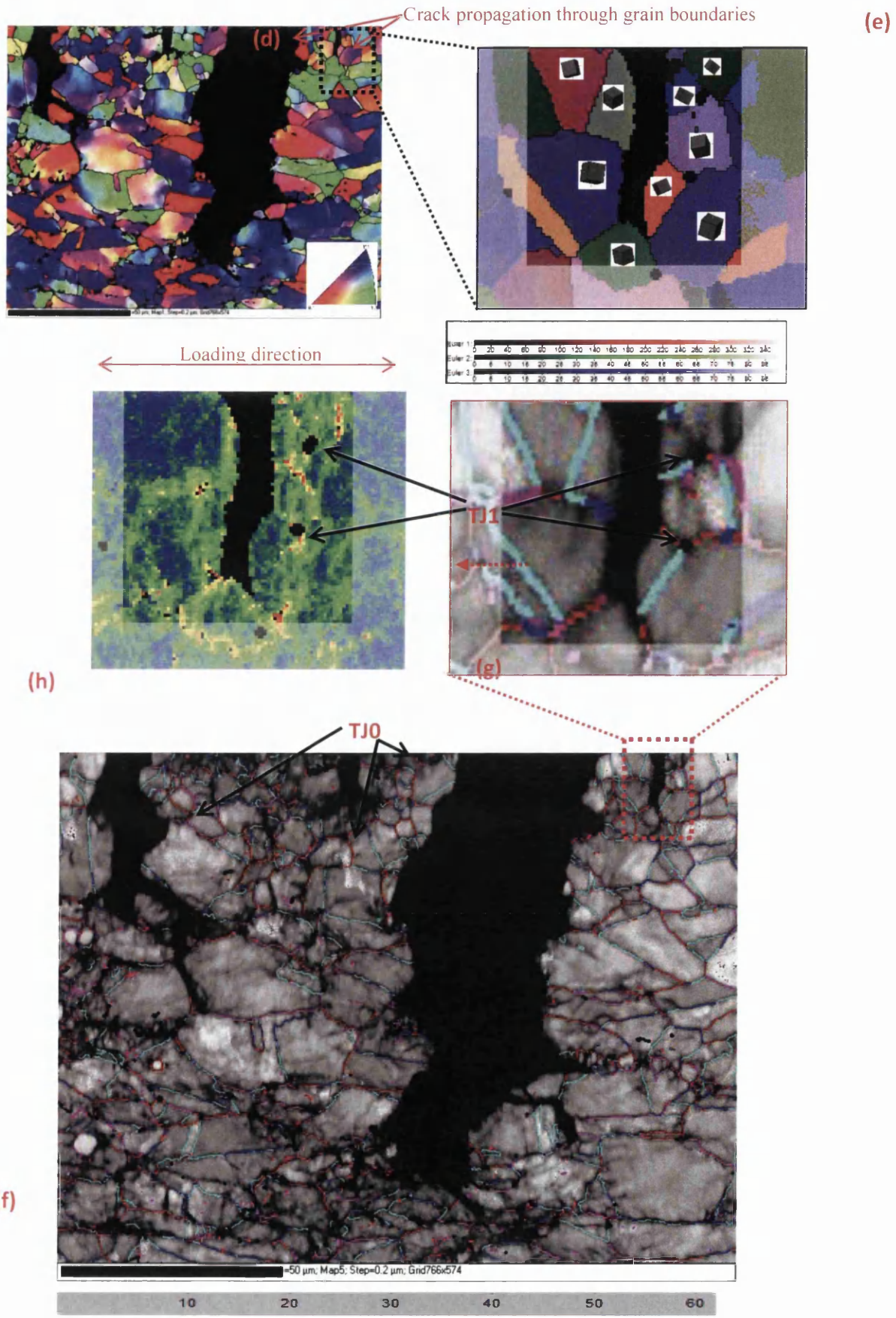


Figure 7.9.8 (a) Shows the in-suit hydrogen charged SSRT tested fractured specimen, (b) shows the EBSD map overlaid on SEM micrograph, (c) shows the local misorientation map and its colour contour, (d) shows the crystallographic orientation and its IPF image on LD and (e) shows the closer view near crack region and it Euler angle and (f) shows the effect of grain boundary character distribution in the form of hydrogen induced crack path, (g) Close up view and (h) Close up view of local misorientation.

All these of these features demonstrate the occurrence of plastic processes and slip localization as the micro-mechanism of hydrogen induced intergranular embrittlement in alloy 718.

Figure 7.9.4 (g) also shows the segregation of carbides in the intergranular region. Segregation of carbon atoms at grain boundaries in alloy 718 were observed in atomic scale investigations using atom probe tomography (APT) as shown in figure 7.9.5 (a). It has been previously reported that carbon at grain boundaries/micro-cracks combining with hydrogen to form methane, equation 7.9.2, enhances micro-crack initiation along grain boundaries.

Void formation along intergranular interfaces can be seen in figure 7.9.5 (b). It has also been previously reported that segregation of impurity atoms also induces intergranular hydrogen embrittlement in a nickel based superalloy (Byun et al., 2003, Ladna et al., 1987).



Figure 7.9.5 (c) shows hydrogen assisted crack initiation and a slip band system consistent with intergranular strain localization and the HELP mechanism. The slip bands on intergranular regions were enhanced by hydrogen uptake due to high stress concentrations. Clusters of hydrogen atoms can form on intergranular slip bands particularly at vacancies. Increasing the density of vacancies eventually leads to the formation of micro-voids along the intergranular region. The formation of micro-voids increases the internal gas pressure within voids due to the formation of molecular hydrogen. High hydrostatic tensile stresses around voids act as a driving force to increase the diffusion of hydrogen towards the void with a higher concentration of hydrogen atoms becoming trapped near the micro-void edges perpendicular to the loading direction. These pressure stresses depend on the

size/area of the micro-voids. The intergranular trapped hydrogen softens the intergranular region by decreasing the cohesive energy between lattice atoms near the grain boundary. This leads to micro-void expansion and merging together and coarsening of neighbouring micro-voids. Growth of micro-voids on the slip lines in the intergranular region may initiate cracks at triple junctions and/or larger micro-void sites, propagating along intergranular regions. This proposed mechanism is illustrated schematically in figures 7.9.5 (d-i).

Combining experimental and numerical results a schematic model is proposed (figure 7.9.6) for a mechanism for hydrogen induced transgranular cracking based on micro-void crack growth. The edges of deformed micro-voids perpendicular to the loading direction in the crystal lattice act as preferential sites for transgranular crack initiation. Initially a Stage 1 crack propagates by the formation and coalescence of voids. At a certain crack length Stage 2 propagation occurs driven towards intergranular regions where the lattice will be more disordered and there will be higher concentrations of hydrogen.

The main aim of this EBSD investigation is to understand relationships between GB misorientation and hydrogen induced intergranular crack nucleation and propagation in alloy 718. In this study, IHE cracking is classified based on grain boundary character distribution (GBCD) as defined by GB misorientation angles (irrespective of axis plane). Five different types are described below

- (1) Low angle GB misorientations (LAM) ($0^\circ \leq \theta \leq 15^\circ$)
- (2) Low end High angle GB misorientation (LHAM) ($15^\circ < \theta \leq 35^\circ$)
- (3) Critical High angle GB misorientation (CHAM) ($35^\circ < \theta \leq 50^\circ$)
- (4) High end High angle GB misorientation (HHAM) ($50^\circ < \theta \leq 55^\circ$)
- (5) Special GB misorientation (SGB) ($55^\circ < \theta$)

Detailed information relating the coincidence site lattice (CSL) grain boundary characteristics (GBC), triple junction connectivity CSL GB and TJ character on IHE crack nucleation and propagation. The uncharged and hydrogen charged fractured specimen microstructures on the wider face of the gauge length section parallel to the loading direction were examined as shown in figures 7.9.7 and 7.9.8 respectively. EBSD scans were performed in the vicinity of the micro-crack front over areas of $490 \times 367 \mu\text{m}^2$ and $153 \times 114 \mu\text{m}^2$ on uncharged and charged specimens respectively. Figures 7.9.7 (a) and (b) show the uncharged fractured

specimen indicating that preferential crack propagation was transgranular and no sub-cracks were observed. A crystallographic orientation map and IPF is shown in figure 7.9.7 (a). Figure 7.9.7 (b) shows the local misorientation map (with red regions having the high levels of local misorientation and blue regions having lower amounts) where local misorientations are higher along the fracture path due to the higher local deformation and fracture is mostly transgranular.

Figure 7.9.8 (a) shows the in-situ hydrogen charged SSRT tested fractured specimen, figure 7.9.8 (b) shows the EBSD map overlaid on the SEM micrograph, figure 7.9.8 (c) shows the local misorientation map. Figure 7.9.8 (b) shows that preferential crack propagation for an in-situ hydrogen charged SSRT tested specimen was intergranular with many macroscopic sub-cracks observed perpendicular to the loading direction and a few micro cracks observed parallel to the loading direction. High local misorientations are observed in the intergranular cracked region. Considering figures 7.9.8 (a-c) it is clear that grain boundaries and triple junctions have been deformed more than the internal crystal lattice. Figure 7.9.8 (d) shows the crystallographic orientation and IPF image. Intergranular cracks are mostly perpendicular to the loading direction. Figure 7.9.8 (e) shows a magnified view of a region near a sub-crack with Euler angles. Figure 7.9.8 (f-h) can be used to attempt to understand the effect of grain boundary character distribution on intergranular hydrogen embrittlement. These results show that the cracks are intergranular with CHAM-type regions observed along the crack path. Also some likely crack nucleation points can be identified at triple junctions with CHAM-CHAM-SGB and CHAM-CHAM-CHAM connectivities. It has previously been observed in experimental studies and numerical modelling that certain types of TJ are more susceptible to HE and therefore more likely to provide crack nucleation points (Koyama et al., 2013, Chen et al., 2000, Meyers et al., 2009).

An attempt was made to quantify the effect of GB misorientation characteristics and triple junction characteristics on hydrogen induced intergranular cracking. Hydrogen induced intergranular cracks were observed at 103 grain boundaries. 58.3% of these grain boundaries within cracks were CHAM, 35% were LHAM, 4.9% were HHAM and 1.9% was SGB. This data is summarised in figure 7.9.9. Interestingly, no intergranular cracks were associated with LAM. Thus LAM, HHAM and SGB are the types of GB misorientations where few or no hydrogen induced cracks were observed.

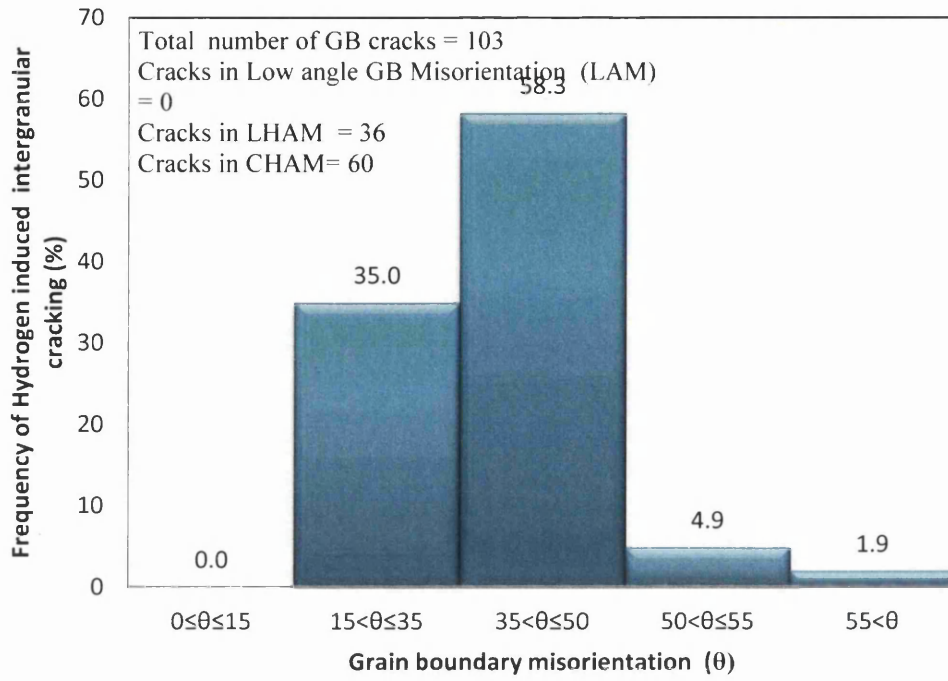


Figure 7.9.9 Relationship between GBC and observed frequencies of hydrogen induced intergranular cracking.

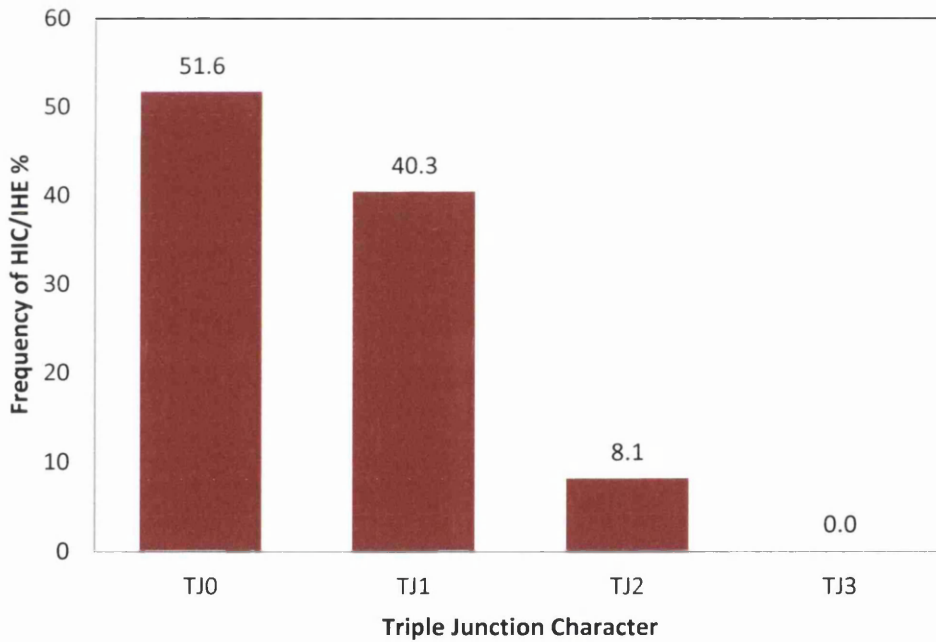


Figure 7.9.10 Relationship between the observed frequencies of hydrogen induced cracking/intergranular hydrogen embrittlement and TJC.

This is attributed to the lower stress concentrations and lower hydrogen trapping characteristics of these types compared to LHAM and CHAM. These results are also

consistent with previous numerical model findings for a bi-crystal pure nickel investigation. During testing localized stress concentrations in the microstructure will arise due to crystal anisotropy. Tensile stresses are accumulated on CHAM and LHAM regions which act as a driving force for hydrogen atoms to form in more concentrated clusters preferentially along CHAM and LHAM regions compared to other sites. Hydrogen trapping in CHAM and LHAM regions reduces the ductility and plastic flow along these grain boundaries due to a reduction in cohesive energy. Once the trapped hydrogen in the CHAM and LHAM exceeds a critical value it results in intergranular hydrogen embrittlement. This behaviour was previously reported in electrodeposited annealed nickel with a combination of multi-scale microstructural modelling and experimental observation. In total 93.3% of hydrogen induced intergranular cracks were observed in CHAM/LHAM boundaries indicating that these types of boundary are the most susceptible sites for hydrogen induced cracking in superalloy 718. This is attributed to a decrease in plastic flow which enhances the localization slip along the intergranular region leading to reduced intergranular ductility resulting in intergranular localized plasticity/intergranular embrittlement. These results also suggest that LAM, HHAM and SGB grain boundary misorientations are effectively more resistant to intergranular hydrogen embrittlement with the LAM GB misorientation having the greatest resistance in the nickel based superalloy 718.

Based on this observation, GB types are now categorised into two types, resistant (R-type) and susceptible (S-type), as given below.

- R-type: HIC/IHE Resistant GB type GBCs = LAM, HHAM, SGB
- S-type: HIC/IHE Susceptible GB type GBCs = LHAM, CHAM

With this definition triple junction connectivity (TJC) can be classified into four different types depending on the possible combinations of R- and S-types at the junction.

1. TJ0 type TJC with zero resistant GBCs connectivity = S-S-S
2. TJ1 type TJC with one resistant GBCs connectivity = S-S-R
3. TJ2 type TJC with two resistant GBCs connectivity = S-R-R
4. TJ3 type TJC with three resistant GBCs connectivity = R-R-R

It has been previously reported that triple junctions play a significant role in hydrogen diffusion and hydrogen induced cracking (Chen et al., 2000). Now we

consider the effect of TJC on HIC in alloy 718. Figure 7.9.10 shows the relationship between HIC and TJC. The HIC data were taken from 62 different TJs. 51.6% of hydrogen induced TJ cracks were detected at TJ0-type triple junctions. 40.3% and 8.1% of TJ cracks were observed at TJ1-type and TJ2-type TJs respectively. No cracks were observed at TJ3-type triple junctions. This indicates that TJs containing the more susceptible GBC connectivity, such as TJ0-type and TJ1-type, are more likely sites for hydrogen induced cracking. TJ3-type TJs appear to be much more resistant to hydrogen induced cracking. Thus hydrogen induced cracking at triple junctions strongly depends on the nature of the triple junction connectivity.

7.9.2 Discussion

Transgranular hydrogen induced cracking can be controlled by reducing the formation of micro-voids/pores in the crystal lattice during manufacturing. One way of controlling intergranular hydrogen embrittlement is by reducing the segregation of carbon atoms along the intergranular region. As reported previously, this can be achieved by adding small amounts of elements such as titanium, niobium and vanadium. Reducing the segregation of carbon atoms along the intergranular region should enhance the ductility and reduce the susceptibility of intergranular hydrogen induced cracking in polycrystalline alloy 718.

Another possibility is grain boundary engineering. Watanabe et al. introduced the concept of grain boundary engineering and design three decades ago to improve the ductility of material (Watanabe, 1984). Grain boundary engineering often involves low temperature heat treatment to induce limited grain growth and rearrangement of grain boundaries. Palumbo et al. have used grain boundary engineering to improve intergranular stress corrosion cracking resistance [166, 181-183]. Watanabe et al. used a GBE approach to control heat affected zone liquation cracking in superalloys and other workers have used GBE design and control to improve material performance [121,176, 181-183, 189]. The author is unaware of such treatments being applied specifically to improve hydrogen embrittlement susceptibility in alloys.

From the results described in this section it seems clear which grain boundary misorientations and triple junction types are more or less susceptible to hydrogen

induced problems. This strongly suggests that grain boundary engineering approaches would be an interesting area for future study for alloy 718.

7.10 Hydrogen Embrittlement in Pulse Plated Nickel

In order to understand the hydrogen embrittlement in Ariane 5 combustion chamber ex-situ hydrogen charged SSRTs were conducted on established grade 1 and newly developed grade 2 PP-Ni materials. Fracture specimens were analysed, using SEM, to investigate the micro-mechanisms of hydrogen induced cracking.

7.10.1 Experimental results

Two different grades of PP-Ni were manufactured using electrodeposition pulse plated techniques by AIRBUS Defence & Space. (Note: Dimensions of samples are reported in chapter section 4.4. The detailed characterization of grade 2 microstructures and grade 1 microstructures using EBSD analysis is shown in sections 7.4 and 7.11 respectively). TDA analysis was done on as-received grade 1 and 2 PP-Ni materials to determine hydrogen content as shown in figure 7.10.1. This shows that the amount of hydrogen present in grade 2 PP-Ni is higher than grade 1 PP-Ni. It also shows that the trapped hydrogen starts being released from the material at 158°C and the hydrogen atoms are completely effused from the material at 358°C and 372°C for grade 2 and grade 1 respectively. Hydrogen charging was performed for 72 hours at 90°C as explained in section 4.4. The charged samples were also analysed using TDA and results are shown in figure 7.10.2. This experimental result reveals the presence of diffusible hydrogen content in grade 1 and grade 2 PP-Ni i.e. 72.1 wt.ppm and 82.7 wt.ppm respectively. The increase in diffusion of hydrogen in grade 2 compared to grades 1 is simply explained by the computational simulation and EBSD experimental results shown in section 7.2 and 7.4 respectively. Hydrogen diffusion in smaller/nano/ultrafine grains is faster and grade 2 PP-Ni possesses such clusters of ultrafine grains compared to grade 1. The slow strain rate tests were carried out at strain rate 10^{-5} s^{-1} at room temperature on grade 1 and grade 2 uncharged PP-Ni specimens (i.e. as-received) and grade 1 and grade 2 charged PP-Ni specimens. The engineering stress-strain curves for these specimens are shown in figure 7.10.3. Figure 7.10.4 clearly demonstrates the effects of hydrogen charging on hydrogen embrittlement and the differences between grades 1 and 2.

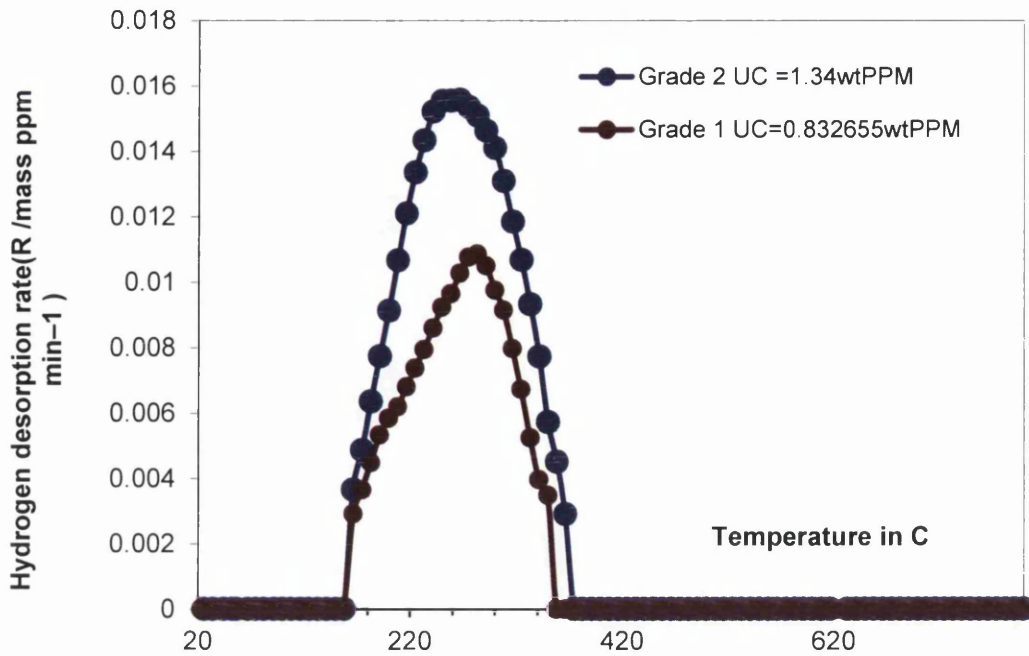


Figure 7.10.1 TDA results showing the amount of hydrogen present in grades 1 and 2 uncharged specimens.

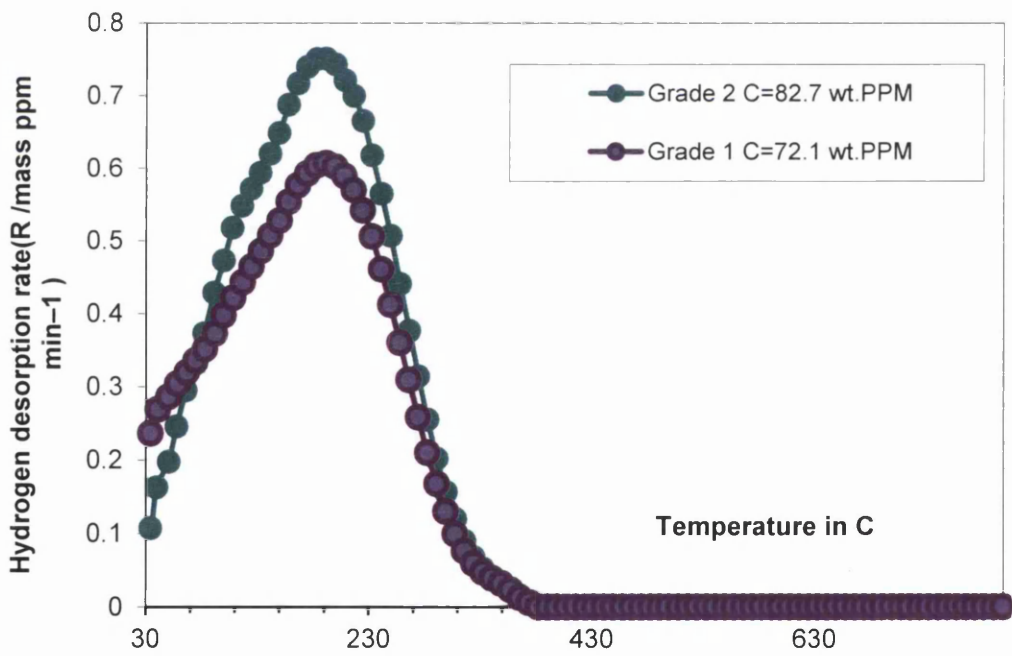


Figure 7.10.2 TDA results showing the amount of hydrogen present in grades 1 and 2 charged specimens.

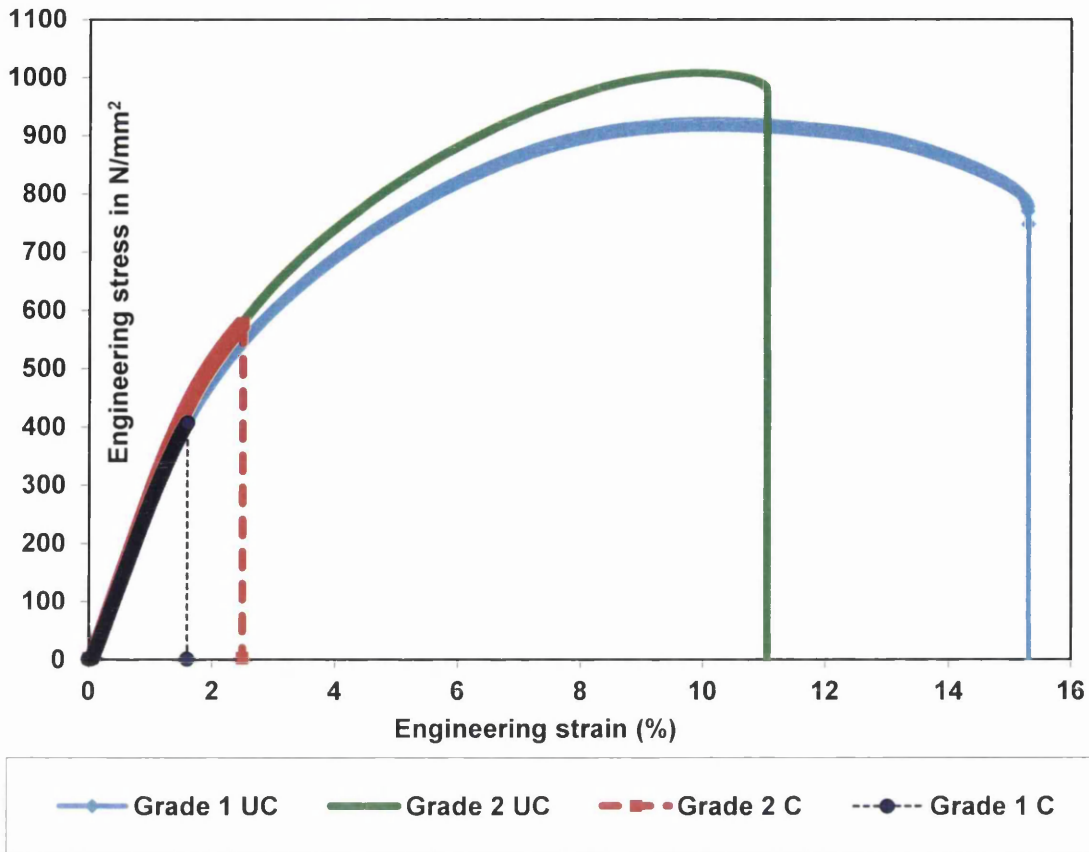


Figure 7.10.3 Engineering stress-strain curves with and without hydrogen pre-charging for grade 1 and grade 2 pulse plated nickel specimens (uncharged = UC and charged = C).

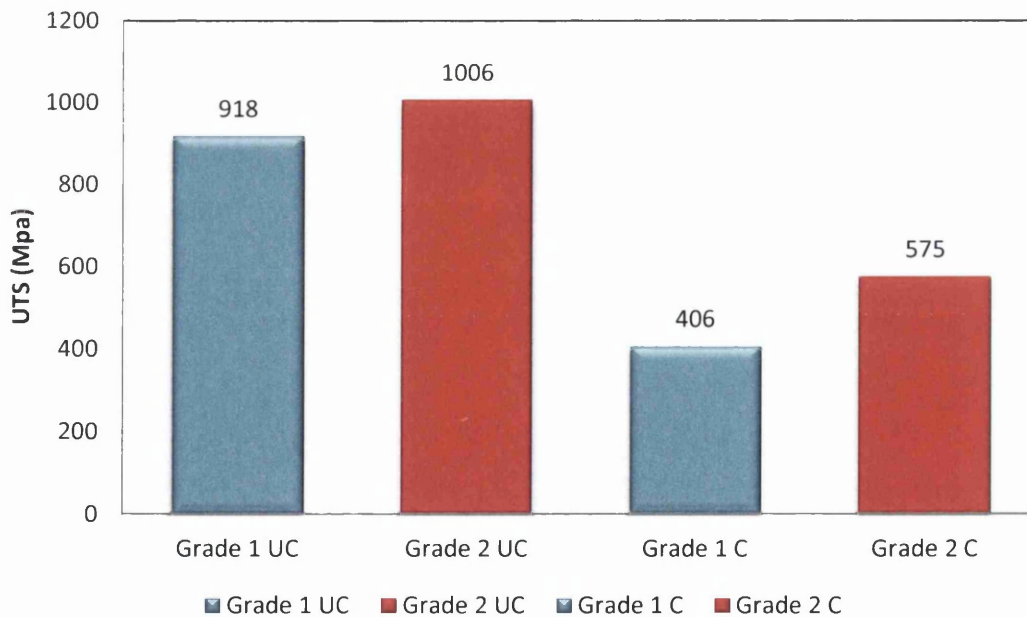


Figure 7.10.4 The effect of hydrogen charging on UTS.

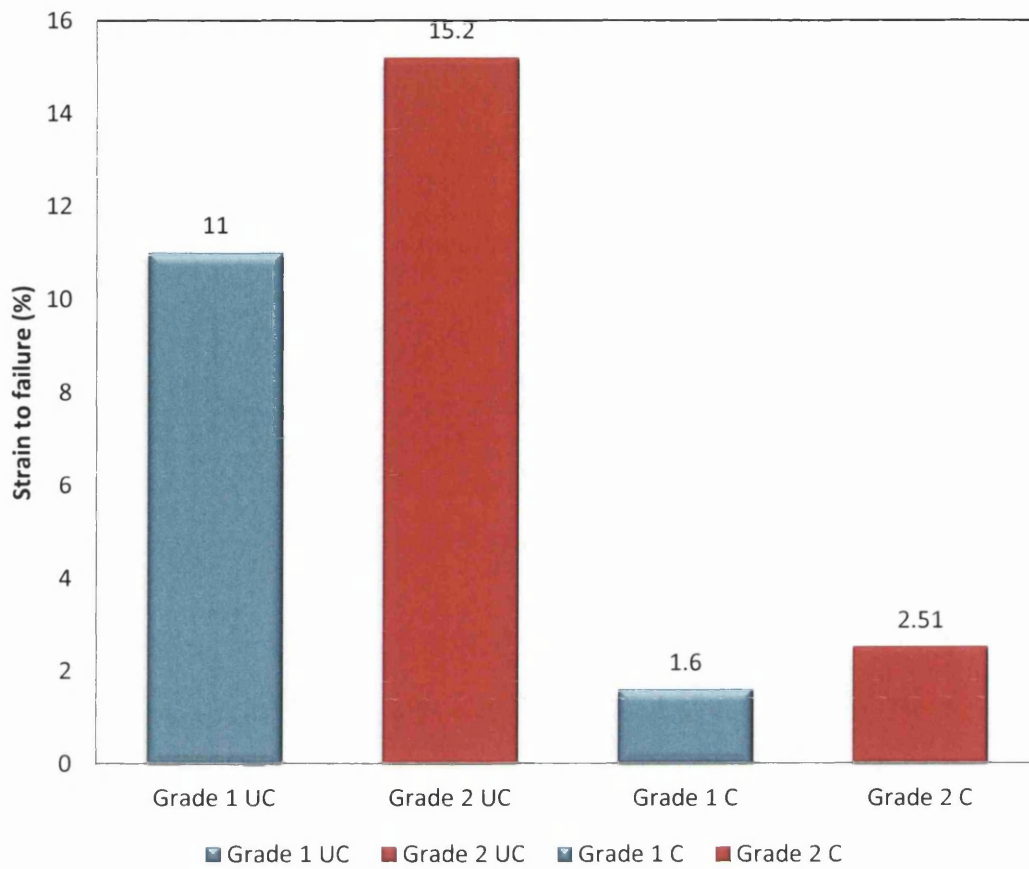
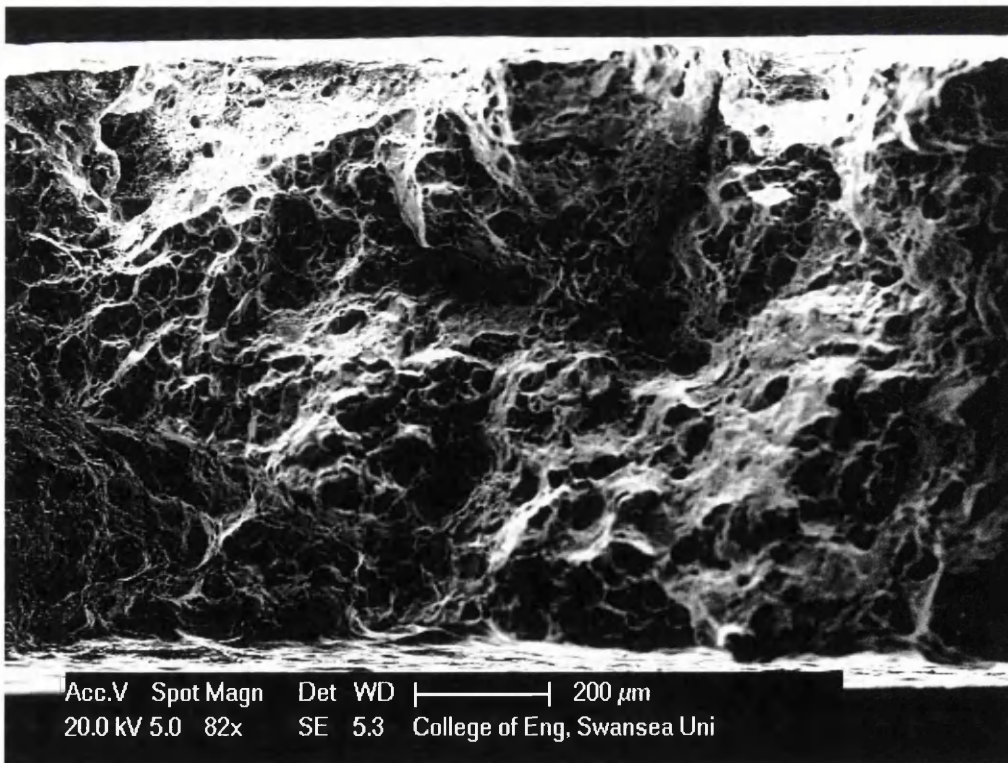


Figure 7.10.5 The effect of hydrogen on strain to failure.



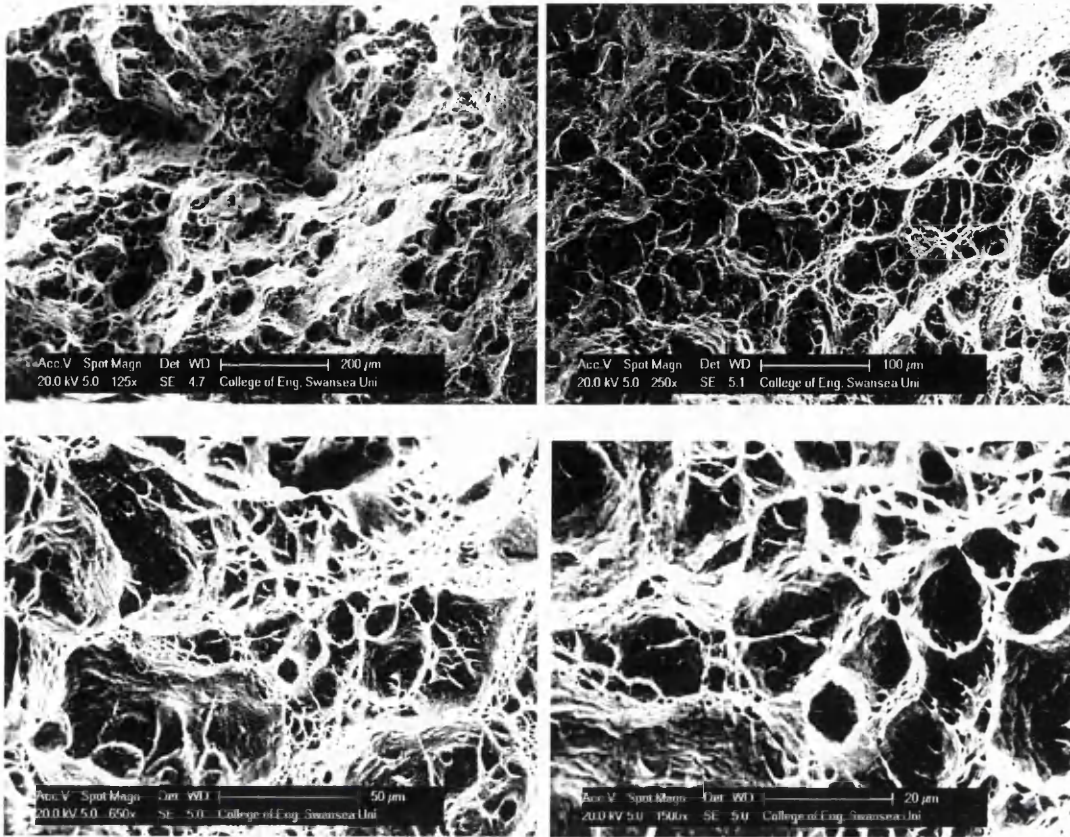
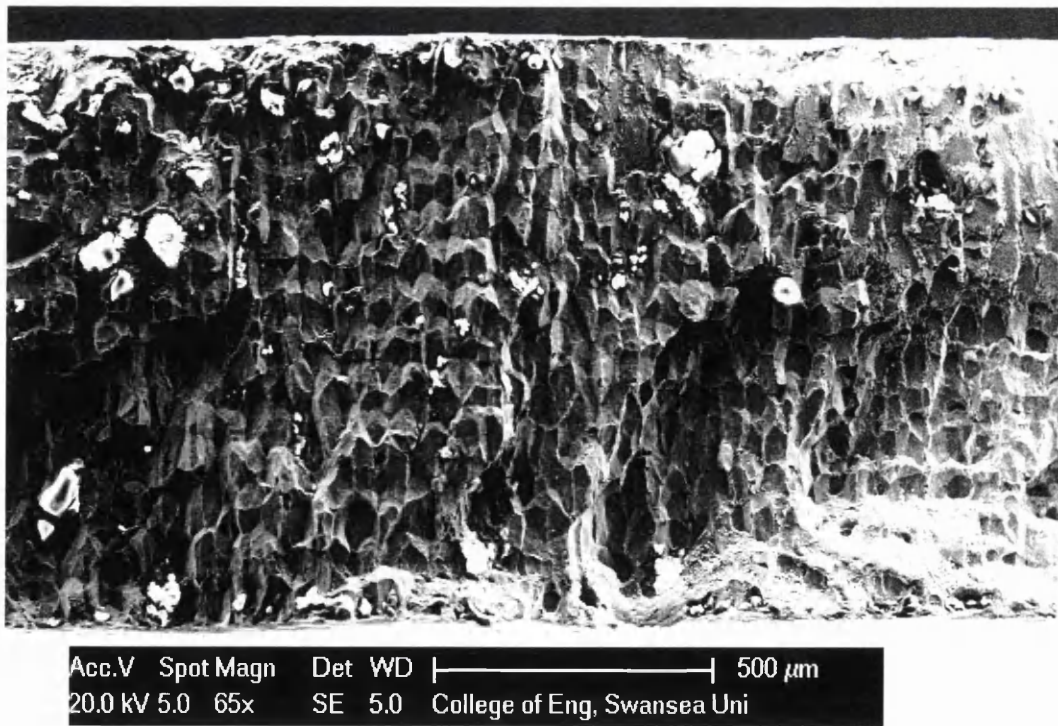


Figure 7.10.6 SEM Fractography results of fracture surface of uncharged grade 1 PP-Ni specimen.



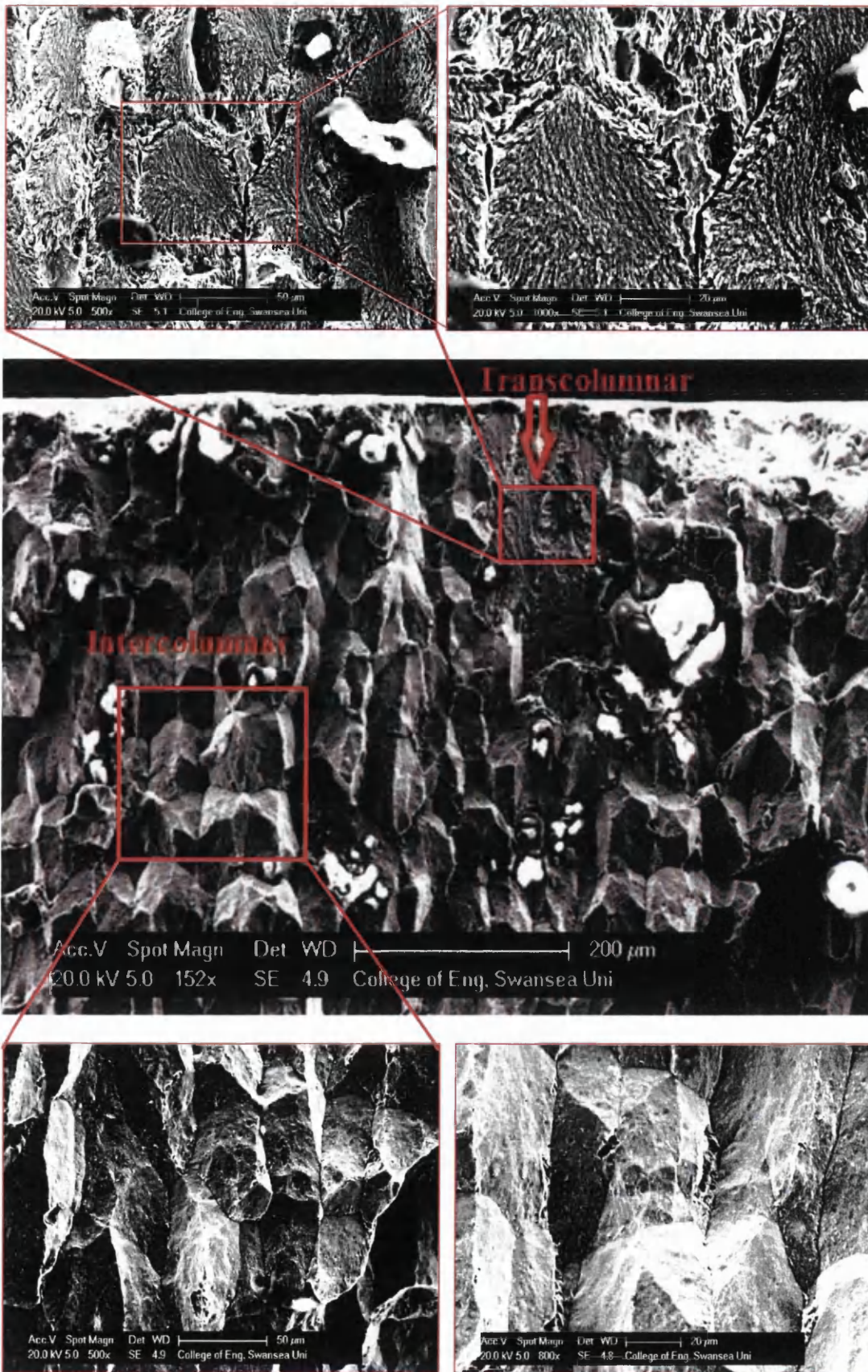


Figure 7.10.7 SEM Fractography results shows of fracture surface of charged grade 1 PP-Ni specimen.

The presence of hydrogen in the PP-Ni decreases the ultimate tensile strength (UTS) of the material. As the author predicted in chapter section 7.1 to 7.6 using multi-scale modelling, microstructure affects hydrogen embrittlement and this experimental result supports the model predictions. Figure 7.10.5 shows the effect of hydrogen on strain to failure. This shows that the increases in the fraction of pores in grade 1 PP-Ni both reduces the UTS and decreases the strain to failure. Figure 7.10.6 and figure 7.10.7 shows SEM fractography images observed on the fracture surface of the uncharged grade 1 PP-Ni specimen and the charged grade 1 PP-Ni specimen respectively. These clearly show the effects of hydrogen on grade 1 PP-Ni. The uncharged grade 1 specimen seems to be more ductile than the charged specimen. Figure 7.10.7 shows that the hydrogen segregates along column boundaries, degrading the ductility of column boundaries leading to intercolumnar hydrogen induced failure and intercolumnar hydrogen embrittlement. Thus column boundaries appear more prone to hydrogen induced cracking. Figures 7.10.8 and 7.10.9 show SEM fractography images observed on the surface of the uncharged grade 2 PP-Ni specimens and charged grade 2 PP-Ni specimens respectively. This also shows that uncharged specimens are more ductile than charged specimens. The charged specimens display intercolumnar hydrogen induced cracking with very few trans-columnar hydrogen induced cracks present due greater amounts of hydrogen segregated along column boundaries compared to segregation of hydrogen atoms around ultrafine grain clusters. This is confirmed by the high resolution scanning Kelvin probe force microscopy (SKPFM) results shown in figure 7.10.10. (NB SKPFM experiments are beyond the scope of this work but further detailed analysis in this area is a future focus for the author.) Figure 7.10.10 shows greater amounts of hydrogen atoms are segregated along column boundaries when compared to the ultrafine grain clusters.

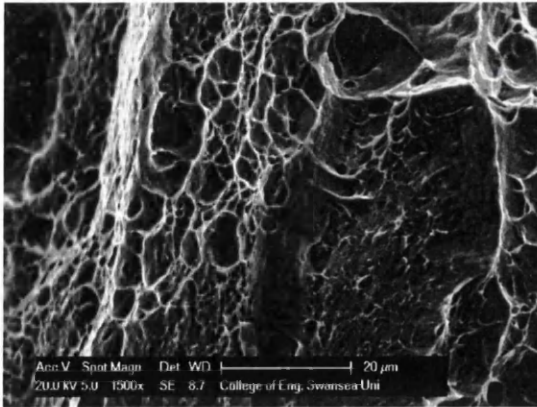
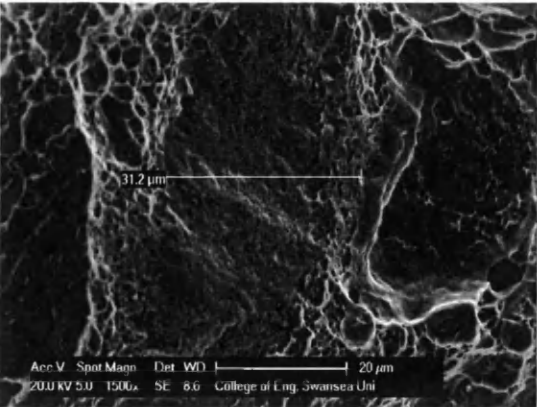
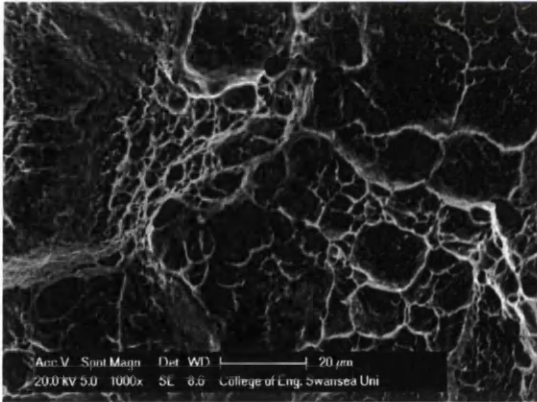
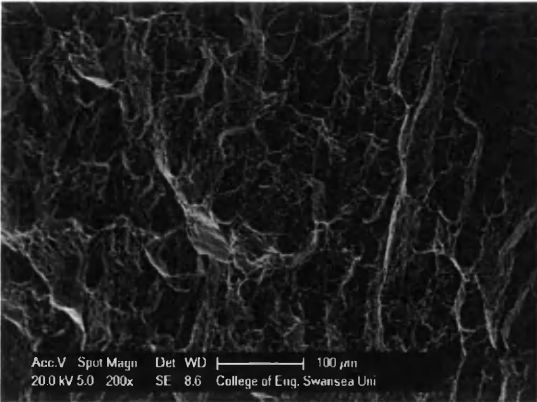
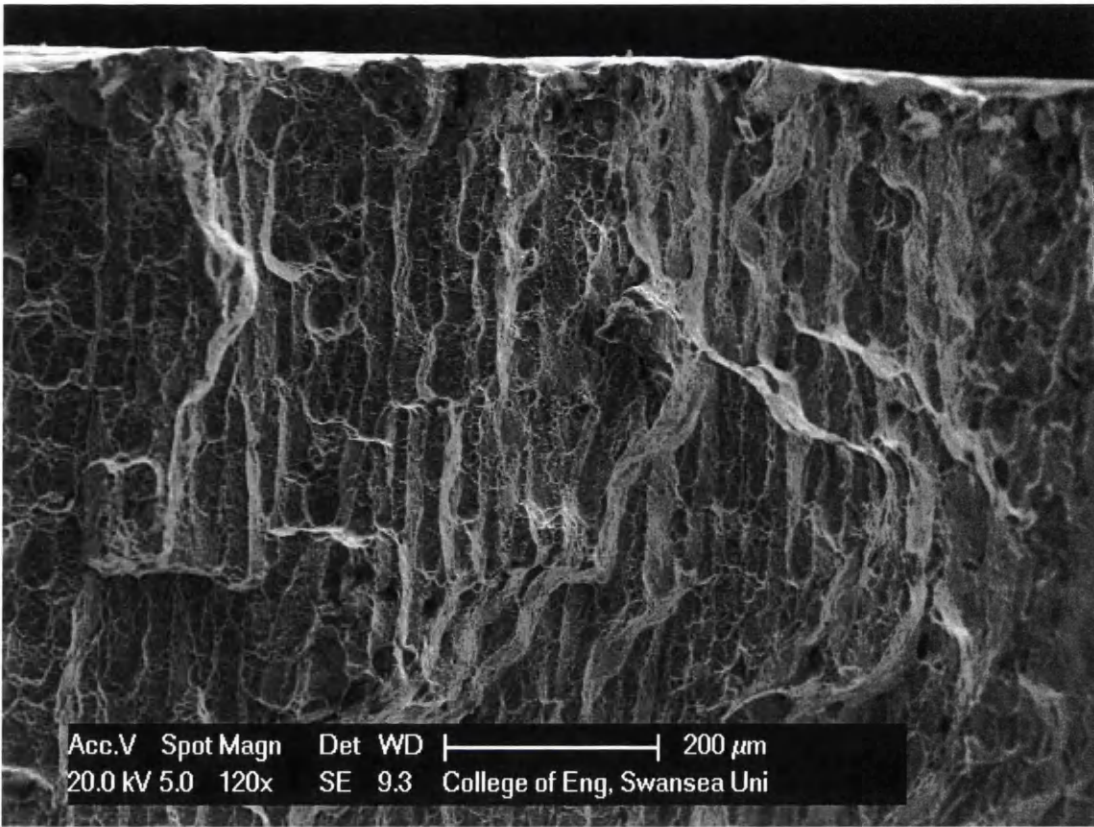
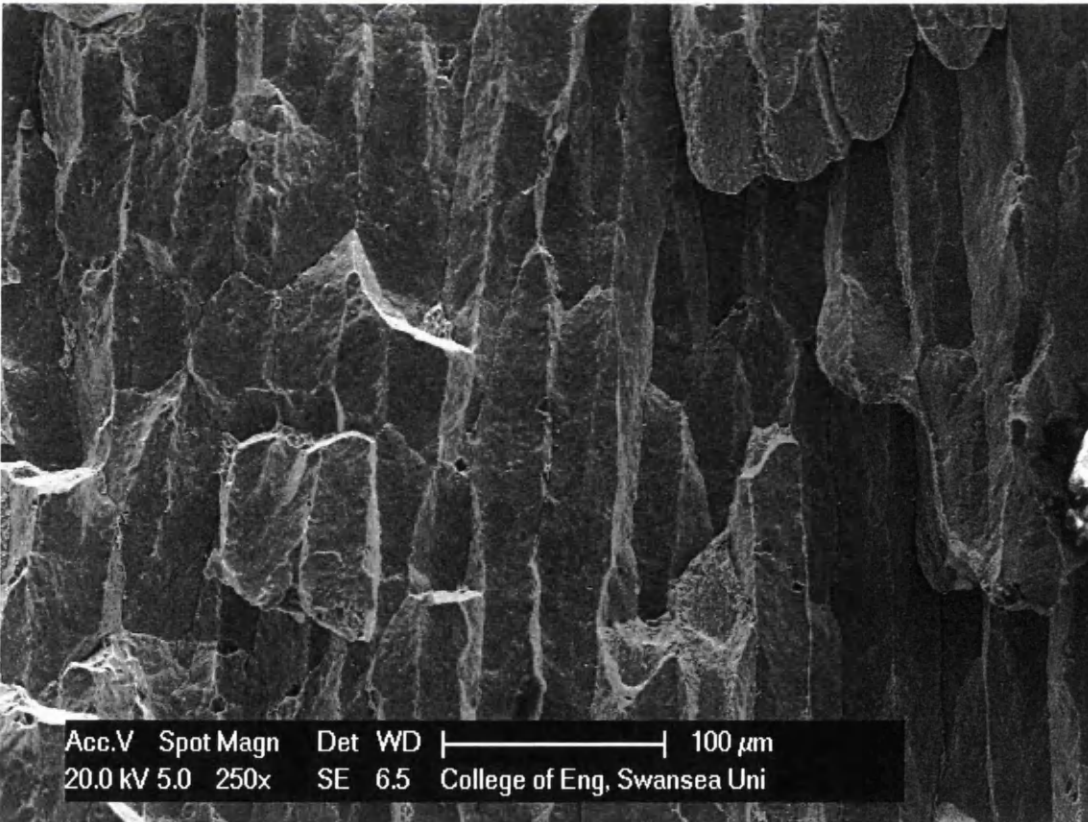
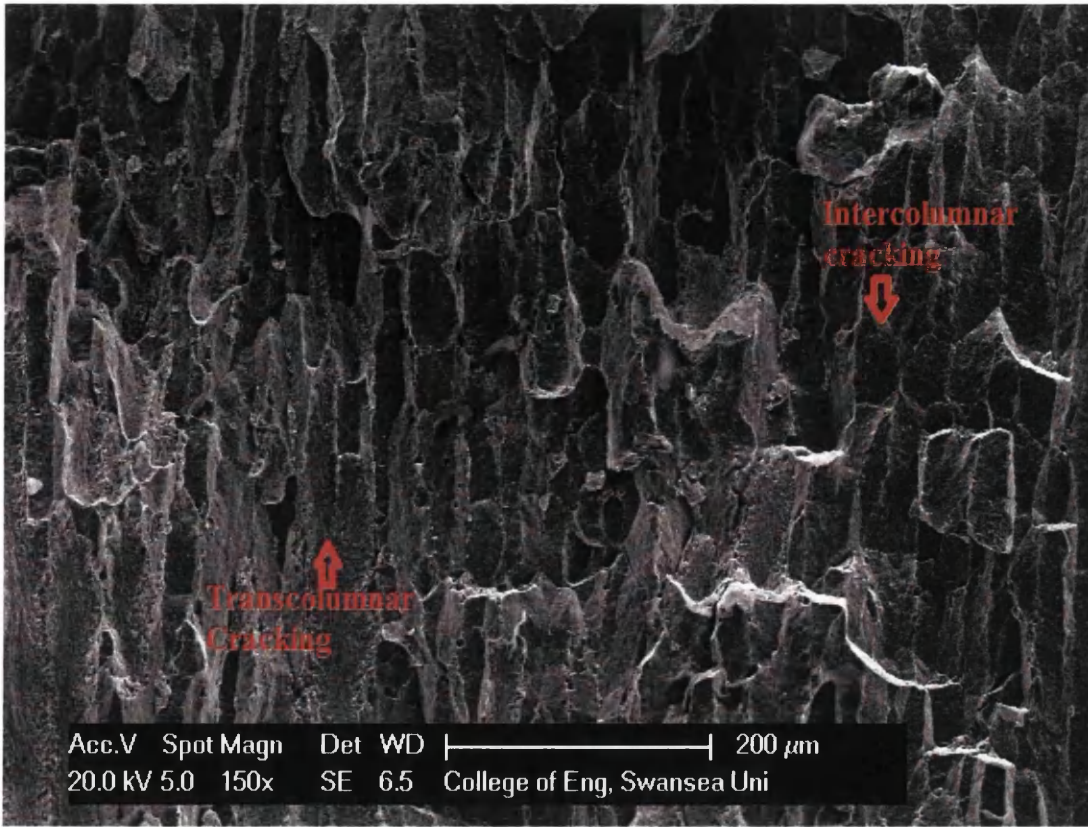


Figure 7.10.8 SEM Fractography analysis results shows the images observed on fracture surface of uncharged grade 2 PP-Ni specimen.



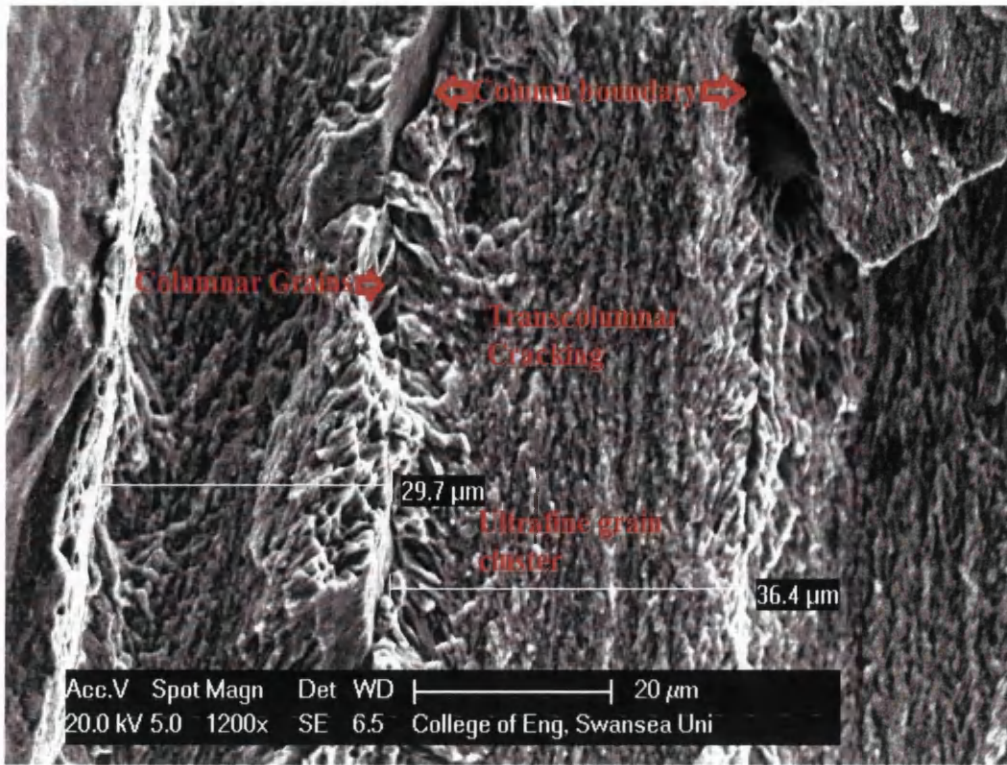
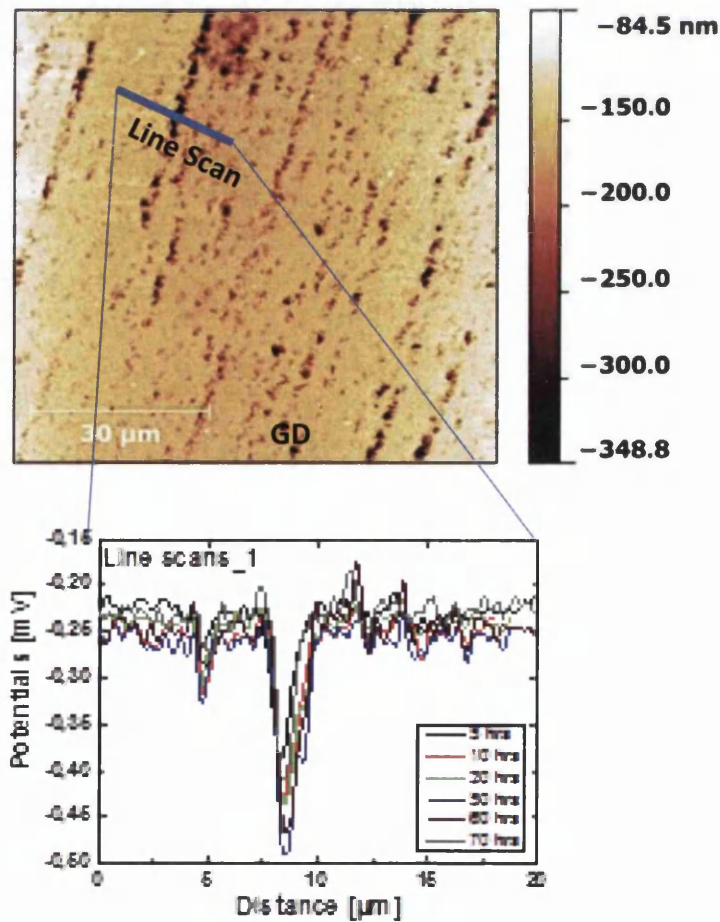


Figure 7.10.9 SEM Fractography analysis results shows the images observed on fracture surface of charged grade 2 PP-Ni specimen.



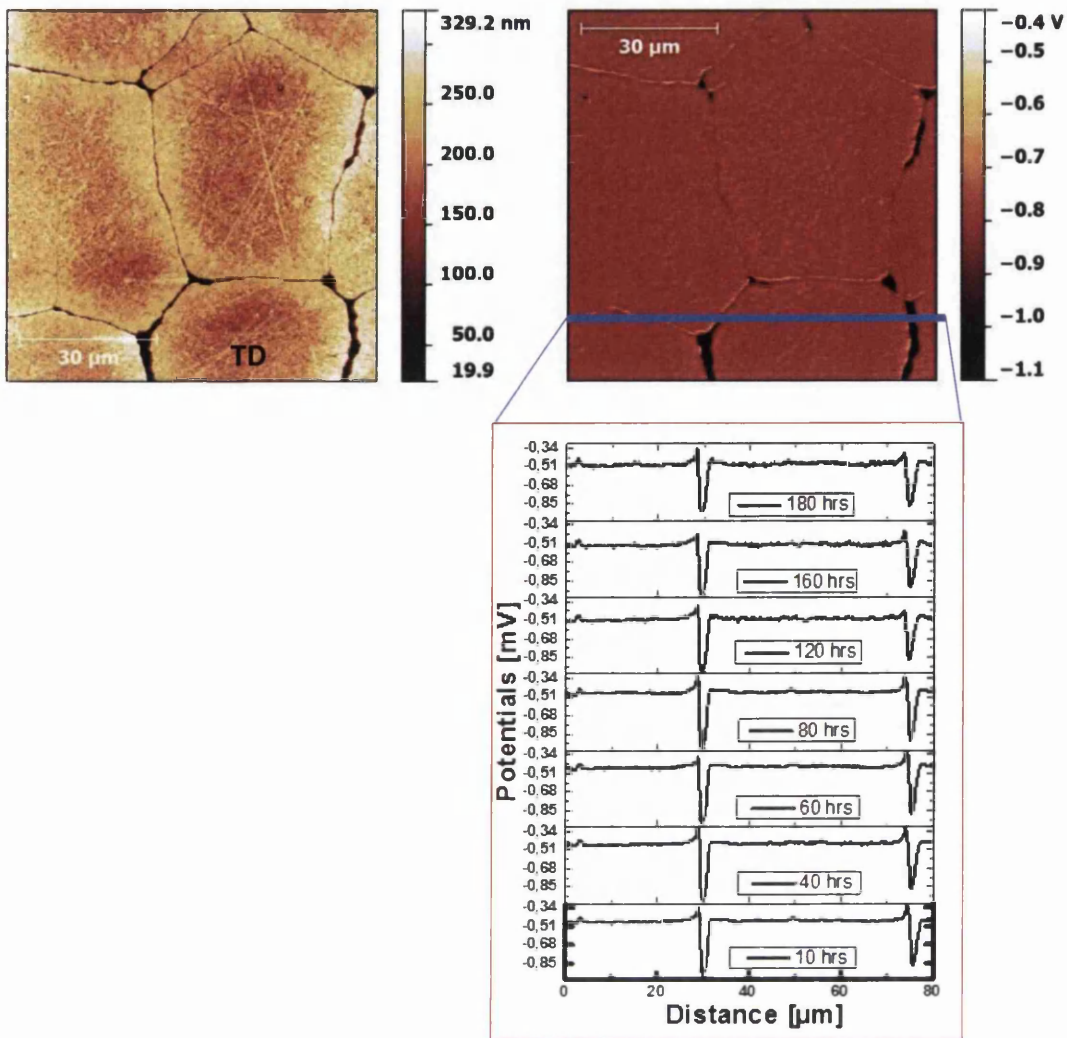


Figure 7.10.10 SKPFM results along the growth direction (GD) and perpendicular to the growth direction (TD) for grade 2 PP-Ni.

7.10.2 Discussion

The established grade 1 PP-Ni material is more susceptible to hydrogen induced cracking and hydrogen embrittlement compared to the newly developed grade 2 material. Increases in pore fractions along columnar grain boundaries leads to hydrogen induced columnar cracking in grade 1 PP-Ni. Decreases in the fraction of pores/voids in grade 2 coupled with increases in the fraction of ultrafine nano grains have the effect of decreasing the susceptibility to hydrogen embrittlement. The ductility of grade 2 PP-Ni could be increased by reducing the amount of column boundaries, reducing the thickness of column boundaries and reducing the amount of voids along the column boundaries since these column boundaries and voids on these columnar boundaries are acting as deep traps for hydrogen atoms.

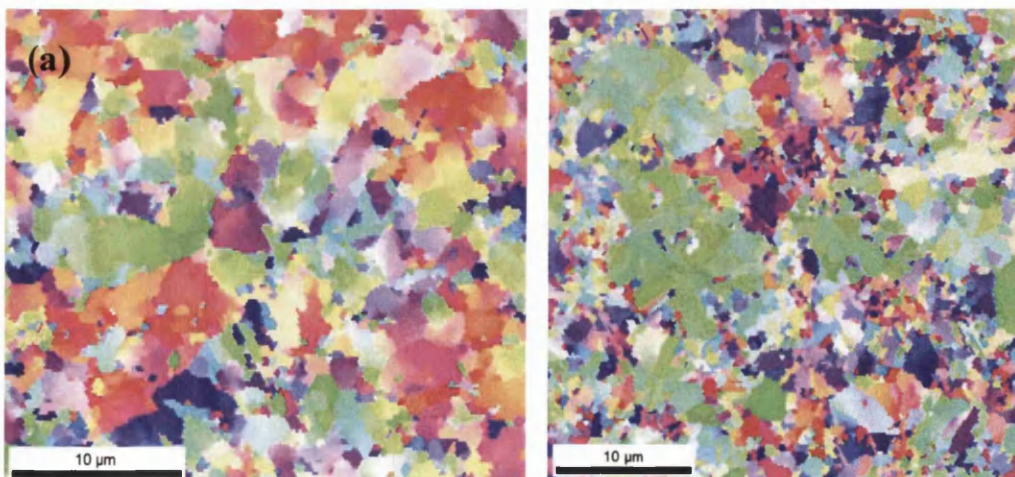
7.11 Weldability test of Ariane 5 combustion chamber Pulse Plated Nickel

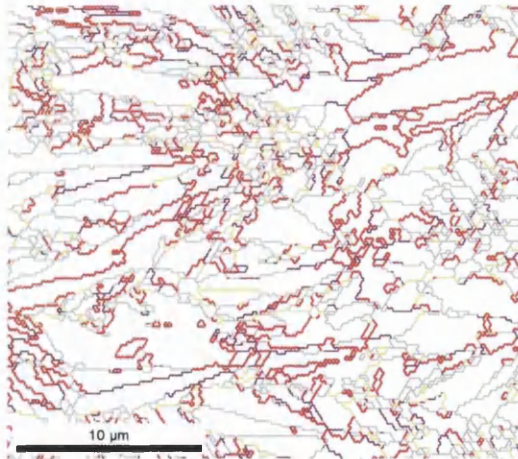
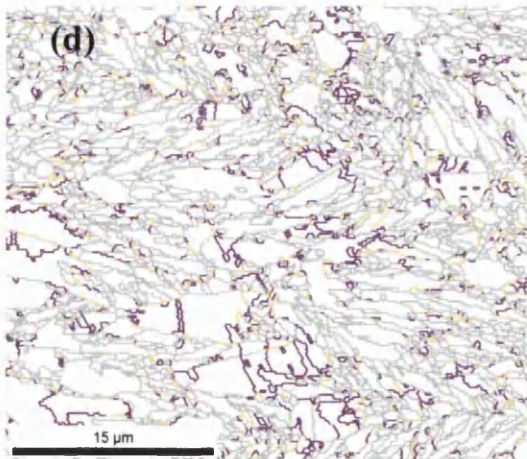
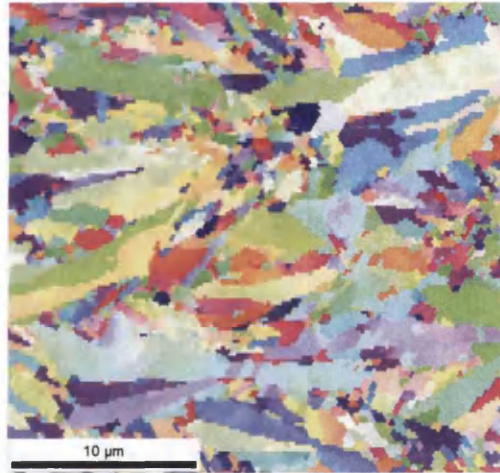
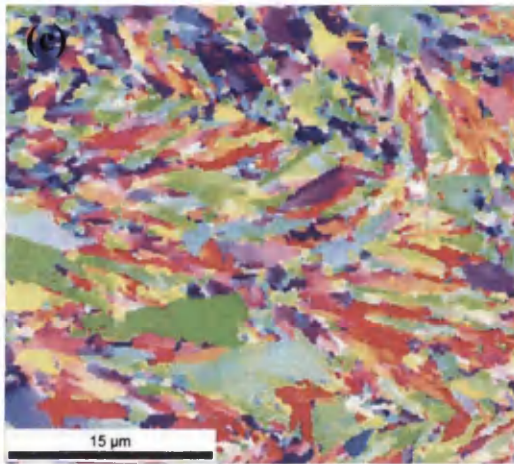
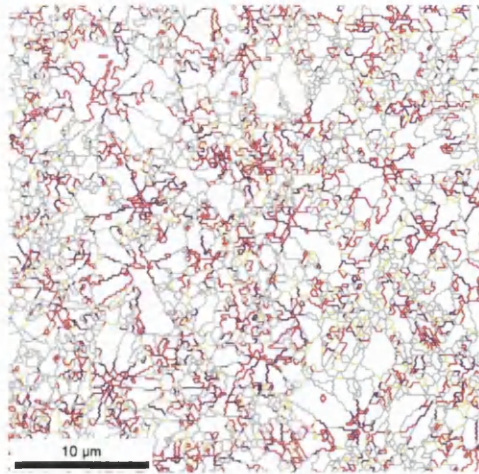
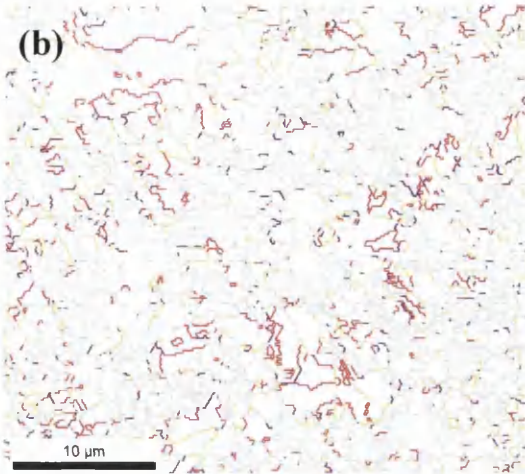
7.11.1 Experimental results

In this section the three different grades of PP-Ni microstructures are characterized using EBSD analysis. Grain boundary character is categorised as follows:

- Special $\Sigma 3$ twin boundaries are defined as $\Sigma 3$ grain boundaries.
- Coincidence site lattice (CSL) boundaries with $\Sigma \leq 11$ other than $\Sigma 3$ twin boundary were defined as special coincidence site lattice (SCSL) grain boundaries.
- Grain boundary misorientations $50^\circ \leq \theta \leq 62^\circ$ other than $\Sigma 3$ & $\Sigma 11$ were defined as special random grain boundary (SRGB)
- All other grain boundaries were defined as random grain boundary (RGB).

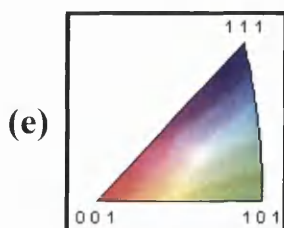
Figure 7.11.1 shows the EBSD results of different grades of pulse plated nickel. The GBCD and $\Sigma 3$ special grain boundary fractions are calculated for the three different grades of PP-Ni and plotted in figure 7.11.2. Only very small amounts of $\Sigma 3$ grain boundary fractions were observed in grade 1, twice as many were observed in grade 2 and twice as many again in grade 3. There is also a decrease in random grain boundaries (RGB) from grade 1 to grade 3.





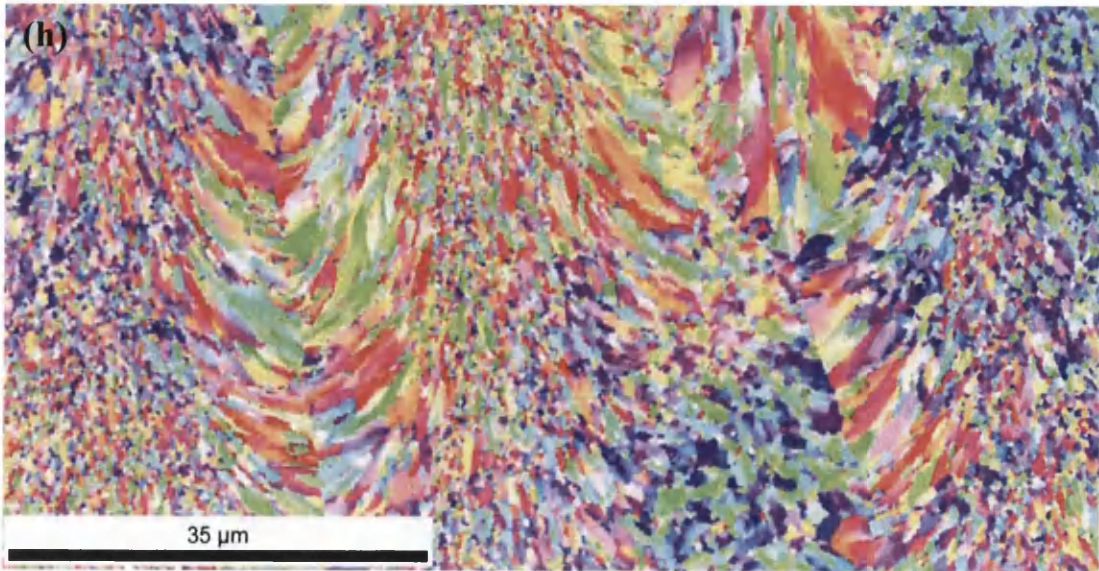
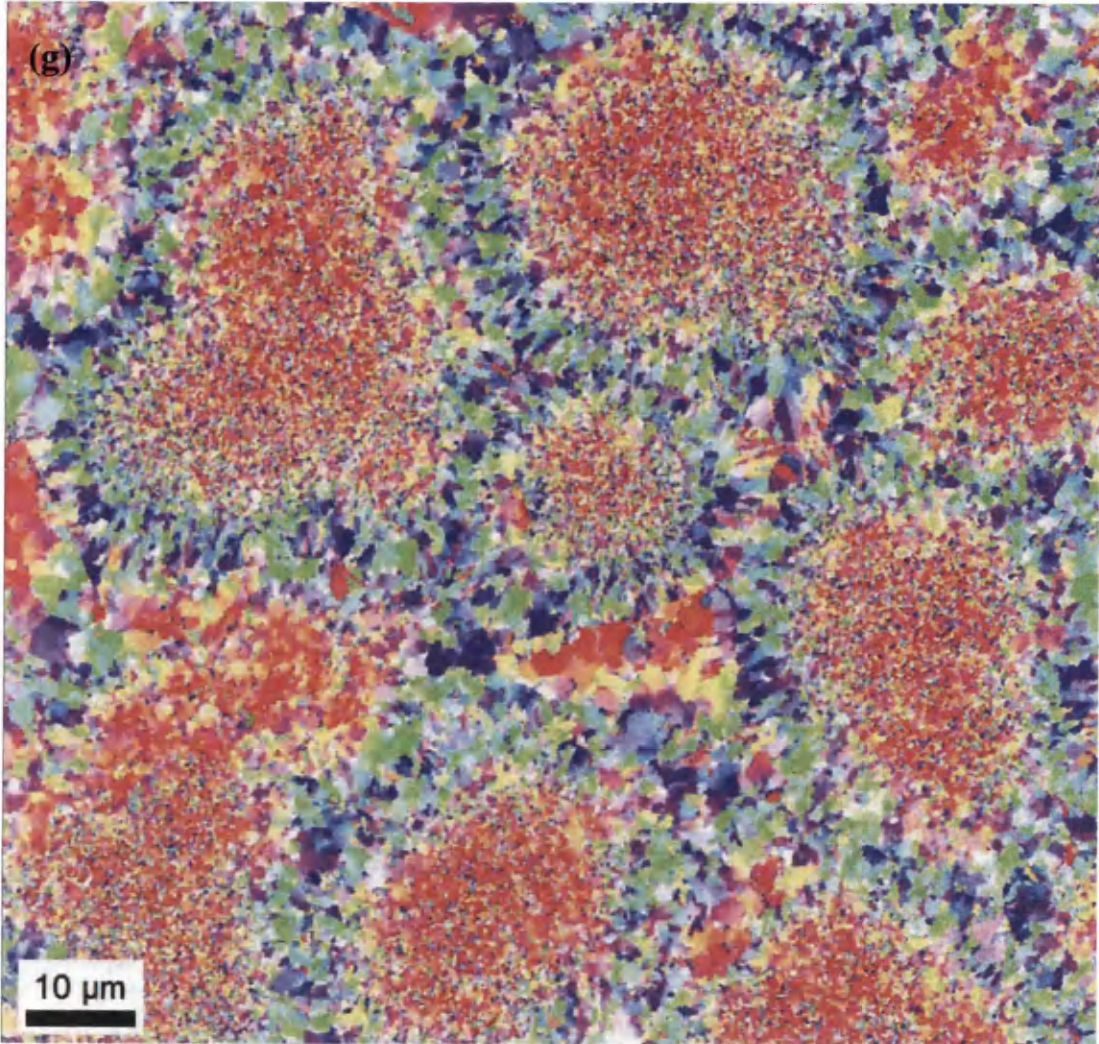
Grade1

Grade3



- $\Sigma 3$
- SCSL
- SRGB
- RGB

(f)



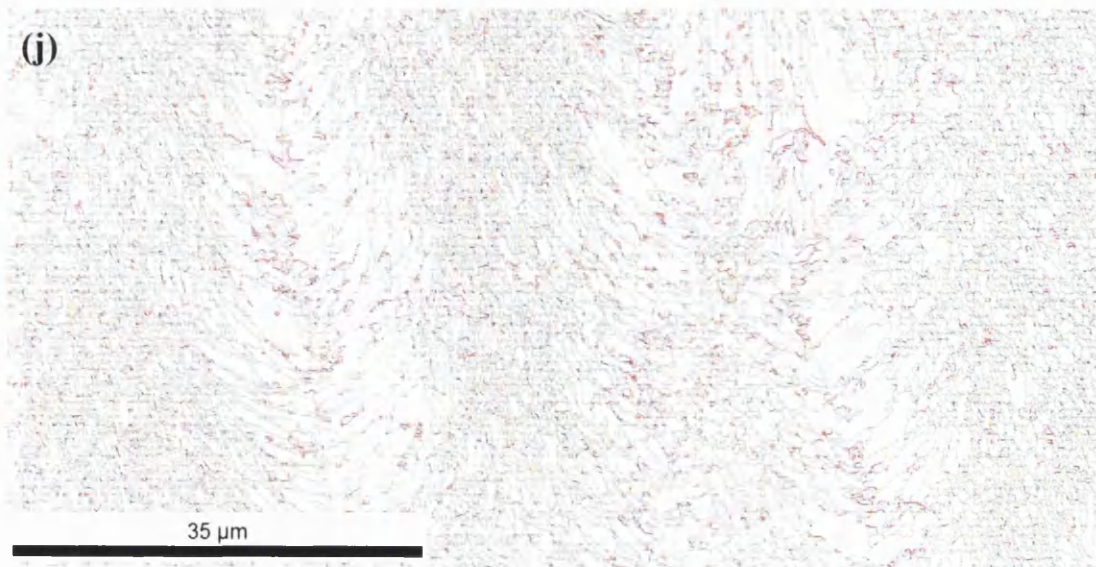
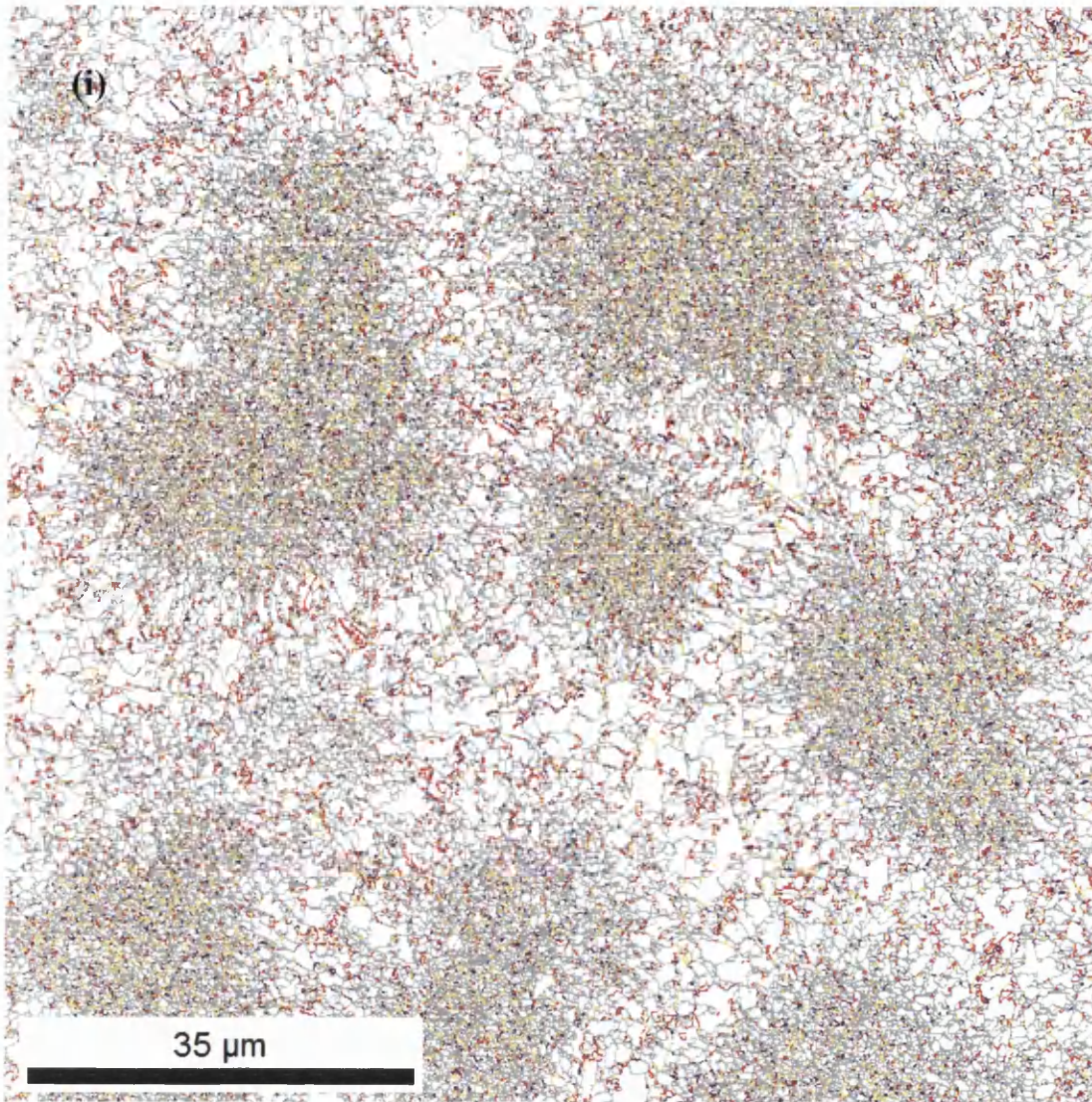


Figure 7.11.1 EBSD results for three different grades of pulse plated nickel (grade 1 and grade 3 left and right columns respectively). (a) Perpendicular to growth

direction (TD). (b) TD GBCD (c) In growth direction (GD). (d) GD GBCD. (e) Inverse pole figure (IPF). (f) GBCD colour contours. (g) Crystal orientations of grade 2 along TD. (h) Crystal orientations of grade 2 along GD. (i) and (j) show the GBCD of grade 2 along TD and GD respectively.

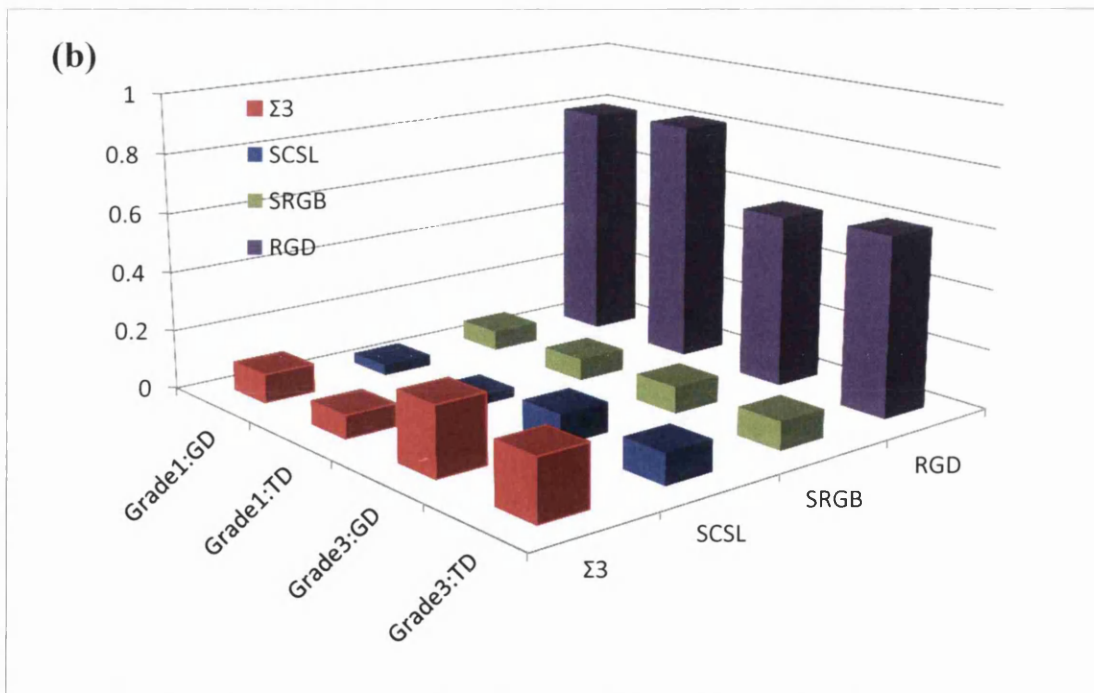
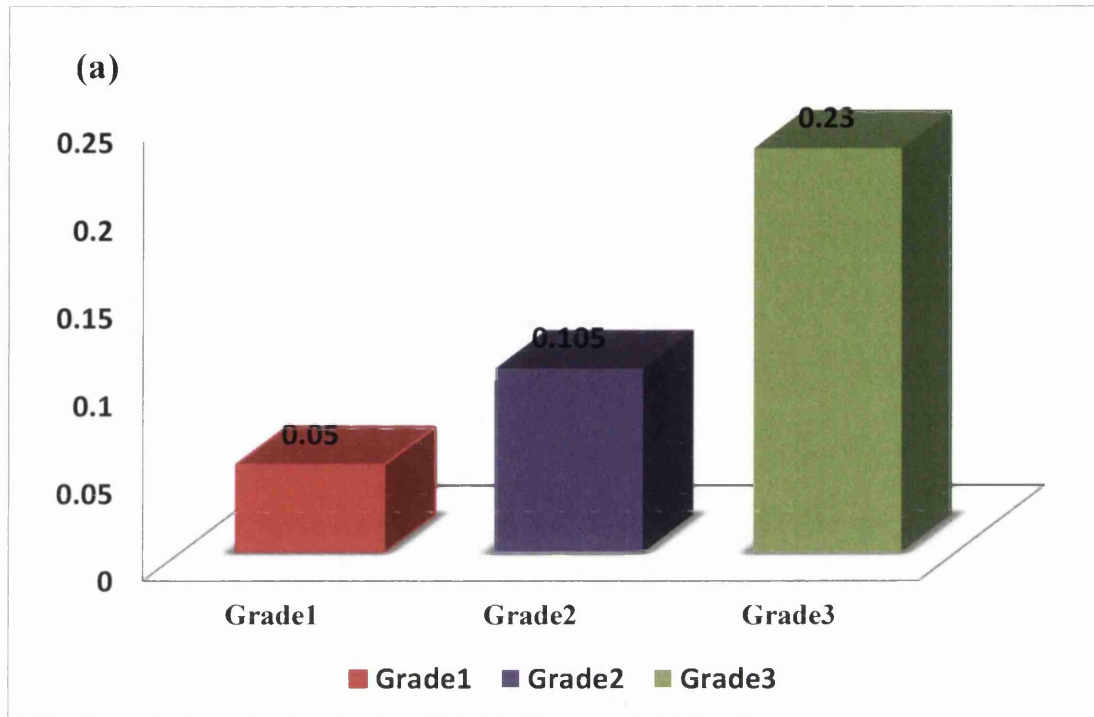


Figure 7.11.2 shows the calculated results. (a) $\Sigma 3$ grain boundary fractions on three different grades of pulse plated nickel along TD. (b) GBCD along GD and TD on three different grades of pulse plated nickel using EBSD analysis. Note: RGD is random grain boundaries.

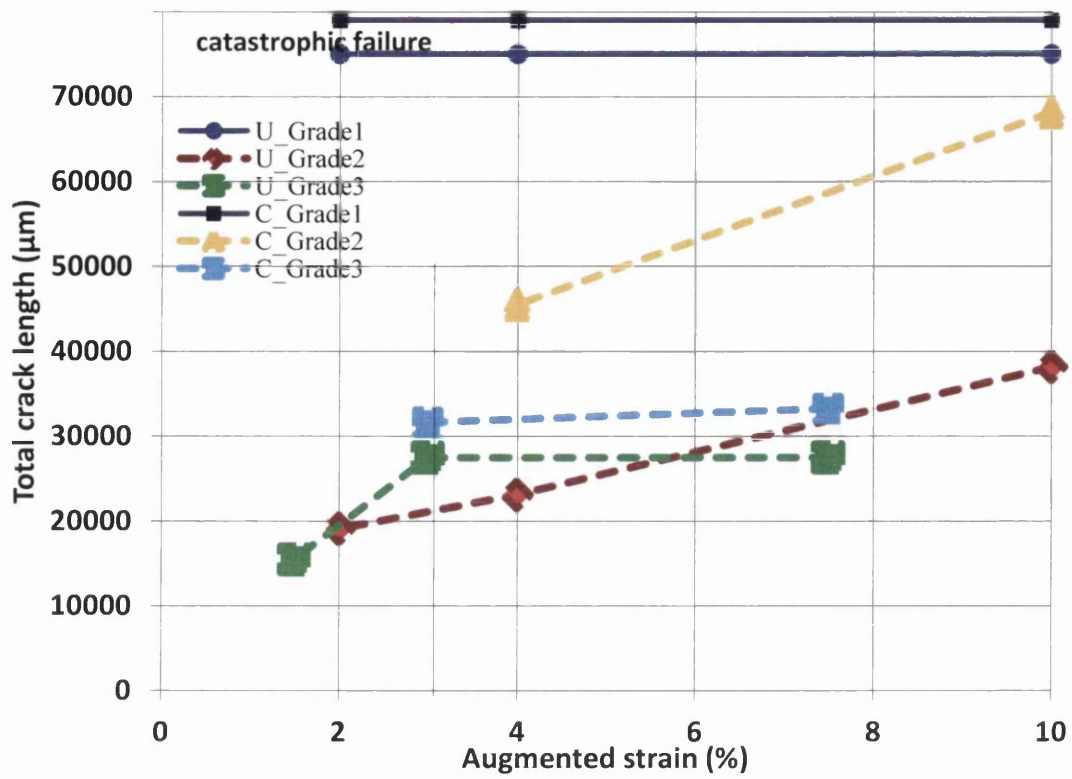


Figure 7.11.3 Varestraint test results for three different grades of pulse plated nickel with and without hydrogen charging (U=uncharged and C=hydrogen charged specimens).

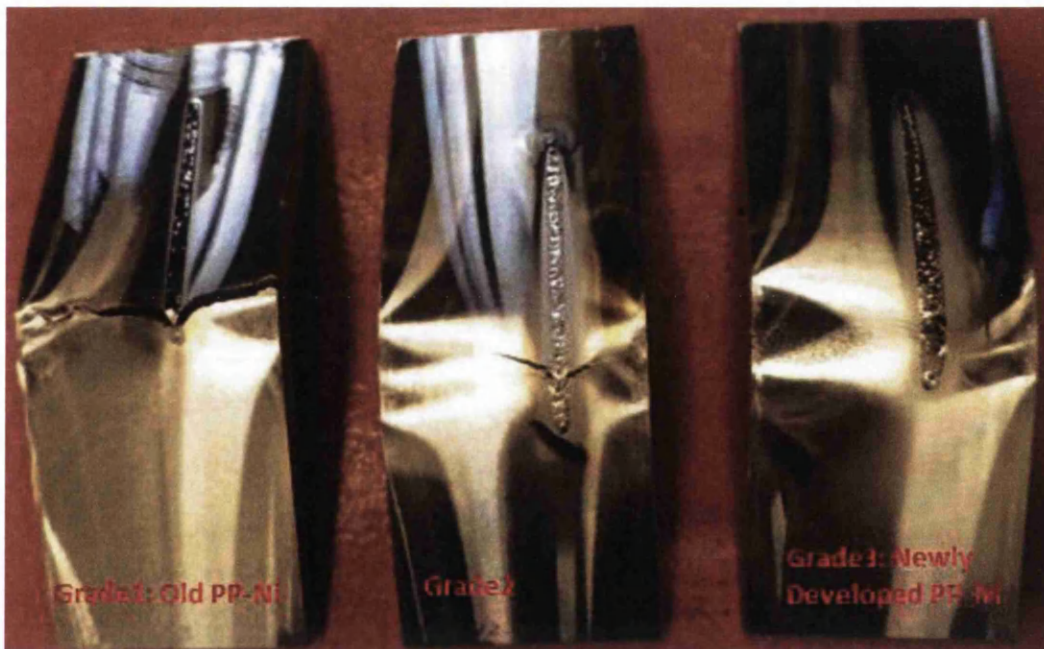


Figure 7.11.4 Results of weldability tested uncharged pulse plated nickel specimen between three different grades of material.

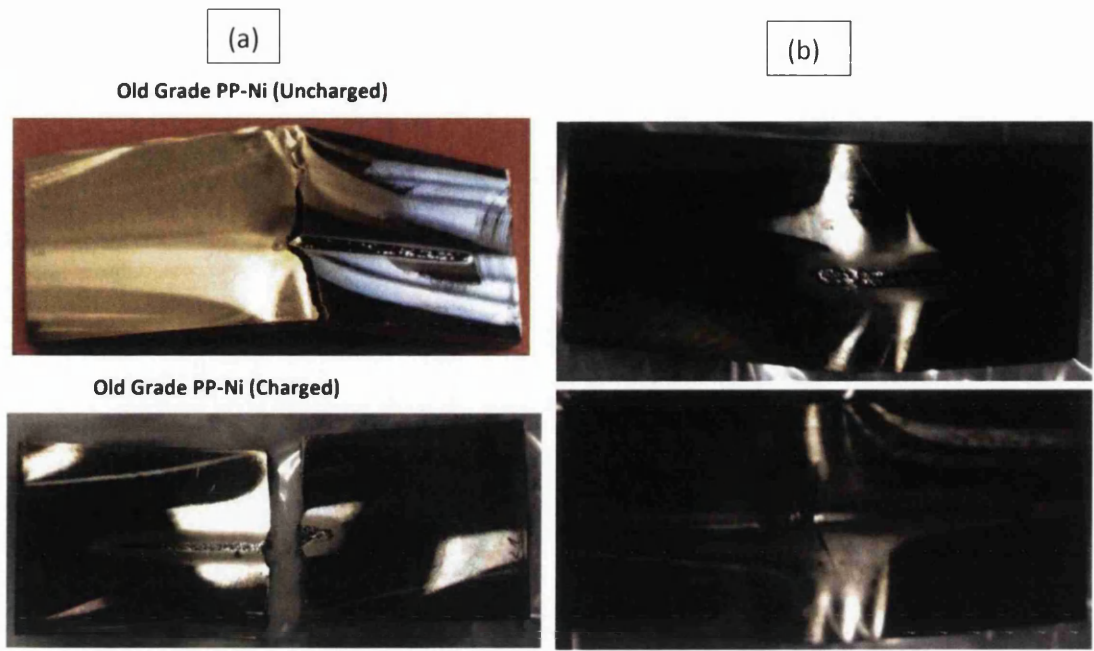


Figure 7.11.5 Weldability tested fractured specimens (a) grade 1 without hydrogen charging (top left) and with hydrogen charging (bottom left). (b) Grade 2 (bottom right) and grade 3 (top right) both with hydrogen charging.

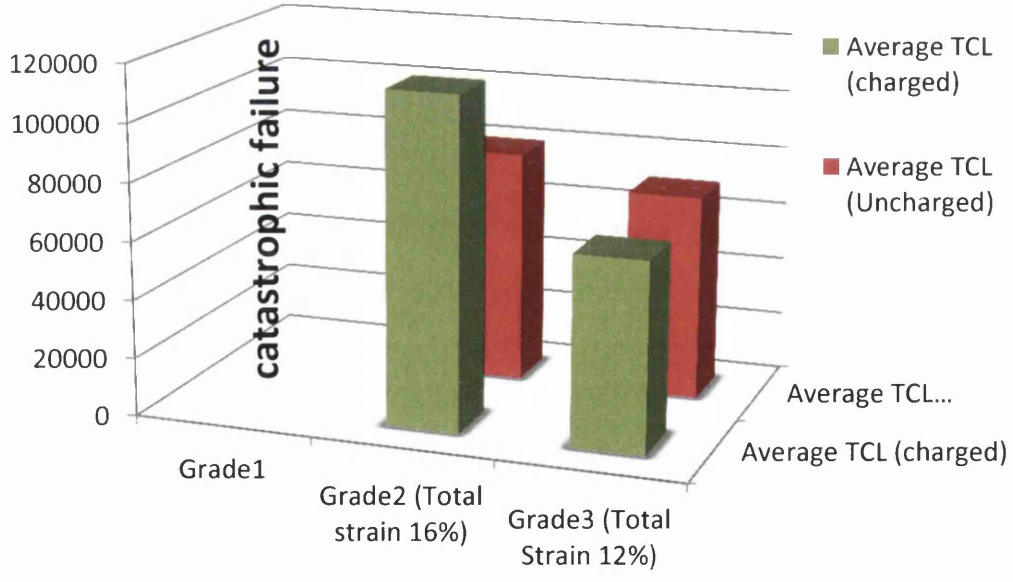


Figure 7.11.6 TCL for different strains (%) for three different grades of PP-Ni material with and without hydrogen charging.

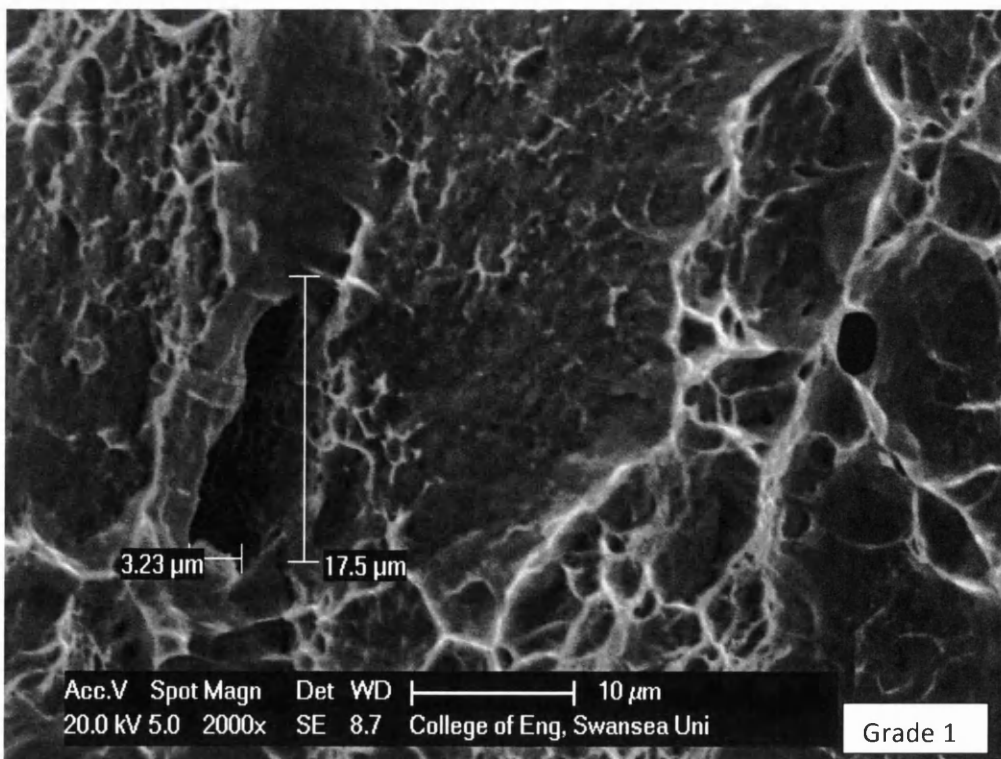
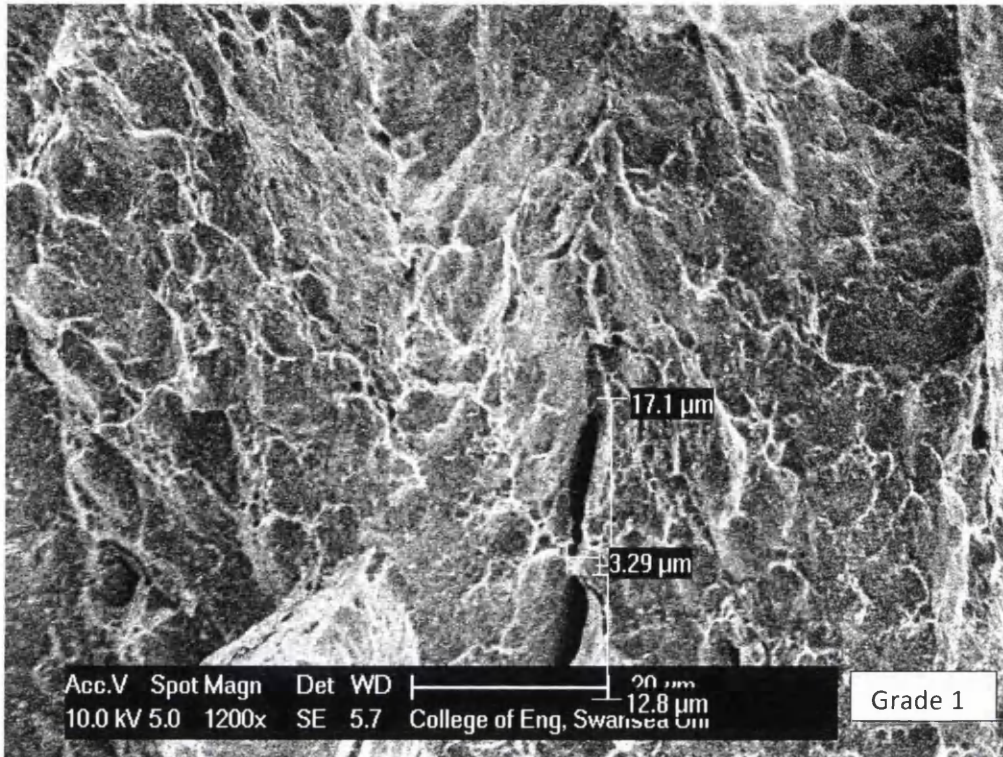
As noted in the chapter 4, section 4.6 Varestraint tests were performed to evaluate the susceptibility to weld cracking of three different grade PPNi materials. The Varestraint test results are presented in terms of average total crack length (i.e. the sum of each crack measured on the surface of individual test specimens) for three different augmented strain specimens of uncharged PP-Ni and also on two different augmented strain specimens of hydrogen charged samples. These results are plotted in figure 7.11.3. The macroscopic images of the Varestraint tested specimens can be found in figures 7.11.4 and 7.11.5.

7.11.2 Discussion

The total crack length, (TCL), measured on various augmented strain tests with and without hydrogen charging is shown in figure 7.11.6. These results show that grade 1 failed catastrophically and is more susceptible to cracking than grades 2 and 3. The newly developed grade 2 was less susceptible to cracking than grade 1 PP-Ni material but more susceptible to cracking than grade 3 PP-Ni material. This also shows that hydrogen charged PP-Ni specimens are more susceptible to cracking when compared to uncharged grades of PP-Ni. Moreover, the newly developed grade 3 material attains a maximum TCL at about 3% strain. Above this 3% augmented strain there were no significant increase in TCL. The better cracking resistance of newly developed grades 2 and 3 PP-Ni can be explained as follows

- (i) An increase in $\Sigma 3$ boundaries and SCSL special grain boundaries with a decrease in random grain boundaries (RGB) as shown in figure 7.11.2. (It has been previously reported that increases in $\Sigma 3$ special grain boundary fraction increases the crack resistance in nickel [Palumbo et al.,1990,1997] and decreases the susceptibility of intergranular hydrogen embrittlement in conventional electrodeposited nickel [Bechtle et al., 2009].
- (ii) A decrease in the number of micro pores (c.f. figure 7.11.7 SEM characterization results show larger micro pores and a higher fraction of micro pores in grade 1, a very small fraction of micro-pores in grade 2 and no micro pores observed in grade 3).

- (iii) Fractography analysis on the Vareststraint tested grade 3 specimen fracture surface in the base metal and heat affected zone (HAZ) using SEM as shown in figure 7.11.8 and figure 7.11.9.



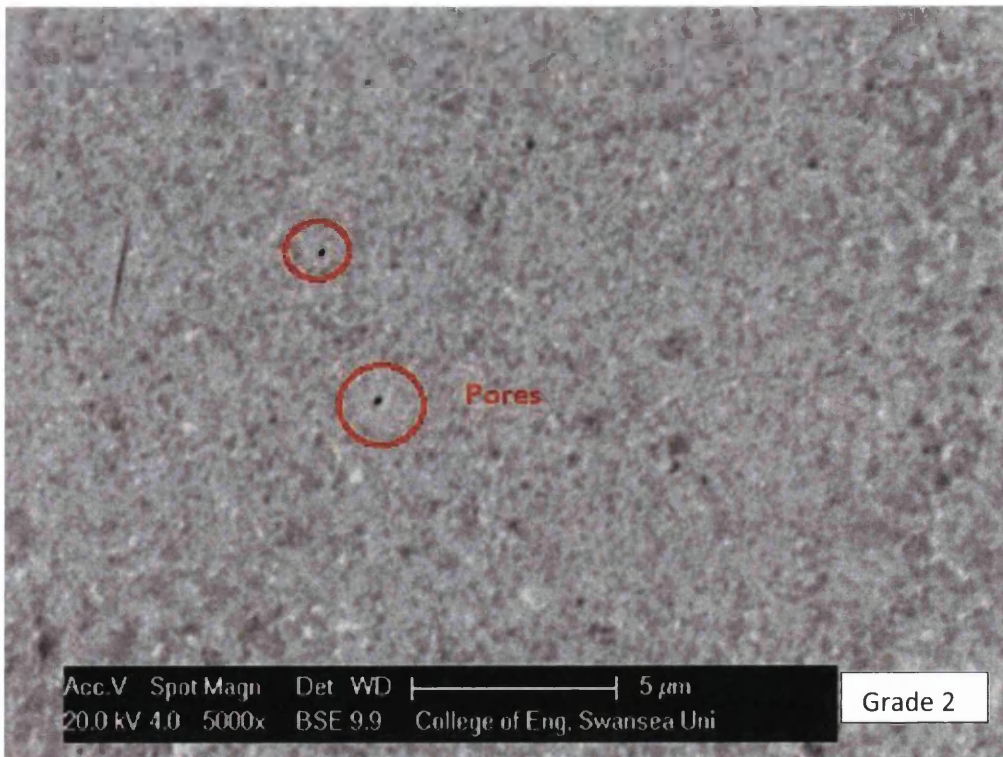
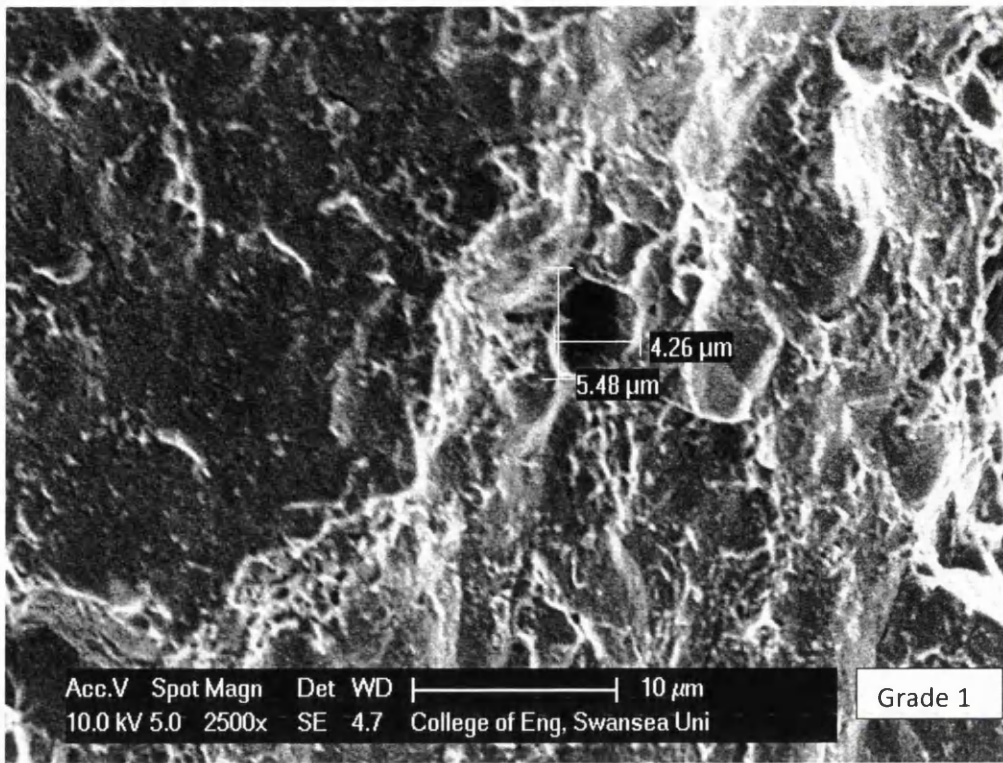


Figure 7.11.7 SEM image showing micro-pores in different grades of PP-Ni.

Fractography observations done on Vareststraint tested uncharged fractured specimen grade 1 PP-Ni base metal (BM) are shown in figure 7.11.8. Figure 7.11.9 shows the fractography image of Vareststraint tested hydrogen charged fractured specimen grade 1 PP-Ni base metal. These observations reveal that the grade 1 PP-Ni based material fractured along columnar grain boundaries and thus columnar boundaries are prone to cracking. This also reveals that hydrogen atoms segregate along columnar grain boundaries making these interfaces brittle. Figure 7.11.10 shows recrystallized grains (in the heat affected zone) and columnar grains in the base metal in the uncharged specimen. Figure 7.11.11 shows the SEM fractography image of Vareststraint tested fractured specimen for uncharged grade 1 PP-Ni in the HAZ. This shows that in the HAZ recrystallization occurs producing smaller polygonal grains and these recrystallized HAZ grains are prone to crack initiation leading to crack propagation causing intergranular HAZ cracking as shown in figure 7.11.11. Figure 7.11.12 shows the SEM fractography image of Vareststraint tested charged fractured specimen of grade 1 PP-Ni in the HAZ.

Temperature differences during welding in the BM, HAZ and weldment produce varying thermal tensile and compressive stresses in the longitudinal, transverse and depth directions of the specimen. The difference in temperature and stress profiles develops differences in the diffusion of hydrogen and nickel atoms. The difference in diffusion rates between nickel and hydrogen atoms and the motion of grain boundaries may lead to void formation due to the Kirkendall effect on recrystallized grain boundaries in the HAZ as shown in figure 7.11.12.

It is well know that increasing temperature and stress will increase the diffusivities of nickel and hydrogen. It is also reported by author in sections 7.1 to 7.4 that differences in grain size, grain boundaries and local microstructure affects the diffusion of hydrogen. These voids/pores in the HAZ act as sinks for vacancies which also act as traps for hydrogen leading to the formation of hydrogen molecules. These hydrogen molecules may react with carbon to form methane. Methane gas in pores/voids increases the pressure. Increases in temperature and thermal stress due to welding may thus form micro-cracks on grain boundaries leading to intergranular hydrogen induced cracking in the HAZ.

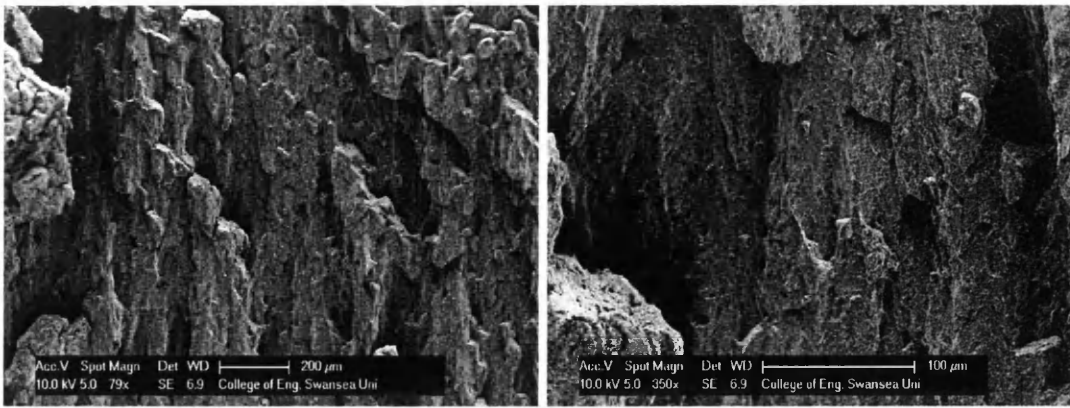


Figure 7.11.8 SEM fractography image of Varestraint tested uncharged fractured specimen grade 1 PP-Ni in the base metal.

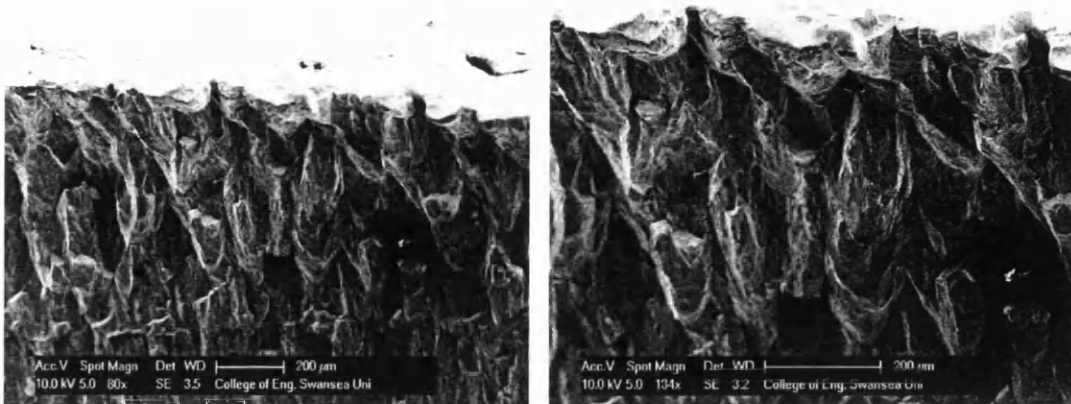


Figure 7.11.9 SEM fractography image of Varestraint tested hydrogen charged fractured specimen grade 1 PP-Ni in the base metal.

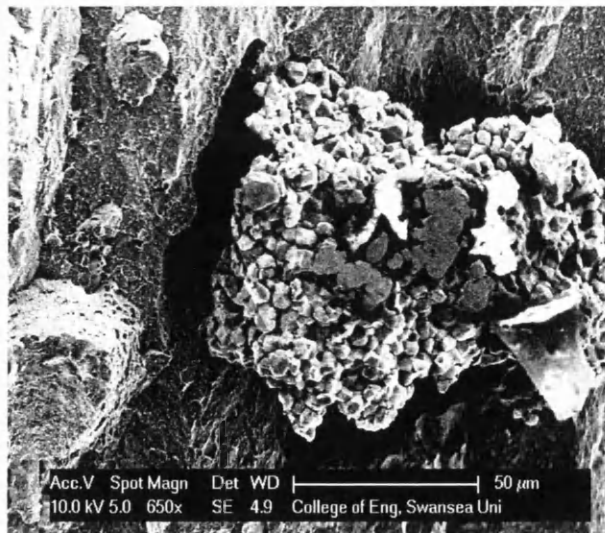
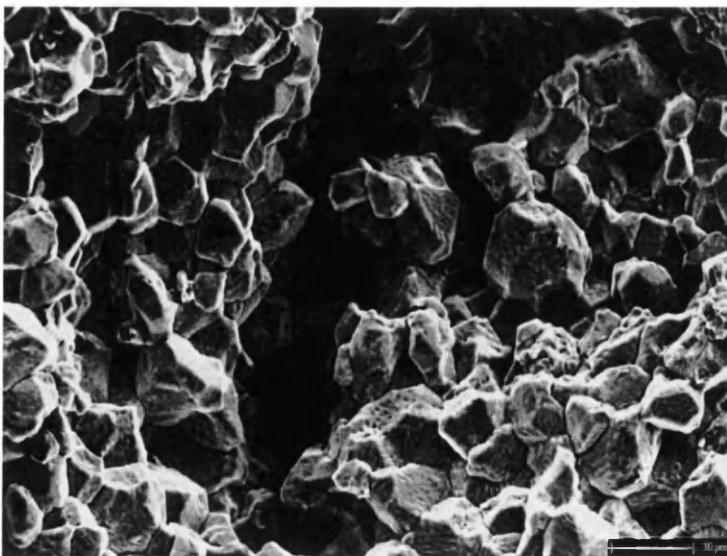
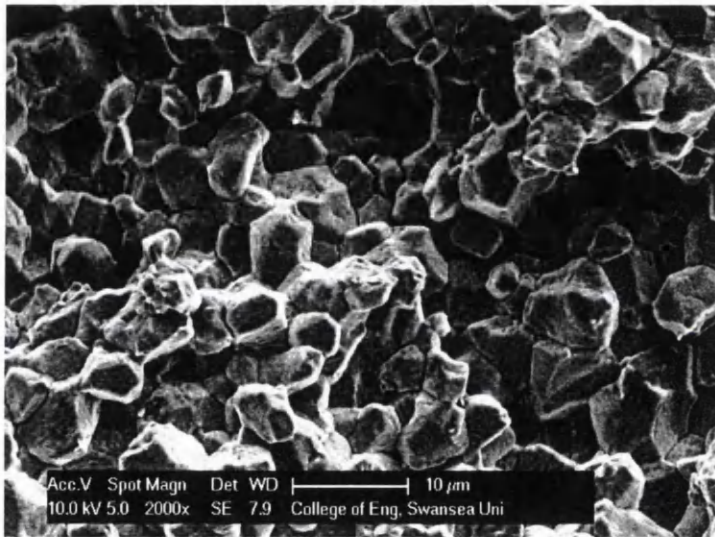
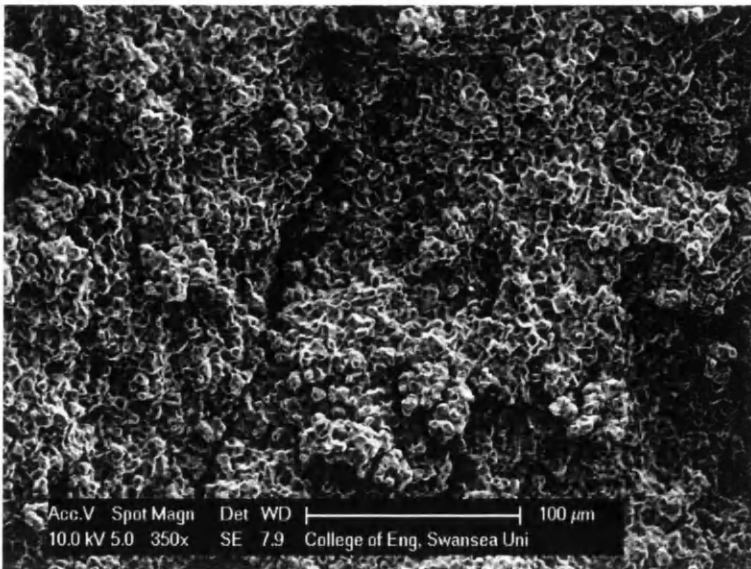


Figure 7.11.10 Recrystallized grains and columnar grains on the Varestraint tested uncharged fractured specimen grade 1 PP-Ni.



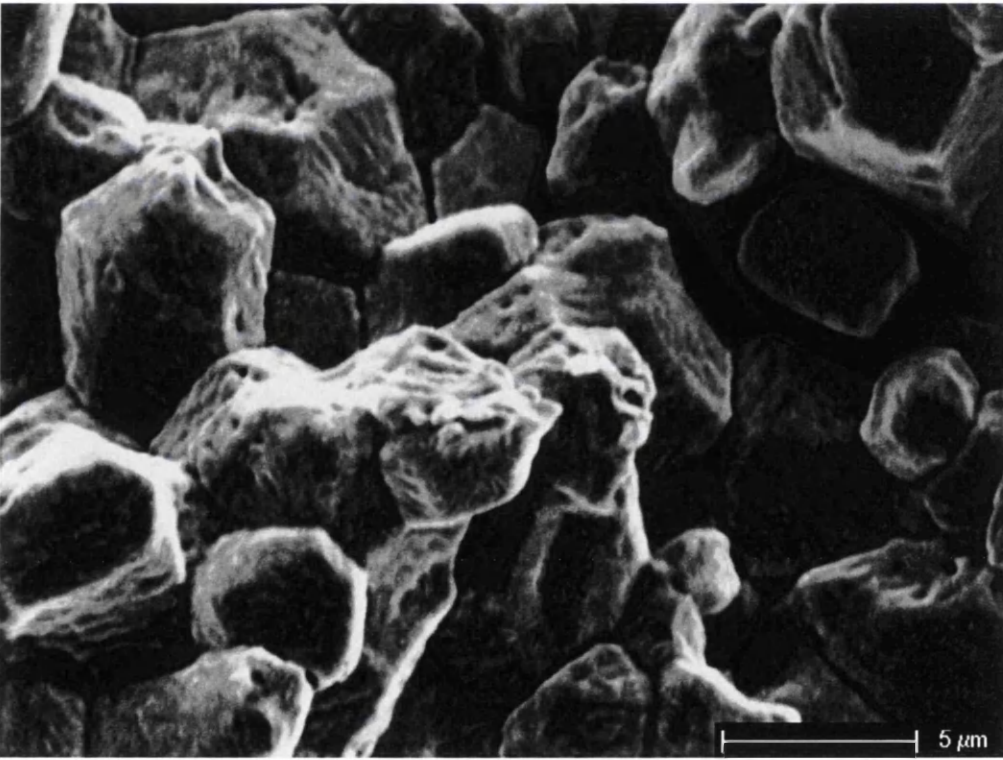
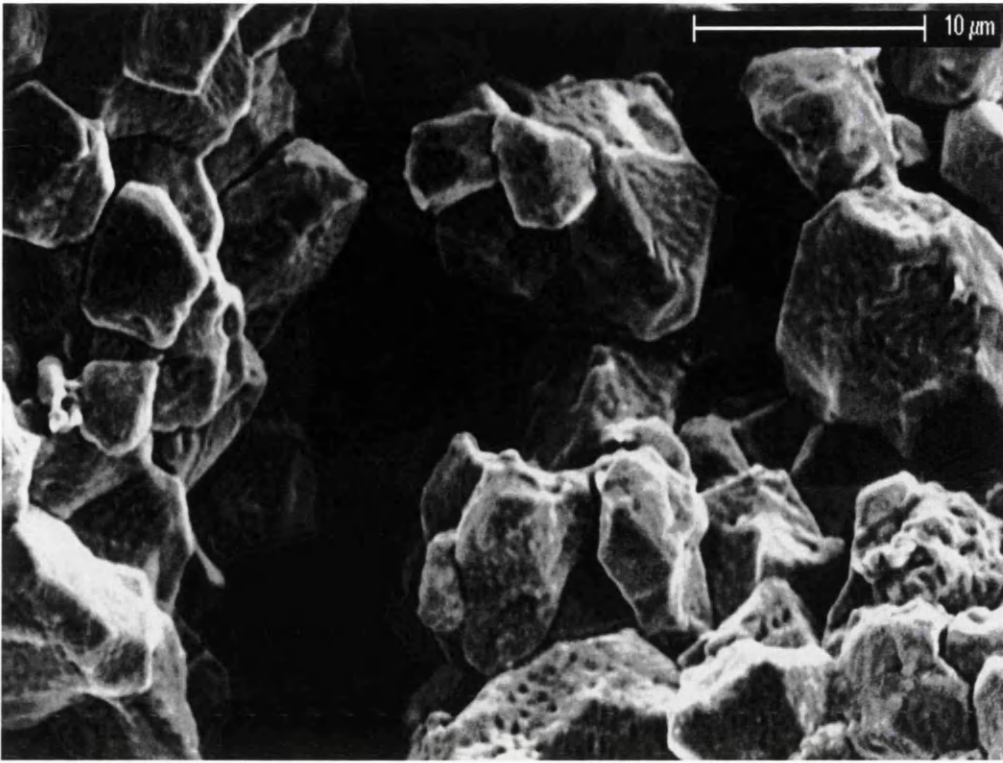
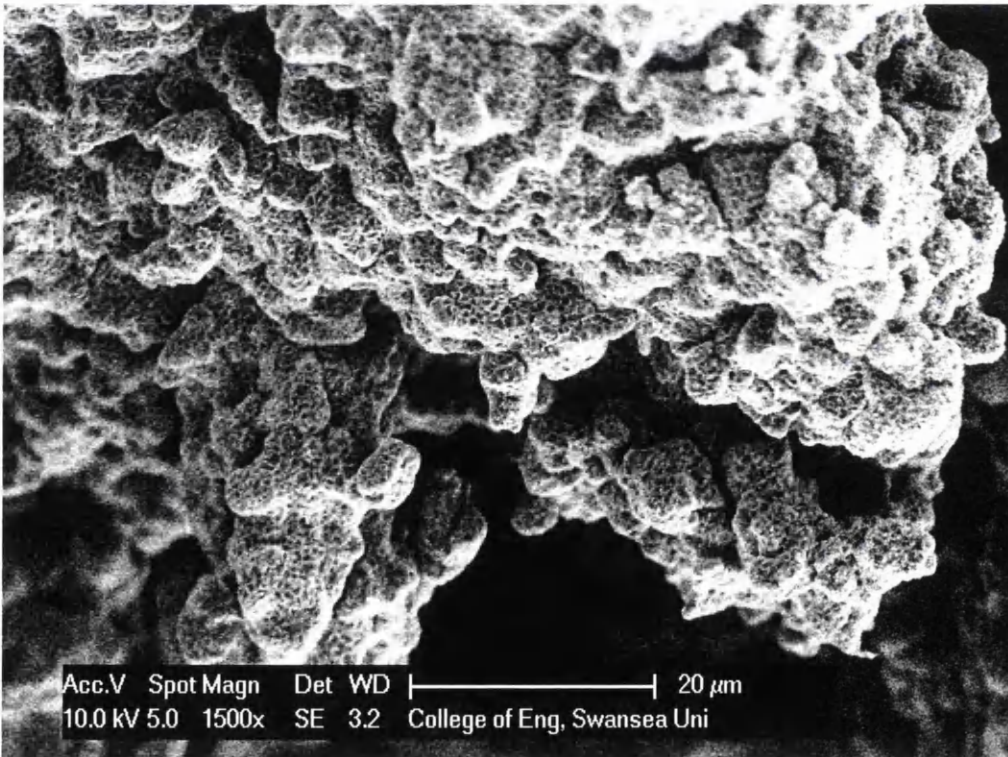
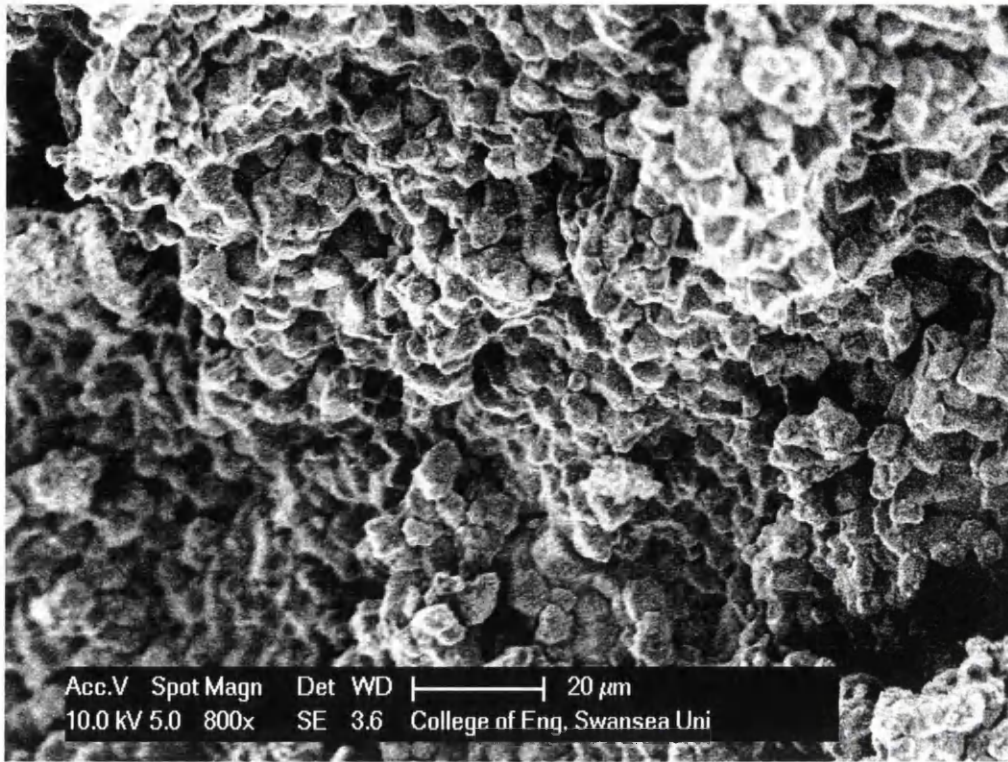
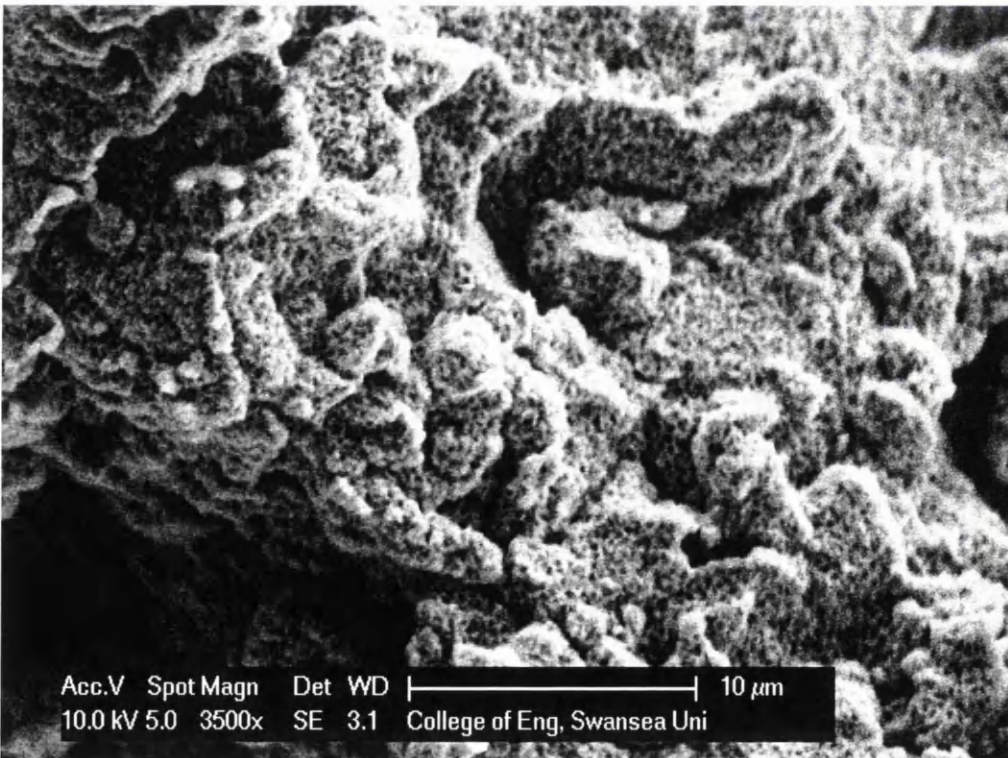
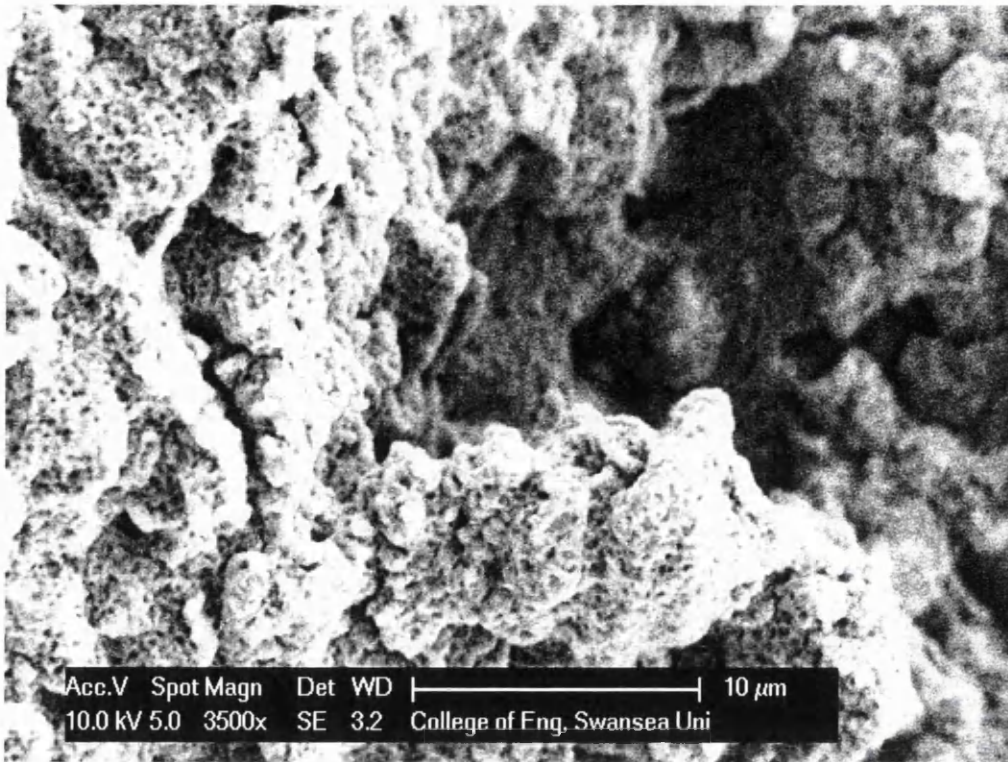


Figure 7.11.11 SEM fractography image of Varestraint tested uncharged fractured specimen grade 1 PP-Ni in the HAZ.





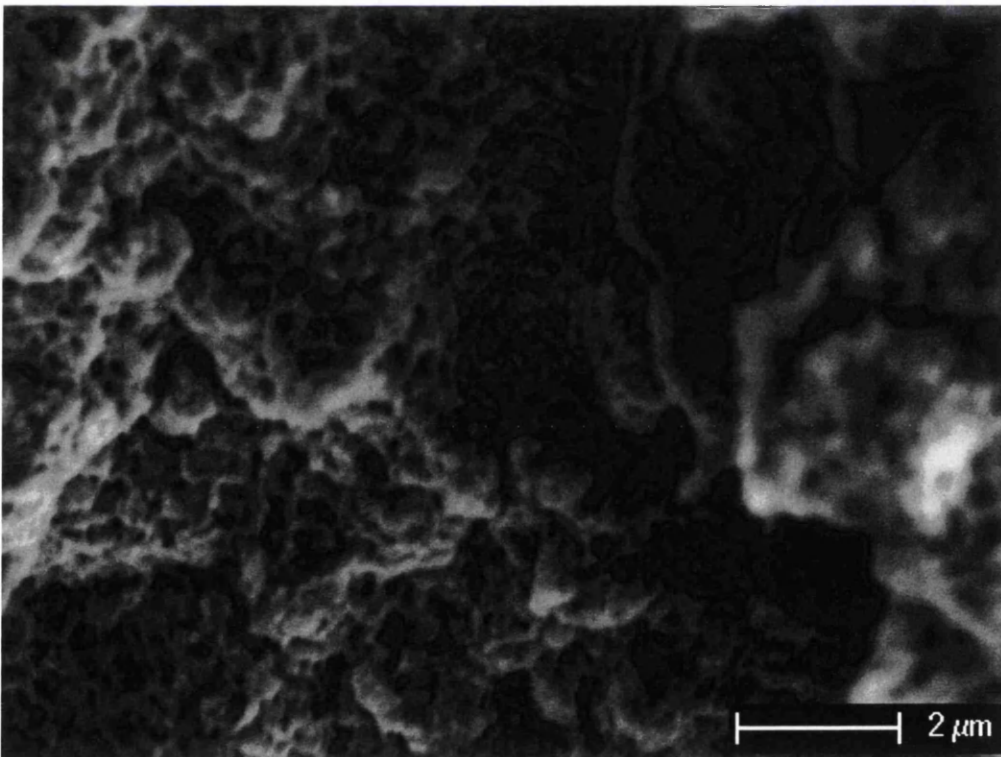
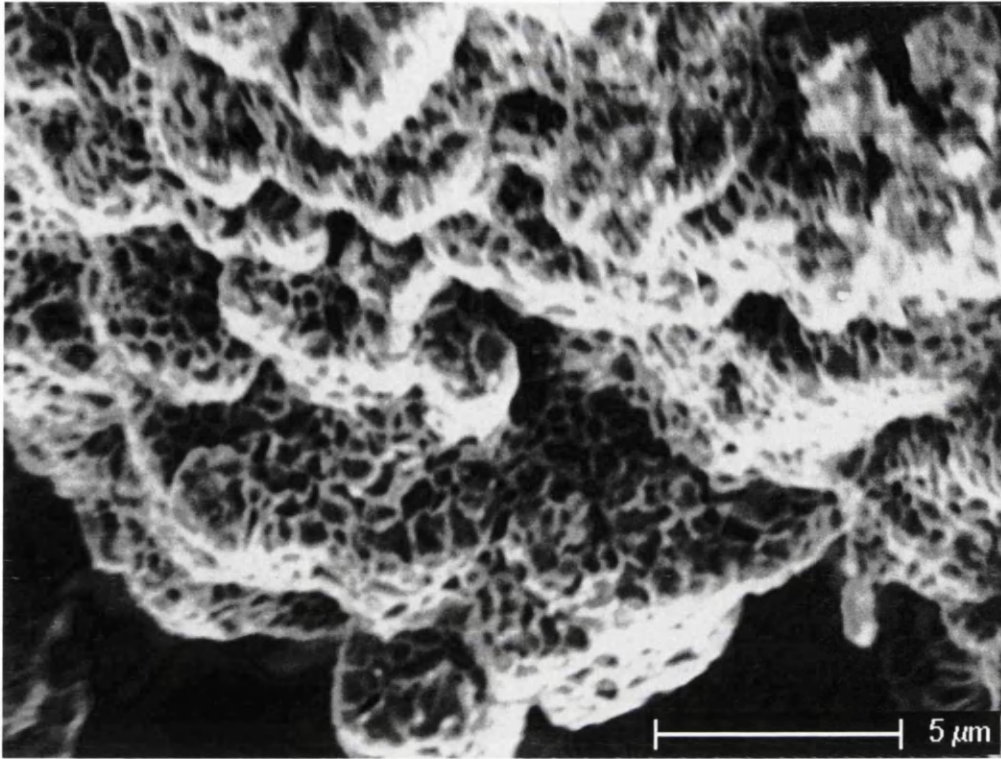


Figure 7.11.12 SEM fractography image of Vareststraint tested hydrogen charged fractured specimen grade 1 PP-Ni in the HAZ.

CONCLUSIONS

Simply determining that hydrogen induced cracking and other forms of hydrogen embrittlement and weldability failure is a problem, is of no particular help to the aerospace industries unless recommendations to avoid such failures in future aerospace applications are provided. In this research thesis the effect of microstructural features on various aspects of hydrogen embrittlement have been determined using multiscale modelling and experimental techniques. The phenomenological and quantitative explanation of hydrogen induced failure process that has been acquired permits several recommendations that may help to reduce the susceptibility of aerospace components made of pulse plated nickel and nickel based super alloy 718 to various forms of hydrogen induced failure.

Conclusions are as follows

- Investigation of hydrogen transport in polycrystalline intergranular and intragranular regions is critical for establishing the relationship between microstructures and effective hydrogen diffusion properties. A multiscale approach was adopted to investigate the influences of numerous intergranular and

intragranular microstructures to quantify effective hydrogen diffusivity. Good correlation between analytical, experimental and computational results was demonstrated. Decreasing grain size and increasing grain boundary fractions in polycrystalline nickel increases effective hydrogen diffusivity.

- The present study shows that hydrogen diffusion in intergranular grain boundary regions becomes increasingly important as the grain size of the material decreases to the nano crystalline scale. For heterogeneous polycrystalline materials, containing micro and nano scale microstructures, the intergranular phase plays an important role and cannot be ignored. The complex hydrogen diffusion mechanisms occurring in these intergranular microstructural phases were successfully modelled by capturing grain size effects in polycrystalline materials.
- Hydrogen diffusion in conventional electrodeposited and pulse plated nickel is enhanced when;
 - ✓ grain sizes are smaller,
 - ✓ the volume fraction of grain boundaries and triple junctions increases,
 - ✓ the thickness of the grain boundary affected zone increases,
 - ✓ triple junctions change shape from ‘sharp corner’ to ‘round corner’,
 - ✓ fine nano grains are present in triple junctions.
- The presence of pores/voids slows down the bulk diffusion of hydrogen in polycrystalline nickel material and these pores/voids may also act as trap sites for hydrogen atoms/molecules. Hydrogen segregation is high in pores/voids.
- Decreasing the fraction of pores increases the resistivity to hydrogen embrittlement in nickel and nickel based super alloy 718.
- Material characterization using SEM/EBSD/OIM of different grades of Ariane 5 combustion chamber pulse plated nickel reveals that grade 1 PP-Ni has a high fraction of pores/void. It also has a lower fraction of special grain boundaries such as $\Sigma 3$ grain boundaries when compared to newly developed grade 2 and grade 3 PP-Ni materials. Clusters of ultrafine grains have been observed in grade 2 PP-Ni which increases the resistivity to hydrogen embrittlement.
- Grade 2 and grade 3 are more resistant to hydrogen embrittlement compared to grade 1 PP-Ni.

- A microstructural FE computational technique has been successfully developed based on real microstructures from experimental material characterization to calculate the intergranular grain boundary diffusivity and bulk isotropic and anisotropic diffusivity of hydrogen in both conventional and Ariane 5 combustion chamber pulse plated nickel material.
- The multiscale FE calculated grain boundary diffusivity is two orders of magnitude higher than the lattice diffusion of hydrogen in nickel. The model results are in good agreement with experimental measurements. Understanding the intergranular diffusion of hydrogen atoms and bulk effective isotropic and anisotropic diffusion of hydrogen aids understanding, control and solution of engineering problem such as hydrogen embrittlement. This method could also be used to design new polycrystalline materials with improved resistance to material degradation and failure.
- The effective bulk diffusivity of conventional electrodeposited polycrystalline nickel was one order of magnitude smaller than the Ariane 5 combustion chamber grade 2 PP-Ni material.
- The effective bulk diffusion of hydrogen in Ariane 5 combustion chamber grade 2 PP-Ni has been observed to be anisotropic along the three principal directions due to structural anisotropy in the microstructure.
- In stress-assisted hydrogen diffusion analyses the dilatational stresses act as a driving force during the evolution of the hydrogen distribution. The evolving hydrogen distribution varies depending on TGB misorientation angles.
- The stresses and hydrogen distributions in bi-crystal and polycrystalline nickel are homogenous for TGB misorientation angles of 0° and 90° and strongly heterogeneous for TGB misorientation angles $0^\circ < \theta < 90^\circ$ under uniform applied mechanical loading.
- The types of stress produced (tensile or compressive) depends on the applied boundary conditions due to deformation constraints arising from crystal misorientations.
- The model results are in agreement with experimental observations, where experimentally it is observed that a large amount of hydrogen is trapped in

regions under tensile stress. Correspondingly, hydrogen trapping is reduced in regions of compressive stress.

- Increasing dilatational mismatch along TGBs and near TGBs increases the hydrostatic stress based on misorientation angles which leads to increased hydrogen segregation. Conversely, decreasing dilatational mismatch decreases hydrostatic stress gradients based on misorientation angles leading to decreased amounts of hydrogen segregation.
- The maximum segregation of hydrogen concentration depends on the TGB misorientation angle. The maximum segregation of hydrogen tends to increase for TGB misorientation angles greater than 0° attaining a maximum for a TGB misorientation angle of 35° . Segregation subsequently decreases for TGB misorientation angles $35^\circ < \theta < 90^\circ$ in the bi-crystal and polycrystalline nickel model.
- A numerical modelling framework has been demonstrated that allows consideration of grain boundary misorientation angles for studying hydrogen segregation and thus intergranular hydrogen embrittlement (associated with induced tensile stresses) and also the suppression of intergranular hydrogen embrittlement (associated with induced compressive stresses).
- The numerical model predicts maximum hydrogen concentrations are accumulated on TGBs with misorientation angles ranging between $15^\circ < \theta < 45^\circ$ and minimum hydrogen concentrations are accumulated on the TGB with misorientation angles ranging between $0^\circ < \theta < 5^\circ$ and $75^\circ < \theta < 90^\circ$. The model therefore predicts that in terms of design TGBs with misorientation angles ranging between $0^\circ < \theta < 5^\circ$ and $75^\circ < \theta < 90^\circ$ are the preferred microstructures in polycrystalline nickel.
- This technique can be used to investigate the importance of GB engineering for designing and optimizing polycrystalline nickel materials to help decrease hydrogen segregation arising from TGB misorientation angles for specific boundary conditions.

- A coupled micro-macro scale model is presented to analyse hydrogen embrittlement of polycrystalline materials that couples the component level macroscopic region with the microstructural region. In the microstructural region, the heterogeneous microstructures, intragranular and intergranular, are geometrically represented. This is a true two-scale technique enabling investigation of the hydrogen embrittlement phenomena of heterogeneous polycrystalline materials using a single micro-macro critical domain, multiple micro-macro critical domains or multiphase heterogeneous micro-macro domains including voids, defects, triple junctions and traps. These models also provide a route for further coupled multiscale modelling by coupling the micro-meso-macro domains depending on the nature of the problem.
- The novel multiscale model represents a tool that can be used in the design stage for life prediction in polycrystalline structural materials. It can also be used to provide a qualitative understanding of the role of a large number of hydrogen embrittlement phenomena such as hydrogen diffusion, aggregation and accumulation mechanisms in the microstructure and at the continuum scale. The models have the potential to study premature brittle rupture or catastrophic intergranular hydrogen embrittlement problems that cannot easily be treated by either fully microstructural models or existing macrostructural models.
- Other conclusions drawn from the model include:
 - ✓ Stresses developed in the polycrystalline nickel microstructure are inhomogeneous, even though the applied stress is uniform. In the model this is due to the anisotropic mechanical response at the microstructural or grain level.
 - ✓ Stresses in the grain boundary affected zone can be significant depending on the relative orientation of neighbouring grains.
 - ✓ Different levels of hydrogen accumulation at grain boundaries and triple junctions are also predicted by the model. The orientation of neighbouring grains and grain boundary angles relative to the applied load gives rise to either tensile or compressive local stresses. It is these local tensile or compressive stresses that determine whether higher or lower local hydrogen accumulation occurs. This highlights the importance of such microstructural features in hydrogen embrittlement.

- ✓ Hydrogen accumulation in the microstructure is heterogeneous due to the inhomogeneous microstructural stress distribution coupled to varying hydrogen diffusivity at different regions in the microstructure.
- ✓ The model appears promising for the systematic investigation of hydrogen embrittlement scenarios in polycrystalline nickel accounting for important microstructural features such grains, grain boundaries and grain orientations.

Hydrogen induced intergranular, transgranular cracking and hydrogen induced localized intergranular plasticity and the effect of GBCs and TJC on HIC/IHE in polycrystalline superalloy 718 were investigated using in-situ hydrogen charged SSRT and SEM/EBSD/OIM methods. The conclusions of these investigations are as follows

- The ultimate tensile strength and tensile ductility are significantly reduced by in-situ hydrogen charging during tensile testing leading a reduction in lifetime of nickel based super alloy 718.
- The presence of internal hydrogen in nickel based 718 alloy leads to increases the reduction of the ultimate tensile strength and plastic flow which leads to a reduction in lifetime.
- Fractography analyses using SEM revealed that micro-voids/pores in the crystal lattice are the crack initiation site for hydrogen induced transgranular cracking and slip localization from micro-voids in intergranular regions leads to hydrogen induced intergranular cracking due to a reduction in intergranular localized plastic flow and ductility.
- Hydrogen induced cracking (HIC) was observed at CHAM and LHAM type boundaries, very little HIC was observed at HHAM and SGB type boundaries and no HIC was observed at LAM type boundaries.
- Hydrogen induced intergranular cracks nucleate predominantly at TJ0 and TJ1 type triple junctions, while HIC was never observed at TJ3 type triple junctions.
- HIC strongly depends on GBCs and TJCS.
- Hydrogen embrittlement in nickel based super alloy 718 can be controlled by reducing and/or eliminating micro-voids/pores and reducing the segregation of carbon atoms along intergranular regions.

Hot cracking and hydrogen induced cracking and the effect of microstructures including GBCs and TJs on hydrogen embrittlement in different grades of PP-Ni were investigated using ex-situ hydrogen charged SSRTs, weldability tests and SEM/EBSD/OIM/TDS analysis. The conclusions of these investigations are as follows

- Grade 1 is more susceptible to hydrogen embrittlement when compared to the newly developed grade 2 PP-Ni. The column boundaries are particularly prone to HIC due to the presence of voids on these boundaries and the large amount of hydrogen atom segregation along them.
- The resistivity to hydrogen embrittlement is increased in the newly developed grade 2 PP-Ni compared to grade 1 due to increased special GBCD, a reduction in pores/voids and the presence of clusters of ultrafine grains.
- Grade 3 is less susceptible to hydrogen induced hot/cold cracking and has enhanced resistance to hydrogen embrittlement when compared to both grade 1 and grade 2 PP-Ni materials.
- Hydrogen embrittlement in PP-Ni can be controlled by reducing and/or eliminating micro-voids/pores on columnar boundaries, by increasing the fraction of special grain boundaries such as $\Sigma 3$ and by reducing grain size.

FUTURE FOCUS

- The present CMCD technique can be extended to implement columnar boundaries and clustered grains to investigate stress assisted hydrogen diffusion.
- Other applications such as coupling atomistic model results such as stress and strain dependent diffusivities for GBCD will be the subject of future work.
- Increasing the fraction of LAM, HHAM and SGB GBs using ‘grain boundary engineering’ (GBE) in order to increase the resistivity to hydrogen embrittlement in solution and precipitate hardened nickel based super alloy 718 will be the subject of future work.
- GBE using heat treatment to enhance the resistivity to hydrogen embrittlement of Ariane 5 combustion chamber PP-Ni material will be the subject of future work. A few such conceptual investigations have already been carried out in this research project by the author using GBE control and design thus increasing the strain to hydrogen induced failure of Ariane 5 pulse plated nickel as shown in figures 9.1 to 9.4.

The GBE concept has been used in Ariane 5 combustion chamber PP-Ni by heat treating the materials at various different temperatures and times in order to

increase the CSL grain boundary fraction and then carrying out hydrogen embrittlement tests. As one such example the hydrogen induced strain to failure in Ariane 5 combustion chamber PP-Ni samples has been increased using GBE (increases in the hydrogen induced elongation to fracture and the ductility of PP-Ni were achieved).

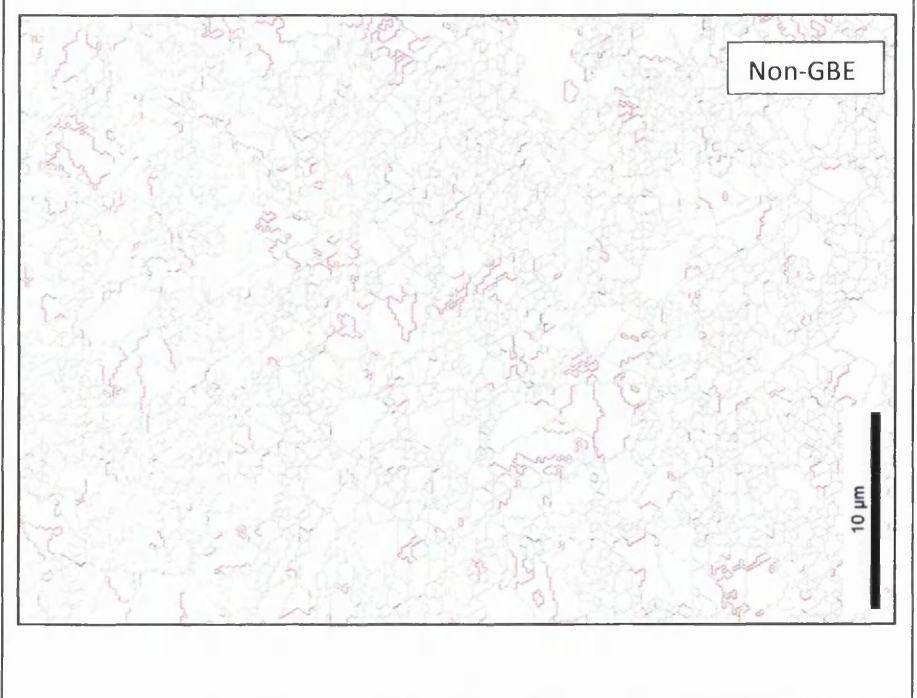
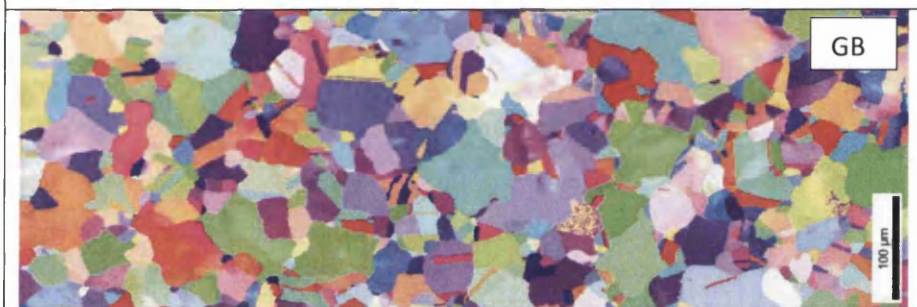
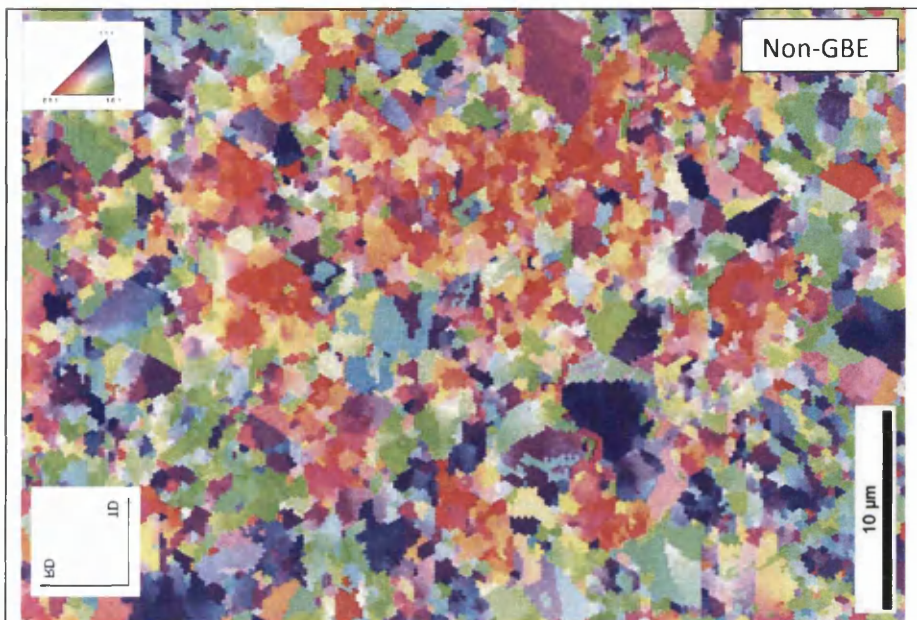
The author reports preliminary results in

- Figure 9.1 EBSD results showing an increase in CSL GB fraction between non-GBE PP-Ni and GBE-PP-Ni.
- Figure 9.2 showing the hydrogen charged SSRT results between GBE and non-GBE PP-Ni.
- Figure 9.3 showing the fracture surface of SSRT tested GBE-PP-Ni hydrogen charged and uncharged specimens. NB the SEM images of non-GBE PP-Ni SSRT tested fracture surface microstructures shown in chapter section 7.10 are more brittle especially along columnar boundaries.
- The SEM images of GBE PP-Ni SSRT tested fracture surface microstructures shown in figure 9.3 are ductile which indicates a reduction in susceptibility to hydrogen embrittlement in GBE-PP-Ni material.

Note that the author also noticed that these techniques not only increase the CSL fraction but also decrease the fraction of pores/void in PP-Ni and released the trapped hydrogen out of material in the PP-Ni as shown in figure 9.4 (TDS results). Future research will also be carried out in this direction.

Atom probe tomography investigation has been carried out to investigate the distribution of impurities in In718 and some results are shown in figure 9.5 Future direction: Grain boundary segregation factors and energy values will be calculated and these values will be used as input for full scale component models.

Figure 9.6 shows the future direction and some preliminary results of this research work via implementation of the newly developed multiscale model incorporating microstructural features of the Ariane 5 combustion chamber components.

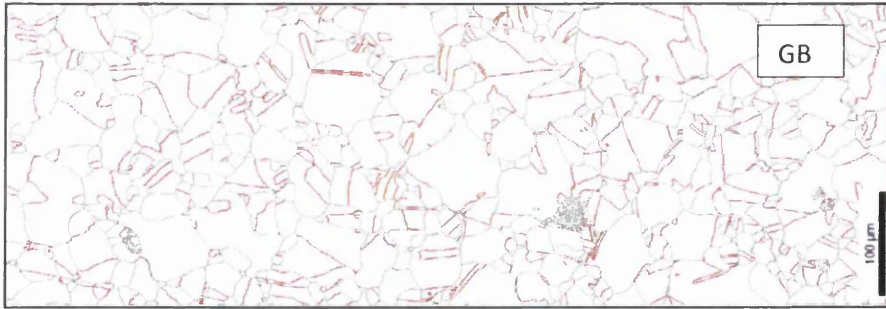
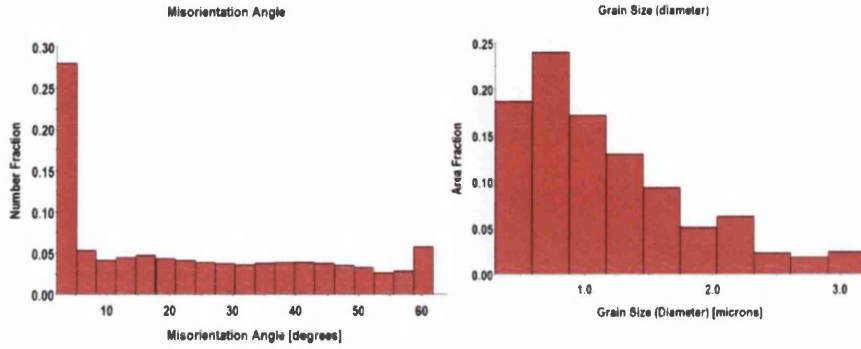


Boundaries: Grain

Non-GBE

Boundaries: CSL

Sigma	Tolerance	Fraction	Volume	MDF Value	Number	Length
3	8.66	0.069	0.0176	3.93	3911	451.603 microns
5	6.71	0.006	0.0123	0.51	354	40.8764 microns
9	5.00	0.014	0.0102	1.40	804	92.8379 microns
27a	2.89	0.003	0.0020	1.40	155	17.8979 microns
27b	2.89	0.003	0.0039	0.66	147	16.9741 microns
summary	-	0.095	0.0458	2.07		



Boundaries: Grain

GB

Boundaries: CSL

Sigma	Tolerance	Fraction	Volume	MDF Value	Number	Length
3	8.66	0.362	0.0176	20.61	22778	1.31509 cm
5	6.71	0.008	0.0123	0.65	502	289.83 microns
9	5.00	0.015	0.0102	1.52	972	561.184 microns
27a	2.89	0.002	0.0020	0.96	118	68.1273 microns
27b	2.89	0.002	0.0039	0.44	107	61.7765 microns
summary	-	0.389	0.0458	8.49		

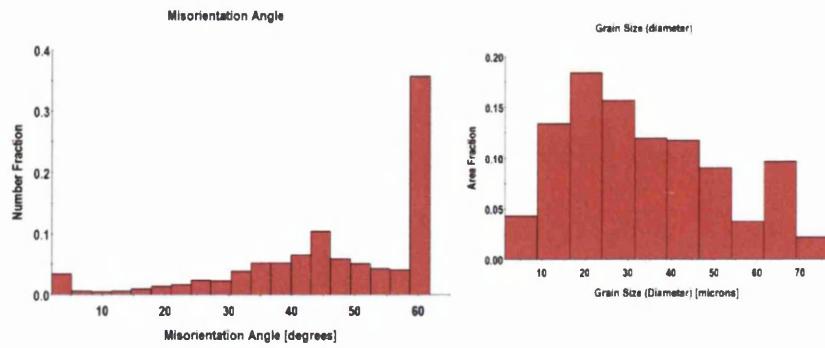


Figure 9.1 EBSD analysis results of GBE and non-GBE Ariane 5 PP-Ni materials. Note: $\Sigma 3$ grain boundaries fraction has been increased from 0.059% to 0.362% in the GBE case.

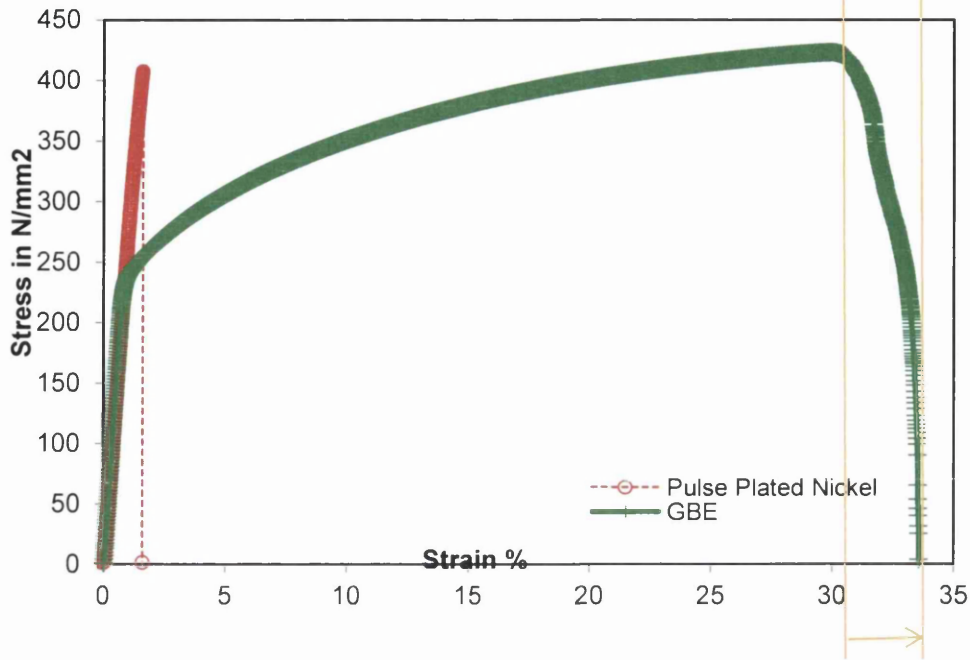
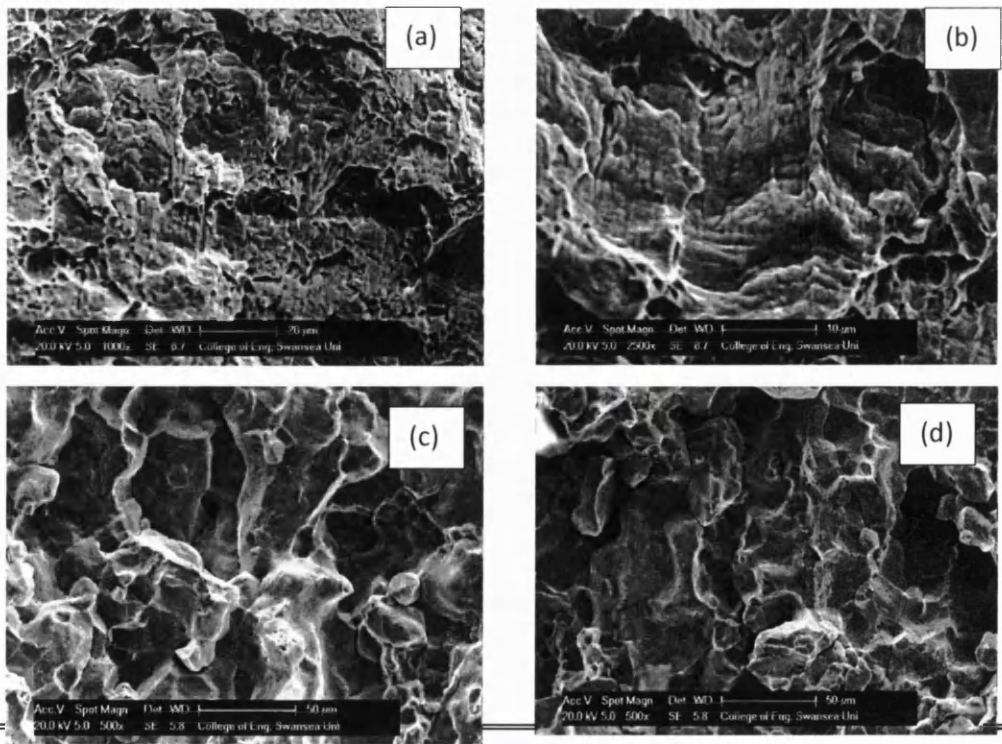


Figure 9.2 Results of SSRT on hydrogen charged GBE and non-GBE Ariane 5 PP-Ni sample materials. Hydrogen charged electrochemically for 72 hour at 30°C just before starting the test. SSRT were been performed at a strain rate of $8.3 \times 10^{-5} \text{ s}^{-1}$.



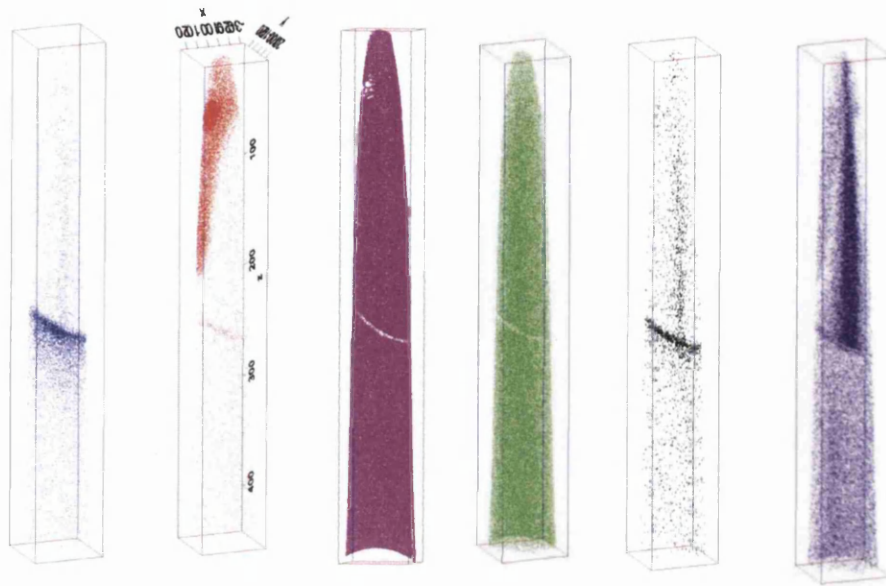


Figure 9.5 APT results showing boron, carbon, iron, nickel, phosphorus and sulphur segregation around a grain boundary in nickel based super alloy 718.

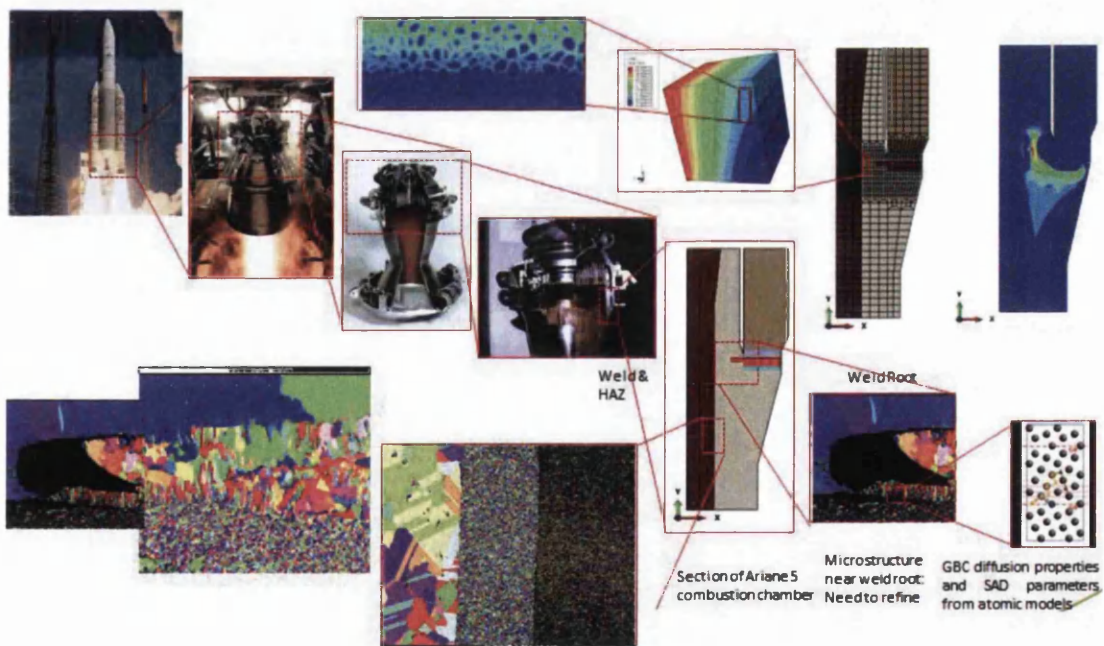


Figure 9.6 Full scale component model of Ariane 5 combustion chamber.

APPENDICES

10.1 Trap model

It has been reported previously that the GND density close to GBs is high when compared to the GND density in centre of the grains [123]. This high GND density region close to the GB is referred to as the grain boundary affected zone (GBAZ) throughout this section. Higher GND densities are due to the geometrical misalignment of two adjacent grain orientations (i.e. GB misorientations). The concentration flux is now determined by the normal grain boundary hydrogen diffusion and a concentration flux due to hydrogen trapping,

$$\frac{\partial C}{\partial t} = \frac{\partial C_{\text{diff}}}{\partial t} - \frac{\partial C_{\text{trap}}^i}{\partial t} \quad (\text{A.1.1})$$

$$\frac{\partial C_{\text{diff}}}{\partial t} = \nabla \cdot (D_{gb} \nabla C) \quad (\text{A.1.2})$$

$$\frac{\partial C_{\text{trap}}^i}{\partial t} = N_t^i \frac{\partial n_i}{\partial t} \quad (\text{A.1.3})$$

$$\frac{\partial n_i}{\partial t} = k_i C (1 - n_i) - p_i n_i \quad (\text{A.1.4})$$

$$N_t^{i=GND} = \frac{\pi \cdot r^2}{2d} \cdot N_L \cdot \sum_{j=1}^{m_{gb}} \frac{1}{S_j} \quad (\text{A.1.5})$$

$$= \frac{\pi.r^2}{b.d} \cdot N_L \cdot \sum_{j=1}^{m_{gb}} \sin\left(\frac{\theta_j}{2}\right) \cdot f_j \quad (\text{A.1.6})$$

Where C_{diff} is the concentration of diffusible hydrogen atoms per unit volume, C_{trap}^i is the concentration of trapped hydrogen atom per unit volume and i represents the number of traps (and trap sites may be of different types in the model such as reversible trap sites, irreversible trap sites, defect trap sites such as void trap sites, GND trap sites etc.), N_t^i is the volume density of traps per unit volume, n_i is the fractional trap occupancy levels for N_t^i traps, k_i is hydrogen entry/capture rate per trap, t is time, p_i is the hydrogen exit/release rate per - for irreversible traps the release rate is zero. N_t^{GND} is the GND density of trap sites, ρ_{GND}^a is the average GND density (m^{-2}) where $\rho_{GND}^a = \frac{1}{2d} \sum_{j=1}^{m_{gb}} \frac{1}{s_j} = \frac{1}{bd} \sin\left(\frac{\theta_j}{2}\right) \cdot f_j$ [3, 125]. The quantity ρ_{GND}^a in any given grain boundary can be calculated through EBSD analysis using the GB misorientation angle and a single dislocation network is necessary to accommodate the GB misorientation [3, 125, 128-131, 205]. Here, r is the effective distance between dislocations, N_L is the density of interstitial sites (m^{-3}) or the number of solvent lattice atoms per unit volume ($N_L = N_A/V_M$, where N_A is Avogadro's number and V_M is the molar volume of the host metal lattice), m_{gb} is the number of types of GBs studied, b is Burgers vector, d is the average grain size, s_j is the distance between two dislocations in a GB misorientation of θ_j where from dislocation theory $s = \frac{b}{2} \sin\left(\frac{\theta}{2}\right)$ [16], f_j is the fraction of GB with misorientation angle θ_j and the transition probabilities are expressed by an Arrhenius expression $\frac{k_i}{p_i} = \frac{1}{N_L} \exp\left(\frac{-E_B}{RT}\right)$ suitable for thermally activated processes.

FE formulation of trap model:

The finite element method discretises the unknown concentration in space and time as follows,

$$C(\mathbf{x}, t) \approx \sum_{k=1}^{r_{nodes}} C_k(t) N_k(\mathbf{x}) \quad (\text{A.1.7})$$

Where $C_k(t)$ is the concentration at k^{th} node and $N_k(\mathbf{x}), k = 1, 2, \dots, r_{nodes}$ are a set of nodal basis functions defined on the finite element mesh. It is assumed that the trap occupancy levels n_i are constant within each element. This assumption leads to a discretisation as follows.

$$n_i(\mathbf{x}, t) \approx \sum_{l=1}^{r_{elements}} n_{l,i}(t) M_l(\mathbf{x}) \quad (\text{A.1.8})$$

Where $n_{l,i}$ is the trap occupancy level for i -type traps in the l^{th} element, $M_l(x, t)$ is a function that is unity everywhere within the l^{th} element and zero outside of it. This approach means the trap occupancy levels are discontinuous, but since their spatial derivatives do not appear in the equations above this is unlikely to cause numerical problems and any problems with the validity of sharply discontinuous results can be resolved by refinement of the mesh [110,152]. Because (a) the spatial derivatives of the trap occupancy levels do not appear in the equations above and (b) the trap occupancy levels can be regarded as derived quantities dependent on the solution variable (i.e. concentration) then the FE formulation does not need to solve a matrix of equations to update explicitly the values of the trap occupancy levels during each step. A detailed explanation can be found elsewhere [263].

Using the standard Galerkin approach and applying the discretisation described above, the full finite element formulation can be shown to be of the form

$$\sum_{w=1}^{r_{node}} \int_{\Omega} N_k N_w \frac{\partial C}{\partial t} + \nabla N_k \cdot (D_{gb} C \cdot \nabla N_w) d\Omega + \sum_{w=1}^{r_{node}} \int_{\partial\Omega} N_k (D_{gb} C \cdot \nabla N_w) \cdot \mathbf{n} dS + \int_{\Omega} N_k \left(N_t^i \sum_{l=1}^{r_{element}} \frac{\partial n_{l,1}}{\partial t} M_l(x) \right) d\Omega = 0, k = 1, 2, 3 \dots r_{node} \quad (\text{A.1.9})$$

Where N_k and N_w are basis functions and N_t^i is the trap density. Ω is the domain of the model, $\partial\Omega$ represents boundaries and \mathbf{n} is the outward unit normal to a given boundary. In practice the boundary integral would be replaced by appropriate boundary conditions, using a Lagrange multiplier if necessary to account for fixed concentration conditions.

UEL Trap Subroutine Implementation:

The trap fluxes in equation (A.1.4) must depend on the local trap occupancy levels and the local hydrogen concentration. The hydrogen concentration is the main solution variable in the model whereas the trap occupancy levels are a user-defined

variable for which values must be calculated as the model runs. The user defined element (UEL) calculates and stores the trap occupancy levels at each time increment overlaying the existing ABAQUS hydrogen diffusion model using the same nodes so that the solution variable and user-defined variables are coupled using the same nodal points as shown in the sketch below. Here hydrogen diffusion elements (red) and trap elements (black) use the same nodes (circles) and connectivity.



From equation (A.1.9) it can be seen that the ABAQUS user element subroutine must generate values for

$$\int_{E_v} N_k \left(N_t^i \frac{\partial n_i}{\partial t} \right) d\Omega \quad (\text{A.1.10})$$

where E_v is the trapping element, for all basis functions (N_k) that correspond to the nodes making up E_v . These expressions have been evaluated using single-point numerical quadrature, since the basis function chosen for the trap occupancy level means that a higher order scheme would not improve the accuracy. Single point quadrature is also used to evaluate the contribution of the trapping term to the stiffness matrix, as required by ABAQUS. The time discretisation has been implemented using the Crank-Nicolson method, rather than the more computationally expensive Backwards Euler method, since it is unlikely that stability problems will occur in this model. Constraints have been added to ensure that the trap occupancy level remains between 0 and 1. Monte Carlo simulations were used to assign the random distribution of crystal orientations and GB misorientations to generate reliable microstructural (i.e. trap) properties for coupling with the FE code for hydrogen diffusion analysis.

GB segregation of hydrogen:

Hydrogen induced intergranular cracking is due to the attainment of critical hydrogen concentration at GBs and segregation of hydrogen at various GBs depends on GB misorientation and GB type. The hydrogen segregated at GB determines the

initiation of intergranular cracks and the crack propagation path. So it is important to understand the segregation at GBs and the relationship between hydrogen segregation at GBs and GB type. The hydrogen segregation at GBs is measured using the segregation co-efficient as shown below. The GB hydrogen segregation coefficient (S_{gb}) can be calculated based on the equation,

$$S_{gb} = \frac{C_{gb}}{C_L} = \exp\left(\frac{-E_B}{RT}\right) \quad (\text{A.1.11})$$

where E_B is the binding energy of a solute to an average GB sites.

The lattice and GB hydrogen concentration can be calculated based on the diffusible hydrogen concentration, $C_{H,diff}$ as shown in below

$$C_{H,diff} = C_L + C_{gb,rev} = n_L N_L + \sum_i^q n_{i,r} N_{gb,r}^i \quad (\text{A.1.12})$$

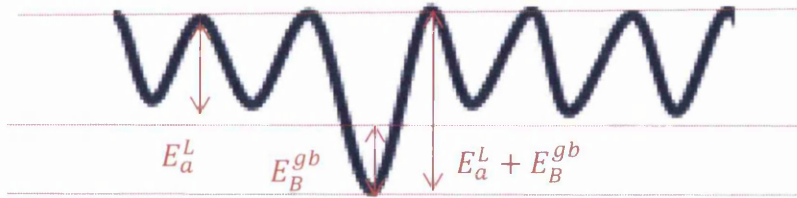
where $C_L = n_L N_L$ is the hydrogen concentration in lattice sites, $C_{gb,rev}$ is the hydrogen concentration of a reversible trap, $n_{i,r}$ is reversible GB trap occupancy level, $N_{gb,r}^i$ is the reversible trap density (m^{-3}) for a number, q , of reversible traps.

D_{eff} is the effective diffusivity of hydrogen given by,

$$D_{eff} = \left[\gamma \cdot a_0^2 v \exp\left(\frac{\beta \Delta H}{RT_{mp}}\right) \right] \cdot \exp\left(\frac{-E_a}{RT}\right) \quad (\text{A.1.13})$$

where $\beta = \frac{d(\mu/\mu_0)}{d(T/T_{mp})}$ and $\gamma \cdot a_0^2 v \exp\left(\frac{\beta \Delta H}{RT_{mp}}\right) = D_0$ is a pre-factor. E_a is the

activation energy for diffusion (kJ/mol). D_0 and E_a can be calculated by using a log plot of calculated D_{eff} over a range of temperatures, γ is the geometric factor, a_0 is the jump distance, v is the frequency with which the solute atom vibrates in the diffusion direction, ΔH is the activation enthalpy for diffusion, T_{mp} is the melting point of the pure metal, μ is the elastic modulus of the pure metal, μ_0 is the elastic modulus at zero degrees absolute, more details can be found in [2,115].



The sketch above shows the simple energy model for grain boundary traps [115], where E_a^L is the activation energy for lattice diffusion and E_B^{gb} is the binding energy for a grain boundary trap. At equilibrium condition, the effective diffusivity can be written as shown below

$$D_{eff} = \frac{D_L}{1 + \frac{C_{gb}^e}{C_L} \left(1 - \frac{C_{gb}^e}{N_{gb}^e} \right)} \quad (A.1.14)$$

Note in the above equation C_{gb}^e is the effective concentration of all GB type sites and is calculated via equation (A.1.15). N_{gb}^e is the effective GB type trap density and it can be calculated based on GB segregations as shown in equation (A.1.11) (i.e. in real polycrystalline microstructure materials there may be different types of possible GB sites based on GB type and GB misorientation). The difference in trap occupancy levels in different types of GB is based on atomic arrangements and the difference in the binding energy for different GB types. For example in FCC nickel, the trap binding energy in the $\Sigma 3$ special type is 0.02eV and in the $\Sigma 5$ general type 0.2eV, an order of magnitude difference in trap binding energies between two types of GB as reported by Mrovec *et al* [138, 145, 260, 266]. Changes in GB trap binding energy will change the hydrogen concentration in GB traps and hydrogen concentration will also change due to the variation in GB trap densities according to equations (A.1.12). The changes in GB trap density vary according to the GB misorientation angle as shown in equation (8).

$$C_{gb}^e = \sum_i^n n_i N_{gb}^n \quad (A.1.15)$$

Where n_i is the trap occupancy level for a number (superscript n) of GB type trap sites and N_{gb}^n is the GB trap density for the different 'n' types of GBs.

The effective diffusivity can be written as shown below in the form of a grain boundary segregation equation,

$$D_{eff} = \frac{D_L}{1 + S_{gb} \left(1 - \left(\frac{S_{gb} C_L}{N_t^{gb}} \right) \right)} \quad (A.1.16)$$

The effective grain boundary trap density for polycrystalline materials can be written as shown below in terms of GB segregation

$$N_{gb}^e = \frac{S_{gb} C_L}{1 + \left(\frac{1}{S_{gb}} \right) \left(1 - \frac{D_L}{D_{eff}} \right)} \quad (A.1.17)$$

Where D_{eff} , based on the segregation factor, can be calculated using the modified Maxwell equation shown below [139, 140],

$$D_{eff} = \frac{s_{gb}D_{gb}((3-2f_{gb})D_L+2s_{gb}D_{gb})}{(1-D_{gb}+s_{gb}f_{gb})(f_{gb}D_L+(3-f_{gb})s_{gb}D_{gb})} \quad (A.1.18)$$

More detailed explanations of trap models including the simplified approach adopted by most workers and the UEL subroutine development and validation can be found elsewhere [23, 92, 104-112].

Effects of hydrogen trapping, segregation factor, GND trapping density, lattice hydrogen concentration on effective diffusivity of hydrogen in polycrystalline materials

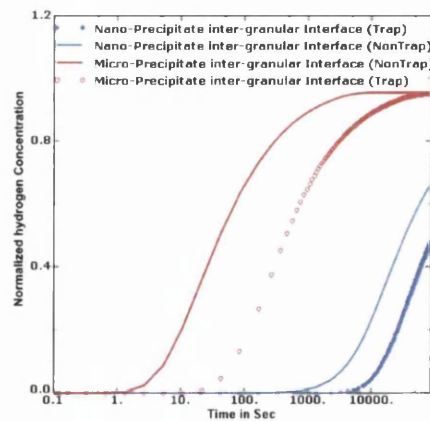
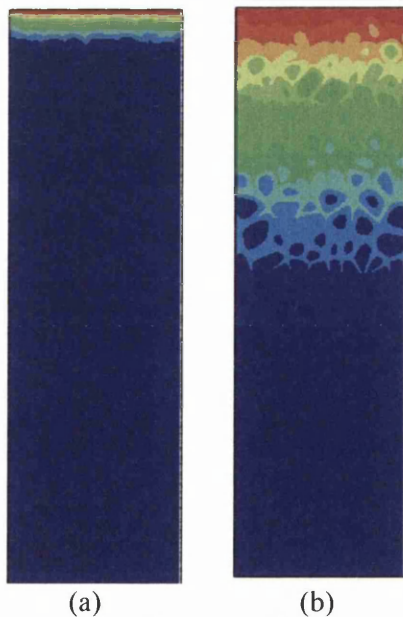
The multistate hydrogen diffusion analysis has been carried using trap model to investigate the effect of hydrogen trapping in microstructure. The results of this analysis are shown in figure A.1.1. Finally, by using Monte Carlo model the relationships between hydrogen segregation factor, hydrogen concentration in lattice sites and density of GND trapping sites in the polycrystalline material on the effective diffusivity of hydrogen in polycrystalline material were investigated. MC statistical models aim to develop a physically realistic insight into the spatial aspects of crystal lattice orientations and GB misorientations during microstructure evolution, quantify the effects of anisotropic GB misorientation properties, and quantify the effects of GND densities for hydrogen trapping sites. For all the GB misorientation simulations a distribution of 10^4 sites was employed. The MC simulations were also performed to calculate effective diffusivities of hydrogen by varying the density of GND trapping sites and by fixing the hydrogen concentration in lattice sites in order to investigate the segregation factors of atomic hydrogen in different GB misorientations. The averages of 10^4 MC samples of atomic lattice concentration of hydrogen, density of GND trapping sites and segregation factors of atomic hydrogen in GB misorientations were used to calculate effective diffusivities of hydrogen. The results of the MC simulation and the statistical sample fluctuation data used can be found in figure A.1.2. Figures A.1.2 (a), (b) and (c) show the distribution of the hydrogen segregation factor, the atomic concentration of hydrogen in the lattice and the density of GND trapping sites respectively for various GB misorientations. Figure A.1.2 (d) shows the distribution of calculated effective diffusivities of hydrogen in the polycrystalline material. It also shows that more than

half of the calculated effective diffusivities are between 2×10^{-16} and $8 \times 10^{-16} \text{ m}^2 \text{ s}^{-1}$, that is, the random sampling in (i) segregation factor between 0 to 100, (ii) lattice hydrogen concentration between 0 to 1 ppm and (iii) GND density trapping sites between 10^{26} to $10^{27} \text{ (m}^{-3}\text{)}$, reduces the effective diffusivity of hydrogen in polycrystalline material by two orders of magnitude compared to the lattice diffusivity of hydrogen. One third of the calculated effective diffusivities are between 8×10^{-16} and $12 \times 10^{-16} \text{ m}^2 \text{ s}^{-1}$. Figures A.1.2 (e) and (f) show the MC simulation results of the effective diffusivity of hydrogen distribution in polycrystalline material with respect to the distribution of the densities of GND trapping sites and lattice hydrogen concentration respectively. Figure A.1.2 (g) shows the distribution of hydrogen segregation factor for respective densities of GND trapping sites. These show that even small variations in any one of these parameters may alter the effective diffusivity of hydrogen significantly. Figure A.1.2 (h) shows the distribution of effective hydrogen diffusivities against respective hydrogen segregation factors. In figure A.1.2 (h), in region I, the hydrogen segregation factor varies from zero to 10 and the effective hydrogen diffusivity varies significantly. Region II is a transition region where the effective diffusivity is moving towards steady state. Steady state is attained in region III. The model suggests that a hydrogen segregation factor of about 10 is a critical value, below this value the effective hydrogen diffusivity of polycrystalline material is affected significantly more when compared to segregation factor values greater than 40. Calculated trap densities based on the statistical distribution of GB misorientations are shown in figure A.1.2 (i). Figures A.1.2 (j) and (k) show the grain boundary trapping site binding energies and respective segregation factor and the distribution of the binding energies. Finally, figure A.1.3 shows a novel one way coupling of MC simulation with the FE multi-scale multi-phase continuum trap model where the hydrogen segregation is based on GB misorientation and this novel coupled model has been used to calculate the local GB/Grain scale segregations factors. In this latter model, MC routines were integrated into the commercial finite element software ABAQUS using PYTHON scripting. The GND densities were generated by MC simulation as inputs for the FE model based on Euler angles. 10^4 Euler angles were simulated randomly using the MC model for each grain. The algorithm converts the 20000 Euler angles between two neighboring grains to develop 10000 GB misorientations in the form of a Gaussian distribution. The average calculated GB

misorientations are used in the GBAZ regions in the FE multi-phase continuum trap model to obtain both low angle grain boundaries (LAGBs) and high angle grain boundaries (HAGBs). It should be stressed that in case of HAGBs the assumption of one GND was still used although the model has the potential to be further developed to deal with multiple GNDs. The coupled MC-FE multi-scale multi-phase continuum trap model is a novel technique to potentially provide physically-realistic crystal lattice orientation and GB misorientation data for simulations of local grain/GB nano/micro scale hydrogen distributions in clean energy power source fuel carrier/storage materials and to study IHE in polycrystalline materials.

This section clearly shows the effects of atomic and microstructural parameters affecting the effective diffusion of hydrogen in polycrystalline material. This reinforces the idea that these microstructural parameters should be taken into account when calculating effective diffusivities. Computational FE modeler should aware that these microstructural parameters plays important role in the effective diffusivities and microstructural parameters based effective diffusivities should be used when modelling macro scale components for studying hydrogen induced intergranular and transgranular embrittlement problems in polycrystalline materials.

Microstructures without trap model. (a) NPDII and (b) MPDII



Microstructures with trap model.
 (d) NPDII
 (e) MPDII

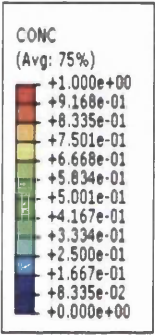
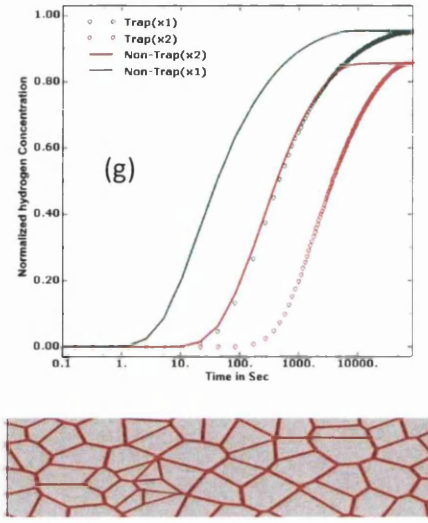
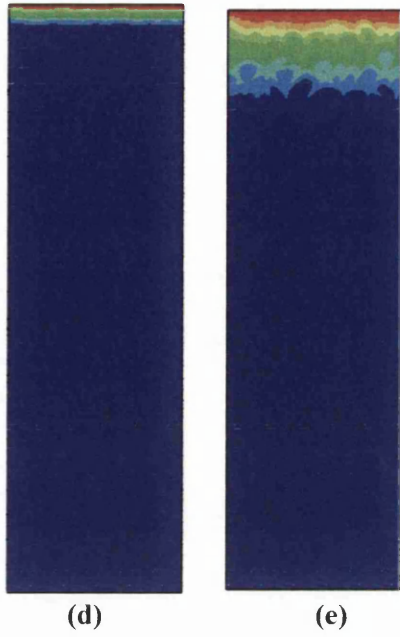
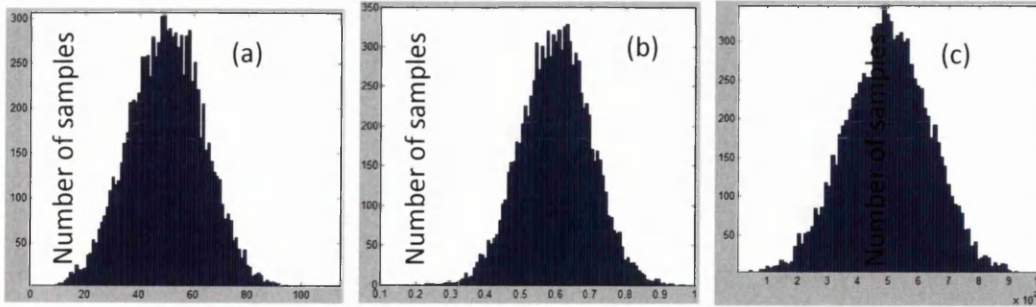


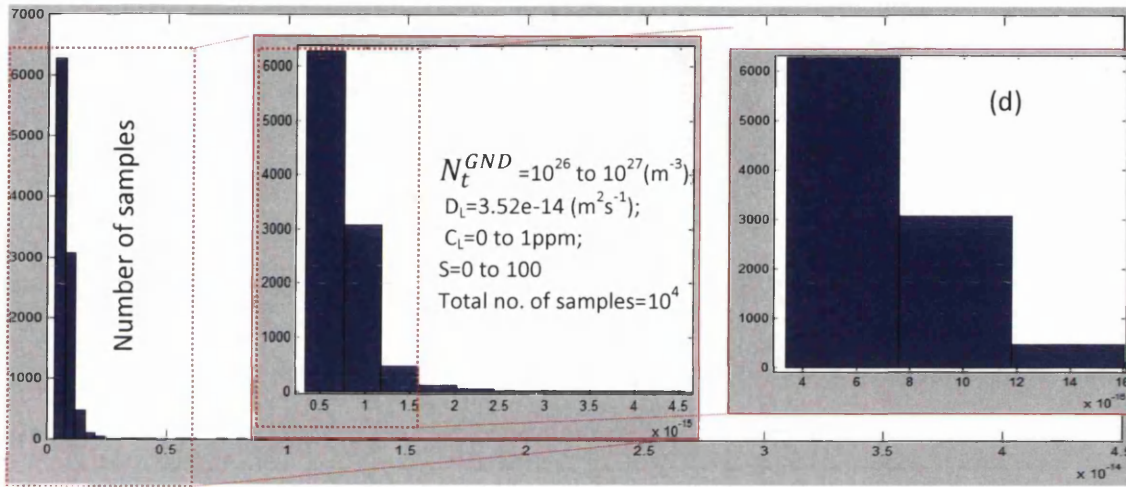
Figure A.1.1 Hydrogen distribution and segregation with and without trapping for NPDII and MPDII interfaces in multi-phase polycrystalline materials. (NB hydrogen diffusivity in MPDII and NPDII is $4 \times 10^{-12} \text{ m}^2 \text{ s}^{-1}$; Diffusivity in GI for both models is $9 \times 10^{-14} \text{ m}^2 \text{ s}^{-1}$; elapsed time is 10^4 s). Colour contours are the same for all results. (c) Shows the normalized hydrogen concentration of multi-phase polycrystalline microstructure for NPDII and MPDII interfaces with and without the trap model. (f) The red color shows the precipitate double layer intergranular interface where the trap elements are implemented; (g) shows the normalized hydrogen concentration for the MPDII interface model with and without the trap model at two different positions.



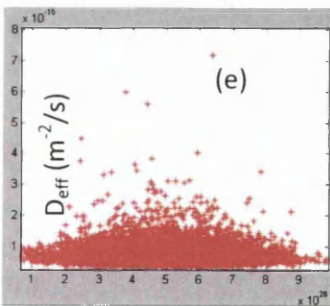
Segregation factor (S)

C_L (ppm)

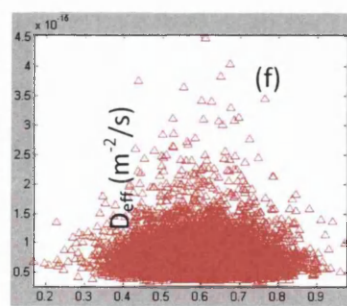
N_t^{GND} (m^{-3})



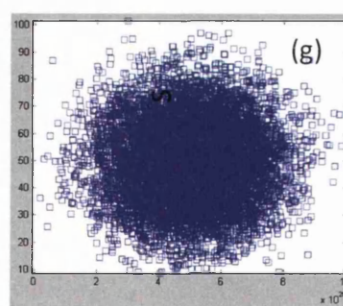
D_{eff} ($m^2 s^{-1}$)



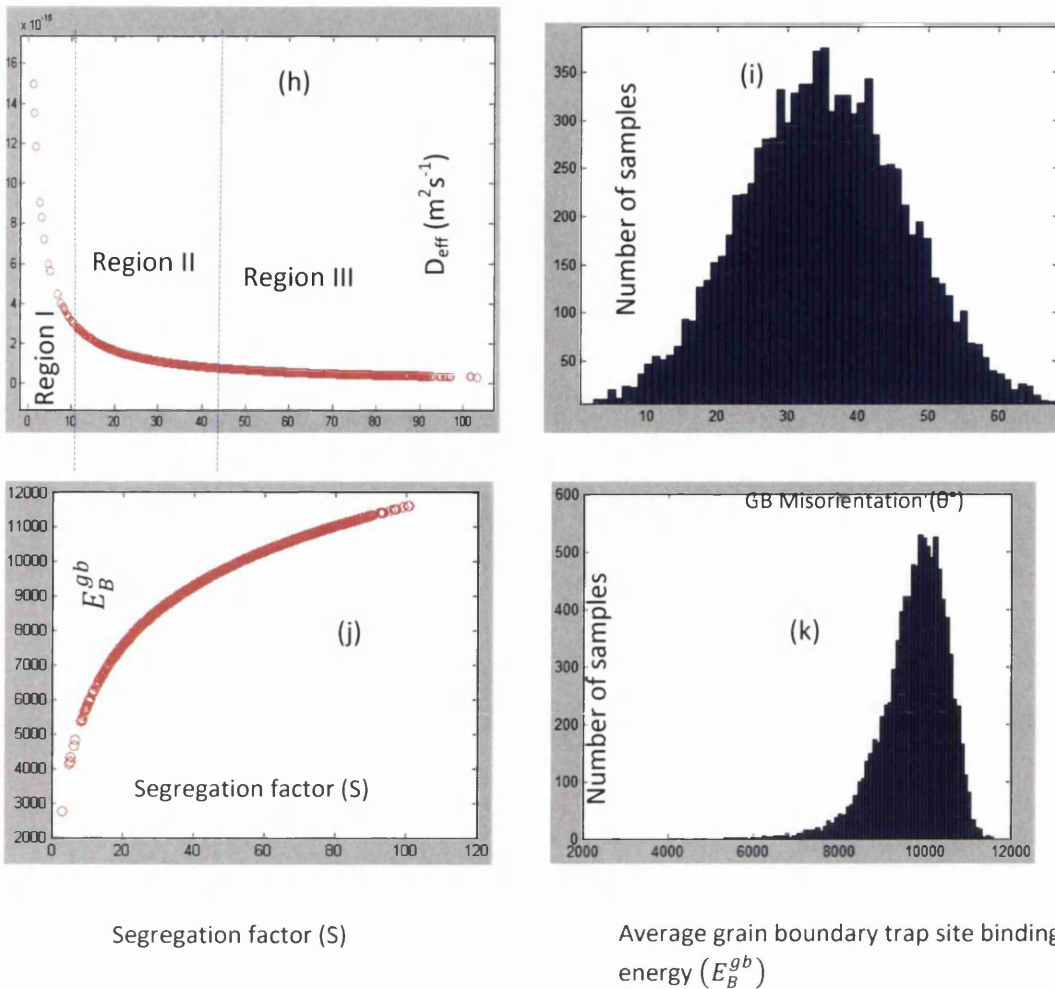
N_t^{GND} (m^{-3})



C_L (ppm)



N_t^{GND} (m^{-3})



Segregation factor (S)

Average grain boundary trap site binding energy (E_B^{gb})

Figure A.1.2 Monte Carlo simulation results of effective diffusivity (D_{eff}) for 10000 sample distributions assuming a lattice concentration (C_L) from 0 to 1 ppm, density of trapping sites based on grain boundary misorientation (N_t^{GND}) from 10^{26} to 10^{27} (m^{-3}), segregation factors (S) from 0 to 100 and a lattice diffusivity of $3.52 \times 10^{-14} \text{m}^2\text{s}^{-1}$. (a) distribution of segregation factors, (b) distribution of lattice concentration of hydrogen, (c) density of trapping sites based on grain boundary misorientation, (d) effective diffusion of hydrogen in polycrystalline material, its closed view and data used for statistical samples floatation's , (e) effective diffusivity of hydrogen as a function of density of trapping sites, (f) effective diffusivity of hydrogen as a function of lattice hydrogen concentration, (g) segregation factor distribution as a function of density of trapping sites, (h) effective diffusivity as a function of segregation factors, (i) statistical distribution of GB misorientations, (j) segregation factors versus average grain boundary trapping sites binding energy (increasing segregation factor with increasing E_B^{gb}) and (k) Shows the distribution of average grain boundary trapping sites binding energy.

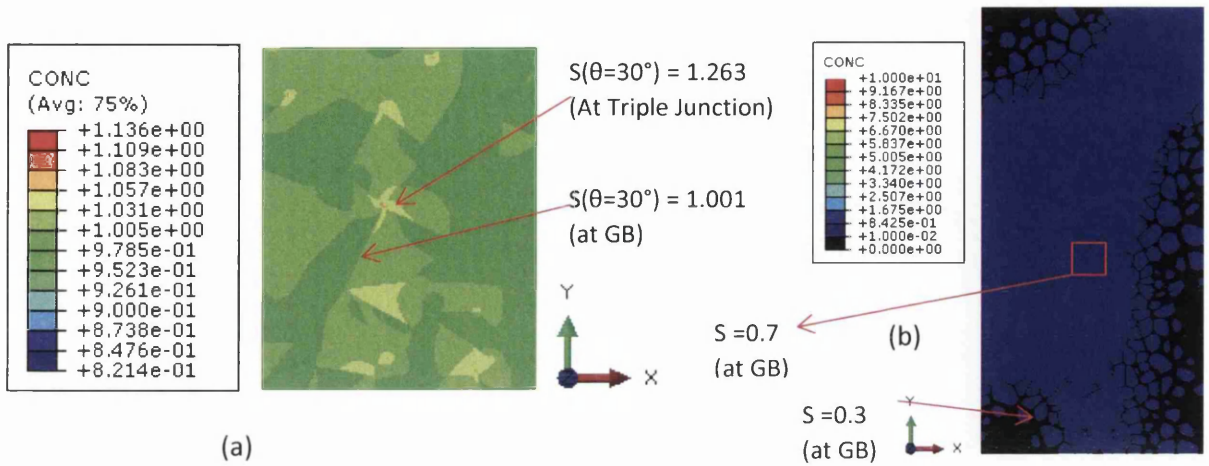
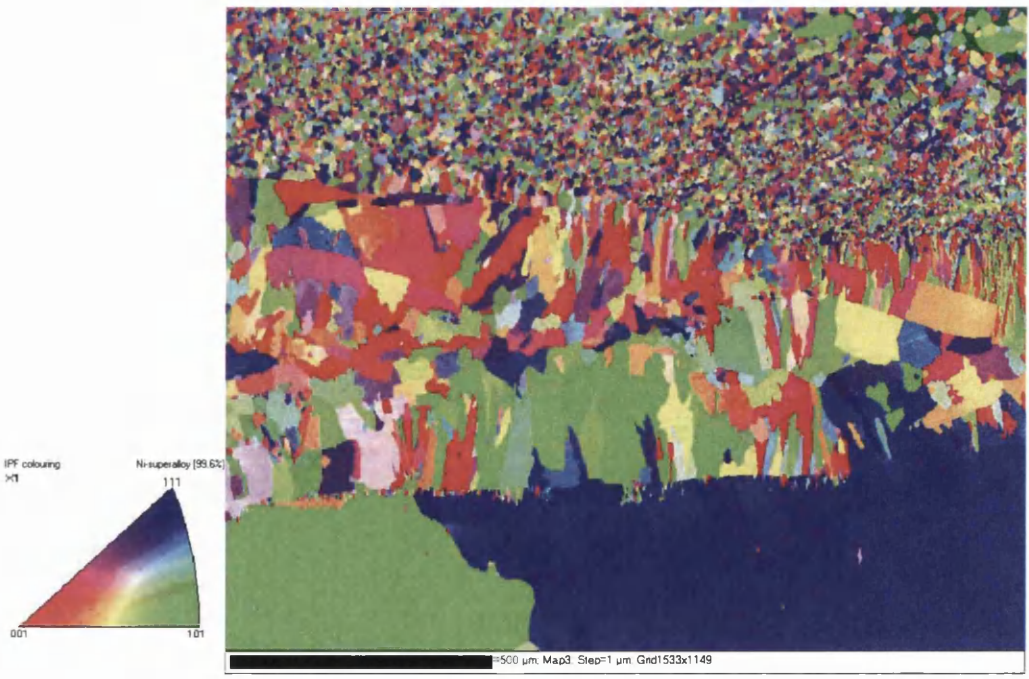


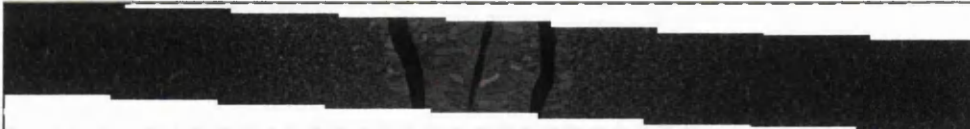
Figure A.1.3 shows the hydrogen segregations results of the Monte Carlo simulation coupled with FE multi-scale multiphase continuum trap model based on (a) GB misorientations and (b) without GB misorientation and its segregations factors (S).

10.2 Experimental EBSD analysis results of Ariane 5 combustion chamber: Supplementary images.



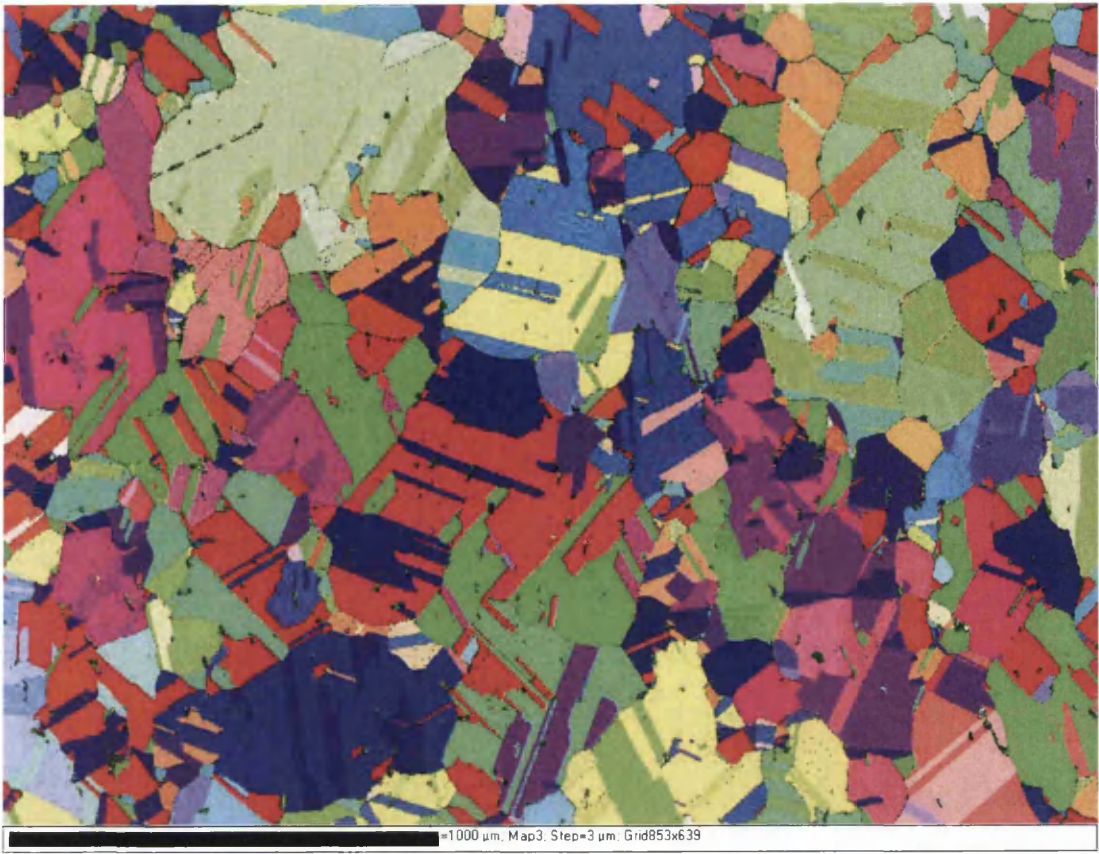


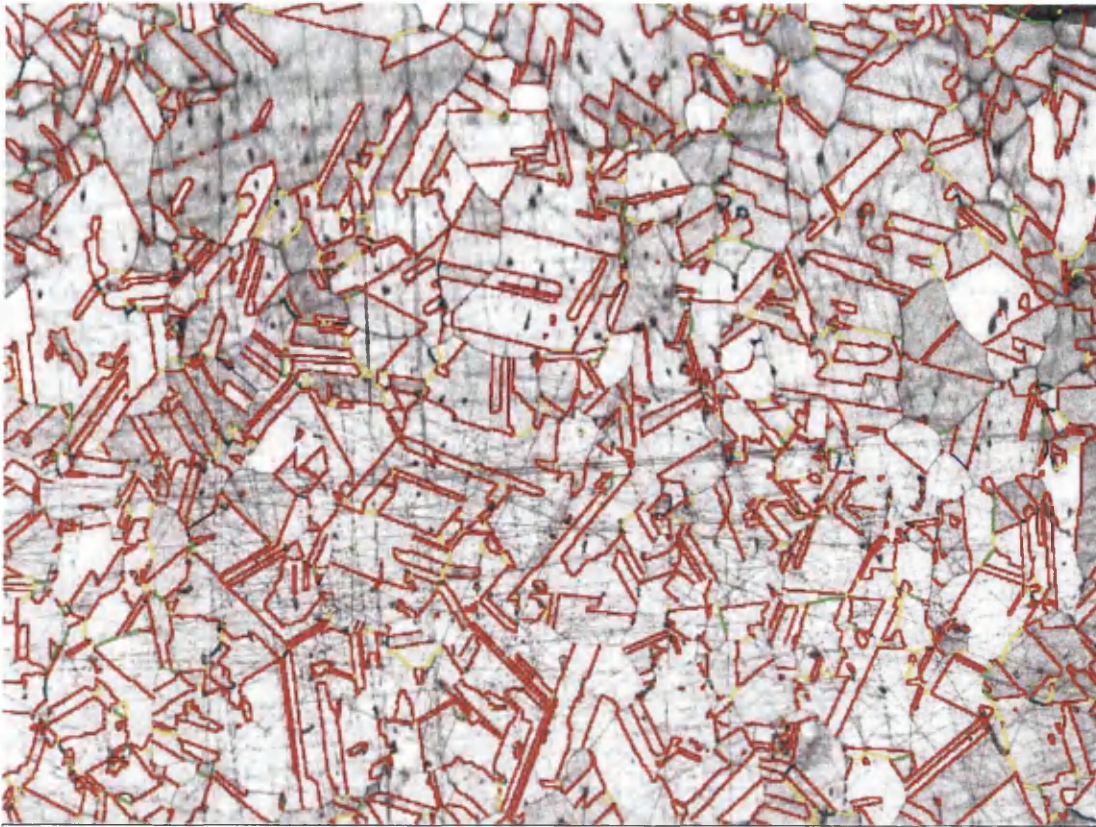
=500 µm; Map1; Step=1 µm; Grid1533x1149



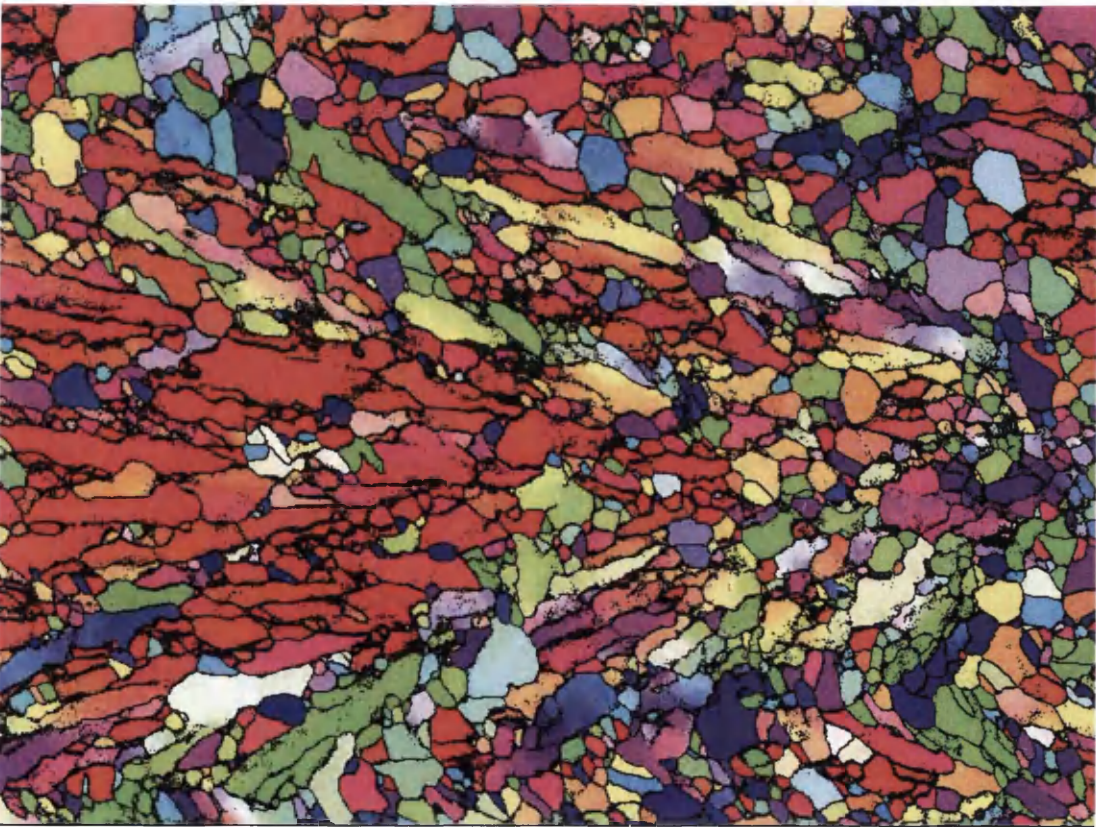
Destination Project :
 F:\Joth\Ni 718 alloy
 weld\BackUp_before_Stitch_L
 weld\weldment_Strain_1to5%E_direch
 Full_Stitched_L_Weld_HAZ_Str
 ain_E.dited.cpi
 # Source Projects : 9
 Resulting Grid Size :
 9525x1298
 Grid Step Size in X : 0.2µm
 Grid Step Size in Y : 0.2µm
 Total area :
 511542.06µm²

Destination Project :
 F:\Joth\Ni 718 alloy
 weld\BackUp_before_Stitch_L
 weld\weldment_Strain_1to5%E_direch
 Full_Stitched_L_Weld_HAZ_Str
 ain_E.dited.cpi
 # Source Projects : 9
 Resulting Grid Size :
 9525x1298
 Grid Step Size in X : 0.2µm
 Grid Step Size in Y : 0.2µm
 Total area :
 511542.06µm²

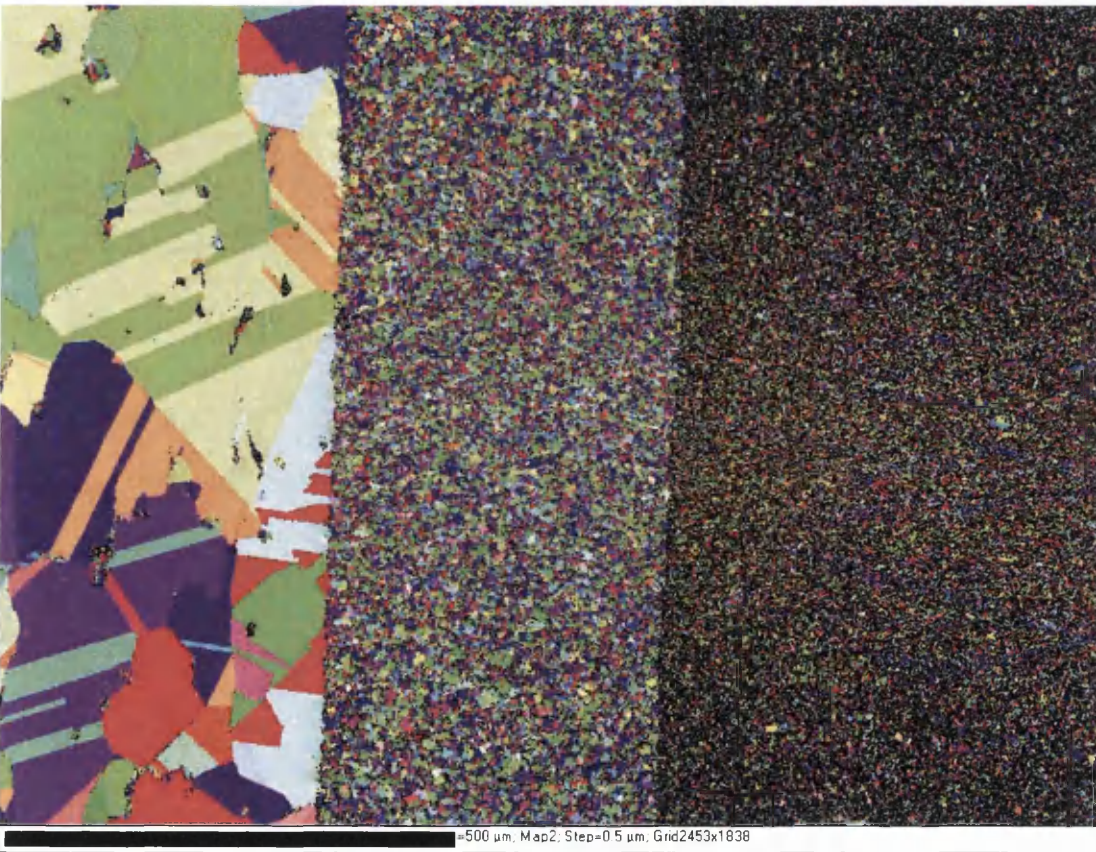
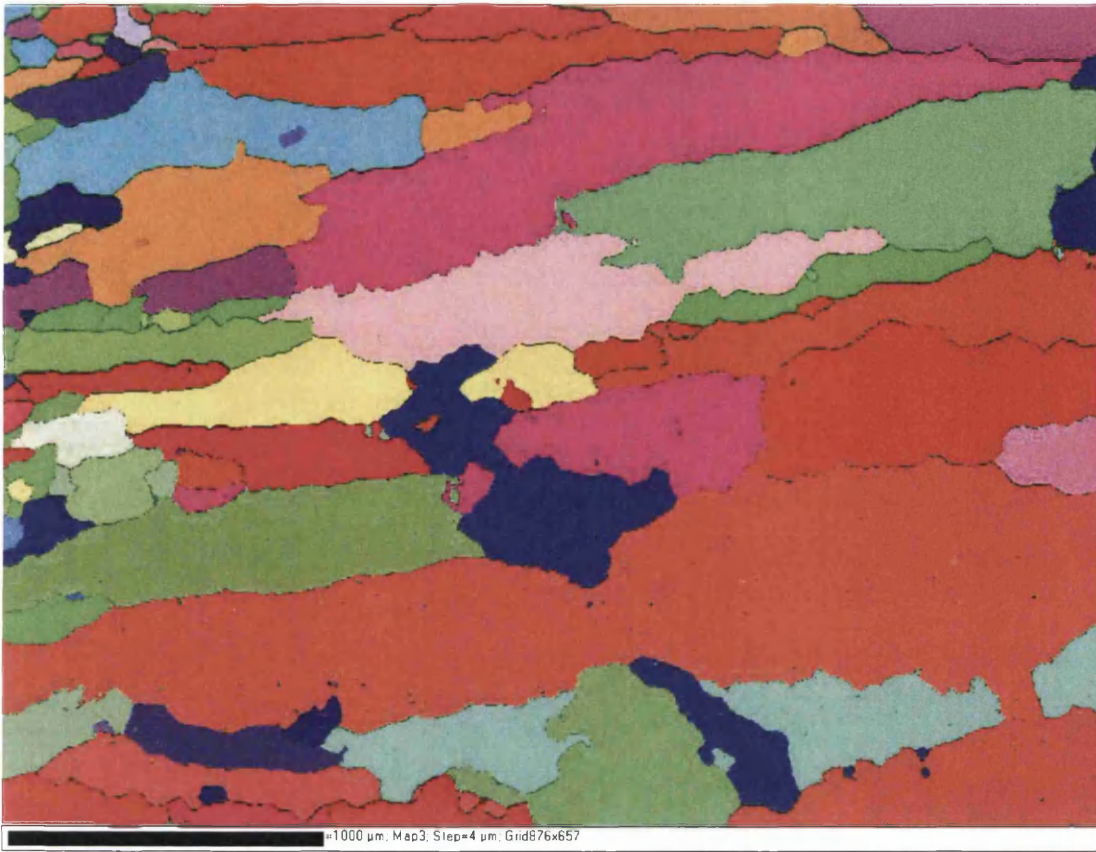


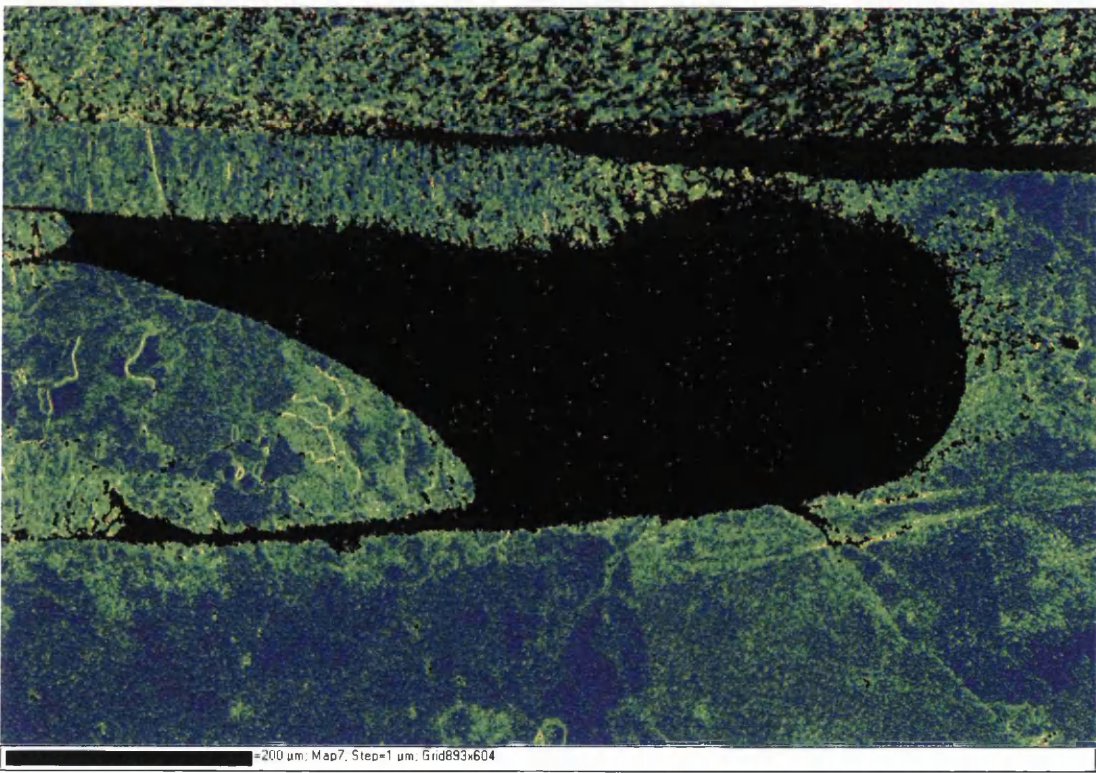
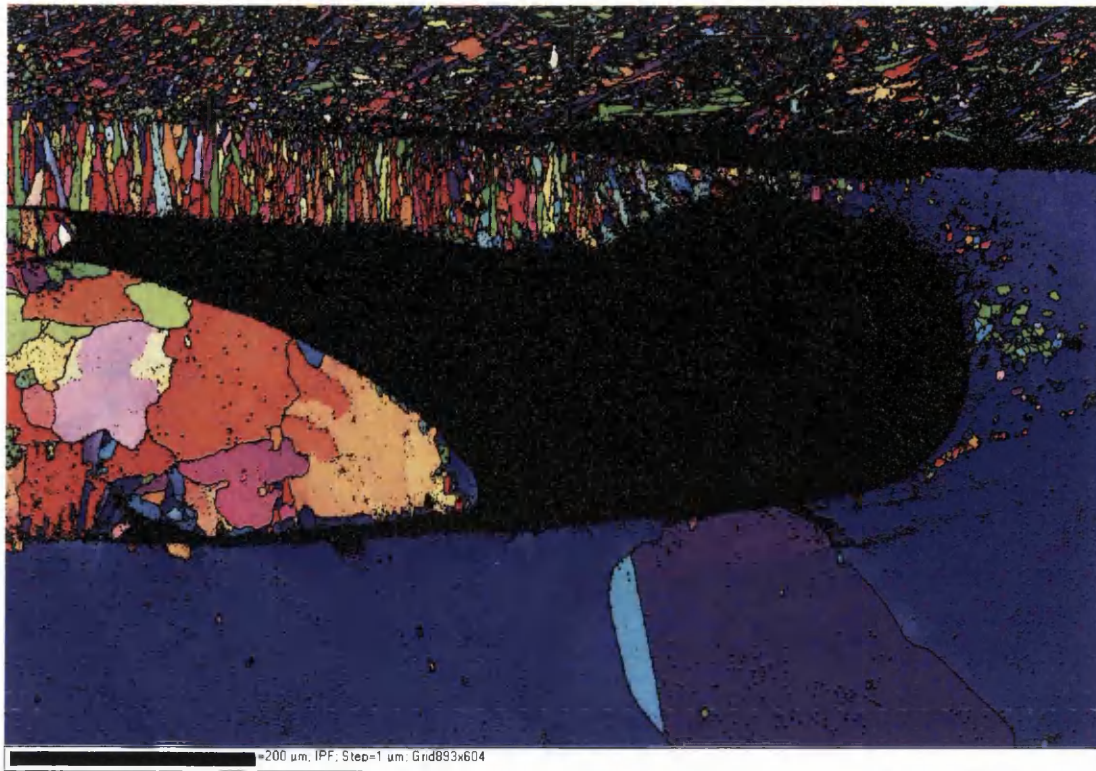


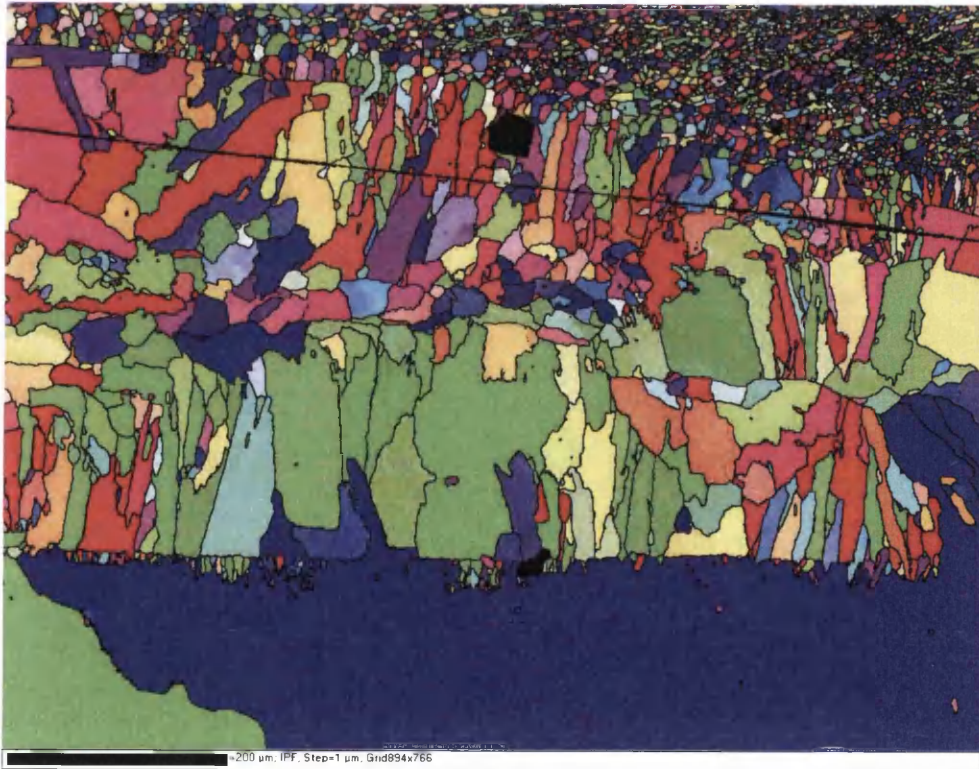
~1000 μm , Map5, Step=3 μm , Grid853x639

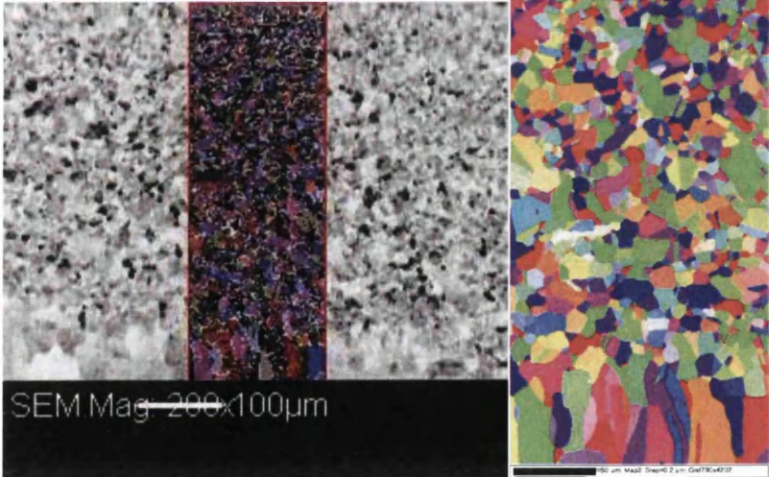


~20 μm , IPF, Step=0.1 μm , Grid817x612









REFERENCES

1. G.Palumbo, D.M. Doyle, A.M.El-Sherik, U.Erb, K.T.Aust, Intercrystalline hydrogen diffusion transport in nanocrystalline nickel, *Scripta Metall.* 25 (1991) 679-684.
2. T.M.Harris, R.M.Latanision, Grain boundary diffusion of hydrogen in nickel, *Metallurgical Transactions A*, 22A (1991) 351-355.
3. A.Oudriss, J.Creus, J.Bouhattate, E.Conforto, C.Berziou, C.Savall, X.Feugas, Grain size and grain boundary effects on diffusion and trapping of hydrogen in pure nickel, *Acta Materialia* 60 (2012) 6814-6828.
4. T.Tsuru, R.M.Latanision, Grain boundary transport of hydrogen in nickel, *Scripta Metall* 16 (1982) 575-578.
5. B.S.Bokstein, H.D.Brose, L.I.Trusov, T.P.Khvostantseva, Diffusion in nanocrystalline nickel, *NanoStructured Materials* 6 (1995) 873-876.
6. A.Portavoce, G.Chai, L.Chow, J.Bernardini, Nanometric size effect on Ge diffusion in polycrystalline Si, *J Appl Phys* 104 (2008) 104910:1-8.
7. Shun Li, Jianqiu Zhou, Lu Ma, Nan Xu, Rongtao Zhu, Xiaohua He, Continuum level simulation on the deformation behaviour of nanocrystalline nickel, *Computational Mater Sci* 45 (2009) 390-397.
8. T.Watanabe, Grain boundary engineering: historical perspective and future prospects, *J Mater Sci* 46 (2011) 4095-4115.
9. C.A.Schuh, M.Kumar, W.E.King, Universal features of grain boundary networks in FCC materials, *J Mater Sci* 40 (2005) 847-852.

10. C.A.Schuh, R.W.Minich, M.Kumar, Connectivity and percolation in simulated grain boundary networks, *Philosophical Magazine* 83 (2003) 711-726.
11. R.M.Latanision, H.Opperhauser Jr., The intergranular embrittlement of nickel by hydrogen: the effect of grain boundary segregation, *Metall Trans* 5 (1974) 483-492.
12. S.Kobayashi, S.Tsurekawa, T.Watanabe, G.Palumbo, Grain boundary engineering for control of sulfur segregation induced embrittlement in ultrafine-grained nickel, *Scripta Mater* 62 (2010) 294-297
13. S.Ghosh, S.Moorthy, Three dimensional Voronoi cell finite element model for microstructures with ellipsoidal heterogeneities, *Computational Mechanics* 34 (2004) 510-531.
14. J.C.Fisher, Calculation of diffusion penetration curves for surface and grain boundary diffusion, *J Appl Phys* 22 (1951) 74-77.
15. R.E.Hoffman, D.Turnbull, Lattice and grain boundary self-diffusion in silver, *J Appl Phys* 22 (1951) 634-639.
16. D.Turnbull, R.E.Hoffman, The effect of relative crystal and boundary orientations on grain boundary diffusion rates, *Acta Metallurgica* 2 (1954) 419-426.
17. E.W.Hart, On the role of dislocations in bulk diffusion, *Acta Metallurgica* 5 (1957) 597.
18. H.Wang, W.Yang, A.H.W.Ngan, Enhanced diffusivity by triple junction networks, *Scripta Materialia* 52 (2005) 69-73.
19. I.V.Belova, G.E.Murch, Diffusion in nanocrystalline materials, *J Phys Chem Solids* 66 (2003) 873-878.
20. I.M.Bernstein, The role of Hydrogen: is the story any clearer?, *Hydrogen effects in Materials*, eds. A.W.Thompson and N.R.Moody (1996) 3-11.
21. A.R.Troiano, The role of Hydrogen and Other Interstitials on the Mechanical Behavior of Metals, *Trans. American Society for Metals* 52 (1960) 54.
22. A.Turnbull, Modelling of environment assisted cracking, *Corrosion Science* 34 (1993) 921-960.
23. A.Turnbull, M.W.Carroll, D.H.Ferriss, Analysis of hydrogen diffusion and trapping in a 13 % chromium martensitic stainless steel, *Acta Metall.* 37 (1989) 2039-2046.
24. J.P.Hirth, The influence of grain boundaries on mechanical properties, *Metallurgical Transactions* 3 (1972) 3047-3067.
25. A.H.M.Korm, Numerical modelling of hydrogen transport in steel, PhD Thesis (1998).
26. R.M.Latanision, H.Opperhauser.Jr, Further observations on the effect of grain boundary segregation in the hydrogen embrittlement of nickel, *Metallurgical Transactions A* 6A (1975) 233-234.
27. G.Palumbo, F.Gonzalez, A.M.Brennenstuhl, U.Erb, W.Shmayda, P.C.Lichtenberger, In-situ nuclear steam generator repair using electrodeposited nanocrystalline nickel, *Nanostructured Materials* 9 (1997) 737-746.
28. M.L.Martin, B.P.Somerday, R.O.Ritchie, P.Sofronis, I.M.Robertson, Hydrogen-induced intergranular failure in nickel revisited, *Acta Materialia* 60 (2012) 2739-2745.
29. A.J.Mortlock, The effect of segregation on the solution diffusion enhancement due to the presence of dislocations, *Acta Metallurgica* 8 (1960)132-134.

30. J.R.Kalnin, E.A.Kotomin, V.N.Kuzovkov, Calculation of the effective diffusion coefficient in inhomogeneous solids, *Defect and Diffusion Forum* 163 (2001) 194-199.
31. J.C.Maxwell Garnett, Colours in metal glasses and in metallic films, *Phil. Trans. R. Soc. London A* 203 (1904) 385-420.
32. M.A.Meyers, A.Mishra, D.J.Benson, Mechanical properties of nanocrystalline materials, *Progress in Materials Science* 51 (2006) 427-556.
33. E.Lauridson, S.Schmit, S.Nielsen, L.Margulies, H.Poulsen, D.Jensen, Non-destructive characterization of recrystallization kinetics using three-dimensional X-ray diffraction microscopy, *Scripta Mater* 55 (2006) 51-56.
34. B.Adams, T.Olson, The mesostructure-properties linkage in polycrystals, *Progress Mater Sci* 43 (1998) 1-88.
35. F.Fritzen, T.Bohlke, E.Schnack, Periodic three-dimensional mesh generation for crystalline aggregates based on Voronoi tessellations, *Comput Mech* 43 (2009) 701-713.
36. M.Groeber, B.Haley, M.Uchic, D.Dimiduk, S.Ghosh, 3D reconstruction and characterization of polycrystalline microstructure using a FIB-SEM, *Mater Characterization* 57 (2006) 259-273.
37. Y.Bhandari, S.Sarkar, M.Groeber, M.Uchic, D.Dimiduk, S.Ghosh, 3D polycrystalline microstructure reconstruction from FIB generated serial sections for FE analysis, *Comput Mater Sci* 41 (2007) 222-235.
38. James Clerk Maxwell, *A Treatise on electricity and Magnetism*, Oxford: Clarendon Press I, II (1873).
39. M.Felberbaum, E.Landry-Desy, L.Weber, M.Rappaz, Effective hydrogen diffusion coefficient for solidifying aluminium alloys, *Acta Materialia* 59 (2011) 2302-2308.
40. Z.Hashin, S.Shtrikman, A variational approach to the theory of the effective magnetic permeability of multiphase materials, *J Appl Phys* 33 (1962) 3125-3131.
41. Y.Chen, C.A.Schuh, Geometric consideration for diffusion in polycrystalline solids, *J Appl Phys* 101 (2007) 063524:1-12.
42. H. Gleiter, Nanocrystalline materials, *Progress in Materials Science* 33 (1989) 223-315.
43. G.Palumbo, S.J.Thorps and K.T.Aust, On the contribution of triple junctions to the structure and properties of nanocrystalline materials, *Scripta Metallurgica et Materialia* 24 (1990) 1347-1350.
44. Y.Chen and C.A.Schuh, Contribution of triple junctions to the diffusion anomaly in nanocrystalline materials, *Scripta Materialia* 57 (2007) 253-256.
45. Lingling Hu, Ruxiao Huo, Jianqiu Zho, Ying Wang and Shu Zhang, The effects of the finest grains on the mechanical behaviours of nanocrystalline materials, *J Nanopart Res*, 14 (2012) 677.
46. W.Bollmann, *Philos. Mag. A*, 57 (1998) 637.
47. M.A.Meyers, E.Ashworth, A model for the effect of grain size on the yield stress of metal, *Phil. Mag. A* 46 (1982) 737.
48. J.Jiang, T.B. Britton, A.J. Wilkinson, Measurement of geometrically necessary dislocations density with high resolution electron backscatter diffraction: Effects of detector binning and step size, *Ultramicroscopy* 125 (2013) 1-9.

49. David J. Benson, Hsueh-Hung Fu, Marc Andre Meyers, On the effect of grain size on yield stress: extension into nanocrystalline domain, *Materials science and Engineering A319-321* (2001) 854-861.
50. E. Legrand, J. Bouhattate, X. Feugas, S. Touzain, H. Garmestani, M. Khaleel, D.S. Li, Numerical analysis of the influence of scale effects and microstructure on hydrogen diffusion in polycrystalline aggregates, *Computational Material Science*, 71 (2013) 1-9.
51. H.Margolin, Polycrystalline yielding-perspectives on its onset, *Acta Mat.* 46 (1998) 6305-6309
52. A.P.Sutton, R.E.Baluffi, *Interfaces in Crystalline Materials*, (2006) Oxford University Press.
53. ABAQUS 12. tutorial manual,2012
54. M. R. Chellali, Z. Balogh, H. Bouchikhaoui, R. Schlesiger, P. Stender, L. Zheng and G. Schmitz, Triple Junction transport and the impact of grain boundary width in nanopolycrystalline Cu, *Nano Lett.* 12 (2012) 3448-3454.
55. A. Portavoce, L. Chow and J. Bernardini, Triple junction contribution to diffusion in nanocrystalline Si, *Applied physics Letters* 96 (2010) 214102.
56. B. Bokstein, V. Ivanov, O. Oreshina, A. Peteline and S. Peteline, Direct experimental observation of accelerated Zn diffusion along triple junctions in Al, *Mate Sci Eng A302* (2001) 151-153.
57. I.M. Mikhailovski, V. B. Rabukhin, O. A. Velikodnaya, On the enhancement of the diffusion permeability near triple junctions, *Phys status Solidi A* 125 (1991) K65.
58. L. M. Klinger, L.A. Levin and A.L. Peteline, The model of triple junction diffusion, *Defect and Diffusion Forum* 143-147 (1997) 1523-1526.
59. A. Vinogradov and S. Hashimoto, Effects of triple junction on fatigue crack growth in copper and copper -3AT.% aluminium tricrystals, *Scripta Mater.* 36 (1997) 417-423.
60. N.Wang, Z. Wang, K.T. Aust and U. Erb, Effect of grain size on mechanical properties of nanocrystalline materials, *Acta Metallurgica et Materialia* 43 (1995) 519-528.
61. C. R. Chen, S. X. Li, J. L. Wen, W. P. Jia, Finite element analysis about effects of stiffness distribution on stresses and elastic strain energy near the triple junctions in a tricrystal, *Materials Science and Engineering A282* (2000) 170-176.
62. L. Lu, M.L. Sui and K. Lu, Superplastic extensibility of nanocrystalline copper at room temperature, *Science* 287 (2000) 1463-1466.
63. Z.B. Wang, N.R. Tao, W.P. Tong, J. Lu and K. Lu, Diffusion of chromium in nanocrystalline iron produced by means of surface mechanical attrition treatment, *Act Materialia* 51 (2003) 4319-4329
64. T. Frolo and Y. Mishin, Molecular dynamics modelling of self-diffusion along a triple junction, *Phy. Rev. B* 79 (2009) 174110
65. Y. Zhou, G. Palumbo, K.T. Aust and U. Erb, Triple junction structure and carbide precipitation in 304L stainless steel, *Journal of Materials Research* 28 (2013) 1589-1600.
66. J. Schiotz, F.D.D. Tolla and K.W. Jacobsen, Softening of nanocrystalline metals at very small grain sizes, *Nature* 391 (1998) 561-563
67. Z. Balogh, C. Oberdorfer, M.R. Chellai, P. Stender, S. Nowak and G. Schmitz (2013) Defect analysis by statistical fitting to 3D atomicmaps, *Ultramicroscopy* 132:86-91.

68. D. Prokoshkina, V.A. Esin, G. Wilde and S.V. Divinski, Grain boundary width, energy and self-diffusion in nickel: Effect of material purity, *Acta Materialia* 61 (2013) 5188-5197.
69. Z. Balogh, P. Stender, M.R. Chellali and G. Schmitz, Investigation of interfaces by atom probe tomography, *Metallurgical and Materials Transactions A44* (2013) 4487-4495.
70. A. Caro and H. Van Swygenhoven, Grain boundary and triple junction enthalpies in nanopolycrystalline metals, *Phys. Rev. B* 63 (2001) 134101.
71. P. Stender, Z. Balogh and G. Schmitz, Triple junction segregation in nanocrystalline multilayers, *Phys. Rev. B* 83 (2011) 121407
72. M.R. Chellai, Z. Balogh, L. Zheng and G. Schmitz, Triple junction and grain boundary diffusion in the Ni/Cu system, *Scr. Mater.* 65 (2011) 343-346
73. A.M. El-Sherik and U. Erb (1994) Production of Nanocrystalline Metals, US Patent No.,5, 352, 266
74. <http://cs.astrium.eads.net/sp/launcher-propulsion/rocket-engines/vulcain-rocket-engine.html> (last accessed 15/October/2013).
75. A.M. El-Sherik, U. Erb and J. Page, Microstructural evolution in pulse plated nickel electrodeposits, *Surface and Coating Technology* 88 (1996) 70-78
76. L. Klinger, I. Gotman and E. Rabkin, A mesoscopic model of dissolution/disintegration of nanocrystalline meals via vacancy diffusion along grain boundaries, *Computational Materials Science* 76 (2013) 37-42
77. L. Klinger and E. Rabkin, Theory of the Kirkendall effect during grain boundary interdiffusion, *Acta Materialia* 59 (2011) 1389-1399
78. L. Klinger, E. Rabkin, L.S. Shvindlerman and G. Gottstein, Grain growth in porous two dimensional nanocrystalline materials, *J Mater Sci* 43 (2008) 5068-5075.
79. A. Alvaro, V. Olden and O.M. Akselsen, 3D cohesive modelling of hydrogen embrittlement in the heat affected zone of an X70 pipeline steel, *International journal of hydrogen energy* 38 (2013) 7539-7549
80. V. Olden, C. Thaulow and R. Johnsen, Modelling of hydrogen diffusion and hydrogen induced cracking in supermartensitic and duplex stainless steels, *Materials and Design* 29 (2008) 1934-1948
81. K. Ebihara, M. Itakura, M. Yamaguchi, H. Kaburaki, T. Suzudo, Evaluation of stress and hydrogen concentration at grain boundary of steels using three dimensional polycrystalline model, *Progress in Nuclear science and Technology*, 2 (2011) 38-43..
82. MATLAB Tutorial manual
83. Arantes, D.R., Huang, X.Y., Marte, C. and Kirchheim, R., Hydrogen Diffusion and Permeation in Micro and Nanocrystalline Nickel, *Acta Metal. Mater.* , 41, No. 11, (1993) 3215-3222.
84. Windle, A.H., Smith, G.C., The effect of hydrogen on the plastic deformation of nickel single crystals, *Metal Sci. J.* 12(1968) 187-191
85. Kurkela, M., Latanision, R.M., The effect of plastic deformation on the transport of hydrogen in nickel, *Scripta Metal.* 13(1979) 927-932.
86. Lynch, S.P., Failures of engineering components due to environmentally assisted cracking, *Practical Failure Analysis* 3 (2003) 33-42.
87. Xu, J., Sun, X.K., Liu, Q.Q., Chen, W.X., Hydrogen Permeation behaviour in IN718 and GH761 Superalloys, *Metall, Mater. Trans.* 25A (1994) 539-544.
88. Byun, T.S., Farrell, K., Tensile properties of Inconel 718 after low temperature neutron irradiation, *J. Nuclear Materials* 318 (2003) 292-299.

89. Liu, L., Tanaka, K., Hirose, A., Kobayashi, K.F., Effects of precipitation phases on the hydrogen embrittlement sensitivity of Inconel 718, *Science and Technology of Advanced Materials* 3 (2002) 335-344.
90. C. Verpoort, D.J. Duquette, N.S. Stoloff, A. Neu, The influence of plastic deformation on the hydrogen embrittlement of nickel, *Materials Science and Engineering* 64 (1984) 135-145.
91. F. Galliano, E. Andrieu, C. Blanc, J.M. Cloue, D. Connetable, G. Odemer, Effect of trapping and temperature on the hydrogen embrittlement susceptibility of alloy 718, *Materials Science and Engineering: A* 611 (2014) 370-382.
92. McNabb, A., Foster, P.K., A New analysis of the diffusion of hydrogen in Iron and Ferritic steels, *Trans Metall. Soc. A.I.M.E.* 227 (1963), pp.618-627.
93. Marte, C., Kirchheim, R., Hydrogen Diffusion in Nanocrystalline Nickel Indicating a Structural Change within the Grain Boundaries After Annealing, *Scripta Mat.*, 37, No.8, 1997, pp. 1171-1175.
94. Richard, P.G. and Brain, P.S., Gaseous hydrogen embrittlement of materials in energy technologies Volume2: Mechanisms, modelling and future developments, 2012, Woodhead Publishing, Cambridge.
95. Brass, A.M., Chanfreau, A., Accelerated Diffusion of Hydrogen along Grain boundaries in Nickel, *Acta Mater.*, 44, No.9, 1996, pp.3823-3831
96. Yao, J. and Meguid, G.A., Hydrogen Diffusion and Intergranular cracking in nickel, *Int. J. Hydrogen Energy*, 22, No.10/11, 1997, pp.1021-1026.
97. Paggi, M., Wriggers, P., A nonlocal cohesive zone model for finite thickness interfaces-Part II: FE implementation and application to polycrystalline materials, *Comp. Mat. Sci.*, 50, 2011, pp.1634-1643.
98. Schaefer, H.-E., Wurschum, R., Birringer, R., and Gleiter, R., Structure of nanometer-sized polycrystalline iron investigated by positron lifetime spectroscopy, *Phys. Rev. B*, 38, No.14, 1988, pp.9545-9554.
99. Kim, K.B., Park, K., Lee, J.S., Hydrogen permeation behavior of nickel electroplated AISI 4340 steel, *Metals and Materials*, 4 (1998) 1013-1016.
100. Rimoli, J.J., Ortiz, M., A three-dimensional multiscale model of intergranular hydrogen-assisted cracking, *Philosophical Magazine* 21 (2010) 2939-2963.
101. Reese, E.D., W., Sebald., "EU FP7 Multi-scale modelling hydrogen Embrittlement- MultiHy" report, EADS report (2014).
102. Reese, E.D., von Bestenbostel, W., Sebald, T., Paronis, G., Vanelli, D., Muller, Y., Hydrogen embrittlement of pulse-plated nickel, *JOM* 66 (2014) pp.1368-1376.
103. Watanabe, T., Structural effects on grain boundary segregation, hardening and fracture, *Journal de Physique*, 1985; 46 C4:555-564.
104. Iino, M., A more generalized analysis of hydrogen trapping, *Acta Metall.* 30 (1982) pp.367-375.
105. Iino, M., Analysis of irreversible hydrogen trapping, *Acta Metall.* 30 (1982) pp.377-383.
106. Leblond, J.B., Dubois, D., A general mathematical description of hydrogen diffusion in steels - I: Derivation of diffusion equations from Boltzmann type transport equations, *Acta Metall.* 31 (1983) pp.1459-1469
107. Leblond, J.B., Dubois, D., A general mathematical description of hydrogen diffusion in steels - II: Numerical study of permeation and determination of trapping parameters, *Acta Metall.* 31 (1983) pp.1471-1478.

108. Oriani, R.A., The diffusion and trapping of hydrogen in steel, *Acta Metall.* 18 (1970) pp.147-157.
109. ABAQUS Version 6.11. User's Manual, Dassault Systemes, 2010
110. Wright, L., Turnbull, A., "EU FP7 Multi-scale modelling hydrogen Embrittlement- MultiHy" report, NPL report (2013).
111. Winzer, N., "EU FP7 Multi-scale modelling hydrogen Embrittlement- MultiHy" report, IWM report (2013).
112. Sun, Y., Peng, Q., Lu, G., Quantum mechanical modeling of hydrogen assisted cracking in aluminum, *Physical Review B* 88 (2013) 104109.
113. Dmitrii Ilin, Simulation of hydrogen diffusion in fcc polycrystals. Effect of deformation and grain boundaries, PhD thesis, Universite de Bordeaux, 2014.
114. Bouhattate, J., Legrand, E., Oudriss, A., Frappart, S., Creus, J., Feaugas, X., Simulation of a hydrogen permeation test on a multilayer membrane, Proceedings of the COSMOL conference 2010 Paris.
115. Harris, T.M., Hydrogen diffusion, and trapping in electrodeposited nickel, PhD Thesis, Massachusetts Institute of Technology, USA, (1989).
116. Lassila, D.H., Birnbaum, H.K, The effect of diffusive hydrogen segregation on fracture of polycrystalline nickel, *Acta Metall.*, 34 (1986) pp.1237-1243
117. McLean, D., Grain boundaries in metals, Oxford University Press (1957).
118. Lee, S-M., Lee, J-Y., The trapping and transport phenomena of hydrogen in nickel, *Met. Trans. A*, 17A (1986) pp.181-187.
119. Raabe, D., Herbig, M., Sandlobes, S., Li, Y., Tytko, D., Kuzmina, M., Ponge, D., Choi, P-P., Grain boundary segregation engineering in metallic alloys: A Pathway to the design of interfaces, *Current opinion in Solid State and Material Science* 18 (2014) 253-261.
120. Raabe, D., Sandlobes, S., Millan, J., Ponge, D., Assadi, H., Herbig, M., Choi, P-P., Segregation engineering enables nanoscale martensite to austensite phase transformation at grain boundaries: A Pathway to ductile martensite, *Acta Mater.* 61 (2013) 6132-6152.
121. Watanabe, T., Tsurekawa, S., The control of brittleness and development of desirable mechanical properties in polycrystalline systems in grain boundary engineering, *Acta Mater.* 47 (1999) 4171-4185
122. Bechtle, S., Kumar, M., Somerday, B.P., Launey, M.E., Ritchie, R.O., Grain-boundary engineering markedly reduces susceptibility to intergranular hydrogen embrittlement in metallic materials, *Acta Mater.* 57 (2009) 4148-4157.
123. Biroasca, S., Di Gioacchino, F., Stekovic, S., Hardy, M., A quantitative approach to study the effect of local texture and heterogeneous plastic strain on the deformation micromechanism in RR1000 nickel-based superalloy, *Acta Mater.* 74 (2014) 110-124
124. Raabe, D., Zhao, Z., Park, S-J., Roters, F., Theory of orientation gradients in plastically strained crystals, *Acta Mater.* 50 (2002) 421-440.
125. Oudriss, A., Creus, J., Bouhattate, J., Savall, C., Peraudeau, B., Feaugas, X.. The diffusion and trapping of hydrogen along grain boundaries in polycrystalline nickel, *Scripta Mater.* 66 (2012) 37-40.
126. Louthan Jr., M.R., Donovan, J.A., Caskey Jr., G.R., Hydrogen diffusion and trapping in nickel, *Acta Metall.* 23 (1975) 745-749.
127. Ladna, B., Birnbaum, H.K., A study of hydrogen transport during plastic deformation, *Acta Metall.* 35 (1987) 1775-1778.

128. Ashby, M.F., The deformation of plastically non-homogeneous materials, *Phil. Mag.* 21 (1970) 399-424.
129. Pesicka, J., Dronhofer, A., Eggeler, G., Free dislocations and boundary dislocations in tempered martensite ferritic steels, *Mat. Sci. Eng. A* 387-389 (2004) 176-180.
130. Nye, J.F., Some geometrical relations in dislocated crystals, *Acta Metall.* 1 (1953) 153-162.
131. Mandal, D., Baker, I., Measurement of the energy of grain boundary geometrically-necessary dislocation in copper, *Scripta Metall. Mater.* 33 (1995) 831-836
132. Sjoberg, G., Cornu, D., Hydrogen embrittlement of cast alloy 718 effects of homogenization, grain size and δ -phase, The Mineral, Metals & Materials Society (2001) , Superalloys 718, 625, 706 and various derivatives Edited by E.A. Loria, pp.679-690.
133. Fritzmeier, L.G., Chandler, W.T., "Hydrogen Embrittlement - Rocket Engine Applications", Superalloys, Supercomposites and Superceramics, Academic Press, Inc., (1989) pp.491-524.
134. Jewett, R.P., Halchak, J.A., The use of alloy 718 in the space shuttle main engine, Superalloys 718, 625 and various derivatives, ed. Loria, E.A., The Mineral, Metals & Materials Society (1991) pp.749-760.
135. Fukuyama, S., Yokogawa, K., Effect of heat treatments on hydrogen environment embrittlement of alloy 718, The Mineral, Metals & Materials Society (1994) Superalloys 718, 625 and various derivatives, ed. Loria, E.A., pp.807-816.
136. Pound, B.G., Hydrogen trapping in precipitation hardened alloys, *Acta Metall. Mater.*, 38 (1990), pp.2373-2381.
137. Angelo, J. E., Moody, A.R., Baskes, M.I., Modeling the segregation of hydrogen to lattice defects in Nickel, Sandia National Laboratories Reprot (1994).
138. Mrovec, M., Stefano, D.D., Elsasser, C., Nazarov, R., Hickel, T., Atomic insights into hydrogen diffusion and trapping, Hydrogen embrittlement: Multi-scale modelling and measurement – What is the impact? Workshop, 6-8 October 2014, NPL, Teddington, UK.
139. Kalnins, J.R., Kotomin, E.A., Maier, J., Calculations of the effective diffusion coefficient for inhomogeneous media, *J. Phys. Chem. Solids*, 63 (2002), pp.449-456.
140. Belova, I.V., Murch, G.E., Analysis of the effective diffusivity in nanocrystalline materials, *J. Metastable and Nanocrystalline Materials*, 49 (2004), pp.25-34.
141. Shan, Z.W., Wiezorek, J.M.K., Stach, E.A., Follstaedt, D.M., Knapp, J.A., Mao, S.X., Dislocation dynamics in nanocrystalline nickel, *Phys. Rev. Lett.*, 98 (2007), pp.1-4
142. Canon, R.F., Stark, J.P., Grain boundary self-diffusion in nickel, *J. App. Phys.*, 40 (1969), pp.4366-4373.
143. P.Lejcek, Grain Boundary Segregation in Metals, R.Hull,C.Jagadish,R.M.Osgood,Jr., J.Parisi,Z.Wang,H.Warlimont, Springer, Berlin (2010).
144. Mills, W.J., Lebo, M.R., Kearns, J.J., Hydrogen embrittlement, grain boundary segregation, and stress corrosion cracking of alloy X-750 in low and high temperature water, *Metall. Mater. Trans. A* 30 (1999), pp1579-1596.

145. Di Stefano, D., Mrovec, M., Elasser, C., First-Principles investigation of hydrogen trapping and diffusion at grain boundaries in nickel, *Acta Mater.* 98 (2015) 306-312.
146. Haftbaradaran, H., Song, J., Curtin, W.A., Geo, H., Continuum and atomistic models of strong coupled diffusion, stress, and solute concentration, *J. Power Sources* 196 (2011), pp.361-370.
147. Song, J., Curtin, W.A., Atomic mechanism, and prediction of hydrogen embrittlement in iron, *Nature Mat.* 12 (2013), pp.145-151
148. Brewer, L.N., Field, D.P., Merriman, C.C., Mapping and assessing plastic deformation using EBSD, In *Electron backscattering diffraction in material science*, eds. Schwartz, A.J., Kumar, M., Adams, B.L., Field, D.P., New York, Springer Science + Business Media (2000).
149. Koyama, M.K., Tasan, C.C., Akiyama, E., Tsuzaji, K., Raabe, D., Hydrogen-assisted decohesion and localized plasticity in dual-phase steel, *Acta Mater.* 70 (2014), pp.174-187.
150. Koyama, M.K., Springer, H., Merzlikin, S.V., Tsuzaki, K., Akiyama, E., Raabe, D., Hydrogen embrittlement associated with strain localization in a precipitation-hardened Fe-Mn-Al-C light weight austenitic steel, *Int. J. Hydrogen Energy* 39 (2014), pp.4634-4646.
151. LaCoursiere, Marissa P., Hydrogen induced stress cracking of materials under cathodic protection, PhD Thesis., Clarkson University (2015).
152. S.Lynch, Hydrogen embrittlement phenomena, and mechanisms, *Corrosion Reviews* 30 (2012) 105-123.
153. C. Herzig, S.V. Divinski, Grain boundary diffusion in metals: Recent development, *Materials Transactions* 44 (2003) pp. 14-27.
154. I. Kaur, Y. Mishin, W. Gust, *Fundamentals of grain and interphase boundary diffusion*, Wiley, Chichester, UK (1995).
155. K.A. Esakul, Ed., *Handbook of case histories in Failure Analysis*, ASM international 1 (1992).
156. I.V. Belova, N.S. Kulkarni, Y.H. Sohn and G.E. Murch, Simultaneous measurement of tracer and interdiffusion coefficients: An isotopic phenomenological diffusion formalism for the binary alloy, *Philosophical Magazine* 93:26 (2013) pp. 3515-3526.
157. S. Brennan, K. Bermudez, N.S. Kulkarni, Y. Sohn, Interdiffusion in the Mg-Al System and intrinsic diffusion in β -Mg₂Al₃, *Metallurgical and Materials Transactions A* 43 (2012) pp. 4043-4052.
158. F.J.J. van Loo, Multiphase diffusion in binary and ternary solid-state systems, *progress in solid state chemistry* 20 (1990) pp. 47-99.
159. N.S. Kulkarni, C.V. Iswaran, R.T. DeHoff, Intrinsic diffusion simulation for single-phase, multicomponent systems, *Acta Materialia* 53 (2005) pp. 4097-4110.
160. M. Mrovec, "EU FP7 Multiscale modelling hydrogen Embrittlement-MultiHy" deliverable 6.2, Swansea University report (2014).
161. S. Brennan, A.P. Warren, K.R. Coffey, N. Kulkarni, P. Todd, M. Kilmov, Y. Sohn, Aluminium impurity diffusion in magnesium, *Journal of Phase Equilibria and Diffusion* 33 (2012) pp. 121-125.
162. G.S. Frankel, R.M. Latanision, Hydrogen transport during deformation in nickel: Part I. Polycrystalline nickel, *Metall Trans A*, 17A (1986), pp. 861-867
163. T. Watanabe, The impact of grain-boundary-character-distribution on fracture in polycrystals, *Mater Sci Eng A Struct*, 176 (1994), pp. 39-49.

164. V.Y. Gertsman, M. Janecek, K. Tangri, Grain boundary ensembles in polycrystals, *Acta Mater*, 44 (1996), pp. 2869–2882.
165. V.Y. Gertsman, K. Tangri, Computer simulation study of grain boundary and triple junction distributions in microstructures formed by multiple twinning, *Acta Metall Mater*, 43 (1995), pp. 2317–2324.
166. G. Palumbo, P.J. King, K.T. Aust, U. Erb, P.C. Lichtenberger, Grain boundary design and control for intergranular stress-corrosion resistance, *Metall Mater*, 25 (1991), pp. 1775–1780.
167. J. Yao, J.R. Cahoon, Experimental studies of grain boundary diffusion of hydrogen in metals, *Acta Metall Mater*, 39 (1991), pp. 119–126.
168. H.S. Levine, C.J. MacCallum, Grain boundary and lattice diffusion in polycrystalline bodies, *J Appl Phys*, 31 (1960), p. 595
169. ABAQUS Version 6.11, User's manual, Dassault Systemes, (2011).
170. R. Cortés, A. Valiente, J. Ruiz, L. Caballero, J. Toribio, Finite element modeling of stress-assisted hydrogen diffusion in 316L stainless steel, *Mater Sci*, 33 (1997), pp. 491–503
171. B. Bokstein, V. Ivanov, O. Oreshina, A. Peteline, S. Peteline, Direct experimental observation of accelerated Zn diffusion along triple junctions in Al, *Materials Science and Engineering A* 302 (2001) 151-153.
172. S. Serebrinsky, E.A. Carter, M. Ortiz, A quantum-mechanically informed continuum model of hydrogen embrittlement, *Journal of the Mechanics and Physics of Solids* 52 (2004) 2403-2430.
173. N. Yazdipour, D. Dunne, E. Pereloma, Effects of grain size on the hydrogen diffusion process in steel using cellular automaton approach, *Materials Science Forum* 706-709 (2012) 1568-1573.
174. A. Turnbull, EU FP7 MultiHY project NPL reports, (2014)
175. P. Novak, R. Yuan, B.P. Somerday, P. Sofronis, R.O. Ritchie, A Statistical, physical-based, micro-mechanical model of hydrogen-induced intergranular fracture in steel, *Journal of the Mechanics and Physics of Solids* 58 (2010) 206-226.
176. L.C. Lim, T. Watanabe, Grain boundary character distribution controlled toughness of polycrystals - a two dimensional model, *Scripta Metall* 1989; 23:489-495.
177. T. Watanabe, T. Murakami and S. Karashima, Misorientation dependence of grain boundary segregation, *Scripta Metall* 1978;12:361-365.
178. S. Kobayashi, T. Maruyama, S. Tsurekawa, T. Watanabe, Grain boundary engineering based on fractal analysis for control of segregation induced intergranular brittle fracture in polycrystalline nickel, *Acta Materialia* 2012;60:6200-6212.
179. T. Watanabe, An approach to grain boundary design for strong and ductile materials, *Res. Mechanica*, 1984;11:47-84.
180. L.C. Lim, T. Watanabe, Fracture toughness and brittle-ductile transition controlled by grain boundary character distribution (GBCD) in polycrystals, *Acta Metallurgica et Materialia* 1990;38:2507-2516.
181. G. Palumbo, K.T. Aust, Structure-dependence of intergranular corrosion in high purity nickel, *Acta Met Mater* 1990;38:2343-2352
182. P. Lin, G. Palumbo, U. Erb, K.T. Aust, Influence of grain boundary character distribution on sensitization and intergranular corrosion of alloy 600, *Scripta Metallurgica et Materialia* 1995;33:1387-1392.

183. E.M. Lehockey, D. Limoges, G. Palimbo, J. Sklarchuk, K. Tomantschger, A. Vincze, On improving the corrosion and growth resistance of positive Pb-acid battery grids by grain boundary engineering, 1999;78:79-83.
184. C. Cheung, U. Erb, Application of grain boundary engineering concept to alleviate intergranular cracking in Alloys 600 and 690, *Materials science and Engineering:A* 1994;185:39-43.
185. E.M. Lehockey, G. Palumbo, On the creep behaviour of grain boundary engineered nickel 1, *Materials Science and Engineering: A* 1997; 237:168-172.
186. D.C. Crawford, G.S. Was, The role of grain boundary misorientation in intergranular cracking of Ni-16Cr-9Fe in 360°C argon and high purity water, *Metall. Mater. Trans.A*, 1992; 23:1195-1206.
187. M.A. Arafin, J.A. Szpunar, A new understanding of intergranular stress corrosion cracking resistance of pipeline steel through grain boundary character and crystallographic texture studies, *Corrosion Science* 2009;51:119-128.
188. C.A. Schuh, M. Kumar, W.E. King, Analysis of grain boundary networks and their evolution during grain boundary engineering, *Acta Materialia* 2003;51:687-700.
189. V. Randle, twinning-related grain boundary engineering, *Acta Materialia* 2004; 52:4067-4081.
190. A.W. Thompson, Effect of grain size on work hardening in nickel, *Acta Metallurgica* 1997; 25:83-86.
191. R.A. Jago, N. Hansen, Grain size effects in the deformation of polycrystalline iron, *Acta Metallurgica* 1986;34:1711-1720.
192. L. St-Pierre, E. Heripre, M. Dexet, J. Crepin, G. Bertolino, N. Bilger, 3D simulations of microstructure and comparison with experimental microstructure coming from O.I.M analysis, *International Journal of Plasticity* 2008;24:1516-1532.
193. Y. Zhao, R. Tryon, Automatic 3-D simulation and micro-stress distribution of polycrystalline metallic materials, *Computational Methods in Applied Mechanics and Engineering* 2004;193:3919-3934.
194. T.J. Turner, P.A. Shade, J.C. Schuren, M.A. Goeber, The influence of microstructure on surface strain distributions in a nickel micro-tension specimen, *Modelling and Simulation in Materials Science and Engineering* 2012;21:015002 (23pp).
195. H. Fukushima, H.K. Birnbaum, Surface and grain boundary segregation of deuterium in nickel, *Acts Metallurgica*, 1984; 32:851-859.
196. C. Herizg, S.V. Divinski, Grain boundary diffusion in Metals: Recent Developments, *Materials Transactions* 2003;44:14-27.
197. V. Randle, *Microtexture determination and its applications*, Bourne Press 1992.
198. V. Randle, *The role of the Coincidence Site Lattice in Grain boundary engineering*, The University Press 1996.
199. S.R. Arwade, M. Grigoriu, Probabilistic model for polycrystalline microstructures with application to intergranular fracture, *Journal of Engineering mechanics* 2004; 997-1005.
200. A.A. Elvin, S. Shyam Sunder, Microcracking due to grain boundary sliding in polycrystalline ice under uniaxial compression, *Acta Mater.* 1996; 44:43-56.
201. M. Martin, I.M. Roberson, B. Somerday, C. San Marchi, P. Sofronis, Multi-scale Investigation of the hydrogen-assisted failure of X65 pipeline steel 16 *Microscopy and Microanalysis* (2010) 778-779.

202. S. Huang, Nano-chemo-mechanics of advanced materials for hydrogen storage and lithium battery applications, Georgia Institute of Technology, USA PhD thesis (2011).
203. T.C.T. Ting, Anisotropic elasticity: Theory and Applications, Oxford: Oxford University Press 1996.
204. J.M.J. den Toonder, J.A.W. van Dommelen and F.P.T. Baaijens, The relation between single crystal elasticity and the effective elastic behaviour of polycrystalline materials: theory, measurement and computation, *Modelling Simul. Mater.Sci. Eng.* 1999;7:909-928.
205. J.F. Nye, Physical properties of Crystals, Oxford: Clarendon 1985.
206. F. Roters, P. Eisenlohr, L. Hantcherli, D.D. Tjahjanto, T.R. Bieler, D. Raabe, Overview of constitutive laws, kinematics, homogenization and multiscale methods in crystal plasticity finite-element modelling: Theory, experiments, applications, *Acta Materialia* 2010;58:1152-1211.
207. C.S. Nichols, R.F. Cook, D.R. Clarke, D.A. Smith, Alternative length scales for polycrystalline materials, *Acta Metall. Mater.* 1991; 39:1657-1665.
208. O. Diard, S. Lecercq, G. Rousselier, G. Cailletaud, Evaluation of finite element based analysis of 3D multicrystalline aggregates plasticity: application to crystal plasticity model identification and the study of stress and strain fields near grain boundaries, *International Journal of plasticity* 2005; 21:691-722.
209. M. Meyers and K. Chawlu, Mechanical behaviour of materials, Second Edition, Cambridge University Press 2009.
210. F. Barbe, S. Forest, G. Cailletaud, Intergranular and intragranular behaviour of polycrystalline aggregates. Part 2. Results, *International Journal of Plasticity* 2001;17:537-563
211. H. Mehrer, Diffusion in solids: Fundamentals, Methods, Materials, Diffusion-Controlled processes, Springer 2007.
212. O. Takakuwa, M. Nishikawa, H. Soyama, Numerical simulations of the effects of residual stress on the concentration of hydrogen around a crack tip, *Surface & Coating Technology* 2012;206:2892-2898
213. T. Kitamura, T. Sumigawa, K. Ohishi, Slip behaviour and local stress near grain boundary in high-cycle fatigue of copper polycrystal, *JSME international journal* 2004;47:92-97.
214. A.H.M. Krom, R.W.J. Koers, A. Bakker, Hydrogen transport near a blunting crack tip, *J Mech Phys Solids*, 1999; 47:971-992
215. D.P. Williams, H.G. Nelson, Gaseous hydrogen embrittlement of Aerospace materials, *Astronautical Research* (1973), pp.323-330.
216. V. Frick, G.R. Janser and J.A. Brown, in *Space Shuttle Materials*, Vol. 3, Society of Aerospace Materials and Process Engineers (1971), pp.597-634
217. R.P. Jewet, R.J. Walter, W.T. Chandler and R.P. Frohberg, Hydrogen-Environment Embrittlement of Metals, *NASA Technology Survey* (1972).
218. Eggert D.Reese, "EU FP7 Multiscale modelling hydrogen Embrittlement-MultiHy" report, Airbus Group Innovations report (2012).
219. Torsten Sebald, "EU FP7 Multiscale modelling hydrogen Embrittlement-MultiHy" report, Airbus Defense and Spaces report (2013).
220. S.J. Klima, A.J. Nachtigall, C.A. Hoffman, Preliminary investigation of effect of hydrogen on stress-rupture and fatigue properties of an Iron-, a Nickel-, and a Cobalt-base Alloy, *NASA Report TN D-1458*, National Aeronautics and Space Administration, Cleveland, Ohio, Dec. 1962.

221. Hugh R. Gray, Hydrogen Environment Embrittlement, Technical paper report (1972).
222. J. Woodtli, R.Kieselbach, Damage due to hydrogen embrittlement and stress corrosion cracking, *Engineering Failure Analysis*, 7 (2000) pp.427-450.
223. M. Kamaya, A simulation on growth of multiple small cracks under stress corrosion, *Int. J. Fract.*, 130 (2004) pp. 787-801.
224. ABAQUS Version 6.11. User's manual, Dassault Systemes, 2013.
225. T. Sumigawa, T. Kitamura, K. Ohishi, Slip behaviour near a grain boundary in high-cycle fatigue of poly-crystal copper, *Fract. Eng. Mater. Struct.* 27 (2004) pp. 495-503.
226. Francis Preli F and Furrer D, 2014: 'Lessons Learned from the Development, Application and Advancement of Alloy 718', Proceeding of the 8th International Symposium on Superalloy 718 and Derivatives, TMS (The Minerals, Metals and Materials Society); ed. By Eric Ott, Anthony Banik, Joel Andersson, Ian Dempster, Tim Gabb, Jon Groh, Karl Heck, Randy Helmink, Xingbo Liu, and Agnieszka Wusatowska- Sarnek, September 28-October 1, 2014, Pittsburgh, Pennsylvania, USA, pp. 3-14.
227. Preli F and Furrer D, 2014: 'Lessons Learned from the Development, Application and Advancement of Alloy 718', Proceeding of the 8th International Symposium on Superalloy 718 and Derivatives, TMS (The Minerals, Metals and Materials Society); ed. by Eric Ott, Anthony Banik, Joel Andersson, Ian Dempster, Tim Gabb, Jon Groh, Karl Heck, Randy Helmink, Xingbo Liu, and Agnieszka Wusatowska- Sarnek, September 28-October 1, 2014, Pittsburgh, Pennsylvania, USA, pp. 3-14 and Sims C T, 1987: 'Superalloy II – High temperature materials for aerospace and industrial power', John Wiley and Son.
228. W.L. Mankins, S.lamb, *Metals Handbook, nickel and Nickel Alloys*, Vol.2, 10th Ed., ASM international 1990;p.428.
229. P.Hicks, C.Alstetter, Hydrogen-enhanced cracking of superalloys, *Metall Trans A* 1992; 23A:237-249.
230. M.G. Fontana, *Corrosion Engineering*, 3rd ed. 1986, McGraw- Hill Book Company, NY
231. P.H. Pumphrey, Grain boundary structure and properties, D.A.Chadwick, G.A. Smiths, eds., Academic Press, London (1976), pp. 139-200
232. L.Priester, *Grain Boundaries from Theory to Engineering*, Springer, (2012).
233. D.G.Brandon, The structure of High-Angle grain boundaries, *Acta Metallurgica* 14 (1966), pp. 1479-1484.
234. O.E. Kebir, A.Szumner, Comparison of hydrogen embrittlement of stainless steels and nickel-based alloys, *Int. J Hydrogen energy* 2002;27:793-800.
235. B. Yildiz, A. Nikiforova, S. Yip, Metallic interfaces in harsh chemo-mechanical environments, 41 (2009) 21-38.
236. M.Seita,J.P.Hanson,S.Gradecak,M.J.Demkowicz, The dual role of coherent twin boundaries in hydrogen embrittlement, *Nature Communications* 6 (2015),pp. doi:10.1038/ncomms7164
237. H.Mori, R.Ito, T.Kozakai, *Mater Sci Eng* 50 (1981), pp.243.
238. Y.Kaneko,K.Kitagawa,S.Hasinoto, *Interface Sci* 7 (1999):147
239. S.Kobayashi,T.Inomata,H.Kobayashi,S.Tsurekawa,T.Watanabe, Effects of grain boundary- and triple junction-character on intergranular fatigue crack nucleation in polycrystalline aluminium, *J Mater Sci* 43(2008), 3792-3799.
240. A.Heinz,P.Neumann, *Act Metall Mater* 38(1933).

241. V.Randle, *Acta Metall* 43(1995), 1741.
242. S.Kobayashi,S.Tsurekawa,T.Watanabe, *Acta Mater* 53(2005), 105
243. S.Onaka, F.Tajima,S.Hashimoto,S.Miura, *Acta Metall Mater* 43(1995), 307.
244. Y..Gao, J.S.Stolken M.Kumar,R.O.Ritchie, High-cycle fatigue of nickel-base superalloy Rene 104 (ME3): Interaction of microstructurally small cracks with grain boundaries of known character, *Acta Mater* 55(2007),3155.
245. Y.Gao,M.Kumar,R.K.Nalla,R.O.Ritchie, *Metall Mater Trans* 36A(2005),3325.
246. B.A.Wilcox, G.C.Smith, Intercrystalline fracture in hydrogen-charged nickel, *Acta Metallurgica* 13(1965), 331-343.
247. N. Winzer, “EU FP7 Multi-Scale Modelling Hydrogen Embrittlement - MultiHy”, IWM report (2015).
248. X. Xu, M. Wen, S. Fukuyama, K. Yokogawa, Simulation of Hydrogen Embrittlement at Crack Tip in Nickel Single Crystal by Embedded Atom Method, *Materials Transactions* 42 (2001) 2283-2289.
249. H. Fukushma, H.K. Birnbaum, Surface and grain boundary segregations of deuterium in nickel, *Acta Matall*, 32 (1984) 851.
250. L. Viskari, M. Hornqvist, K.L. Moore, Y. Cao, K. Stiller, Intergranular crack tip oxidation in a Ni-base superalloy, *Acta Materialia* 61 (2013) 3630-3639.
251. J.C. Liu, A.D. Marwick, F.K. LeGoues, Hydrogen segeration and trapping in the Al/Si(111) interface, *Physical Review B* 44 (1991) 1861-1874.
252. D. Drabble, The effect of grain boundary engineering on the properties of Incoloy 800H/HT, PhD Thesis , University of Canterbury, (2010).
253. B.Landa, H.K.Birnbaum, *Acta Metallurgica* 35(1987) 2537-2542
254. A.Kimura and H.K. Birnbaum, *Act Metall.* 36 (1988) 757-766.
255. J.Yao, J.R. Cahoon, *Scripta Metallurgica* 22 (1988) 1817-1820.
256. Wert, Zener, *Phys. Rev.* 76 (1949) 1169.
257. Kehr, *Hydrogen in Metals I*, Alefeld & Volkl (1978).
258. E. Wimmer et al., *Physical Review B* 77.13 (2008) 1343
259. D.E.Jiang, E.A.Carter, *Physical Review B* 70 (2004) 064102.
260. D.D.Stefano,M.Mrovec, C.Elasasser, MultiHy meeting presentation (2014).
261. Oskar J.Haidn, *Advanced Rocket Engines*, Report RTO-EN-AVT-150
262. H.K.Birnbaum, B. Ladna and A. Kimura, *Journal De Physique* 49 (1988) C5-397-401.
263. F.D. Fischer, G. Mori, J. Sovoboda, Modelling the influence of trapping on hydrogen permeation in metals, *Corrosion Science* 76 (2013) 382-389.
264. A.N. Brass, A. Chanfreau, Electrochemical permeation of hydrogen in high purity nickel at 100°C, *Scripta Metallurgica et Materialia* 24 (1990) 499-504.
265. E. Demir, D.Raabe,N.Zaafarani,S.Zaefferer, *Acta Mater* 57 (2009) 559
266. N.Winzer, M.Mrovec, D.D.Stefano, C.Elasasser, “EU FP7 Multiscale modelling hydrogen Embrittlement- MultiHy” report, IWM report.